I. INTRODUCTION

In recent years significant research has been carried out aimed at developing a fundamental understanding of the phenomena involved in the transport of mixtures in nanoporous systems, such as adsorbents and membranes, which are crucial to many industrial separation processes. Carbon molecular-sieve membranes (CMSM) were the key focus early on in our DOE/BES-supported investigations (see Section II below). They are thought to be more stable and versatile than polymeric membranes, and capable of operating at higher temperatures, up to 300 ^{o}C. In our research the emphasis was on understanding the factors determining the ability of the CMSM to separate mixtures based on differences in molecular mobility, and in affinity to the pore surface. Our study involved: (1) the preparation and characterization of the CMSM; (2) the computational modeling of their structure, and (3) the measurement and computer simulations of sorption and transport of mixtures through the membranes. The membranes developed are currently undergoing field-testing by Media & Process Technology (M & PT), our industrial collaborators in the project.

In this research project we adopted the methodology and tools developed with the nanoporous CMSM to the preparation of novel membranes and films made of SiC.[1-5] Our efforts were motivated here by the growing interest in the hydrogen economy, which has necessitated the development of robust nanoporous films that can be used as membranes and sensors in high-temperature and pressure processes related to H_2 production. SiC is a promising material for these applications due to its many unique properties, such as high thermal conductivity,[6] thermal shock resistance,[7] biocompatibility,[8] resistance in acidic and alkali environments,[9] chemical inertness (e.g., towards steam, H_2S, NH_3, and HCl, of

particular concern for H_2 production from biomass and coal), and high mechanical strength.[10,11] Though the CMSM exhibit many similar good properties, they are themselves unstable in the presence of O_2 and steam at temperatures higher than 300 ^oC (conditions typically encountered in reactive separations for H_2 production). Other inorganic membranes, like ceramic (e.g., alumina, silica, and zeolite) and metal (Pd, Ag, and their alloys) membranes have, so far, also proven unstable, in such high-temperature applications in the presence of steam and H_2S.

The preparation of SiC nanoporous membranes involves two important steps. First, the preparation of appropriate SiC porous supports,[3] and second the deposition on these supports of crack- and pinhole-free, thin nanoporous SiC films.[1,2,4,5] Our early research, in collaboration with M & PT, focused on the preparation of quality porous SiC substrates.[3] Our recent efforts involved the deposition of thin nanoporous films on these substrates by the pyrolysis of pre-ceramic polymeric precursors.[4,5] We have made substantial strides in this area (as discussed further in Section II) preparing hydrogen-selective membranes and films.

The objective of the project was not only to advance the "state-of-the-art" of preparing the SiC membranes and films, but also to significantly broaden our understanding of factors that determine the ability of the SiC materials to separate gas mixtures, based on differences in molecular mobility and molecule-pore surface interactions. It is only such an improved fundamental understanding that will lead to further substantial improvements in the techniques for preparing such materials. In our studies we proceeded along two paths: (1) the preparation and characterization of SiC membranes, and the computational modeling of their molecular structure, and (2) the

measurement and simultaneous computer simulation of sorption and transport of mixtures through the membranes. Coupling experiments and simulations facilitated our efforts to relate the membrane's structure with its transport properties, and separation efficacy. This, in turn, enabled progress towards the long-term goal of first-principle molecular engineering and design of improved materials for adsorption and separation.

Understanding the transport characteristics of gas mixtures in SiC membranes is a problem of technological significance, as well as challenging technical complexity. A number of important issues that our study addressed, which are generic to the area of transport of gas mixtures through nanoporous systems, included:

- *The effect of preparation conditions on the degree and size/scale of heterogeneity of the membrane materials, and its implications for the degree of molecular-level understanding attainable*. Using the fundamental understanding at the nanoscale level to predict the overall transport and sorption behavior is a classical problem, which has yet to receive a satisfactory solution. The novel approaches that were developed here, e.g., of coupling network simulations at the macroscale level with detailed atomistic calculations at the nanoscale level have provide, in our opinion, great promise and are worth pursuing further. With the advent of modern computational techniques, of course, the interface between what is possible and not possible to simulate is constantly shifting, and the possibility of full atomistic simulations at the meso- and even the macro-scale level may not be that far away.
- *The relationship between atomistic models of nanoporous materials with the structures prepared and studied experimentally*. For studying amorphous nanoporous materials, one has at his/her disposal an array of techniques, such as surface analysis,

low-pressure sorption experiments, and transport measurements, all of which we used in this research. These techniques, to a varying degree, provide macroscopic rather than molecular-level understanding. A key issue that our research addressed is how atomistic structural models of SiC surfaces, validated with experiments using dense, solid thin films, performed in predicting the behavior of nanoporous systems. One key observation with the SiC materials (see discussion in Section II, below) is that transport characteristics of mixtures, predicted by atomistic calculations, are sensitive to the atomistic model parameters.

II. SUMMARY OF KEY PROJECT FINDINGS

Nanoporous membranes and adsorbents are important industrially. Though progress has been made in understanding their behavior, fundamental issues still remain unresolved. Chief among them is the effect of the material's morphology, such as its pore size distribution (PSD) and interconnectivity, on its transport characteristics and its ability to separate gas mixtures. Our project initially focused on the study of the transport and separation of gas mixtures through nanoporous CMSM. Our findings, as well as the methodology and tools developed, however, are of general applicability to all nanoporous materials prepared through the pyrolysis of polymeric precursors, including SiC membranes, which became the focus of the latter phases of our research. The following describes our key findings of our Project.

II1. Theoretical and Simulation Results

Towards gaining a deeper understanding of the transport/separation of gas mixtures in these materials, we developed realistic molecular models of the CMSM. A key focus was the development of an algorithm for generating 3-D porous CMSM

structures based on a Voronoi tessellation of space. As a first approximation, the solid membrane matrix was taken to consist of carbon (C) atoms with a graphitic structure. Large 3-D molecular pore networks were then generated by tessellating a simulation box of such C atoms by inserting a number of Poisson points (each utilized to construct a single Voronoi polyhedron), and designating a fraction of the polyhedra as the pores, with the remaining representing the solid matrix. The porosity and PSD of such a pore network can be controlled by adjusting the number of Poisson points and the procedure of allocating the pore space polyhedra. The structural model produces PSD in close agreement with the experimental data. We studied by MD simulations the adsorption of gas mixtures in such CMS molecular pore networks. To generate a realistic representation of the CMSM solid structure, we also developed efficient algorithms for generating such amorphous structures. We start with a crystalline C material (e.g., diamond), and heat it up (through MD simulations) until the material melts. We then quench the melted material back to the desired temperature, generating in the process an amorphous C material. We used the Brenner semi-empirical potential to represent the bonding between the C atoms. In order to speed up the computations, we use a parallel computational strategy. To create the CMSM pore structure, the simulation box is tessellated using the Voronoi algorithm. Non-equilibrium molecular dynamics (NEMD) simulations of the transport of gas mixtures in the 3D porous structures were carried out.

We also carried out NEMD simulations in the CMSM of the transport of CO_2, CH_4, and their mixtures under high-pressure, subcritical and supercritical conditions. The effect of various factors, such as the membrane's pore size, pore structure, fluid composition, temperature, and external pressure gradient, were investigated in detail. We

showed that, under such conditions, there is an optimal pore size and external pressure gradient during separation of a mixture into its constituents. We also considered mixtures of CO_2 and CH_4 together with low M.W. alkanes. We carried out experimental investigations of such mixtures in CMSM, as well as NEMD simulations in carbon nanopores at low (<10 atm) pressures. We showed that the 3-D membrane structure plays a fundamental role in mixture separation, significantly more so than for the CO_2/CH_4 case, and the single carbon nanopore is not an adequate model of the CMSM. This validates the need for using the 3-D models. To simulate mixtures of CO_2 with longer-chain flexible alkanes, we developed a NEMD code making use of a united-atom model, in which the CH_2 and CH_3 groups are considered as one interaction site. Bending and torsion potentials are included, and bond lengths are kept constant using the RATTLE algorithm. We also applied the configurational-bias Monte Carlo method in the NEMD control volumes, and studied the effect of the pore structure, and the imposed external potential on quantities such as the fluid fluxes, and the adsorption isotherms for a range of conditions. We also studied experimentally the separation characteristics of hexane/CO_2 mixtures under high-pressure subcritical/supercritical conditions utilizing nanoporous CMSM. In addition to providing a reality check for our simulations, these studies are of practical interest in the use of such membranes in various environmental applications, including *in situ* soil remediation.

II2. Experimental Results

As noted previously, the methodology and tools developed for the CMSM were utilized in the latter phases of our project for the study of SiC nanoporous membranes. Though CMSM exhibit many good properties, they are themselves unstable in the

presence of O_2 and steam at temperatures higher than 300 ^oC (conditions typically encountered in reactive separations for H_2 production). SiC is a promising material for these applications due to its many unique properties, particularly its chemical inertness towards steam, H_2S, NH_3, and HCl, of key concern for H_2 production from biomass and coal. Two different approaches have been utilized. One involves using CVD/CVI techniques, by which we have succeeded in preparing defect-free nanoporous membranes. The second approach involves the pyrolysis of pre-ceramic polymeric precursors, and was the technique of choice in this project.

Prior to our own study, we knew of only a handful of previous studies using CVD/CVI to prepare porous SiC membranes. None of these studies, however, reported the preparation of defect-free, nanoporous SiC membranes. Hong and Lai[16] used a hot-wall CVD reactor with the $SiH_4/C_2H_2/NH_3$ system. SiC-Si_3N_4 nanoparticles were formed in the gas phase at 1323 K, and deposited on and within the pore structure of a macroporous α-alumina support disk. The deposition resulted in a decrease in the average membrane pore size from 0.3 μ to 0.21 μ, and in a reduction in permeability by ~ 20%. Takeda *et al*[17] prepared SiC membranes by CVI into γ-Al_2O_3 membrane tubes, using SiH_2Cl_2/C_2H_2 in H_2, supplied to the porous tube during heating at 800-900 ^oC, followed by a period of evacuation. The support tube was subjected to a number of CVI evacuation cycles, each cycle reducing the H_2 permeance through the membrane. The final membranes had a H_2 permeance of $1x10^{-8}$ $mol.m^{-2}.s^{-1}.Pa^{-1}$ at 350 ^oC, with an ideal selectivity towards N_2 of 3.36 (the Knudsen value is 3.74). Lee and Tsai [18] prepared asymmetric SiC membranes by low-pressure CVD of SiH_4/ C_2H_2/Ar mixtures at 800 ^oC on the surface of Al_2O_3-doped SiC macroporous supports. The support itself had an

asymmetric structure, i.e., the Al_2O_3 content decreased from its center to the surface. The CVD process reduced the pore size from 297 nm to 14 nm, at the cost, however, of a large reduction in permeance. Sea *et al.*[19] formed a SiC membrane within the pores of support tube via CVD of $(C_3H_7)_3SiH$ (tri-isopropylsilane or TPS) at 700-750 ^oC. After CVD, the resulting membrane was calcined at 1000 ^oC in Ar. XPS analysis showed the membrane to consist of pure SiC. The membranes were tested with pure-gas (He, H_2, N_2, CO_2, H_2O, CH_4, propane, i-butane, and SF_6) permeation experiments between 30-400 ^oC. A gas permeation test was also carried out with a H_2-H_2O-HBr mixture at a molar ratio of 0:49:0.5:0.01 between 200-400 ^oC. Single-gas permeation followed a Knudsen mechanism, with a H_2 permeance in the range (4-6) $x10^{-7}$ mol/m^2.s.Pa.

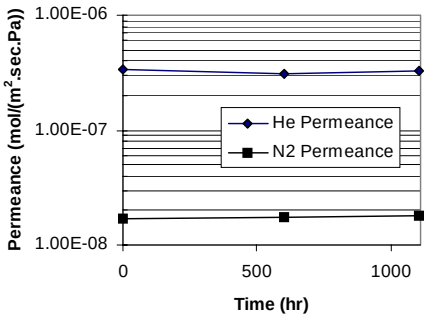

Fig. 1: SiC membrane thermal stability. Permeances as a function of time at 500 ºC.

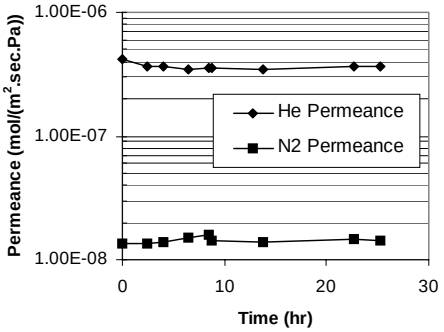

Fig. 2: Hydrothermal stability of a SiC membrane in steam (1-3 bar) at 400 ^oC.

The H_2:H_2O separation factor in the mixture was originally higher than the Knudsen value (~ 5), but membrane exposure to the mixture at 400 ^oC resulted in H_2 permeance decline during the first 50 h (~ 2.5 times), while the H_2O permeance remained constant. The H_2 permeance stabilized after that, for the remainder of the run (120 h). Pages *et al.*[20] prepared Si:C:H membranes on alumina supports using plasma-enhanced CVD of

diethylsilane; the resulting membranes had a permeance in the range of (10^{-7}-10^{-6}) mol m^{-2} s^{-1} Pa^{-1} for H_2, but with an ideal separation factor for H_2/N_2 in the range (3-4).

In our work, we have used a preparation procedure which is a variant of that of Sea *et al.*[19] Our CVD/CVI apparatus and further details are described elsewhere.[1] We used γ-Al_2O_3 membranes as substrates for the TPS deposition. They were calcined for 4 h in air at 1000 °C, which enlarges their pore size from 40 to 100 Å, but further treatment at this temperature leaves their size unaffected. For deposition, the membrane is sealed in a stainless-steel housing made of Swagelok-type fittings using graphite packing. The membranes were deposited with TPS in He at 700-750 ºC for various times (2-20 min), until a certain pressure drop across the membrane developed (~ 0.55–0.7 atm). Following the deposition, the membranes are further annealed at 1,000 ºC for 2 h for further conversion to SiC, and then finally activated at 700-750 ºC in the presence of ~ 1.7 atm of steam to eliminate excess carbon, if present**.** XRD indicates that the membranes calcined at 1000 °C are mostly amorphous (SiC converts to a crystalline material at higher calcination temperatures).

The membranes were then characterized for their permeance, selectivity, and hydrothermal stability. Depending on the preparation conditions, the He permeance ranges from 8.06×10^{-8} mol/m^2sPa to 1.72×10^{-6} mol/m^2sPa with a He/N_2 selectivity from 4 to larger than 100 (He was used in these tests as a safe surrogate gas to H_2 for the routine characterization; their H_2 permeance is approximately 60-70 % of that of He).[1,2] The He permeance increases significantly with temperature, indicative of activated diffusion, whereas the permeances of gases with larger kinetic diameters (N_2, CH_4, CO_2, CO, and H_2O) decrease with temperature, indicative of Knudsen flow. These H_2-selective SiC

membranes exhibit excellent thermal stability at 500 °C for more than 1000 h (Fig. 1.), and are also stable in high-pressure and -temperature steam (Fig. 2).

The results above highlight the desired separation characteristics and thermal and hydrothermal stability of the SiC membranes prepared by our group with the CVD/CVI technique using TPS. The membranes are suitable for applications requiring H_2 separation at high temperature and harsh environments. However, the preparation procedure involves multiple steps, which makes it costly, and requires a very high-temperature ($\geq$ 1000 ^{o}C) treatment, which places a great burden on glass end-seals and membrane housing during the CVD/CVI process. More importantly, the high-temperature post-treatment further modifies the nanoporous structure of the membranes prepared at lower temperatures. Thus, the final product quality is difficult to predict and control, and from a membrane-manufacturing standpoint, the advantage of the *on-line* control of the CVD/CVI technique is lost. To overcome these challenges, we also pursued in this project another method for membrane preparation. It involved the conventional dip-coating technique through the use of a novel pre-ceramic polymeric precursor, and its controlled temperature pyrolysis.

Pre-ceramic polymers are currently attracting attention for producing ceramics, because they can be processed and formed at relatively low temperatures compared to the production of conventional ceramics. For example, ceramic films, fibers, and composites can all be prepared by shaping and curing of various pre-ceramic polymers, followed by further pyrolysis in order to obtain the desired ceramic materials.[21-25] Many different polyorganosilicon compounds, such as polysilazenes $(SiR_2NH)_n$,[25] polysilanes $(SiR_2Si_2)_n$,[24] and polysiloxanes $(SiR_2O)_n$[26] can be used as precursors to ceramics such as

SiC, SiOC, SiO_2, SiNC, and Si_3N_4. One of the most important families of SiC precursors are polycarbosilanes $(SiR_2CH_2)_n$ (PCS).[27,28] The first generation PCS produced by Yajima *et al.*[28] were cured using O_2. Consequently, the final ceramic product was silicon oxycarbide, containing oxygen in the backbone.

Morooka and coworkers[29-31] used such PCS to produce Si-O-C membranes on γ- and α-Al_2O_3 tubular substrates with an oxygen content of 13-18 wt%, using polystyrene (PS) as the pore former. A membrane prepared with 1% PS had a H_2 permeance of $4x10^{-8}$ $mol/m^2.s.Pa$ and an ideal H_2:N_2 selectivity of 20 at 773 K. The membranes were unstable in Ar at 1223 K. When exposed to a 7.8 wt.% H_2O in He at 773 K, the H_2 and N_2 permeances decreased by half during the first 24 h, and slowly after that for the remainder of the 72 h experiment. Suda *et al.*[32] followed a similar approach to prepare SiC membranes, but did not test their hydrothermal stability. Related is the work of Lee and Tsai,[33,34] who prepared Si-O-C membranes by the pyrolysis of polydimethylsilane (PMS). The PMS layer undergoes a thermolytic reaction at 733 K for 14 h under 1 atm of Ar (and is, likely, converted to a PCS-like material[33,35]), followed by O_2 curing at 473 K for 1 h. The layer was finally pyrolyzed at various temperatures from 523 to 1223 K to produce the membranes. The membrane pyrolyzed at 873 K had the best separation characteristics, exhibiting a He permeance of ~ $1.4 x10^{-9}$ $mol/m^2.s.Pa$, a H_2 permeance of ~ $2.7 x10^{-9}$ $mol/m^2.s.Pa$, and an ideal H_2:N_2 selectivity of 20 at 473 K. Membranes prepared at higher temperatures were not microporous. Exposure to steam increases the permeance, and returns the separation selectivities to their Knudsen values.[36] The materials were all XRD amorphous, consistent with prior work on silicon oxycarbide,[22]

showing that these materials convert to SiC only at temperatures >1400 ^{o}C, with emission of CO and SiO.

More recently, newer PCS types have been developed, which use other curing methods, such as UV radiation,[37,38] electron beam,[39] or heat treatment under an inert atmosphere,[40] in order to achieve a low-oxygen content in the final product, and with a Si:C ratio ~ 1. In our own research we utilize allyl-hydridopolycarbosilane (AHPCS), a partially allyl-substituted hydridopolycarbosilane (HPCS). Allyl substitution provides an added degree of control over the Si:C ratio, and the ceramic yield. Use of HPCS was first proposed by Interrante *et al.*[41-44] The primary pyrolysis product of both HPCS and AHPCS is a SiC ceramic. The increasing fraction of allyl groups slightly increases the carbon content and also makes the polymer cross-linkable at lower temperatures. In our initial efforts[1] the membranes were prepared with conventional dip-coating of macroporous SiC flat-disk substrates, made by pressureless sintering of SiC powders (the use of appropriate SiC substrates is key in the preparation of defect-free membranes, as the alumina substrates used in all prior investigations have different thermal expansion coefficients than the nanoporous SiC film, and are, therefore, prone to cracking during thermal cycling). The membranes possessed H_2 permeance in the range (10^{-8}-10^{-7}) mol m^{-2} s^{-1} Pa^{-1}, and had an ideal separation factor of about 20 for H_2/N_2 at 200 ^{o}C[1]. They proved thermally stable, but did not fare well in the presence of high-temperature steam, proving unstable. Since our early study[1], two other groups have prepared membranes by pyrolysis of PCS-type polymers cured in the absence of O_2. Suda *et al.*[45] prepared SiC membranes by dip-coating PCS on α-alumina tubes (PS was used as the pore former for some of the membranes). Their membranes exhibited ideal separation factors of (90-150)

for H_2/N_2, and H_2 permeance in the range of (1-3) × 10^{-8} mol m^{-2} s^{-1} Pa^{-1} at 373 K. Nagano *et al.*[46] prepared SiC membrane by dip-coating of PCS on γ-alumina supports, and reported H_2 permeance ~10^{-7} mol m^{-2} s^{-1} Pa^{-1}, and an ideal separation factor of (8-12) for H_2/N_2 at 873 K.

In summary, previous studies presented only single-gas permeation data. Moreover, other than the membranes prepared by our group using TPS CVD[1], the rest were shown to be unstable in steam. Our initial membranes prepared by AHPCS pyrolysis[1] showed good separation factors and thermal stability, but also proved unstable in steam. Subsequent to our initial effort[1], we focused our attention on developing a technique combining slip-casting with dip-coating[4] to significantly improve the reproducibility in preparing high quality membranes on tubular macroporous SiC substrates.

Fig. 3: SiC tubular supports sintered at 1700 °C for 3 h.

These were prepared using uniaxial cold-pressing of β-SiC powder together with the appropriate sintering aids. Planar supports used in the initial stages of the project, though

appropriate for the study of membranes at the lab-scale, are not suitable for scale-up and the preparation of large area membranes. In the latter stages of our project these substrates were, therefore, replaced with tubular SiC supports. Fig. 3 exhibits several such SiC supports, prepared using a home-made die. They were characterized using SEM, Archimedes, and permeation techniques (the supports in Fig. 3 have a porosity of ~28%, average pore size of 150 nm, tortuosity of 2).

The membranes prepared by combining slip-casting with dip-coating of these substrates exhibited an ideal H_2/CO_2 selectivity in the range of (42-96), a H_2/CH_4 ideal selectivity in the range of (29-78), and H_2 permeance in the range (10^{-9}-10^{-8}) mol m^{-2} s^{-1} Pa^{-1}see Table 1.

Table 1. Range of single-gas permeances and separation factors, measured at 200 ^oC, prepared by pyrolysis at 750 ^oC for 2 h.

		Single gas	
	H_2	**CH_4**	**CO_2**
Permeance×10^8 (mol m^{-2} s^{-1} Pa^{-1})	0.54-1.18	0.007-0.041	**0.006-0.028**
S.F. (H_2/gas)		**29-78**	**42-96**

Extrapolated to a temperature of 500 ^oC, the expected permeance for H_2 is of the order ~10^{-7} mol m^{-2} s^{-1} Pa^{-1}. By comparison, Pd and Pd-alloy membranes exhibited, around 500 ^oC, permeances in the range (10^{-7}-10^{-6}) mol m^{-2} s^{-1} Pa^{-1}. However, Pd membranes are known to be sensitive to the presence of H_2S and hydrocarbon impurities; use of Pd-

alloy membranes (e.g., Pd-Ag) also faces challenges for long-term usage at temperatures significantly higher than 500 ^{o}C. Separation factors measured with the same membranes, using equimolar binary mixtures of H_2 in CO_2 and H_2 in CH_4, were similar to the ideal selectivity values. More importantly, steam stability experiments with the membranes lasting 21 days[4], using an equimolar flowing mixture of He/H_2O at 200 ^{o}C, indicated some initial decline in the permeance of He, after which the permeance became stable at these conditions.

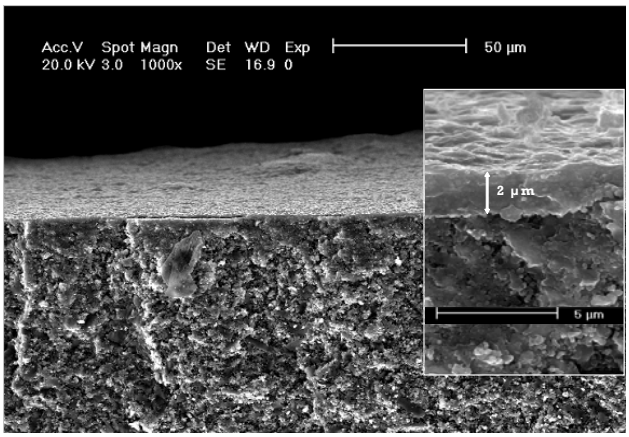

Fig 4: SEM pictures showing the cross-section and the top view of a SiC membrane

Slip-casting results in the formation of a film which adheres strongly onto the underlying SiC support, and provides a strong anchor for the thin dip-coated films. It is this film that is responsible for the superior hydrothermal stability of these membranes (compared to our initial membranes[1], which were prepared without support surface conditioning). In addition, the success rate in preparing "good" microporous membranes using the porous SiC tubes modified by slip-casting was much higher than when preparing membranes using the original support tubes. Figure 4 is the SEM picture of the cross-section and the top surface of one of these membranes. The thickness of the membrane layer is about 2 µ, and sits on the top of the SiC support.

Our most recent efforts make use of sacrificial interlayers for the preparation of nanoporous SiC membranes.[5] The method involves periodic and alternate coatings of polystyrene sacrificial interlayers and SiC pre-ceramic AHPCS layers on the top of slip-casted tubular SiC supports (a schematic of the preparation process is shown in Fig. 5).

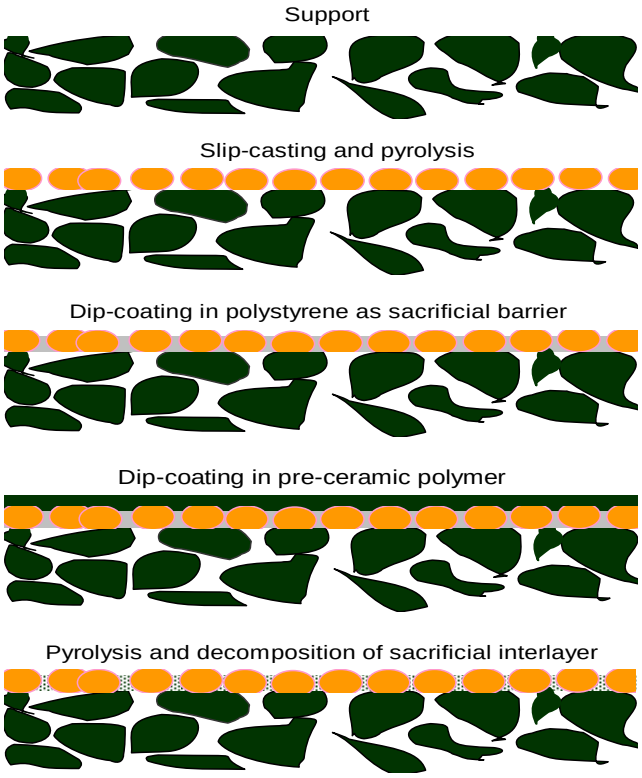

Fig. 5: A schematic of the new preparation technique.

Membranes prepared by this technique exhibit single-gas ideal separation factors of He and H_2 over Ar in the range of (176-465) and (101-256), respectively,[5] with permeances that are typically two to three times higher than those of SiC membranes prepared previously by us by the more conventional techniques (see Table 2).[4] Mixed-gas experiments with the same membranes indicate separation factors as high as 117 for an equimolar H_2/CH_4 mixture.[5] We speculate that the improved membrane characteristics are due to the sacrificial interlayers that fill the pores in the underlying structure and prevent their blockage by the pre-ceramic polymer.

Table 2. Range of single-gas permeances and separation factors, measured at 200 °C, for membranes prepared by pyrolysis at 750 °C for 2 h.

	He	**H_2**	**Ar**
Permeance×10^8 (mol m^{-2} s^{-1} Pa^{-1})	1.8-4.3	1.05-2	0.01
S.F. (gas/Ar)	176-465	101-258	

We have succeeded with our technique in increasing the membrane permeance, but without negatively impacting the membrane separation characteristics. Other researchers previously employed PS as a pore-forming agent (mixed in the PCS prior to layer formation) in order to increase the hydrogen permeance,[29,31,45] but their resulting membranes had a lower separation factor. This was attributed to phase separation and formation of PS domains during pyrolysis[29,45,47] to form mesoporous and macroporous regions, and potentially membrane defects. Sacrificial layers to prepare microporous inorganic membranes were previously utilized to prepare silica and zeolite membranes. Gavalas and coworkers,[48,49] for example, formed a carbon barrier layer (by polymerization and carbonization of furfuryl alcohol) inside the support pores during the preparation of silica and zeolite ZSM-5 membranes. Hedlund and coworkers[50,51] used wax as a masking layer against infiltration of precursors into the support for preparing MFI membranes. In these studies, the role of the sacrificial layer was to prevent infiltration of the membrane layer into the underlying support in order to reduce the membrane thickness, and to prevent crack formation. Though preventing film penetration into the underlying porous structure is also one of the roles that the PS sacrificial layers

play during SiC membrane preparation, their role during membrane formation is likely more complex, as PS has been shown previously[47] to impact not only the cross-linking process, but also the formation of the 3-D pore structure during PCS pyrolysis.

III. **REFERENCES**

1. Ciora, R.J., Fayyaz, B., Liu, P.K.T., Suwanmethanond, V., Mallada, R., Sahimi, M., and Tsotsis, T.T., *Chem. Eng. Sci*. 59 , 4957 (2004).

2. Fayyaz, B., Molaai-Nehzad, K., Patel, H.; Ciora, R., Liu, P., Sahimi, M., and Tsotsis T.T., F.T. Akin and Y.S. Lin, Eds., Inorganic Membranes. Proc. 8th Int. Symposium, p. 180-184, (2004).

3. Suwanmethanond, V., Goo, E., Johnston, G., Liu, P.K.T, Sahimi, M., and Tsotsis, T.T., *Ind. Eng. Chem. Res*. 39, 3264 (2000).

4. Elyassi, B., Sahimi, M., and Tsotsis, T.T., *J. Memb. Sci*. 288, 290 (2007).

5. Elyassi, B., Sahimi, M., and Tsotsis, T.T. *J. Mem. Sci*. 316, 73 (2008).

6. Takeda, K., Nakamura, K. Maeda, Y. Matsushita, T., *J. Am. Ceram. Soc.* 70, 266 (1987).

7. Schulz, K., and Durst, M., *Filtr. Sep*. 31, 25 (1994).

8. Rosenbloom, A.J., Sipe, D.M. , Shishkin, Y., Ke, Y., Devaty, R.P., and Choyke, W.J., *Biomed. Microdevice,* 6, 261 (2004).

9. Li, Z., Kusakabe, K., and Morooka, S. *J. Memb. Sci*. 118, 159 (1996).

10. Zorman, C. A., Fleischman, A.J., Dewa, A.S., Mehregany, M., Jacob, C., Nishino, S. and Pirouz, P., *J. Appl. Phys.* 78, 5136 (1995).

11. Kenawy, S.H., and Nour, W.M.N., *J. Mater. Sci.* 40, 3789 (2005).

12. Rajabbeigi, N., Elyassi, B., Sahimi, M., and Tsotsis, T.T., A Molecular Pore Network Model for Nanoporous Materials, Paper Presented at the 10th International Conference on Inorganic Membranes, Tokyo, Japan, August 18-22 (2008).

13. Gupta, P., Wang, W., and Fan, L.S., *Ind. Eng. Chem. Res*. 43, 4732 (2004).

14. Keller, N., Pham-Huu, C., Estournes, C., and Ledoux, M.J., *Cat. Lett.* 61, 151 (1999).

15. Keller, N., Pham-Huu, C., Roy, S., and Ledoux, M.J, *J. Mater. Sci*. 34, 3189 (1999).

16. Hong, L.S., and Lai, H.T., *Ind. Eng. Chem. Res*. 38, 950 (1999).

17. Takeda, Y., Shibata, N., and Kubo, Y., *J. Cer. Soc. Jpn*. 109, 305 (2001).

18. Lee, L. L., and Tsai, D.S., *J. Amer. Ceram. Soc*. 81, 159 (1998).

19. Sea, B.K., Ando, K., Kusakabe, K., and Morooka, S., *J. Memb. Sci*. 146, 73 (1998).

20. Pages, X., Rouessac, V., Cot, D., Nicias, G., and Durand, J., *Sep. Purif. Technol*. 25, 399 (2001).

21. Zheng, G. B., Sano, H., Uchiyama, Y., Kobayashi, K., and Cheng, H.M., *J. Mater. Sci.* 34, 827 (1999).

22. Sato, K, Tezuka, A, Funayama, O, Isoda, T, Terada, Y, Kato, S, and Iwata, M, *Compos. Sci. Tech*. 59, 853 (1999).

23. Tanaka, T., Tamari, N., Kondo, I., and Iwasa, M., *Ceram. Intern*. 24, 365 (1998).

24. Chew, K.W., Sellinger, A., and Laine, R.M., *J. Am. Ceram. Soc*. 82, 857 (1999).

25. Jones, R.; Szweda, A., and Petrak, D., *Composites, Part A: Appl. Sci. Manufacturing* 30, 569 (1999).

26. Suttor, D., Erny, T., and Greil, P., *J. Am. Ceram. Soc*. 80, 1831 (1997).

27. Shimoo, T., Tsukada, I., Narisawa, M., Seguchi, T., and Okamura, K., *J. Ceram. Soc. Jpn*. 105, 559 (1997).

28. Yajima, S., Okamura, K., Hayashi, J., and Omori, M., *J. Amer. Cer. Soc*. 59, 324 (1976).

29. Li, Z., Kusakabe, K., and Morooka, S., *Sepn. Sci. Technol*. 32, 1233 (1997).

30. Kusakabe, K., Li, Z.Y., Maeda, H., and Morooka, S., *J. Memb. Sci*. 103, 175 (1995).

31. Li, Z., Kusakabe, K., and Morooka, S., *J. Memb. Sci*. 118, 159 (1996).

32. Suda H., Yamauchi H., Uchimaru Y., Fujiwara I., Haraya K., Paper PM-036, Presented at ICOM2005, Seoul, Korea, August 21-26 (2005).

33. Lee, L. L., and Tsai, D.S., *J. Amer. Cer. Soc*. 82, 2796 (1999).

34. Lee, L. L., and Tsai, D.S., *Ind. Eng. Chem. Res*. 40, 612 (2001).

35. Williams, H.M., Dawson, E.A., Barnes, P.A., Rand, B., Brydson R.M.D., and Brough, A.R., *J. Mater. Chem*. 12, 3754 (2002).

36. Chen, C.L., and Tsai, D.S., 2004. *J. Memb. Sci*. 237, 163 (2004).

37. Takeda, M., Saeki, A., Sakamoto, J., Imai, Y., and Ichikawa, H., *J. Amer. Ceram. Soc*. 83, 1063 (2000).

38. Chu, Z. Y., Song, Y.C., Xu, Y.S., and Fu, Y.B., *J. Mater. Sci. Lett*. 18, 1793 (1999).

39. Seguchi, T., *Radiation Phys. Chem.* 57, 367 (2000).

40. Matthews, S., Edirisinghe, M. J., and Folkes, M. J., *Ceram. Intern*. 25, 49 (1999).

41. Interrante, L.V., Whitmarsh, C.K, Sherwood, W., Wu, H.J., Lewis, R., and Maciel, G.E., "Better Ceramics Through Chemistry IV" 346, 593 (1994).

42. Interrante, L.V., Whitmarsh, C.K.; Yang, C.Y., Sherwood, W., Schmidt, W.R., Marchetti, P.S., and Maciel, G.E., Ceramic Transaction, "Silicon-Based Structural Ceramics" 57, 42 (1994).

43. Interrante, L.V., Whitmarsh, C.K., Sherwood, W., Wu, H.J., Lewis, R., and Maciel, G.E., NATO ASI Series Volume, "Application of Organometallic Chemistry in the Preparation and Processing of Advanced Materials", J.F. Harrod and R. Laine, eds., Kluwer Academic Publishers, 173 (1995).

44. Interrante, L.V., Whitmarsh, C.K., and Sherwood, W., "High Temperature Matrix Composites II, Ceramic Transaction" 58, 111 (1995).

45. Suda, H., Yamauchi, H., Uchimaru, Y., Fujiwara, I., and Haraya, K., *Desalination* 193, 252 (2006).

46. Nagano, T., Sato, K., Saitoh, T., and Iwamoto, Y., *J. Ceram. Soc. Jpn*. 114, 533 (2006).

47. Suda, H., Yamauchi, H., Uchimaru, Y., Fujiwara, I., and Haraya, K. *J. Ceram. Soc. Jpn*. 114, 539 (2006).

48. Jiang, S., Yan, Y., and Gavalas, G.R., *J. Memb. Sci*. 103, 211 (1995).

49. Yan, Y., Davis, M.E., and Gavalas, G.R., *J. Membr. Sci*. 126, 53 (1997).

50. Hedlund, J., Sterte, J., Anthonis, M., Bons, A.J. , Carstensen, B., Corcoran, N., Cox, D., Deckman, H., de Gijnst, W., de Moor, P.P., Lai, F. , McHenry, J. , Mortier, W., Reinoso, J. , Peters, J., *Microporous Mesoporous Mater*. 52, 17 (2002).

51. Hedlund, J., Jareman, F., Bons, A.J., and Anthonis, M., *J. Memb. Sci*. 222, 163 (2003).

IV. PUBLICATIONS RESULTING FROM THE PROJECT

- Firouzi, M., Molaai-Nehzad, K., Tsotsis, T.T., and Sahimi, M., Molecular Dynamics Simulations of Transport and Separation of Carbon Dioxide-Alkane Mixtures in Carbon Nanopores, *J. Chem. Phys*, 120, 8172, 2004.
- Fayyaz, B., Molaai-Nehzad, K., Patel, H.; Ciora, R., Liu, P., Sahimi, M., and Tsotsis T.T., "Nanoporous Silicon Carbide Membranes, Preparation and Reactive Applications," *Inorganic Membranes. Proceedings of the Eighth International Symposium on Inorganic Membranes*, F.T. Akin and Y.S. Lin, Eds., 180-184, 2004.
- Ciora, R.J., Fayyaz, B., Liu, P.K.T., Suwanmethanond, V., Mallada, R., Sahimi, M., and Tsotsis, T.T. "Preparation and Reactive Applications of SiC Membranes," *Chem. Eng. Sci.,* 59, 4957, 2004.
- Firouzi, M., Sahimi, M., and Tsotsis T.T., "Supercritical Fluids in Porous Composite Materials: Direction-Dependent Flow Properties," *Phys. Rev. E.,* 73, 036312, 2006.
- Elyassi, B., Sahimi, M., and Tsotsis, T.T., "Silicon Carbide Membranes for Gas Separation Applications," *J. Membrane Sci*., 288, 290, 2007.
- Firouzi, M., Sahimi, M., and Tsotsis T.T., "Molecular dynamics simulations of transport and separation of supercritical carbon dioxide-alkane mixtures in supported membranes," *Chem. Eng. Sci.*,62, 2777, 2007.

- Lim, S.Y, Kim, N, Tsotsis, T.T., and Sahimi, M., "Molecular Dynamics Simulation of Diffusion of Gases in Carbon Nanotube-Polyetherimide Polymer Composites," *Phys. Rev. E*, 76, 011810, 2007.
- Elyassi, B., Sahimi, M., and Tsotsis, T.T. "A novel sacrificial interlayer-based method for the preparation of silicon carbide membranes," *J. Membrane Sci.*, 316, 73, 2008.
- Chen, F., Mourhatch, R., Tsotsis, T.T., and Sahimi, M. "Experimental Studies and Computer Simulation of the Preparation of Nanoporous Silicon-Carbide Membranes by Chemical-Vapor Infiltration/Chemical-Vapor Deposition Techniques," *Chem. Eng. Sci.*, 63, 1460, 2008.
- Chen, F., Mourhatch, R., Tsotsis, T.T., and Sahimi, M., " Pore Network Model of Transport and Separation of Binary Gas Mixtures in Nanoporous Membranes," *J. Membrane Sci.*, 315, 48, 2008.
- Rajabbeigi, N, Elyassi, B., Tsotsis, T.T., Sahimi, M., "Molecular Pore-network Model for Nanoporous Materials. I: Application to Adsorption in Silicon-carbide Membranes," *J. Membrane Sci.*, 335, 5, 2009.
- Elyassi, B., Sahimi, M., and Tsotsis, T.T., "Fabrication of Amorphous Silicon-Carbide Nanofibers by a Template Technique," In Press, *J. Phys. Chem.*

Molecular dynamics simulations of transport and separation of carbon dioxide–alkane mixtures in carbon nanopores

Mahnaz Firouzi, Kh. Molaai Nezhad, Theodore T. Tsotsis, and Muhammad Sahimi[a)]
Department of Chemical Engineering, University of Southern California, Los Angeles, California 90089-1211

(Received 24 October 2003; accepted 29 January 2004)

The configurational-bias Monte Carlo method, which is used for efficient generation of molecular models of *n*–alkane chains, is combined for the first time with the dual control-volume grand-canonical molecular-dynamics simulation, which has been developed for studying transport of molecules in pores under an external potential gradient, to investigate transport and separation of binary mixtures of *n*–alkanes, as well as mixtures of CO_2 and *n*–alkanes, in carbon nanopores. The effect of various factors, such as the temperature of the system, the composition of the mixture, and the pore size, on the separation of the mixtures is investigated. We also report the preliminary results of an experimental study of transport and separation of some of the same mixtures in a carbon molecular-sieve membrane with comparable pore sizes. The results indicate that, for the mixtures considered in this paper, even in very small carbon nanopores the energetic effects still play a dominant role in the transport and separation properties of the mixtures, whereas in a real membrane they are dominated by the membrane's morphological characteristics. As a result, for the mixtures considered, a single pore may be a grossly inadequate model of a real membrane, and hence one must resort to three-dimensional molecular pore network models of the membrane.
 [DOI: 10.1063/1.1688313]

I. INTRODUCTION

Nanoporous materials, such as carbon molecular-sieve membranes (CMSM's) and zeolites, have been used extensively in separation and purification processes involving, for example, multicomponent gaseous mixtures. The typical sizes of the pores in such materials are near molecular dimensions, which enables us to separate the components of a mixture on the basis of differences in the rate of transport of the components, their adsorption on the pores' surfaces, and/or the differences in their shapes and molecular sizes. In addition, silica aerogels, which are nanoporous materials with highly unusual properties (such as very high porosity and mechanical strength), and nanoporous thin films have wide applications in manufacturing of low-dielectric constant materials, optical coatings, sensors, and insulating films.

Given the usefulness of nanoporous materials to a wide variety of practical applications, it is clearly important to understand how fluids and their mixtures are transported in their pore space,[1–4] and the mechanism(s) by which the mixtures' components are separated in such nanoporous materials as membranes. Since the main resistance to any transport process in such materials is offered primarily by their nano- and mesopores, and due to the exceedingly small sizes of such pores, the molecular interactions between the mixture's molecules, and also between them and the pores' walls, are important and cannot be ignored. Hence molecular modeling of these materials and the transport processes that take place in their pore space have attracted considerable attention. Many recent molecular studies have investigated transport of fluid mixtures in nanopores, resulting in a better understanding of the effect of confinement on the behavior of the fluids and their mixtures.

In this paper, we focus on separation of mixtures of normal alkanes (*n*–alkanes), and also mixtures of CO_2 and an *n*–alkane, by CMSM's. Although separation of *n*–alkanes by zeolites has been studied by many groups,[5–9] our study is, to our knowledge, the first that investigates their separation by CMSM's. Due to their thermal and mechanical stability and also versatility, CMSM's have been used by many groups,[10–20] as well as our own,[21–23] in studies involving separation of $CO_2/H_2/CH_4/N_2$ mixtures. In addition to their practical significance, these membranes allow one to carry out steady-state transport investigations, thus significantly simplifying the burden of data analysis and interpretation. Moreover, these membranes can be prepared with well-controlled porosity and a narrow pore size distribution. In this paper, the first one of a series, we report our preliminary results of experimental studies and molecular simulation of transport and separation of several binary mixtures involving *n*–alkanes in CMSM's.

Our molecular modeling is based on nonequilibrium molecular dynamics (NEMD) simulation, a technique ideally suited for the experimental situation in which an external driving force, such as a chemical potential or pressure gradient, is applied to the membrane. We utilize a dual control-volume grand-canonical MD (DCV-GCMD) technique, which has been used extensively in recent years.[24–38] We have used this method for molecular simulations of transport and separation of subcritical[39–42] as well as supercritical fluid

[a)]Corresponding author. Electronic mail: moe@iran.usc.edu

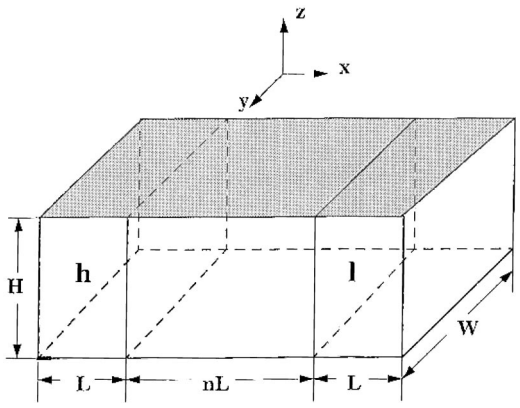

FIG. 1. Schematics of the slit pore used in the simulations. The h and ℓ regions represent the high- and low-pressure control volumes, respectively.

mixtures[43] in carbon nanopores, and in CMSM's with a pore space consisting of interconnected pores.[42] The alkane chains are generated by the configurational-bias Monte Carlo method. To our knowledge, this is the first time that the DCV-GCMD method is combined with the configurational-bias Monte Carlo technique.

The plan of this paper is as follows. In the next section, we describe the pore model that we employ in our simulations. Next, the molecular models of the gases are described, after which we describe the growth of the alkane chains by the configurational-bias Monte Carlo method. We then describe the DCV-GCMD technique. The results are then presented and analyzed.

II. MODEL OF CARBON NANOPORE

As the first step toward understanding transport and separation in CMSM's of the mixtures of interest to us in this paper, we consider the same phenomena in a single carbon nanopore. Recent molecular simulations by Düren *et al.*[44] indicate that transport in a nanopore is hardly influenced by the pore's shape, so long as the correct average radius, transport length, and enclosing gradient are used. Therefore we consider a slit pore, the schematics of which are shown in Fig. 1, in which the origin of the coordinates is at the center. The two carbon walls are located at the top and bottom of the xy planes. The external driving force is a chemical potential or, equivalently, a pressure gradient applied in the x direction. The system is divided into three regions. The h and ℓ regions represent, respectively, the two control volumes (CV's) exposed to the bulk fluid at high and low chemical potential or pressure, while the middle region represents the pore. The pore's length is nL with n being an integer.

The pore's walls are assumed to be smooth (structureless), since our previous MD studies of various mixtures[39–43] in such pores indicated that the walls' atomistic structure has little effect on the transport and separation properties. The dimensions of the pore used were, $W=20\sigma_1$ and $L=40\sigma_1$, while its height H was varied, in the range of typical pore sizes for which CMSM's exhibit molecular sieving properties, in order to study the effect of the pore size on the results. Here, σ_1 is the effective molecular size of CH_4 (see below).

TABLE I. The conversion between the dimensionless and the actual units. Subscript 1 refers to the value of the parameters for CH_4.

Variable	Reduced form
Length L	$L^*=L/\sigma_1$
Energy U	$U^*=U/\varepsilon_1$
Mass M	$M^*=M/M_1$
Density ρ	$\rho^*=\rho\sigma_1^3$
Temperature T	$T^*=k_BT/\varepsilon_1$
Pressure P	$P^*=P\sigma_1^3/\varepsilon_1$
Time t	$t^*=t(\varepsilon_1/M_1\sigma_1^2)^{1/2}$
Flux J	$J^*=J\sigma_1^3(M_1/\varepsilon_1)^{1/2}$
Permeability K	$K^*=K(M_1\varepsilon_1)^{1/2}/\sigma_1$

III. MOLECULAR MODELS OF THE GASES AND THE INTERACTION POTENTIALS

We consider binary mixtures of CH_4/C_3H_8, CH_4/C_4H_{10}, and CO_2/C_3H_8. The CH_4 and CO_2 molecules are represented as Lennard-Jones (LJ) spheres, characterized by effective LJ size and energy parameters, σ and ε. All the quantities of interest are made dimensionless with the help of the CH_4 parameters, σ_1 and ε_1. Table I lists the conversions between the dimensionless and dimensional quantities.

The C_3H_8 and C_4H_{10} molecules are grown by a configurational-bias Monte Carlo method, which is described in the next section. These molecules are represented by a united-atom (UA) model.[45] In this model, the CH_2 and CH_3 groups are considered as single interaction centers with their own effective potentials. The nonbonded interactions between interaction centers of different molecules are described with a cut-and-shifted LJ potential,

$$U(r)=\begin{cases} U_{\mathrm{LJ}}(r)-U_{\mathrm{LJ}}(r_c), & r\leqslant r_c, \\ 0, & r>r_c, \end{cases} \tag{1}$$

where $U_{\mathrm{LJ}}(r)$ is the standard LJ 6-12 potential, and we used, $r_c=11.43$ Å. No tail corrections were applied to this potential. The Lorentz–Berthelot mixing rules, $\epsilon_{ij}=\sqrt{\epsilon_i\epsilon_j}$ and $\sigma_{ij}=\frac{1}{2}(\sigma_i+\sigma_j)$, were used in the simulations to compute the size and energy parameters of the unlike molecules. For simplicity the total molecular mass of an alkane was equally divided between the C atoms and therefore CH_2 and CH_3 groups had equal molecular mass. Table II lists the size and energy parameters of CH_4, CO_2, and those of the CH_2 and CH_3 groups.

The atoms and the UA centers are connected by harmonic potentials. The distance between the atoms is fixed at 1.53 Å. The intramolecular interactions consist of the contributions by bond-bending (BB) and torsional forces. For the BB term, the van der Ploeg–Berendsen potential[46] is used,

$$U_{\mathrm{BB}}(\theta)=\tfrac{1}{2}k_\theta(\theta-\theta_0)^2, \tag{2}$$

where θ is the angle between the atomic bonds. For the torsional potential, the original Ryckaert–Bellemans[47] potential is used,

TABLE II. Values of the molecular parameters used in the simulations. k_B is the Boltzmann's constant.

Parameter	Numerical value
σ_{CH_2} (Å)	3.905
σ_{CH_3} (Å)	3.905
σ_{CH_4} (Å)	3.810
σ_{CO_2} (Å)	3.794
ε_{CH_2}/k_B (K)	59.38
ε_{CH_3}/k_B (K)	88.06
ε_{CH_4}/k_B (K)	148.1
ε_{CO_2}/k_B (K)	225.3
Bond length (Å)	1.53
k_θ (K rad^{-2})	62,500
θ_0 (degrees)	112
c_0 (K)	1116
c_1 (K)	1462
c_2 (K)	−1578
c_3 (K)	−368
c_4 (K)	3156
c_5 (K)	−3788

$$U_{\text{tor}}(\phi)=\sum_{k=0}^{5} c_k \cos^k(\phi), \tag{3}$$

where ϕ is the dihedral angle. Numerical values of all the parameters are also listed in Table II.

As mentioned earlier, the pore's walls were assumed to be smooth and structureless. Therefore the 10-4-3 potential of Steele,

$$U_{iw}(z)=2\pi\rho_c\varepsilon_{iw}\sigma_{iw}^2\Delta\left\{\frac{2}{5}\left(\frac{\sigma_{iw}}{z}\right)^{10}-\left(\frac{\sigma_{iw}}{z}\right)^{4}-\frac{\sigma_{iw}^4}{3\Delta(0.61\Delta+z)^3}\right\}, \tag{4}$$

was used to compute the interaction between a molecule and the wall, where $\Delta=0.335$ nm is the space between the adjacent carbon layers, $\rho_c=114$ nm^{-3} is the number density of carbon atoms in the layer, z is the distance from the wall, and σ_{iw} and ε_{iw} are the LJ parameters between the walls and molecule i.

IV. CONFIGURATIONAL-BIAS MONTE CARLO METHOD

Because direct generation of the n−alkanes and their insertion into the CV's that are connected to the nanopore greatly slows down the simulations, we used the configurational-bias Monte Carlo (CBMC) technique[48–55] to grow the alkane molecules. We then combined the CBMC method with the grand-canonical MC technique to insert the grown alkane chains in the two CV's and therefore in the nanopore. The atom-by-atom growth of the molecules is done in such a way that regions of favorable energy are identified, and overlap with other molecules are avoided, hence speeding up the computations greatly.

More specifically, we consider the potential energy of an atom as the sum of two contributions, namely, the internal energy u^{int} which includes parts of the intramolecular interactions, and the external energy u^{ext} which contains the intermolecular interactions and those intramolecular interactions that are not part of the internal energy. The division is, of course, to some extent arbitrary and depends on the details of the model. The procedure to grow an n−alkane atom by atom consists of the following steps:[54]

(i) One inserts the first atom at a random position and computes the energy $u_1(n)$ along with a quantity $w_1=\exp[-\beta u_1(n)]$, where $\beta=(k_BT)^{-1}$, with k_B being the Boltzmann's constant, T is the temperature of the system, and n indicates the new state in which the system is in.

(ii) k trial orientations, denoted by $\{\mathbf{b}_k\}=\mathbf{b}_1,\mathbf{b}_2,\ldots,\mathbf{b}_k$, are then generated with a probability $p_l^{\text{int}}(\mathbf{b}_i)$, given by

$$p_l^{\text{int}}(\mathbf{b}_i)=\frac{1}{C}\exp[-\beta u_l^{\text{int}}(\mathbf{b}_i)], \tag{5}$$

in order to insert the next atom l, where C is a normalization factor. For each trial orientation, the *external energy* $u_l^{\text{ext}}(\mathbf{b}_i)$ is also computed, along with the quantity, $w_l(n)=\Sigma_{j=1}^{k}\exp[-\beta u_l^{\text{ext}}(\mathbf{b}_j)]$. One orientation, out of the k trial positions, is then selected with the probability

$$p_l^{\text{ext}}(\mathbf{b}_i)=\frac{1}{w_l(n)}\exp[-\beta u_l^{\text{ext}}(\mathbf{b}_i)]. \tag{6}$$

Typically, five trial orientations were generated, since our preliminary simulations with as many as $k=20$ trial orientations did not result in large differences.

(iii) Step (ii) is repeated $M-1$ times until the entire alkane molecule is grown, and the Rosenbluth factor,[56] $W(n)=\Pi_{l=1}^{M}w_l(n)$, is computed. Any given molecular conformation is generated with a probability given by

$$P(n)=\prod_{l=2}^{M} p_l^{\text{int}}(n)p_l^{\text{ext}}(n)=\frac{1}{C^{M-1}W(n)}\exp[-\beta U(n)], \tag{7}$$

with $U=\Sigma_{l=1}^{M}u_l=\Sigma_{l=1}^{M}(u_l^{\text{int}}+u_l^{\text{ext}})$.

V. CONFIGURATIONAL-BIAS GRAND-CANONICAL MONTE CARLO METHOD

After generating the n−alkanes and accepting them, the next step is to insert them into the two CV's. To do this, we combine the CBMC method described above with a grand-canonical MC method and refer to it as the CBGCMC technique. This is a method for computing the sorption thermodynamics of linear-chain molecules when the sorbates are represented with a UA force field and have flexible dihedral and bond angles, and consists of two steps: First, it generates the chain configurations one atom at a time by the CBMC method described above. Second, as the chain molecule is generated, the Rosenbluth weight[56] W is accumulated and

utilized in the acceptance rule of the GCMC method for insertion of the molecules into the system.

The probability of adding a single chain to a system of N_i chains is given by[55]

$$p^+ = \min\left[1, \frac{\exp(\beta\mu_i)V}{\Lambda_i^3(N_i+1)}W(n)\right], \tag{8}$$

where μ_i is the chemical potential of chain i, V is the volume of the CV, and Λ_i is the thermal de Broglie wavelength of component i. Equation (8) is completely similar to the probability of inserting a molecule into a system in a standard GCMC computation, with the main difference being the inclusion of the Rosenbluth weight W. For a deletion from the system, the Rosenbluth weight is evaluated by *pretending* to grow the alkane chain into its current position. To accomplish this, the quantities, $w_1(o)=\exp[-\beta u_l(o)]$, $w_l(o)=\Sigma_{j=1}^{k}\exp[-\beta u_l^{\text{ext}}(\mathbf{b}_j')]$, and $W(o)=\Pi_{l=1}^{M}w_l(o)$ are computed, using $k-1$ trial orientations, together with the actual current position of the atom l, which form the set $\{\mathbf{b}_k'\}$, where o indicates the old state of the molecules. The probability of deletion of a chain from the system is then given by

$$p^- = \min\left[1, \frac{N_i\Lambda_i^3}{\exp(\beta\mu_i)V}\frac{1}{W(o)}\right], \tag{9}$$

which, aside from the Rosenbluth weight, is again similar to that of a standard GCMC computation. To insert the CO_2 and CH_4 molecules in the two CV's, the probabilities p^+ and p^- are computed according to the standard GCMC method, namely, the Rosenbluth factor W is replaced by $\exp(-\beta\Delta U)$, where ΔU is the potential-energy change of the system as a result of adding to, or removing a molecule from, the CV's.

VI. NONEQUILIBRIUM MOLECULAR DYNAMICS SIMULATIONS

The NEMD simulations consist of integration of Newton's equation of motion in the entire system, combined with the CBGCMC insertions and deletions in the two CV's. In the MD simulations the Verlet velocity algorithm was used to solve the equations of motion. During the motion of the n−alkanes in the system, the RATTLE algorithm[57] was used to satisfy the constraints imposed on the n−alkane chains. Isokinetic conditions were maintained by rescaling the velocity independently in all the three directions. It is essential to maintain the densities of each component in the two CV's at some fixed values, which are in equilibrium with two bulk phases, each at a fixed pressure and fluid concentration. The densities, or the corresponding chemical potentials of each

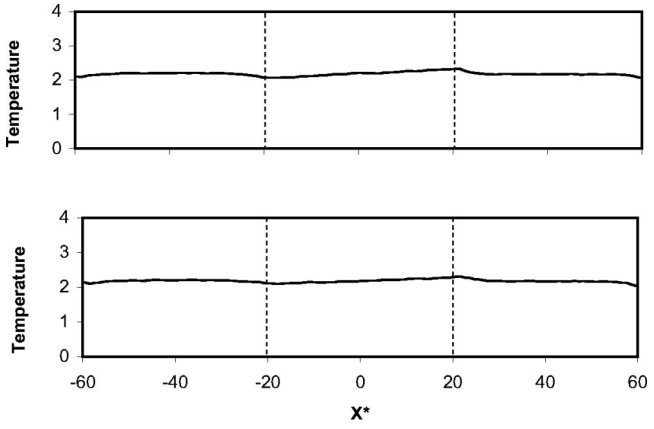

FIG. 2. Dimensionless temperature distribution in a pore of size $H^*=5$ and the two control volumes, containing mixtures of CH_4 and C_3H_8 with methane mole fraction in the feed being 0.7 (top) and 0.5 (bottom). Dashed lines indicate the boundaries of the pore region.

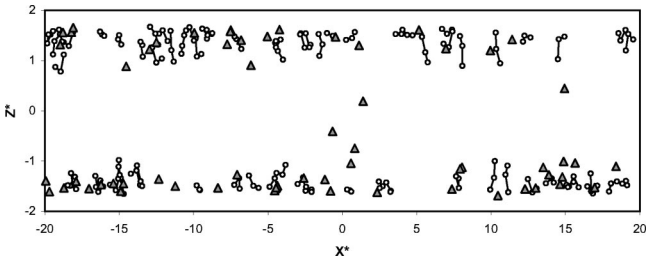

FIG. 3. Snapshot of the pore containing CH_4 (triangles) and C_3H_8 (chains), at steady state. The mole fraction of CH_4 in the feed is 0.9, and the pore size is $H^*=5$.

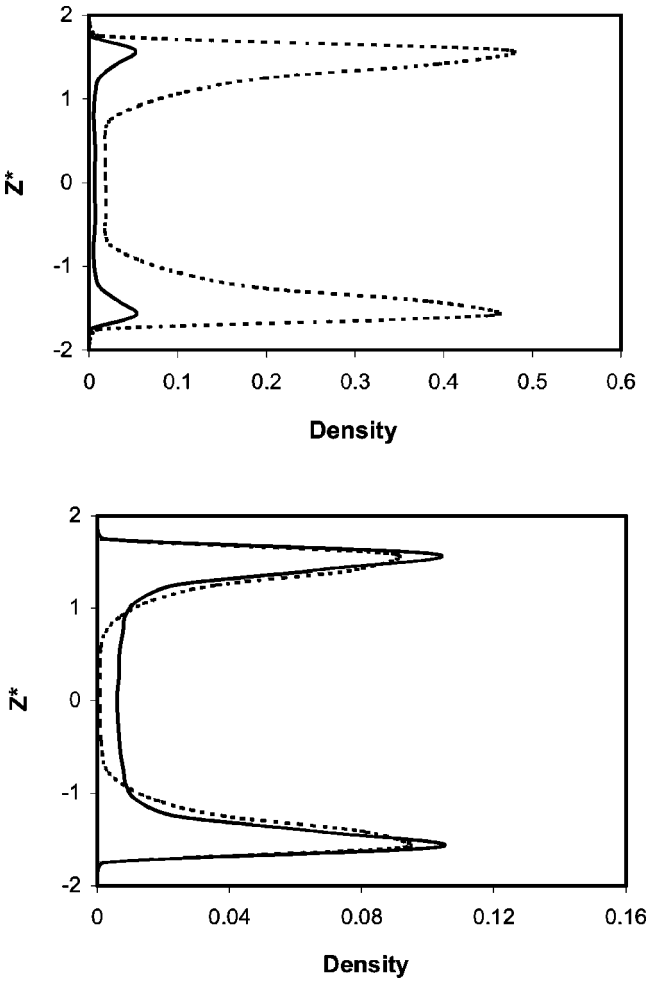

FIG. 4. Time-averaged density profiles of CH_4 (solid curves) and C_3H_8 (dashed curves) in the transverse direction (perpendicular to the walls), measured near the pore's center at $T=50\,^{\circ}\text{C}$. The pore size is $H^*=5$, while the mole fraction of CH_4 in the feed is 0.5 (top) and 0.9 (bottom).

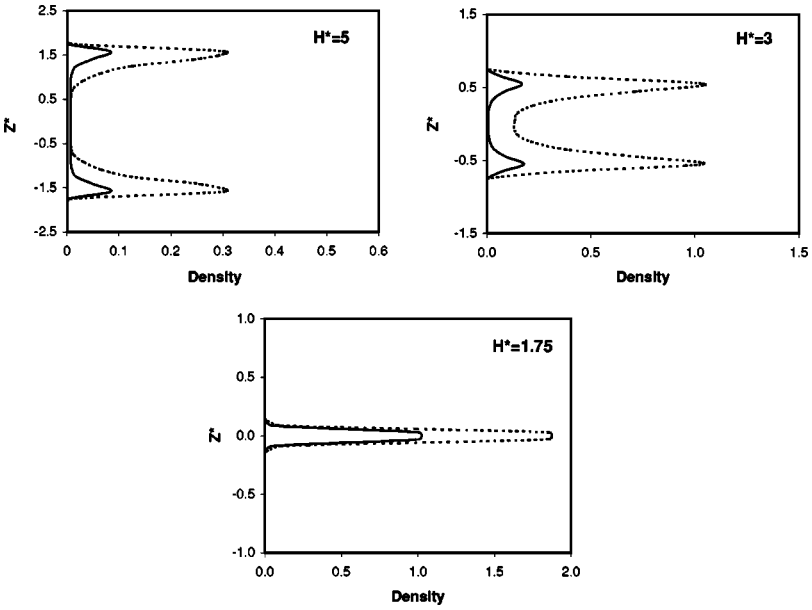

FIG. 5. Comparison of the time-averaged density profiles of CH_4 (solid curves) and C_3H_8 (dashed curves) in the transverse direction (perpendicular to the walls), measured near the pore's center at $T=50\,^{\circ}C$, in three pores. The mole fraction of CH_4 is 0.7.

component in the CV's, were maintained by carrying out a sufficient number of CBGCMC insertions and deletions of the particles, as described above. The chemical potentials were converted to equivalent pressures using a LJ equation of state.[58]

When a molecule is inserted in a CV, it is assigned a thermal velocity selected from the Maxwell–Boltzmann distribution at the given temperature T. An important parameter of the NEMD simulations is the ratio $\mathcal{R}$ of the number of CBGCMC insertions and deletions in each CV to the number of MD steps between successive CBGCMC steps. This ratio must be chosen appropriately in order to maintain the correct density and chemical potentials in the CV's, and also reasonable transport rates at the boundaries between the CV's and the pore region. In our simulations $\mathcal{R}$ was typically 10:1. During the MD computations molecules crossing the outer boundaries of the CV's were removed. The number of such molecules was, however, very small; typically about 1% of the total number of molecules that were deleted during the CBGCMC simulations with a probability that is given by Eq. (12). In addition, for each component we allowed for a nonzero streaming velocity (the ratio of the flux to the concentration of each component) in the pore region, consistent with the presence of bulk pressure/chemical potential gradients along the flow direction. Since the two CV's are assumed to be well-mixed and in equilibrium with the two bulk phases that are in direct contact with them, there should be no *overall* nonzero streaming velocity in these regions. However, the discontinuity of the streaming velocities at the boundaries between the CV's and the pore region slows down the computations. To address this problem, a very small streaming velocity was added to the thermal velocity of all the inserted molecules within each CV that were located within a very small distance from the boundaries between the CV's and the pore.[39–43,59,60] In the case of the *n*–alkanes, this was done when the lead atom or UA center was within that small distance, in which case the small velocity was assigned to all of the atoms and UA center of the alkanes. However, the actual streaming velocities of the molecules in the pore region were still determined by the MD simulations. To study the transport of a mixture due to a pressure gradient, the temperature of the system must be held constant in order to eliminate any contribution of the temperature gradient to the transport; hence special care was taken to achieve this (see also below).

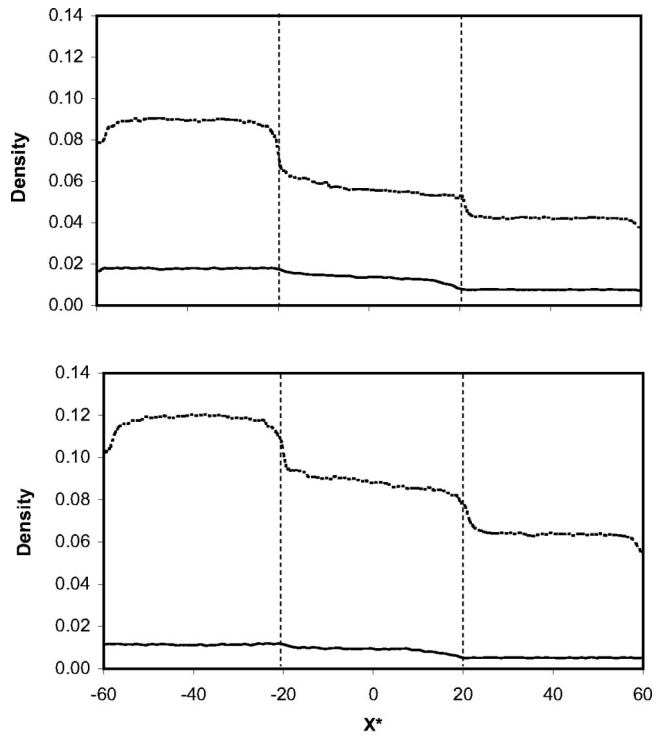

FIG. 6. Time-averaged density profiles of CH_4 (solid curves) and C_3H_8 (dashed curves) in the transport direction x in a pore of size $H^*=5$, in which the methane mole fraction in the feed is 0.7 (top) and 0.5 (bottom), and $T=50\,^{\circ}C$. Dashed lines indicate the boundaries of the pore region.

We computed several quantities of interest, including the density profiles of the component i along the x and z direc-

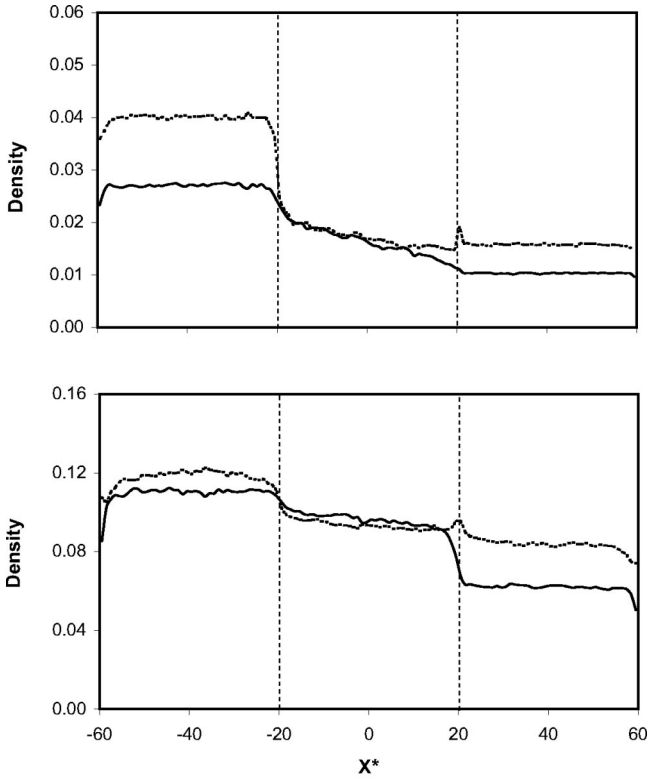

FIG. 7. Time-averaged density profiles of CH_4 (solid curves) and C_3H_8 (dashed curves) in the transport direction x in a pore of size $H^*=5$ in which the CH_4 mole fraction is 0.9. The upstream and downstream pressures are, respectively, 3 and 1 atm (top), and 30 and 10 atm (bottom). Dashed lines indicate the boundaries of the pore region.

tions, $\rho_i^z(x)$ and $\rho_i^x(z)$, respectively. To calculate $\rho_i^z(x)$ the simulation box was divided in the x direction into grids of size σ_1, and for each MD step the density profiles $\rho_i^z(x)$ were obtained by averaging the number of particles of component i over the distance σ_1. A similar procedure was used for computing $\rho_i^x(z)$, with the averaging done over a small distance which was about $0.16\sigma_1$. As discussed below, these quantities are important to understanding adsorption and transport properties of the fluids in the pore and between its walls.

For each component i we also calculated its flux J_i by measuring the net number of its particles crossing a given yz plane of area A_{yz}:

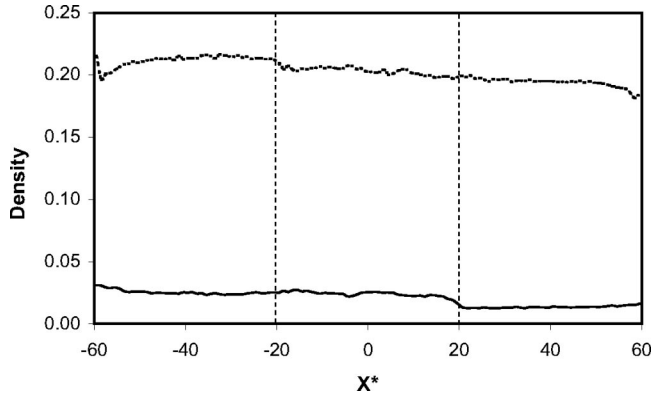

FIG. 8. Time-averaged density profiles of CH_4 (solid curve) and C_3H_8 (dashed curve) in the transport direction x in a pore of size $H^*=3$. The CH_4 mole fraction in the feed is 0.7, and $T=50\,^\circ$C.

$$J_i=\frac{N_i^{LR}-N_i^{RL}}{N_{\mathrm{MD}}\Delta t A_{yz}}, \tag{10}$$

where N_i^{LR} and N_i^{RL} are the number of the molecules of type i moving from the left to the right and vice versa, respectively, Δt is the MD time step (we used a dimensionless time step, $\Delta t^*=5\times10^{-3}$, which is equivalent to, $\Delta t \simeq 0.006\,85$ ps), and N_{MD} is the number of the MD steps over which the average was taken (we typically used $N_{\mathrm{MD}}=30{,}000$). The system was considered to have reached a steady state when the fluxes calculated at various yz planes were within 5% from the averaged values, after which the fluxes were calculated at the center of the pore region. The equations of motion were integrated with up to 3×10^6 time steps.

The permeability K_i of species i was calculated using

$$K_i=\frac{J_i}{\Delta P_i/nL}=\frac{nLJ_i}{\Delta P_i}, \tag{11}$$

where $\Delta P_i=x_i\Delta P$ is the partial pressure drop for species i along the pore, with x_i being the mole fraction of component i, and ΔP the total pressure drop imposed on the pore. A most important property that we wish to study is the dynamic separation factor S_{21}, defined as

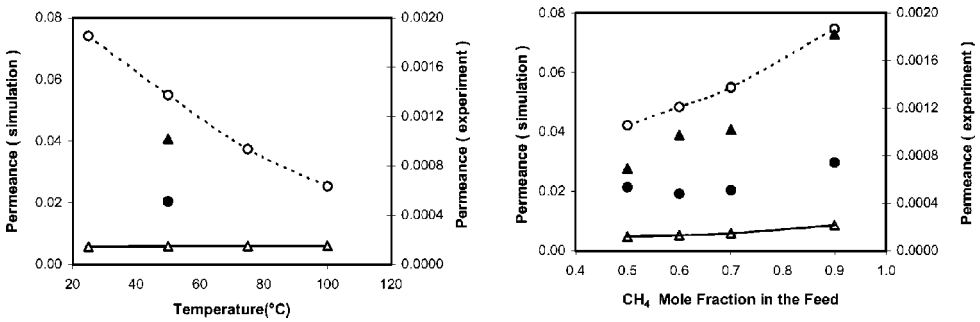

FIG. 9. Comparison of the simulation results for the permeance of CH_4 (open triangles) and C_3H_8 (open circles) with the corresponding experimental data (solid symbols). The mole fraction of CH_4 in the feed in the left figure is 0.7, while $T=50\,^\circ$C in the right figure. The pore size is $H^*=5$.

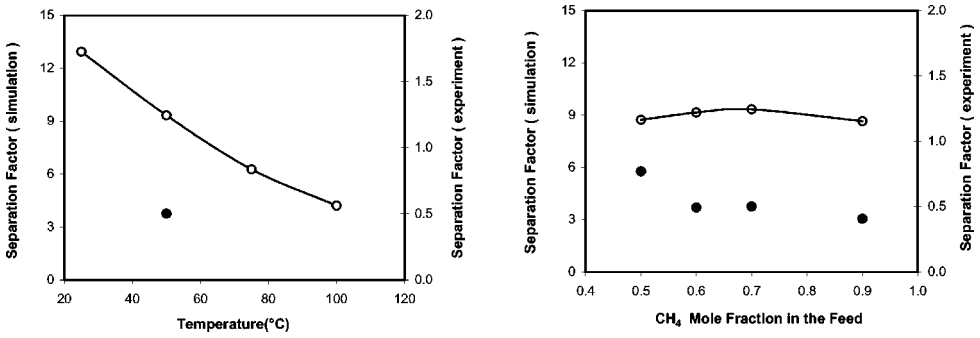

FIG. 10. Comparison of the computed separation factors (open circles) with the experimental data (solid circles) for a CH_4/C_3H_8 mixture. The mole fraction of CH_4 in the feed in the left figure is 0.7, while $T=50\,^{\circ}C$ in the right figure.

$$S_{21}=\frac{K_2}{K_1}. \tag{12}$$

VII. EXPERIMENTAL STUDY

We have also measured transport and separation properties of three mixtures, namely, CH_4/C_3H_8, CO_2/CH_4, and CO_2/C_3H_8 mixtures, in a CMSM. The average pore size of the membrane is about 4.5 Å, which is in the range of the pore sizes used in our simulations. The techniques for preparation of the membrane, as well as measuring its transport and separation properties, have all been described previously,[21–23] and need not be repeated here. All the experiments were carried out at $T=50\,^{\circ}C$. The pressure drop that was applied to the membrane was the same as the one used in the molecular simulations.

VIII. RESULTS AND DISCUSSIONS

We have carried out extensive NEMD simulations of three binary mixtures involving an *n*–alkane. In what follows, we present and discuss the results for each mixture separately, and compare the results with our experimental data, when possible. Unless otherwise specified, in all the cases discussed below, the pressures in the upstream and downstream CV's, that are in equilibrium with the two bulk states, are 3 and 1 atm, respectively.

A. Methane–propane mixtures

Figure 2 presents the time-averaged distribution of the dimensionless temperature in the carbon nanopore, for two different binary mixtures of CH_4 and C_3H_8. In this and the subsequent figures, the dashed lines indicate the boundaries of the pore region. The pore size is $H^*=H/\sigma_{CH_4}=5$, the mole fractions of CH_4 in the two mixtures are 0.5 and 0.7 and, in both cases, the temperature of the system is set at $T=50\,^{\circ}C$. As can be seen, the temperature in both cases is constant throughout the pore and its two CV's and, moreover, the two systems' temperatures are equal, as they should be.

Figure 3 shows a snapshot of the mixture in a pore of size $H^*=5$ at $T=50\,^{\circ}C$, in which the mole fraction of CH_4 in the feed is 0.9. Both components are mostly distributed near the pore's walls by forming two condensed layers there. These results are also consistent with equilibrium molecular simulations. The densities of both components decrease from the left to the right. To understand better the distribution shown in Fig. 3, we present in Fig. 4 the density profiles of the two components, in two different mixtures, over the cross section of a pore of size $H^*=5$, computed near its center. In the mixture in which the mole fraction of CH_4 in the feed is 0.9 (the bottom panel), the two density profiles are almost identical, except that CH_4 density is somewhat larger near the center, which is consistent with the snapshot of the system shown in Fig. 3. However, in the equimolar mixture (top

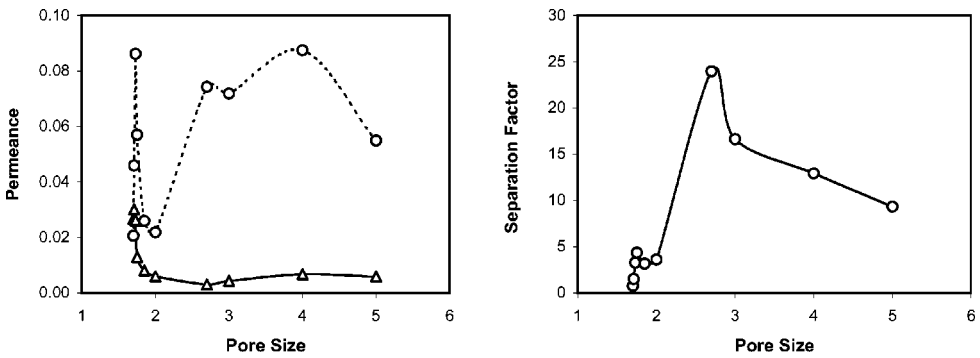

FIG. 11. The effect of pore size on the permeances of CH_4 and C_3H_8 and the corresponding separation factors in a binary mixture in which the CH_4 mole fraction in the feed is 0.7, and $T=50\,^{\circ}C$.

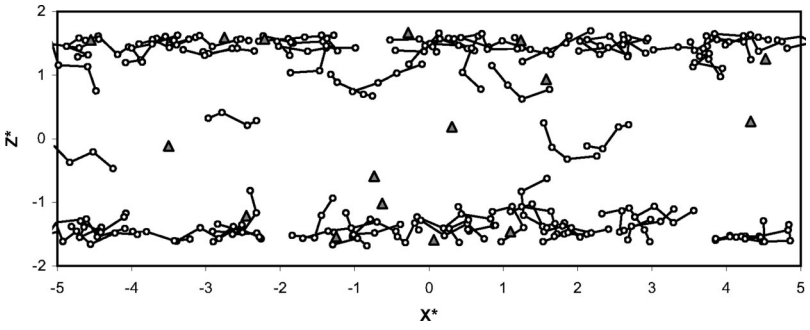

FIG. 12. A snapshot of the pore containing CH_4 (triangles) and C_4H_{10}, at steady state in a pore of size $H^*=5$ at $T=50\,^\circ$C. The CH_4 mole fraction in the feed is 0.9.

panel), the density of propane is larger than that of CH_4 everywhere in the pore. This is due to the much larger density of C_3H_8 under the bulk conditions (in the two CV's), which results in much larger amounts of propane entering the pore. At the same time, the C_3H_8 chains have a ''shielding'' effect in that, they prevent CH_4 from entering the pore region. Reducing the size of the pore shifts the profiles to the pore's center, since the location of the fluid-wall potential minima changes: Shown in Fig. 5 is the comparison between such density profiles for a mixture in which the CH_4 mole fraction in the feed is 0.7, in pores of sizes $H^*=5$,3, and 1.75 at $T=50\,^\circ$C. In all the cases, the density of C_3H_8 is much larger than that of CH_4, since the shielding effect mentioned above is even stronger for tighter pores. The fact that, in all cases, there is great overlap between the two density profiles is indicative of the mixture's tendency not to segregate into two distinct regions, each essentially filled with one of the components.

Another way of understanding the density profiles shown in Figs. 4 and 5 is as follows. If we were to represent C_3H_8 as a simple LJ sphere, then its effective energy parameter $\varepsilon_{C_3H_8}\simeq 1.6\varepsilon_{CH_4}$. Since the energy parameters control the interaction of the molecules with the pore's walls, it becomes clear why the density of C_3H_8 near the walls is much larger than that of CH_4, since it is energetically more favorable for C_3H_8 to adsorb on the pore's walls than CH_4. On the other hand, the effective LJ size parameter of C_3H_8 is not much larger than that of CH_4, hence explaining why the locations of the peaks in the density profiles of the two components are not far apart.

To shed further light on the properties of this system, we also study the density profiles in the two CV's and the pore along the transport ($x-$) direction. These are shown in Fig. 6, where we present the time-averaged density profiles for both components in two different mixtures in a pore of size $H^*=5$. The density profiles are essentially flat in the two CV's (in the region $-60<X^*<-20$ and $20<X^*<60$), with numerical values that match those obtained by the standard GCMC method under the same conditions, indicating that the chemical potentials in the two CV's have been properly maintained during the NEMD simulations. The small fluctuations in the profiles in the CV regions represent numerical noise. The small downward curvature at $X^*=-60$ (in the C_3H_8 profile) is due to the ''leakage'' of the molecules out of the two CV's. These are the molecules that, as described above, cross the outer boundaries of the CV's and leave the system. However, such deviations from a flat profile are insignificant. Note that even when the mole fraction of C_3H_8 in the feed is only 0.3 (top panel), its density in the two CV's is much larger than that of CH_4. In the pore region ($-20<X^*<20$), the two profiles decrease from left to right, which is expected. Due to the existence of the overall bulk pressure gradient (or an overall nonzero streaming velocity in the pore), however, the density profiles are not linear, as the total flux is the sum of the diffusive and convective parts,

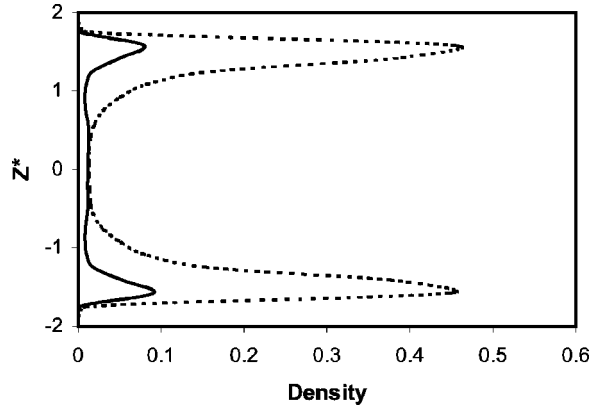

FIG. 13. Time-averaged density profile of CH_4 (solid curve) and C_4H_{10} (dashed curve), between the upper and lower walls of a pore of size $H^*=5$ at $T=50\,^\circ$C. The profiles were calculated in the middle of the pore, and CH_4 mole fraction in the feed is 0.9.

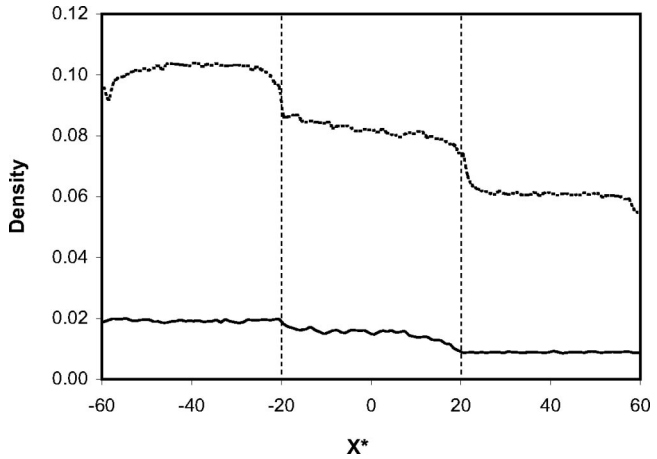

FIG. 14. Same as in Fig. 13, but in the transport direction x. Dashed vertical lines indicate the boundaries of the pore region.

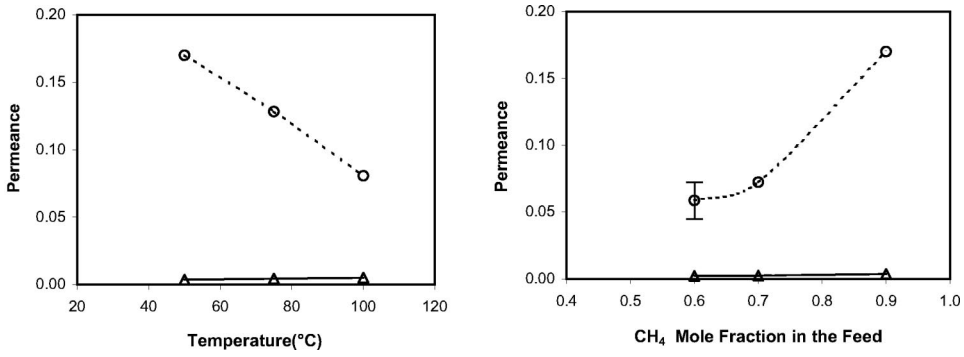

FIG. 15. The computed permeances of CH_4 (triangles) and C_4H_{10} (circles). The mole fraction of CH_4 in the feed in the left figure is 0.9, while $T=50\,^{\circ}C$ in the right figure.

resulting in nonlinear profiles for C_3H_8 in both mixtures. For CH_4, on the other hand, the convective effect is much weaker and therefore the decrease in its density and the associated nonlinearity are also much weaker. The qualitative aspects of the profiles shown in Fig. 6 will not change if we impose a larger pressure gradient on the pore system. Shown in Fig. 7 are the density profiles of the two components along the transport direction for two different systems. In one (the top panel) the upstream and downstream pressures are, respectively, 3 and 1 atm, while the corresponding pressures in the second pore system (the bottom panel) are ten times larger, 30 and 10 atm. The pore size for both cases is $H^*=5$. The CH_4 mole fraction in the feed for both cases is 0.9, and the simulations were carried out at $T=50\,^{\circ}C$. All the qualitative aspects of Figs. 6 and 7 are similar, except that the densities and their fluctuations in the pore under the larger pressure gradient are somewhat larger, as one might expect. These fluctuations will eventually vanish if the simulations are continued for much longer times. Our simulations also indicate that the separation factor of this system is insensitive to the applied pressure gradient. At the same time, the qualitative features of these profiles are not very sensitive to the pore size (unless, of course, the pore is too small). We show in Fig. 8 the density profiles in a pore of size $H^*=3$. The CH_4 mole fraction in the feed is 0.7, with the rest of the parameters being the same as in Figs. 6 and 7. The similarities between these profiles and those shown in Figs. 6 and 7 are clear.

Figures 9 present the dependence of the permeance (permeability per unit length of the pore) of the two components on the temperature and feed composition, and compare them with the experimental data. Several features of these figures are noteworthy:

(i) The experimental permeances are about two orders of magnitude smaller than those obtained by the molecular simulations. This is expected, as the CMSM possesses a tortuous three-dimensional pore space and therefore the gas permeances of such a pore space must be smaller than those of a single straight pore with no spatial tortuosity.

(ii) Both the simulations and experiments indicate that the permeances are not very sensitive to the composition of the mixture in the feed. For example, as the mole fraction of C_3H_8 in the feed increases from 0.5 to 0.9, its permeance (both computed and measured) changes by a factor which is less than 2, and an even smaller change is seen in the permeance of CH_4.

(iii) The permeance of CH_4 is practically independent of the temperature, while that of C_3H_8 decreaeses essentially linearly with increasing temperature.

Figures 10 present the separation factor $S_{21}=K_{C_3H_8}/K_{CH_4}$ for the mixture and its dependence on the temperature and feed composition. Although both the simulations and experiments suggest that the separation factor is not very sensitive to the feed composition, the experimental data do not agree with the simulation results. The reason is that the most effective mechanism of separating a CH_4/C_3H_8 mixture into its components is by molecular sieving and kinetic effects (the rates of transport of the two components), as it is much more difficult for the C_3H_8 chains to pass through the membrane with the same rate as the CH_4 molecules.

To study the effect of the pore size on the separation factors, we carried out extensive simulations using a range of pore sizes. Figures 11 show the results for the permeances and separation factors and their dependence on the pore size.

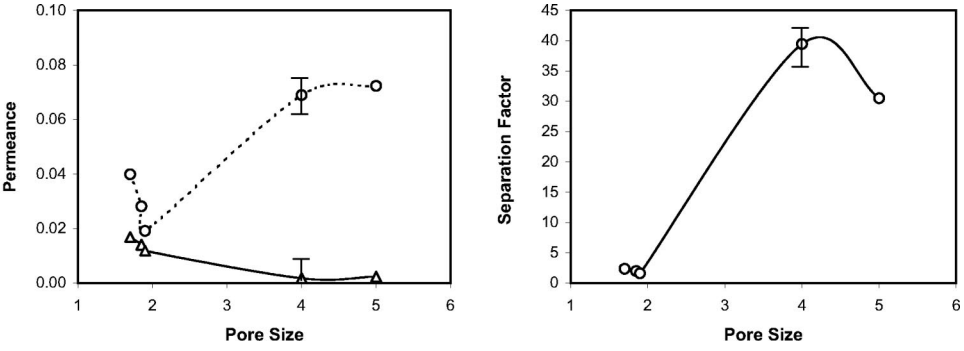

FIG. 16. The effect of pore size on the permeances of CH_4 (triangles) and C_4H_{10} (circles), and the corresponding separation factors at $T=50\,^{\circ}C$. The CH_4 mole fraction in the feed is 0.7.

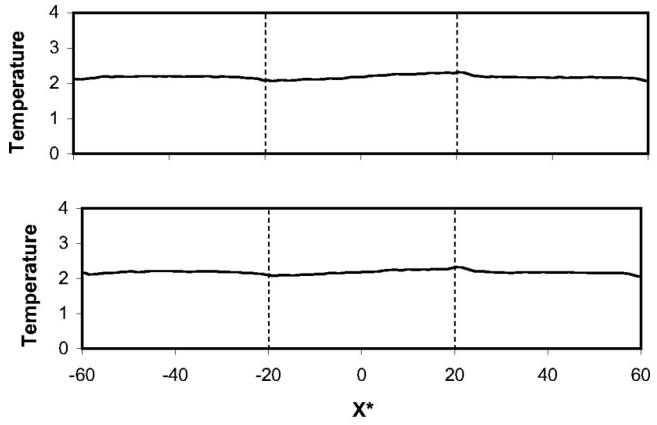

FIG. 17. Time-averaged temperature distribution in a pore of size $H^*=5$ and the two CV's that contain a binary mixture of CO_2 and C_3H_8. The mole fraction of CO_2 is 0.7 (top) and 0.5 (bottom). Dashed vertical lines indicate the boundaries of the pore.

The mole fraction of CH_4 in the feed is 0.7, and $T=50\,^{\circ}C$. Only when the pore size is $H^*=1.7$, does the separation factor fall below one (its value for a pore of size $H^*=1.7$ is about 0.8) and in the range of the experimental values (which, for this mixture, is about 0.5). This critical pore size is in fact the same as what we previously determined[41,42] to be the optimal size for the separation of certain binary mixtures, such as CO_2 and CH_4. Note also that, had we represented the C_3H_8 chains as LJ spheres, the critical pore size would have been about $H^*=2.15$, indicating the significance of the proper model of these molecules.

Therefore, to obtain quantitative results for the transport and separation properties of binary mixtures of CH_4 and C_3H_8, one must resort to three-dimensional (3D) molecular pore network models of CMSM's (Refs. 42, 61, and 62) in which interconnected pores of various shapes and sizes are distributed in the space. In such a system, one may have a type of phase separation such that the smaller pores carry CH_4, while larger pores contain the C_3H_8 chains. However, if the pores are not interconnected, then, no flux of the two components can pass through the pore network. Therefore the interconnectivity of the pores plays a fundamental role in the separation of the two components.

B. Methane–butane mixtures

Figure 12 presents a snapshot of the system at steady state in a pore of size $H^*=5$, in which the mole fraction of methane in the feed is 0.9. Clearly, despite the mixture being rich in CH_4, there is a lot more C_4H_{10} in the pore than CH_4, which is again attributed to the shielding effect described above. The corresponding time-averaged density profiles of CH_4 and $n-C_4H_{10}$ at $T=50\,^{\circ}C$ and in the same system are shown in Fig. 13. Similar to the CH_4/C_3H_8 mixtures, and consistent with Fig. 12, the density of n–butane is much larger than that of CH_4. This feature of the system can again be explained by defining an effective LJ energy parameter for n–butane, which would be larger than that of CH_4 by a factor of about 1.5, hence making it energetically more favorable for $n-C_4H_{10}$ to form a thick layer near the pore's walls. At the same time, the effective LJ size parameter of n–butane is about twice as large as that of CH_4. This, together with the fact that the actual molecular structure of n–butane is a chain with four atoms or UA centers, imply that as the components of the mixture attempt to enter the pore from a CV, there is a shielding effect that prevents many of the CH_4 molecules from entering the pore, as a result of which the density of n–butane inside the pore is much larger than that of CH_4.

Figure 14 depicts the time-averaged density profiles of the two components in the transport direction, both inside the two CV's and a pore of size $H^*=5$. The densities of the two molecules are essentially constant in the two CV's, with the density of $n-C_4H_{10}$ being much larger than that of CH_4. In between the two CV's, the two densities decrease from the upstream area to the downstream area in a nonlinear fashion, with the nonlinearity being due to the convective effect imposed on the system by the applied pressure gradient.

We show in Fig. 15 the dependence of the two components' permeances on the temperature and feed composition, in a pore of size $H^*=5$. The qualitative features of these results are similar to those for the CH_4/C_3H_8 mixture, shown in Fig. 9. Once again, the CH_4 permeance is essentially independent of its mole fraction in the feed, as well as the temperature of the system, while the permeance of $n-C_4H_{10}$ appears to vary linearly with both variables. As a result, the separation factor of the pore system, defined as $S_{21}=K_{C_4H_{10}}/K_{CH_4}$, also varies essentially linearly with the feed composition and the temperature. In addition, the simulations, for a range of pore sizes, yield large separation factors in favor of C_4H_{10}. Although we do not yet have experimental data for this mixture, we suspect, based on the CH_4/C_3H_8 mixtures discussed above and the physics of the problem, that in real membranes the separation factor would

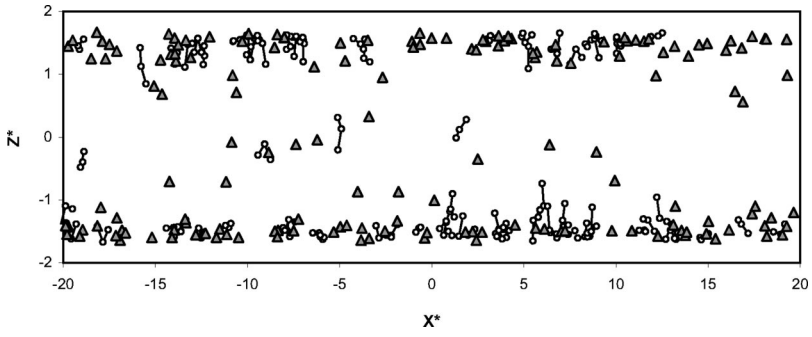

FIG. 18. Distribution of CO_2 (triangles) and C_3H_8 chains in a pore of size $H^*=5$ at $T=50\,^{\circ}C$, obtained at steady state. The CO_2 mole fraction in the feed is 0.9.

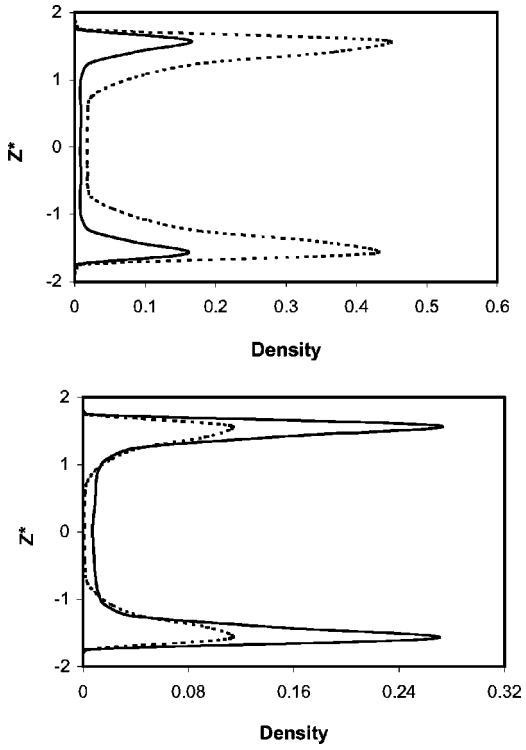

FIG. 19. Density profiles of CO_2 (solid curves) and C_3H_8 (dashed curves) between the upper and lower walls of a pore of size $H^*=5$, computed at the pore's center and obtained at steady state. The CO_2 mole fraction in the feed is 0.5 (top) and 0.9 (bottom), and $T=50\,^\circ$C.

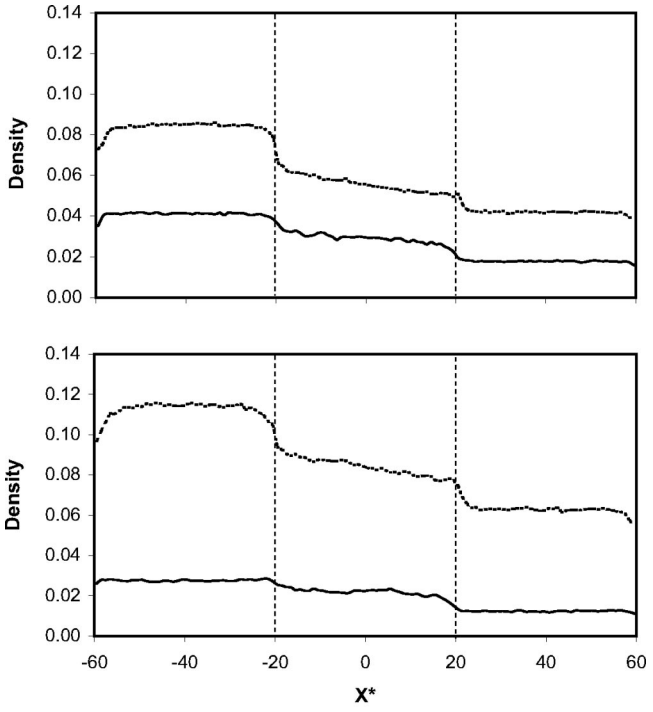

FIG. 20. Same as in Fig. 19, but in the transport direction x. The CO_2 mole fraction in the feed is 0.7 (top) and 0.5 (bottom), and $T=50\,^\circ$C. Dashed vertical lines indicate the boundaries of the pore.

be in favor of CH_4, the opposite of what the simulations indicate. To show this, we carried out extensive simulations to investigate the effect of the pore size on the permeances and the separation factors. Figure 16 presents the results, obtained at $T=50\,^\circ$C, for a mixture in which the CH_4 mole fraction is 0.7. Even for a pore as small as $H^*=1.7$, the separation factor is still about 2.4, indicating that a single pore is a gross representation of a membrane, at least so far as this mixture is concerned.

Let us mention in passing that insertion of n–alkanes in a tight pore by the CBMC method is difficult, since the atom or UA center of the chain that is closest to the pore's walls interacts with the walls much more strongly than the rest of the chain. As a result, the standard CBMC method fails when the pores are too tight and the alkane chains are initially inserted into the system near the walls. To address this problem, we initially inserted the alkane chains into the system only near its center.

C. Carbon dioxide–propane mixtures

In previous papers[21–23,39–43] we studied the CO_2/CH_4 mixtures in carbon nanopores. Figure 17 presents the (time-averaged) dimensionless temperature distribution in a pore of size $H^*=5$ and the two CV's, obtained with two different mixtures of CO_2 and C_3H_8. Once again, the temperature is essentially constant throughout the entire system, indicating that the isothermal condition has been maintained. A snapshot of the same system that contains a binary mixture in which the CO_2 mole fraction in the feed is 0.9 is shown in Fig. 18, indicating that most of the CO_2 molecules are near the pore's walls, forming a layer near each wall. This is confirmed by the (time-averaged) density profiles shown in Fig. 19 for two different mixtures of CO_2 and C_3H_8 in a pore of size $H^*=5$. The temperature of the system is $T=50\,^\circ$C, and the data are collected at the center of the pore. In the equimolar mixture (the top panel), the density of C_3H_8 near the walls is much larger than that of CO_2, since there is much more C_3H_8 in the pore than is CO_2. However, when the C_3H_8 mole fraction decreases to only 0.1 (the bottom

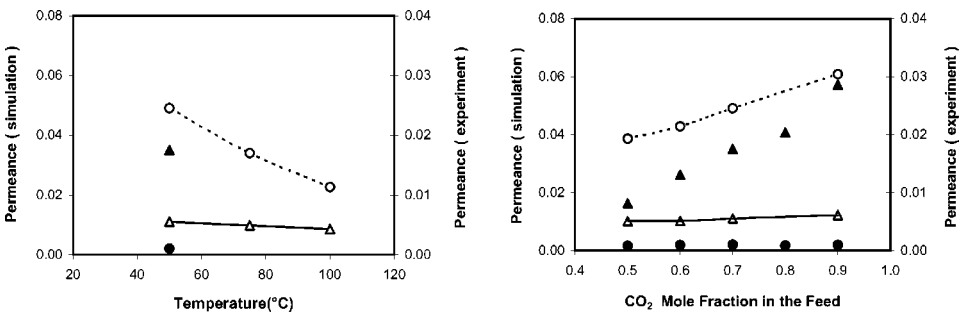

FIG. 21. Comparison of the computed permeances of CO_2 (open triangles) and C_3H_8 (open circles), for a pore of size $H^*=5$, with the corresponding experimental data (solid symbols). The CO_2 mole fraction in the feed in the left figure is 0.7, while $T=50\,^\circ$C in the right figure.

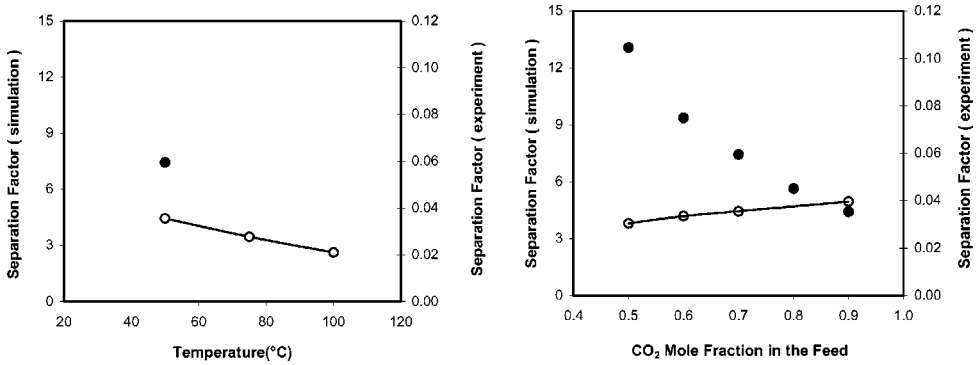

FIG. 22. Comparison of the computed separation factors of CO_2/C_3H_8 binary mixtures (open circles), for a pore of size $H^*=5$, with the experimental data (solid circles). The CO_2 mole fraction in the feed in the left figure is 0.7, while $T=50\,^\circ C$ in the right figure.

panel), its density inside the pore is much smaller than that of CO_2, which, together with the strong affinity of carbon dioxide for adsorption on carbon surfaces, mean that C_3H_8 can be present in the two layers near the walls only in relatively small amounts.

Figure 20 depicts the (time-averaged) density profiles of the two components, for two different binary mixtures, in the transport direction of the same pore as in Fig. 19. In both cases, the densities of the two components are constant in the two CV's, while they decrease nonlinearly from the upstream region to the downstream region. Although, in both cases, the mole fraction of CO_2 in the feed is larger than that of propane, the density of C_3H_8 is larger in both cases. This can be explained again based on the higher density of C_3H_8 under the bulk condition (in the two CV's) and the shielding effect described earlier.

The experimental data for the dependence of the two components' permerances on the temperature and feed composition are compared in Fig. 21 with the simulation results. The size of the pore is $H^*=5$. There are two noteworthy features in these results:

(i) The CO_2 permeance is essentially independent of the temperature and feed composition. This is due to the affinity of this molecule to adsorb on carbon surfaces, which means that CO_2 does not really "see" the pore structure. At the same time, the permeance of C_3H_8 varies essentially linearly with the temperature and composition.

(ii) Although there is quantitative agreement between the simulation results and the experimental data, so far as the order of magnitude of their numerical values is concerned, the trends in the two sets of results do not agree with each other: While the simulations indicate that $K_{C_3H_8}>K_{CO_2}$, the experimental data indicate the opposite trend.

This discrepancy is reflected in the separation factor, defined as, $S_{21}=K_{C_3H_8}/K_{CO_2}$. Shown in Fig. 22 are the separation factors, obtained for a pore of size $H^*=5$, where they are compared with the experimental data. Whereas the simulations indicate that $S_{21}>1$, the data indicate the opposite. To further study the effect of the pore size, we carried out extensive simulations at $T=50\,^\circ C$, using a mixture in which the CO_2 mole fraction in the feed was 0.7, and varied the pore size. The results are presented in Fig. 23. Only when the pore size H^* is below 1.97, does the separation factor fall below 1. For $H^*=1.95$, one has a separation factor of about 0.94, still about one order of magnitude larger than the experimental value. Had we represented C_3H_8 as a LJ sphere, the corresponding critical pore size would have been $H^*=2.28$, indicating again the significance of a proper model of n–alkanes.

Hence, similar to the mixtures of CH_4/C_3H_8 and CH_4/C_4H_{10}, the results for CO_2/C_3H_8 mixtures indicate that a single pore is inadequate for modeling a membrane which has a 3D pore space consisting of interconnected

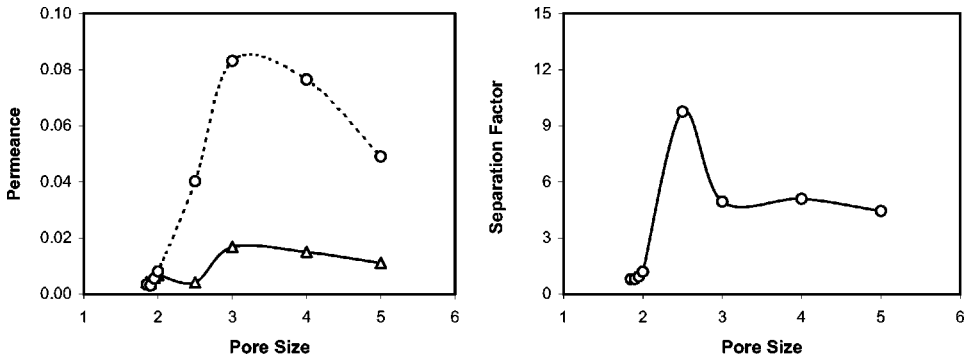

FIG. 23. The effect of the pore size on the permeances of CO_2 (triangles) and C_3H_8 (circles), and the corresponding separation factors at $T=50\,^\circ C$. The CO_2 mole fraction in the feed is 0.7.

pores of various shapes and sizes. That is, for the mixtures considered in this paper, the morphological characteristics of a membrane—its topology, or pore connectedness, and its geometry representing the pores' shapes and sizes—control its separation properties.

Let us mention that our previous studies[21,22,41,42] of CO_2/CH_4 mixtures in a single carbon nanopore, as well as in a molecular pore network, indicated qualitative agreement between the simulations results and the experimental data. This is due to the fact that for this mixture energetic effects dominate the separation process, as a result of which even a single pore model is adequate for obtaining qualitative insight into these phenomena. However, as our study described in this paper indicates, while transport and separation of mixtures involving CO_2 and $n-$alkanes ($n>1$), and also mixtures of various $n-$alkanes (and presumably many other mixtures) in a single pore, with almost any realistic size, are dominated by energetic effects, the same phenomena in a real membrane are controlled by its morphology, implying that a single pore is not a reasonable model of a real membrane, although such a model has been used extensively in the past.

IX. SUMMARY

Extensive molecular simulations, combining, for the first time, the configurational-bias Monte Carlo method and the dual control-volume-nonequilibrium molecular-dynamics technique, were carried out to study transport and separation of binary mixtures of $n-$alkanes, and also those involving CO_2 and an $n-$alkane, in a carbon nanopore. The driving force was a pressure (chemical potential) gradient. The effect of the composition of the feed and the size of the pore, as well as that of the temperature of the system, on the transport and separation of the mixtures were studied, and were compared with the experimental data. Our study indicates that, in a real membrane, transport and separation of the mixtures considered in this paper are dominated by the geometrical and topological characteristics of the membrane. As a result, a single carbon nanopore, in which only energetics of the system mostly control the transport and separation phenomena, is a grossly inadequate model and therefore one must resort to full three-dimensional molecular pore network models[42,63] for modeling these phenomena in a real membrane.

ACKNOWLEDGMENTS

We are grateful to the National Science Foundation, the Department of Energy, the Petroleum Research Fund, administered by the American Chemical Society, and Media & Process Technology for partial support of this work.

[1] M. Sahimi, *Heterogeneous Materials, Volume II* (Springer-Verlag, New York, 2003), Chap. 9.
[2] *Access in Nanoporous Materials*, edited by T.J. Pinnavaia and M.F. Thorpe (Plenum, New York, 1995).
[3] S. Torquato, *Random Heterogeneous Materials* (Springer-Verlag, New York, 2002).
[4] *Characterization of Porous Solids*, edited by K.K. Unger, J. Rouquerol, K.S.W. Sing, and H. Kral (Elsevier, Amsterdam, 1988).
[5] F. Kaptejin, W.J.W. Bakker, G. Zheng, J. Poppe, and J.A. Moulin, Chem. Eng. J. **57**, 145 (1995).
[6] H.H. Funke, M.G. Kovalchick, J.L. Falconer, and R.D. Noble, Ind. Eng. Chem. Res. **35**, 1575 (1996).
[7] K. Kusakabe, S. Yoneshige, A. Murata, and S. Morooka, J. Membr. Sci. **116**, 39 (1996).
[8] Z.A.E. Vroon, K. Keizer, M.J. Gilde, H. Verweij, and A.J. Burggraaf, J. Membr. Sci. **113**, 293 (1996).
[9] J.M. van de Graaf, F. Kaptejin, and J.A. Moulin, AIChE J. **45**, 497 (1999).
[10] J.E. Koresh and A. Soffer, Sep. Sci. Technol. **18**, 723 (1983).
[11] V.M. Linkov, R.D. Sanderson, and E.P. Jacobs, J. Membr. Sci. **95**, 93 (1994).
[12] C.W. Jones and W.J. Koros, Ind. Eng. Chem. Res. **34**, 164 (1995).
[13] Y.D. Chen and R.T. Yang, Ind. Eng. Chem. Res. **33**, 3146 (1994).
[14] G. Afrane and E.H. Chimowitz, J. Membr. Sci. **116**, 293 (1996).
[15] W. Shusen, Z. Meiyun, and W. Zhizhong, J. Membr. Sci. **109**, 267 (1996).
[16] A. Madhav, A.R. Brenda, H.C. Foley, M.P. Harold, and J.J. Lerou, Ind. Eng. Chem. Res. **36**, 2924 (1997).
[17] J. Peterson, M. Matsuda, and K. Haraya, J. Membr. Sci. **131**, 85 (1997).
[18] T. Naheiri, K.A. Ludwig, M. Anand, M.B. Rao, and S. Sircar, Sep. Sci. Technol. **32**, 1589 (1997).
[19] T. Steriotis, A.K. Beltsios, A.C. Mitropoulos, N. Kanellopoulos, S. Tenisson, A. Wiedenman, and U. Keiderling, J. Appl. Polym. Sci. **64**, 2323 (1997).
[20] M.B. Shiflett and H.C. Foley, Science **285**, 1902 (1999).
[21] M.G. Sedigh, W.J. Onstot, L. Xu, W.L. Peng, T.T. Tsotsis, and M. Sahimi, J. Phys. Chem. A **102**, 8580 (1998).
[22] M.G. Sedigh, L. Xu, T.T. Tsotsis, and M. Sahimi, Ind. Eng. Chem. Res. **38**, 3367 (1999).
[23] M.G. Sedigh, M. Jahangiri, P.K.T. Liu, M. Sahimi, and T.T. Tsotsis, AIChE J. **46**, 2245 (2000).
[24] E.J. Maginn, A.T. Bell, and D.N. Theodorou, J. Phys. Chem. **97**, 4173 (1993).
[25] G.S. Heffelfinger and F. van Swol, J. Chem. Phys. **100**, 7548 (1994).
[26] J.M.D. MacElroy, J. Chem. Phys. **101**, 5274 (1994).
[27] M. Lupkowski and F. van Swol, J. Chem. Phys. **95**, 1995 (1991).
[28] M. Sun and C. Ebner, Phys. Rev. A **46**, 4813 (1992).
[29] R.F. Cracknell, D. Nicholson, and N. Quirke, Phys. Rev. Lett. **74**, 2463 (1995).
[30] D.M. Ford and E.D. Glandt, J. Phys. Chem. **99**, 11543 (1995).
[31] D. Nicholson, R.F. Cracknell, and N. Quirke, Langmuir **12**, 4050 (1996).
[32] S.K. Kjelstrup and B. Hafskjold, Ind. Eng. Chem. Res. **35**, 4203 (1996).
[33] S. Sunderrajan, C.K. Hall, and B.D. Freeman, J. Chem. Phys. **105**, 1621 (1996).
[34] S. Furukawa, K. Hayashi, and T. Nitta, J. Chem. Eng. Jpn. **30**, 1107 (1997).
[35] G.S. Heffelfinger and D.M. Ford, Mol. Phys. **94**, 659 (1998).
[36] D.M. Ford and G.S. Heffelfinger, Mol. Phys. **94**, 673 (1998).
[37] A.P. Thompson, D.M. Ford, and G.S. Heffelfinger, J. Chem. Phys. **109**, 6406 (1998).
[38] P.I. Pohl and G.S. Heffelfinger, J. Membr. Sci. **155**, 1 (1999).
[39] L. Xu, M.G. Sedigh, M. Sahimi, and T.T. Tsotsis, Phys. Rev. Lett. **80**, 3511 (1998).
[40] L. Xu, T.T. Tsotsis, and M. Sahimi, J. Chem. Phys. **111**, 3252 (1999).
[41] L. Xu, M.G. Sedigh, T.T. Tsotsis, and M. Sahimi, J. Chem. Phys. **112**, 910 (2000).
[42] L. Xu, T.T. Tsotsis, and M. Sahimi, Phys. Rev. E **62**, 6942 (2000).
[43] M. Firouzi, T.T. Tsotsis, and M. Sahimi, J. Chem. Phys. **119**, 6810 (2003).
[44] T. Düren, S. Jakobtorweihen, F.J. Keil, and N.A. Seaton, Phys. Chem. Chem. Phys. **5**, 369 (2003).
[45] J.-P. Ryckaert and A. Bellemans, Faraday Discuss. Chem. Soc. **66**, 95 (1978).
[46] P. van der Ploeg and H.J.C. Berendsen, J. Chem. Phys. **76**, 3271 (1982).
[47] J.-P. Ryckaert and A. Bellemans, Chem. Phys. Lett. **30**, 123 (1975).
[48] J. Harris and S.A. Rice, J. Chem. Phys. **88**, 1298 (1988).
[49] G.C.A.M. Mooij, D. Frenkel, and B. Smit, J. Phys.: Condens. Matter **4**, L255 (1992).
[50] M. Laso, J.J. dePablo, and U.W. Suter, J. Chem. Phys. **97**, 2817 (1992).
[51] J.I. Siepmann and D. Frenkel, Mol. Phys. **75**, 59 (1992).
[52] J.J. dePablo, M. Bonnin, and J.M. Prausnitz, Fluid Phase Equilib. **73**, 187 (1992).

[53] D. Frenkel, G.C.A.M. Mooij, and B. Smit, J. Phys.: Condens. Matter **4**, 3053 (1992).
[54] B. Smit, S. Karaborni, and J.I. Siepmann, J. Chem. Phys. **102**, 2126 (1995).
[55] M.D. Macedonia and E.J. Maginn, Mol. Phys. **96**, 1375 (1999).
[56] M.N. Rosenbluth and A.W. Rosenbluth, J. Chem. Phys. **23**, 356 (1955).
[57] H.C. Andersen, J. Comput. Phys. **52**, 24 (1983).
[58] J.K. Johnson, J.A. Zollweg, and K.E. Gubbins, Mol. Phys. **78**, 591 (1993).
[59] M.G. Martin, A.P. Thompson, and T.M. Nenoff, J. Chem. Phys. **114**, 7174 (2001).
[60] G. Arya, H.-C. Chang, and E.J. Maggin, J. Chem. Phys. **115**, 8112 (2001).
[61] J. Ghassemzadeh, L. Xu, T.T. Tsotsis, and M. Sahimi, J. Phys. Chem. B **104**, 3892 (2000).
[62] L. Xu, T.T. Tsotsis, and M. Sahimi, J. Chem. Phys. **114**, 7196 (2001).
[63] M. Sahimi and T.T. Tsotsis, Physica B **338**, 291 (2003).

ELSEVIER

Chemical Engineering Science 59 (2004) 4957–4965

Chemical Engineering Science

www.elsevier.com/locate/ces

Preparation and reactive applications of nanoporous silicon carbide membranes

Richard J. Ciora[a], Babak Fayyaz[b], Paul K.T. Liu[a], Varaporn Suwanmethanond[b], Reyes Mallada[b], Muhammad Sahimi[b], Theodore T. Tsotsis[b,*]

[a]*Media and Process Technology Inc, 1155 William Pitt Way, Pittsburgh, PA 15238, USA*
[b]*Department of Chemical Engineering, University of Southern California, 925 Bloom Walk, HED 216 Los Angeles, CA 90089-1211, USA*

Received 1 March 2004
Available online 19 August 2004

Abstract

SiC nanoporous membranes have been prepared by chemical-vapor deposition/chemical-vapor infiltration of two different precursors, namely tri-isopropylsilane (TPS) and 1,3-disilabutane (DSB). Both precursors produce nanoporous membranes. The TPS-derived membranes are hydrothermally stable, while the DSB membranes produced, so far, are not. SiC nanoporous membranes have also been prepared by conventional dip-coating techniques using a novel pre-ceramic polymeric precursor allyl-hydridopolycarbosilane (AHPCS), a partially allyl-substituted hydridopolycarbosilane (HPCS). These membranes are stable in air-treatment at 450 °C, but have, so far, also proven unstable to high-temperature steam. The nanoporous hydrogen selective SiC membranes show promise for application in membrane reactors for the water gas shift and steam reforming reactions.

Keywords: Silicon carbide; Membranes; Catalytic membrane reactor; Steam reforming

1. Introduction

Membranes find industrial applications in the separation of gas and liquid mixtures. Polymeric membranes are generally utilized in applications that occur at low temperatures and unreactive environments. Several applications exist, however, for which polymeric membranes may not be appropriate because their use is limited to temperatures below 150 °C. As a result, in recent years there has been a considerable effort to produce high-temperature ceramic (alumina, silica, zeolite), and metal (Pd, Pt, Ag, and their alloys) membranes, with improved properties. They have, so far, all proven unsatisfactory in terms of performance and/or material stability, however, in high-temperature applications, particularly in the presence of steam. A new membrane, which shows potential to overcome some of these difficulties, is made of SiC (Suwanmethanond et al., 2000). SiC is a promising material, having high fracture toughness, good thermal shock resistance, and being capable of withstanding high temperatures and corrosive environments (Somiya and Intomata, 1991).

In this paper we present the results of our research on the preparation of SiC nanoporous membranes. Two different approaches have been utilized. One involves the use of chemical-vapor deposition (CVD)/chemical-vapor infiltration (CVI) techniques. We have utilized two different precursors, and have succeeded in preparing defect-free nanoporous membranes. The second approach involves the pyrolysis of pre-ceramic polymeric precursors. In contrast with prior efforts, a polymeric precursor that is capable of producing pure SiC membranes was selected. We envision the SiC membranes to eventually be utilized in reactive applications with the water gas shift (WGS) and methane steam reforming (SMR) reactions, where the membrane has to function in the presence of high-temperature steam.

* Corresponding author. Tel.: +1-213-740-2069; fax: +1-213-740-8053.
E-mail address: tsotsis@usc.edu (T.T. Tsotsis).

0009-2509/$ - see front matter © 2004 Elsevier Ltd. All rights reserved.
doi:10.1016/j.ces.2004.07.015

Membrane reactors (MR) have been previously applied to these two reactions (Sanchez and Tsotsis, 2002) utilizing mostly metal (Pd, Pt, and their alloys) membranes. Using such noble metal membranes is dictated by the fact that other available membranes cannot withstand the high temperatures required (e.g., polymeric membranes), are sensitive to steam (e.g., SiO_2 membranes), or are not permselective enough towards H_2 (e.g., Al_2O_3 or zeolite membranes) under the prevailing high temperature, pressure, and steam conditions. Noble metal membranes perform well (Sanchez and Tsotsis, 2002); however, they are costly, are susceptible to deactivation from coke and sulfur impurities, and must be handled with great care to avoid embrittlement and mechanical failure. SiC membranes show, as a result, good potential for SMR and WGS MR applications. The performance of our group's SiC membranes in high-temperature steam environments, relevant to the aforementioned two reactive applications, is discussed in this paper. Using the experimentally determined transport characteristics of one of the SiC membranes, we have modeled its performance in a SMR MR, in order to demonstrate its potential for this application.

2. Membrane preparation by CVD/CVI techniques

We know only a few prior published studies using the CVD/CVI approach for the preparation of porous SiC membranes. Hong and Lai (1999) used a hot-wall CVD reactor with the $SiH_4/C_2H_2/NH_3$ reaction system. SiC–Si_3N_4 nanoparticles were formed in the gas phase at 1323 K, and deposited on and within the pore structure of a macroporous α-alumina support disk. The deposition resulted in a decrease of the average membrane pore size from 0.3 to 0.21 μ, and in a reduction in the overall permeability by ∼20%, which the authors estimated to be less than what was expected from dense layer deposition on the support pore walls.

Takeda et al. (2001) prepared SiC membranes by CVI into asymmetric γ-Al_2O_3 membrane tubes. As source gases, they used SiH_2Cl_2 and C_2H_2 diluted with H_2, which were supplied to the porous tube during heating at 800–900 °C, followed by a period of evacuation. The membrane support tube was subjected to a number of CVI and evacuation cycles, each reducing the H_2 permeance through the membrane. The final membranes had a H_2 permeance of 1×10^{-8} mol m^{-2} s^{-1} Pa^{-1} at 350 °C, with an ideal selectivity towards N_2 of 3.36, somewhat lower than the corresponding Knudsen value of 3.74.

Of direct relevance to the present paper is the work of Sea et al. (1998), who formed a SiC membrane within the macropores of a tubular membrane support tube via CVD of $(C_3H_7)_3SiH$ (tri-isopropylsilane or TPS) at 700–750 °C. After CVD, the resulting membrane was calcined at 1000 °C in Ar. XPS analysis showed the membrane to consist of pure SiC. The resulting membranes were tested with pure gas (He, H_2, N_2, CO_2, H_2O, CH_4, propane, i-butane, SF_6) permeation experiments between 30 and 400 °C. A gas permeation test was also carried out with an H_2–H_2O–HBr mixture at a molar ratio of 0:49:0.5:0.01 between 200 and 400 °C. Single gas permeation followed a Knudsen mechanism, with H_2 permeance in the range (4–6) $\times 10^{-7}$ mol m^{-2} s^{-1} Pa^{-1}. The H_2:H_2O separation factor in the mixture was originally higher than the Knudsen value (∼ 5), but exposure of the membrane to the mixture at 400 °C resulted in a decline of the H_2 permeance during the first 50 h (by a factor of ∼2.5), while the H_2O permeance remained constant. The H_2 permeance stabilized after that, and remained constant for the remainder of the run, which lasted 120 h.

3. CVD/CVI of TPS

The work of Sea et al. (1998) is important in showing that TPS is a precursor that results in the formation of a pure SiC membrane, though the resulting membranes did not have the desired final characteristics required for reactive gas separations. In our own work we have utilized a preparation procedure which is a variant of that followed by Sea et al. (1998). A schematic of our CVD/CVI apparatus is shown in Fig. 1, and further details can be found elsewhere (Lin et al., 1994). In our experiments we utilized our commercial γ-Al_2O_3 membranes (prepared by sol–gel deposition on macroporous α-Al_2O_3 substrates 25.4 cm long, with 5.7 mm OD × 3.5 mm ID), with an average pore size of 40 Å as substrates for the TPS deposition. These membranes were calcined for 4 h in air at 1000 °C. This treatment enlarges the pore size of the membrane to 100 Å, but further treatment at this temperature leaves the pore size unaffected. For deposition the membrane is sealed in a stainless steel housing constructed of Swagelok-type fittings using graphite packing.

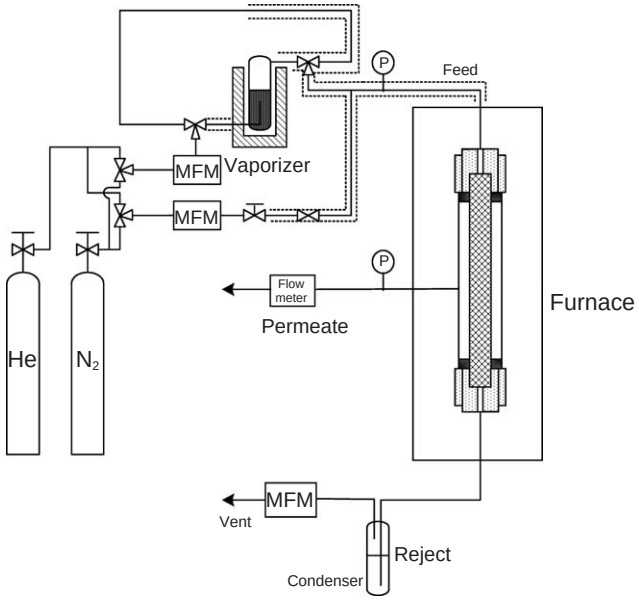

Fig. 1. Schematic of the CVD/CVI experimental apparatus.

TPS (Aldrich, Milwaukee, WI and Gelest, Inc., Tullytown, PA) was used as received with no further purification. The deposition furnace's length is 122 cm. The membrane in the module is set at the center of this furnace, with a preheating zone of ∼48 cm in front of the reactor.

The membrane is heated to the deposition temperature in He gas (⩾99.997% purity). During this time, the vaporizer and feed lines are equilibrated at the desired operating temperatures (for the membranes reported here, the vaporizer temperature was maintained at 90 °C). When the lines, the vaporizer, and the membrane module stabilized at the desired temperature, the pure He was switched to He containing the TPS, and the membranes were exposed to the TPS vapor for the CVD step. The membranes were deposited with TPS at 700–750 °C for various times (2–20 min) until a pre-determined pressure drop across the membrane developed (in the range from 0.55 to 0.7 atm). The residence time of the precursor containing feed in the membrane zone was 0.5 s. Following the deposition, the membranes were further annealed at 1000 °C for 2 h (heating and cooling rates of 100 °C/h) for further conversion to SiC, and then finally activated at 700–750 °C in the presence of ∼1.7 atm of steam to eliminate excess carbon, if present. XRD indicates that the membranes calcined at 1000 °C are mostly amorphous (SiC converts to a crystalline material at higher calcination temperatures). Electron microscopy studies indicate that the SiC layer forms inside the γ-Al_2O_3 layer (which has on the average a thickness of less than 3 μ). As a result, it is difficult to study its structural characteristics or determine its exact thickness. EDAX studies of Si across a membrane cross-section indicate the infiltration depth to be on the average equal to that of the γ-Al_2O_3 layer. However, the effective thickness of the SiC layer, which is responsible for the membrane's good gas separation characteristics, is unknown, but it is expected to be less than the total depth of the SiC penetration observed.

The membranes were then characterized for their permeance, selectivity, and hydrothermal stability. Depending on the preparation conditions, the He permeance ranges from 8.06×10^{-8} to 1.72×10^{-6} mol/m^2 s Pa with a He/N_2 selectivity from 4 to larger than 100 (He is used as a safe surrogate gas to H_2 for the routine characterization of these membranes; the H_2 permeance of these membranes is approximately 60% of that of He). The He permeance increases significantly with temperature, indicative of activated diffusion, whereas the N_2 permeance, and that of other gases with larger kinetic diameters such as CH_4, CO_2, CO, and H_2O, decrease with temperature, indicative of Knudsen flow for these gases. These H_2-selective SiC membranes exhibit excellent thermal stability at 500 °C for >1000 h, as shown in Fig. 2 (this particular membrane was prepared with a 2 min TPS deposition at 700 °C, a 2 h calcination at 1000 °C, and 1 h steam activation at 730 °C). These membranes are also stable in the presence of high-pressure and -temperature steam, as shown in Fig. 3. The He and N_2 permeances remain relatively unchanged at 400 °C in the presence of various partial pressures of steam ranging from 1 to 3 bar steam for a total of 25 h (this membrane was prepared under identical conditions with the membrane of Fig. 2). Fig. 4 shows

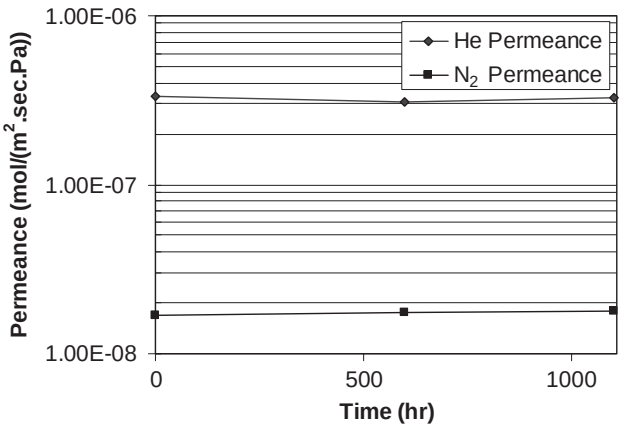

Fig. 2. Thermal stability of a SiC membrane (using TPS as a precursor): He and N_2 permeances as a function of time on stream at 500 °C.

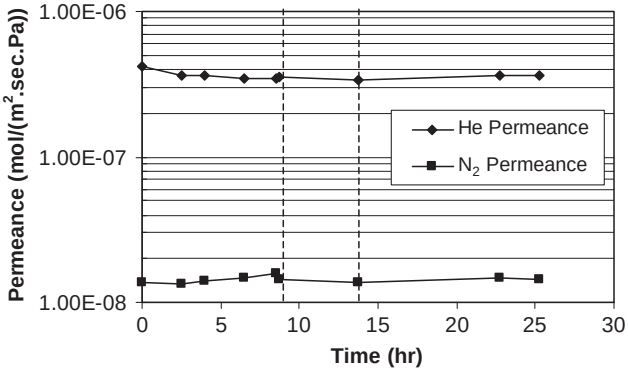

Fig. 3. Hydrothermal stability of a SiC membrane (using TPS as a precursor) exposed to steam at 400 °C. Prior to the initiation of the 400 °C experiments the membrane was exposed to 1 bar partial pressure of steam at 350 °C (∼80% steam and 20% He). After 8.5 h of exposure to 1 bar of steam at 400 °C, the pressure of steam was increased to 2 bar, and 5.25 h after that to 3 bar of steam.

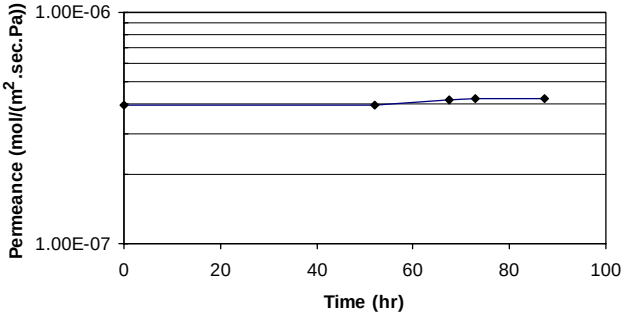

Fig. 4. Hydrothermal stability indicated by the He permeance of a SiC membrane (using TPS as a precursor) exposed to 0.5 bar partial pressure of steam at 750 °C. (The N_2 permeance for this membrane at the beginning of the experiment was 7.56×10^{-10} mol/m^{2}s Pa).

a similar hydrothermal stability test for a different membrane (prepared with a 3 min TPS deposition at 750 °C, a 2 h calcination at 1000 °C, and 20 min steam activation at 750 °C) at a higher temperature, i.e., 750 °C for up to nearly 100 h. Again, the membrane is hydrothermally stable under this condition in terms of its He permeance.

The experimental results above highlight the desired separation characteristics and thermal/hydrothermal stability of the SiC membranes prepared by CVD/CVI using TPS; these membranes are suitable for applications requiring H_2 separations at high temperature and harsh environments. However, the preparation procedure involves multiple steps, which makes it costly, and requires a very high temperature ($\geqslant$1000 °C) treatment, which places a great burden on glass end-seals and membrane housing during the CVD/CVI process. More importantly, this high temperature post-treatment further modifies the nanoporous structure of the CVD/CVI membrane prepared at the lower temperature. Thus, the final product quality is difficult to predict and control, and from a membrane manufacturing standpoint, the advantage of the on-line control of the CVD/I technique is lost. To overcome these challenges, we have pursued in tandem with TPS CVD/CVI two other avenues for membrane preparation. The first involves the use of a different precursor that allows membrane preparation by low-temperature CVD/CVI. The second involves a conventional dip-coating technique through the use of a novel pre-ceramic polymeric precursor, and its controlled temperature pyrolysis. Both approaches are currently under investigation. In what follows, we will outline some of the successes, as well as the challenges that still remain.

4. CVD/CVI of DSB

1,3-disilabutane (DSB) ($CH_3SiH_2CH_2SiH_3$) was selected as the low-temperature SiC CVD/CVI precursor, since a number of prior papers (Lee et al., 1997; Stoldt et al., 2002) have indicated that it can be utilized to produce thin SiC films at CVD temperatures from 650 to 800 °C, primarily for microelectronic applications. The mechanism of SiC deposition from DSB on Si(1 0 0) substrates in an LPCVD system (50 mTorr) was recently studied theoretically by Valente et al. (2004). At lower temperatures (<750 °C), SiC growth is dominated by the surface adsorption and decomposition of DSB. At higher temperatures gas phase decomposition reactions become important to produce Si_2R_2 species (particularly $CH_3SiH_2CH_2SiH$) which adsorb on the surface and decompose to SiC. The Si:C ratio of the material prepared by DSB is perfect (especially for decomposition temperatures <750 °C), close to 1 with no excess carbon (Wijesundara et al., 2004); thus, a one-step lower-temperature CVD/CVI technique to prepare a nanoporous SiC membrane appears technically feasible. For the DSB deposition our commercial 40 Å (5.7 mm OD × 3.5 mm ID) γ-Al_2O_3 membranes were utilized as substrates. Prior to installing the membranes in the CVD apparatus (Fig. 1), they were calcined in air at 750 °C. DSB (Gelest) was used as received with no further purification. The membrane is sealed in a stainless steel housing constructed of Swagelok-type fittings using graphite packing. It is then heated to the deposition temperature, and annealed at this temperature for 4 h under a He purge ($\geqslant$99.997% purity). During this time, the vaporizer and feed lines are equilibrated at the desired operating temperatures. Following the annealing step, the membranes are exposed to the DSB vapor for CVD at temperatures between 650 and 750 °C for deposition times from 2 to 20 min, until a predetermined pressure drop (~0.55–0.7 atm) develops across the membrane. Because of the high volatility of DSB, the vaporizer was operated at sub-ambient temperatures. Unlike the TPS membranes, high-temperature annealing and steam-activation post-CVD/CVI are not required with the DSB membranes for the reasons discussed above. Instead, the membranes were simply annealed at the deposition temperature for a number of hours following CVD, and then cooled to room temperature. The membranes were then characterized for their permeance, selectivity, and hydrothermal stability. As with the TPS membranes electron microscopy studies indicate that the SiC layer forms inside the γ-Al_2O_3 layer. EDAX studies of the Si profile across a membrane cross-section indicate the Si infiltration depth to be equal or less than that of the γ-Al_2O_3 layer.

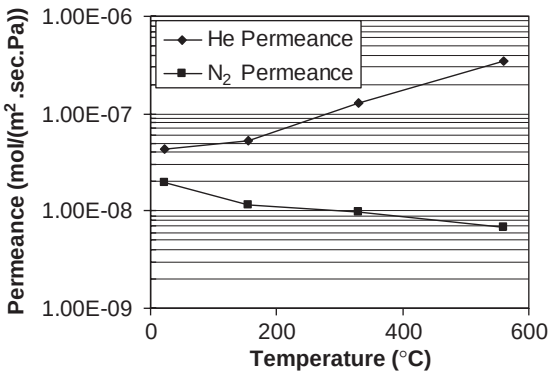

Fig. 5. He and N_2 permeances as a function of temperature for a SiC membrane prepared by CVD/I using DSB as a precursor.

Using CVD/CVI of DSB, high quality, defect-free nanoporous membranes have been prepared. Fig. 5 shows the He and N_2 permeances as a function of temperature for one of the membranes (the membrane in Fig. 5 was prepared with a 20 min DSB deposition at 750 °C, and a 2 h post-deposition annealing at the same temperature). As the temperature increases, the He permeance increases, indicative of activated transport, while the N_2 permeance decreases. The He permeance reaches 3.5×10^{-7} mol/m^2 s Pa, with the selectivity of He/N_2 of ~55 at 550 °C. The DSB membranes are thermally stable, but have, so far, not fared well in the presence of high-temperature steam. The behavior typically observed is shown in Fig. 6. The membrane

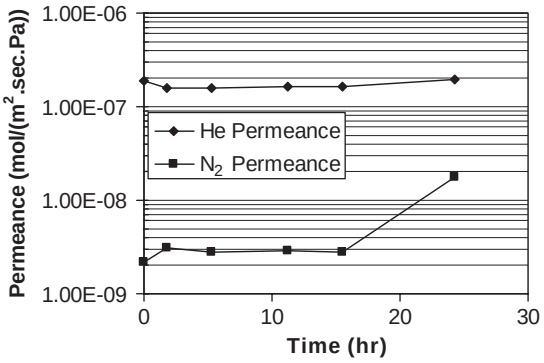

Fig. 6. He and N_2 permeances during hydrothermal treatment at 550 °C in a 0.5 bar partial pressure of steam.

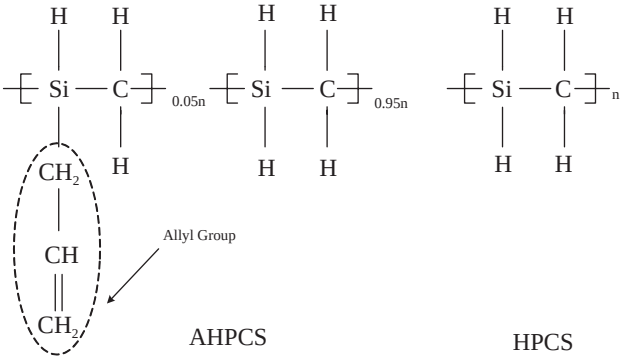

Fig. 7. The structure of AHPCS and HPCS.

appears stable for a number of hours initially, but then the permeances of He and N_2 begin to increase, and the separation factor deteriorates. The ratio of the incremental increase in He and N_2 permeances is consistent with the behavior expected from the development of mesoporous cracks, through which both He and N_2 transport by Knudsen diffusion. The reasons for this behavior are currently under investigation to determine whether the degradation reflects an intrinsic sensitivity of the produced films to steam, or relates to an instability involving the interface between the nanoporous film and the underlying alumina substrates.

5. Membrane preparation by pre-ceramic precursor pyrolysis

Pre-ceramic polymers are currently attracting growing attention as a means of producing ceramics, particularly non-oxide ceramics, because they can be processed and formed at relatively low temperatures compared to the production of conventional structural ceramics. For example, ceramic films, fibers, and composites can all be easily prepared by shaping and curing by different methods of various pre-ceramic polymers, followed by further pyrolysis in order to obtain the desired ceramic materials (Zheng et al., 1999; Sato et al., 1999; Tanaka et al., 1998; Chew et al., 1999). Many different polyorganosilicon compounds, such as polysilazenes $(SiR_2NH)_n$ (Jones et al., 1999), polysilanes $(SiR_2Si_2)_n$ (Chew et al., 1999), polycarbosilanes $(SiR_2CH_2)_n$ (Shimoo et al., 1997; Yajima et al., 1976), and polysiloxanes $(SiR_2O)_n$ (Suttor et al., 1997) can be used as precursors to ceramics such as SiC, SiOC, SiO_2, SiNC, and Si_3N_4.

One of the most important families of SiC precursors is polycarbosilanes (PCS). The first generations of polycarbosilanes, like the early PCS produced by Yajima et al. (1976), are cured using O_2. Consequently, the final ceramic product is silicon oxycarbide, which contains significant amounts of oxygen in the backbone. Morooka and coworkers (Li et al., 1996, 1997; Kusakabe et al., 1995) used such a PCS to produce Si–O–C membranes on γ- and α-Al_2O_3 tubular substrates with an oxygen content of 13–18 wt%, using polystyrene (PS) as the pore former. A PCS membrane prepared with 1% PS had a H_2 permeance of 4×10^{-8} mol m^{-2} s^{-1} Pa^{-1} and an ideal H_2:N_2 selectivity of 20 at 773 K. The membranes were unstable in Ar at 1223 K. When exposed to a 7.8 wt% H_2O in He mixture at 773 K, the H_2 and N_2 permeances decreased by half during the first 24 h, and slowly after that for the remainder of the 72 h of the experiment.

Related is the work of Tsai and coworkers (Lee and Tsai, 1999, 2001) who prepared Si–C–O membranes by the pyrolysis of polydimethylsilane (PMS). The PMS layer undergoes a thermolytic reaction at 733 K for 14 hr under 1 atm of Ar (and is likely converted to a PCS-like material (Lee and Tsai, 1999; Williams et al., 2002)), followed by O_2 curing at 473 K for 1 h. The layer was finally pyrolyzed at various temperatures from 523 to 1223 K to produce the membranes. The membrane pyrolyzed at 873 K had the best separation characteristics, exhibiting a He permeance of $\sim 1.4 \times 10^{-9}$ mol/m^2 s Pa, a H_2 permeance of $\sim 2.7 \times 10^{-9}$ mol/m^2 s Pa, and an ideal H_2:N_2 selectivity of 20 at 473 K. Membranes prepared at the higher pyrolysis temperatures were not microporous. Exposure to steam increases the permeance, and returns the separation selectivities to their Knudsen values (Chen and Tsai, 2004).

More recently, newer PCS types have been developed, which use other curing methods, such as UV radiation (Takeda et al., 2000; Chu et al., 1999), electron beam (Seguchi, 2000), or heat treatment under an inert atmosphere (Matthews et al., 1999), in order to achieve a low-oxygen content in the final product, and with a Si:C ratio close to unity. In our own work we have used such a PCS, namely allyl-hydridopolycarbosilane (AHPCS), a partially allyl-substituted hydridopolycarbosilane (HPCS). Allyl substitution provides an added degree of control over the Si:C ratio, and ceramic yield in the resulting ceramics. The structures of AHPCS and HPCS are shown in Fig. 7. Use of HPCS was first proposed by Interrante et al. (1994a,b, 1995a,b). The primary pyrolysis product of both HPCS and

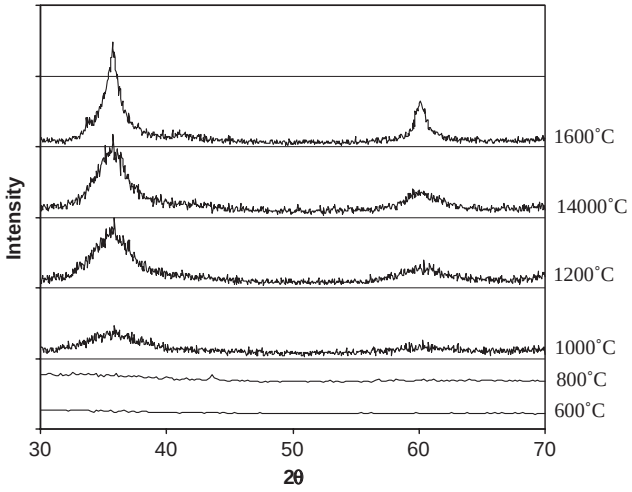

Fig. 8. XRD patterns of AHPCS powders calcined at temperatures between 600 and 1600 °C.

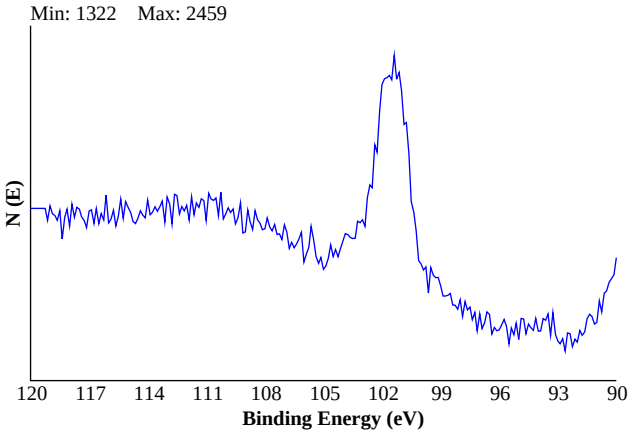

Fig. 9. XPS spectra of Si 2p photoelectron peak of a SiC powder prepared by pyrolysis of AHPCS at 600 °C.

AHPCS is a SiC ceramic, having a Si–C bond linkage. The increasing fractions of allyl groups slightly increases the carbon content, and also make the polymer cross-linkable at lower temperatures.

To prepare nanoporous membranes we have used a 10 wt% solution of AHPCS in hexane and dip-coated one side of macroporous SiC flat-disk substrates, made by pressureless sintering of SiC powders (Suwanmethanond et al., 2000). Prior to dip-coating, the SiC substrates are ultrasonically cleaned in acetone, and then dried in the oven. After each coating, the coated substrates are heated in flowing Ar in an alumina tube furnace with a heating rate of 120 °C/h, up to a temperature of 400 °C, where they are kept for 1 h. The temperature is then raised (with a heating rate of 60 °C/h) to the desired calcination temperature (ranging from 600 to 1600 °C), where they are kept for an additional 2 h, and cooled down to the room temperature (with a cooling rate of 15 °C/h). In parallel, we have also prepared a number of SiC powders from the AHPCS using the same preparation protocols with the SiC membranes.

AHPCS pyrolysis produces SiC, as indicated by the XRD analysis (done with a Rigaku X-ray Diffractometer) of pyrolyzed powder samples, shown in Fig. 8 (the diffraction peaks at 35-2θ and 60-2θ correspond to β-SiC). At lower pyrolysis temperatures the XRD spectra are very noisy, potentially signifying the presence of amorphous SiC, which begins to crystallize at higher temperatures. As the temperature increases the amorphous SiC is converted into crystalline SiC. Fig. 9 shows the XPS spectra of a SiC powder prepared by pyrolysis at 600 °C (because of our prior experience with these samples, and the extent of ubiquitous hydrocarbon contamination, the fraction of the surface layer composed of SiC was determined solely from detailed scans of the silicon 2p photoelectron region). Within the binding energy range of 120–90 eV, SiC (101.0–100.4 eV) can be easily distinguished. The various processes that occur during AHPCS pyrolysis have also been investigated using in situ DRIFTS, indicating a rather complex reaction mechanism. The polymer-to-ceramic conversion process is characterized by a number of distinct changes. The bonds, involving hydrogen (Si–H, C_2–SiH_2), and the double bonds disappear upon cross-linking and pyrolysis at temperatures below 500 °C, as the polymer becomes infusible and low molecular-weight compounds leave the polymer matrix. The organometallic to inorganic conversion begins at ∼500 °C. During this stage, most of the C–H and Si–H bonds in the polymer chain break, and only the peaks corresponding to the polymer backbone (Si–CH_2–Si) remain and broaden. Nucleation and crystallization accelerate in the temperature range between 800 and 1000 °C. After 1200 °C, the DRIFTS spectrum stays the same due to the complete conversion to crystalline SiC. The DRIFTS data are consistent with the XRD and XPS data, and with what is known on the pyrolysis of similar materials Interrante et al., 1994a,b; Williams et al., 2002).

For the membranes prepared by pyrolysis at different temperatures the permeance of single gases and the corresponding separation factors have been measured. Fig. 10 shows the He and N_2 permeances and the ideal separation factors for three membranes, which were pyrolyzed at 600, 1000, and 1200 °C. As with TPS and DSB membranes the He permeation is activated, increasing with temperature, while N_2 transport appears to be Knudsen-like, decreasing with temperature. The He permeance and the separation factor both generally decrease with the temperature of pyrolysis (membranes pyrolyzed at 1400 and 1600 °C are not permselective). The transport data indicate that these membranes are nanoporous consistent with BET investigations of the same membranes (see Fig. 11), which also show them to be nanoporous. The SiC membranes prepared have, so far, are stable to air oxidation at 450 °C (in between layer deposition the membranes are oxidized at 450 °C to burn away any unreacted carbon), but have not proven stable to high-temperature steam-treatment. The reasons for the steam

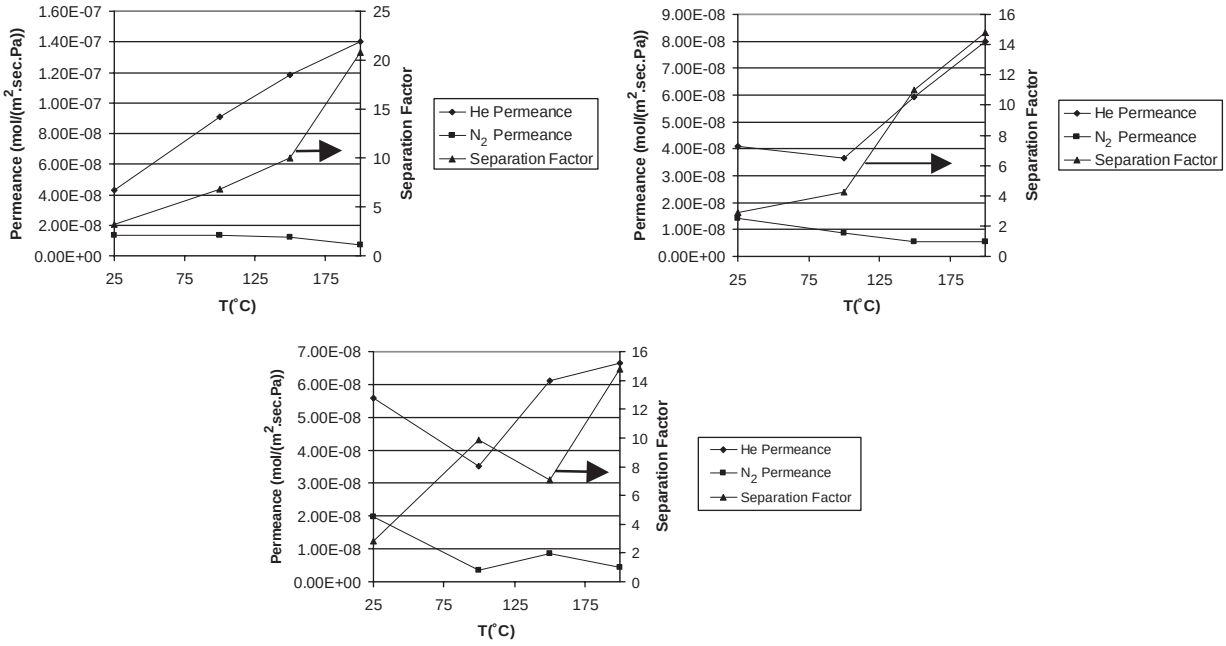

Fig. 10. Top left, He and N_2 permeances and separation factor of the membrane pyrolyzed at 600 °C. Top right, He and N_2 permeances and separation factor of the membrane pyrolyzed at 1000 °C. Bottom, He and N_2 permeances and separation factor of the membrane pyrolyzed at 1200 °C.

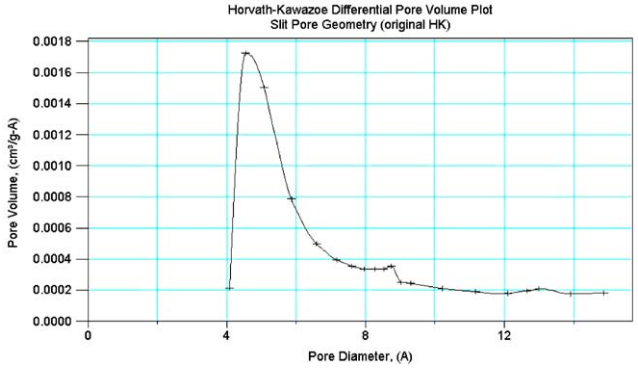

Fig. 11. Pore size distribution of membrane in the microporous region using the HK model.

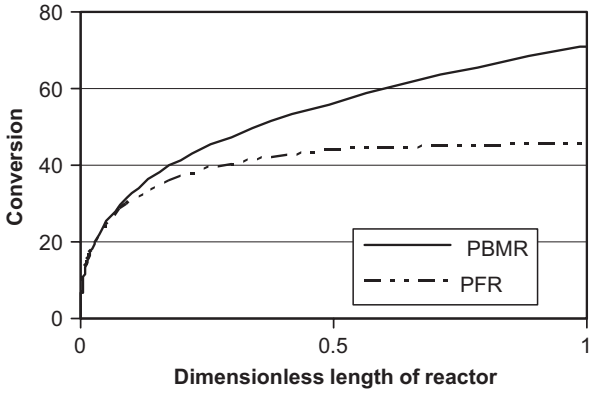

Fig. 12. Comparison of methane conversion along the reactor length in the PBMR and PFR. Reactor side pressure 5 atm, permeate 1 atm, reactor temperature 600 °C, sweep (steam) ratio 0.1.

sensitivity are not exactly clear at this stage. For example, XRD studies of steam-treated powders, do not appear different than those of the as prepared materials, and BET studies indicate no changes, i.e., the membranes remain nanoporous. Work in this area is continuing, aiming to improve the hydrothermal stability of the resulting membranes.

6. Membrane reactor application

Due to their excellent material stability SiC inorganic membranes are potentially useful for reactive separation applications under harsh environments, specifically involving high-temperature steam. The functional performance of the SiC membranes obtained in this study is evaluated here in catalytic methane steam-reforming membrane reactor applications. SMR, which consists of two reversible reactions, the highly endothermic reforming reaction (1), and the moderately exothermic water-gas shift reaction (2).

$$CH_4 + H_2O \rightleftharpoons CO + 3H_2 \quad \Delta H = +206\,\text{kJ/mol} \tag{1}$$

$$CO + H_2O \rightleftharpoons CO_2 + H_2 \quad \Delta H = -41\,\text{kJ/mol} \tag{2}$$

is the key process by which H_2 and synthesis gas are produced industrially. Carrying the SMR reaction in a membrane reactor has the potential for improving conversion and yield, in addition to providing a means for in situ separation of the H_2 product. Fig. 12 shows the results of simulations with the SMR being carried out in a packed-bed membrane

reactor (PBMR). The mathematical equations and further details about the SMR-PBMR model have been presented previously (Sanchez and Tsotsis, 2002; Onstot et al., 2001; Onstot, 2003). Briefly, the reactor is assumed to operate under isothermal conditions, with plug-flow prevailing both in the feed- and permeate side. Pressure drop in the feed-side is accounted by the Ergun equation. Steam is used as the sweep gas. We utilize experimentally validated SMR kinetics (Onstot, 2003) with a nickel-based Haldor-Topsøe R-67 reforming catalyst at temperatures in the range of 450–850 °C. The performance of one of our own TPS membranes is utilized here, 2.27×10^{-7}, and 4.55×10^{-9} mol/m^2 s Pa, for the permeance of hydrogen and nitrogen, respectively. The other gases are assumed to transport by Knudsen diffusion; their permeance are estimated on the basis of the nitrogen data. Fig. 12 shows the improvement in methane conversion in a PBMR vs. a conventional plug flow reactor (PFR). The PBMR conversion is 25.7% higher than the conversion in the PFR, indicating the significant potential these membranes show for application to SMR.

7. Conclusions

SiC membranes have been prepared using CVD/CVI approaches with two different precursors, namely TPS and DSB that have been proven capable of producing SiC by the CVD method. The membranes prepared under different experimental conditions are shown to be nanoporous and hydrogen permselective. The TPS-based membranes have good stability in the presence of high-temperature steam. SiC membranes have also been prepared by dip-coating techniques through the pyrolysis of a novel polymeric preceramic precursor. They are also nanoporous, are stable to high-temperature air oxidation, but have, so far, not proven stable to high-temperature steam.

SiC membranes are well-suited for the SMR application, since they can tolerate the high temperatures required, and the presence of steam. The performance of the SiC membranes obtained in this study shows potential for application in high-temperature catalytic membrane reactors producing H_2 through the SMR reaction on the basis of mathematical simulations. By removing H_2 by the membrane from the reaction mixture in situ, one not only reduces the need for additional downstream separation steps, but also significantly enhances CH_4 conversion.

Acknowledgements

The support of NSF, NASA and the U.S. Department of Energy is gratefully acknowledged. We also thank Superior Graphite Co., USA and Sumitomo Osaka Cement Co., Ltd. for providing us the SiC powders.

References

Chen, C.L., Tsai, D.S., 2004. Permeation properties of microporous membranes prepared via coating of evaporated polydimethylsilane. Journal of Membrane Science 237, 163–165.

Chew, K.W., Sellinger, A., Laine, R.M., 1999. Processing aluminum nitride silicon carbide composites via polymer infiltration and pyrolysis of polymethylsilane, a precursor to stoichiometric silicon carbide. Journal of The American Ceramic Society 82, 857–866.

Chu, Z.Y., Song, Y.C., Xu, Y.S., Fu, Y.B., 1999. Enhanced irradiation cross-linking of polycarbosilanes. Journal of Materials Science Letters 18, 1793–1795.

Hong, L.S., Lai, H.T., 1999. Pores structure modification of alumina support by SiC–Si_3N_4 nanoparticles prepared by the particle precipitation aided chemical vapor deposition. Industrial and Engineering Chemistry Research 38, 950–957.

Interrante, L.V., Whitmarsh, C.K., Sherwood, W., Wu, H.J., Lewis, R., Maciel, G.E., 1994a. High yield polycarbosilane precursors to stoichiometeric SiC, synthesis pyrolysis and application. Materials Research Society Symposium Proceedings, Proceedings of the Symposium on “Better Ceramics Through Chemistry IV” 346, 593–603.

Interrante, L.V., Whitmarsh, C.K., Yang, C.Y., Sherwood, W., Schmidt, W.R., Marchetti, P.S., Maciel, G.E., 1994b. Processing of Si-based ceramics and ceramic composites using hydridopolycarbosilane (HPCS). Ceramic Transaction 42(Silicon-Based Structural Ceramics), 57–69.

Interrante, L.V., Whitmarsh, C.K., Sherwood, W., Wu, H.J., Lewis, R., Maciel, G.E., 1995a. Hydridopolycarbosilane precursors to silicon carbide. Synthesis, pyrolysis and application as a SiC matrix source. NATO ASI Series Volume. In: Harrod, J.F., Laine, R. (Eds.), Application of Organometallic Chemistry in the Preparation and Processing of Advanced Materials. Kluwer Academic Publishers, Dordrecht, pp. 173–183.

Interrante, L.V., Whitmarsh, C.K., Sherwood, W., 1995b. Fabrication of SiC matrix composites using a liquid polycarbosilane as a matrix source. High Temperature Matrix Composites II. Ceramic Transaction 58, 111–118.

Jones, R., Szweda, A., Petrak, D., 1999. Polymer derived ceramic matrix composites. Composites, Part A: Applied Science and Manufacturing 30, 569–575.

Kusakabe, K., Li, Z.Y., Maeda, H., Morooka, S., 1995. Preparation of supported composite membrane by pyrolysis of polycarbosilanes for gas separation at high temperature. Journal of Membrane Science 103, 175–180.

Lee, K.W., Yu, K.S., Kim, Y., 1997. Heteroepitaxial growth of 3C-SiC on Si(0 0 1) without carbonization. Journal of Crystal Growth 179, 153–160.

Lee, L.L., Tsai, D.S., 1999. A hydrogen permselective silicon oxycarbide membrane derived from polydimethylsilane. Journal of the American Ceramic Society 82, 2796–2800.

Lee, L.L., Tsai, D.S., 2001. Synthesis and permeation properties of silicon-carbon-based inorganic membrane for gas separation. Industrial Engineering Chemistry Research 40, 612–616.

Li, Z., Kusakabe, K., Morooka, S., 1996. Preparation of thermostable amorphous Si–C–O membrane and its application to gas separation at elevated temperature. Journal of Membrane Science 118, 159–168.

Li, Z., Kusakabe, K., Morooka, S., 1997. Pore structure and permeance of amorphous Si–C–O membranes with high durability at elevated temperature. Separation Science and Technology 32, 1233–1254.

Lin, C.L., Flowers, D.L., Liu, P.K.T., 1994. Characterization of ceramic membranes. II. Modified commercial membranes with pore size under 40 Å. Journal of Membrane Science 92, 45–58.

Matthews, S., Edirisinghe, M.J., Folkes, M.J., 1999. Effect of pre-pyrolysis heat treatment on the preparation of silicon carbide from a polycarbosilane precursor. Ceramics International 25, 49–60.

Onstot, W., 2003. Design considerations in the application of membrane reactors for use in steam-CO_2 reforming environments. Ph.D. Thesis, University of Southern California.

Onstot, W.J., Minet, R.G., Tsotsis, T.T., 2001. Design aspects of membrane reactors for dry reforming of methane for the production of hydrogen. Industrial and Engineering Chemistry Research 40, 242–251.

Sanchez, J., Tsotsis, T.T., 2002. Catalytic Membranes and Membrane Reactors. Wiley VCH, New York, Weinheim.

Sato, K., Tezuka, A., Funayama, O., Isoda, T., Terada, Y., Kato, S., Iwata, M., 1999. Fabrication and pressure testing of a gas-turbine component manufactured by a preceramic-polymer-impregnation method. Composites Science and Technology 59, 853–859.

Sea, B.K., Ando, K., Kusakabe, K., Morooka, S., 1998. Separation of hydrogen from steam using a SiC-based membrane formed by chemical vapor deposition of tri-isopropylsilane. Journal of Membrane Science 146, 73–82.

Seguchi, T., 2000. New trend of radiation application to polymer modification—irradiation in oxygen free atmosphere and at elevated temperature. Radiation Physics and Chemistry 57, 367–371.

Shimoo, T., Tsukada, I., Narisawa, M., Seguchi, T., Okamura, K., 1997. Change in properties of polycarbosilane-derived SiC fibers at high-temperatures. Journal of the Ceramic Society of Japan 105, 559–563.

Somiya, S., Intomata, Y. (Eds.), 1991. SiC Ceramics-2. Elsevier, New York, NY.

Stoldt, C.R., Carraro, R., Ashurst, W.R., Gao, D., Howe, R.T., Maboudian, R., 2002. A low-temperature CVD process for SiC MEMS. Sensors and Actuators A 97-98, 410–415.

Suttor, D., Erny, T., Greil, P., 1997. Fiber-reinforced ceramic-matrix composites with a polycarbosiloxane/boron-derived matrix. Journal of the American Ceramic Society 80, 1831–1840.

Suwanmethanond, V., Goo, E., Liu, P.K.T., Jonhston, G., Sahimi, M., Tsotsis, T.T., 2000. Porous silicon carbide sintered substrates for high-temperature membranes. Industrial and Engineering Chemistry Research 39, 3264–3271.

Takeda, M., Saeki, A., Sakamoto, J., Imai, Y., Ichikawa, H., 2000. Effect of hydrogen atmosphere on pyrolysis of cured polycarbosilane fibers. Journal of the American Ceramic Society 83, 1063–1069.

Takeda, Y., Shibata, N., Kubo, Y., 2001. SiC coating on porous γ-Al_2O_3 using alternative—supply CVI method. Journal of the Ceramic Society of Japan 109, 305–309.

Tanaka, T., Tamari, N., Kondo, I., Iwasa, M., 1998. Fabrication of three-dimensional Tyranno fiber reinforced SiC composite by the polymer precursor method. Ceramics International 24, 365–370.

Valente, G., Wijesundara, M.B.J., Maboudian, R., Carraro, C., 2004. Single-source CVD of 3C-SiC films in a LPCVD reactor. II. Reactor modeling and chemical kinetics. Journal of the Electrochemical Society 151, C215–C219.

Wijesundara, M.B.J., Valente, G., Ashurst, W.R., Howe, R.T., Pisano, A.P., Carraro, C., Maboudian, R., 2004. Single-source chemical vapor deposition of 3C-SiC films in a LPCVD reactor. Journal of the Electrochemical Society 151, C210–C214.

Williams, H.M., Dawson, E.A., Barnes, P.A., Rand, B., Brydson, R.M.D., Brough, A.R., 2002. High temperature ceramics for use in membrane reactors: the development of porosity during the pyrolysis of polycarbosilanes. Journal of Materials Chemistry 12, 3754–3760.

Yajima, S., Okamura, K., Hayashi, J., Omori, M., 1976. Synthesis of continuous silicon carbide fibers with high tensile strength. Journal of the American Ceramic Society 59, 324–327.

Zheng, G.B., Sano, H., Uchiyama, Y., Kobayashi, K., Cheng, H.M., 1999. The properties of carbon fibre SiC composites fabricate through impregnation and pyrolysis of polycarbosilane. Journal of Materials Science 34, 827–834.

Supercritical fluids in porous composite materials: Direction-dependent flow properties

Mahnaz Firouzi, Muhammad Sahimi,* and Theodore T. Tsotsis
Department of Chemical Engineering and Materials Science, University of Southern California, Los Angeles, California 90089-1211, USA

(Received 18 August 2005; revised manuscript received 18 October 2005; published 24 March 2006)

The results of extensive nonequilibrium molecular dynamics simulations of flow and transport of a pure fluid, as well as a binary fluid mixture, through a porous material composed of a macropore, a mesopore, and a nanopore, in the presence of an external pressure gradient, are reported. We find that under supercritical conditions, unusual phenomena occur that give rise to *direction*-dependent and pressure-dependent permeabilities for the fluids' components. The results, which are also in agreement with a continuum formulation of the problem, indicate that the composite nature of the material, coupled with condensation, give rise to the direction-dependent permeabilities. Therefore, modeling flow and transport of fluids, in the *supercritical regime*, in porous materials with the type of morphology considered in this paper (such as supported porous membranes) would require using effective permeabilities that depend on both the external pressure drop and the direction along which it is applied to the materials.

DOI: 10.1103/PhysRevE.73.036312 PACS number(s): 47.56.+r, 02.70.Ns

I. INTRODUCTION

Equilibrium and nonequilibrium properties of fluids and their mixtures in confined media are of much current interest [1,2]. Examples of such media include nanoporous and mesoporous materials, such as catalysts, adsorbents, skin and biological tissues, and nanoporous thin films that are used as low-dielectric constant composites, optical coatings, sensors, and insulating materials. For practical applications, it is important to understand how flow and transport processes occur in the pore space of such materials, because even if the properties of their matrix are of interest, understanding transport of fluids in their pore space is still critical to *characterization* of their morphology, including their matrix.

An important class of nanoporous materials consists of membranes—either biological or synthetic. The former play a fundamental role in biological activities of living organisms, while the latter, the focus of the present paper, are under active investigations, both experimentally and by computer simulations, for separation of fluid mixtures into their constituent components, and for sensors that can detect trace amounts of certain chemical compounds. Since molecular interactions between the fluid molecules, and between them and the nanopores' walls, cannot be ignored, one must resort to atomistic models [3]. Such models, that are typically based on atomistic simulation of flow and transport of a fluid mixture through a single nanopore, yield an effective permeability for each component of the mixture flowing through the nanopore. In practice, however, most membranes consist of a porous support made of at least two layers of macropores and mesopores, and a nanoporous film deposited on the support. Flow and transport of fluids in such composite porous materials have rarely been studied.

In this paper we report the results of the first atomistic simulation of flow and transport of supercritical (SC) fluid mixtures—those that are in a thermodynamic state above their critical temperature and/or pressure—in a composite porous material that consists of three distinct pores, referred to as the macropores, mesopores, and nanopores. SC fluids have recently attracted much attention [4], due to the potential of SC fluid extraction (SCFE) utilizing CO_2 for removal of contaminants from water [5], sludges and soils [6], spent catalysts [7], aerogels [8], and adsorbents [9]. They are also used for preparing nanosize particles for drug delivery. CO_2 is preferred in such applications because it is nontoxic and nonflammable. The most promising SCFE method is one that combines a SC fluid with a porous membrane, which preferentially and continuously extracts the solute, leaving behind a solute-depleted, recyclable SC solvent stream. Experiments [10] indicate the existence of complex and unusual phenomena: hysteresis in the permeability isotherms at some temperatures but not at others; pressure-dependent permeabilities that exhibit a maximum as a function of the temperature, and solute rejection that can be positive or negative, depending on the type of the porous material and the solutes used. There is currently little fundamental understanding of such phenomena. We use molecular dynamics (MD) simulations to study flow and transport of a SC fluid mixture in a model composite membrane. In practice, a fluid mixture passes through a porous membrane by applying a pressure gradient to two opposing external surfaces of the membrane. To simulate this process we use the dual control-volume grand-canonical MD (DCV-GCMD) simulation technique which is most suitable for simulating transport processes in systems that operate under an extermal potential gradient. Due to their thermal/mechanical stability and versatility, carbon molecular-sieve membranes (CMSMs) have been used by many groups [11,12] in experimental studies involving separation of fluid mixtures. Thus, in this paper we utilize a model CMSM to carry out the MD studies. One goal of the paper is to understand the effects of the membrane structure, and the pressure gradient applied to the membrane, on the flow properties of the fluid mixture passing through the membrane.

*Corresponding author. Electronic address: moe@iran.usc.edu

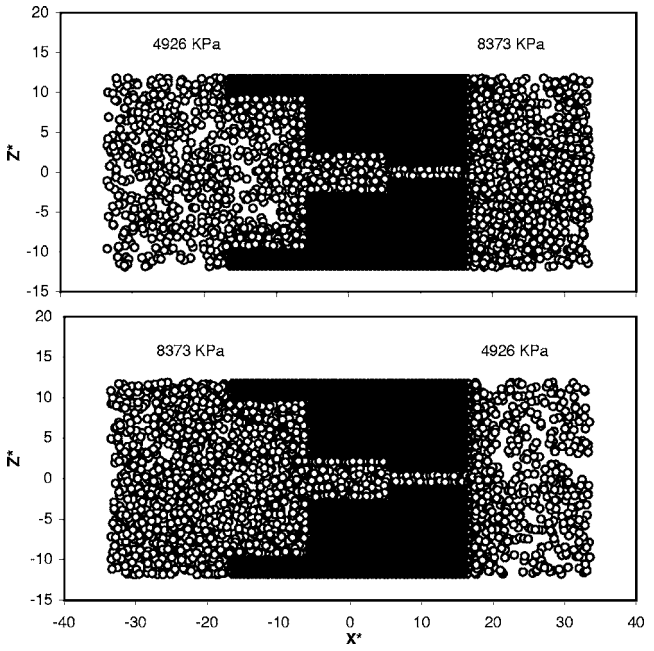

FIG. 1. A snapshot of the three-pore system and the distribution of pure CO_2 in it, when the upstream condition (higher pressure) is maintained either in the control volume which is connected to the macropore, or that connected to the nanopore.

The plan of this paper is as follows. In the next section we describe the details of the model of the membrane that we use and the MD simulation technique that we utilize. The results are presented and discussed in Sec. III. The paper is summarized in Sec. IV.

II. MOLECULAR DYNAMICS SIMULATION

Recent MD simulations [13] indicate that atomistic-scale transport in a pore is hardly influenced by the pore's shape. Thus, as a prelude to understanding flow and transport of SC fluid mixtures in a real membrane, we consider the same phenomena in the composite pore system shown in Fig. 1, which consist of three slit pores in series. (A somewhat similar pore model was utilized by Düren *et al.* [13] in their study of gas transport through a membrane.) Each pore represents one layer of a three-layer supported membrane. The pores' heights are 77, 23, and 10 Å, while they all have the same length, about 43 Å. The membrane is connected to two control volumes (CVs) that are exposed to the bulk fluid at high and low chemical potentials μ or pressures P. Periodic boundary conditions are used only in the y direction (perpendicular to the plane of this page). The external driving force is a chemical potential or pressure gradient applied in the x direction.

We consider flow and transport of pure CO_2, as well as a mixture of CH_4 (component 1) and CO_2 (component 2), in the membrane. The two components, as well as the carbon atoms that the pores' walls consist of, are represented by Lennard-Jones (LJ) spheres and are characterized by effective LJ size and energy parameters, σ and ε, respectively. We used $\sigma_C=3.4$ Å, and $\varepsilon_C/k_B=28$ K for the carbon atoms; $\sigma_1=3.81$ Å and $\varepsilon_1/k_B=148.1$ K for CH_4, and $\sigma_2=3.79$ Å and $\varepsilon_2/k_B=225.3$ K for CO_2. For the cross-term LJ parameters the Lorentz-Berthelot combining rules were used, namely, $\varepsilon_{12}=\sqrt{\varepsilon_1\varepsilon_2}$, and $\sigma_{12}=\frac{1}{2}(\sigma_1+\sigma_2)$. We also used a more realistic model for CO_2 that consisted [14] of three LJ interaction sites on the three atoms, plus point charges to account for the quadrupole moment of CO_2 molecules, but found no significant effect on the results.

Although MD simulations have been used for studying SC fluids in the bulk [15], very few such studies have investigated the behavior of SC fluids in small pores [16,17]. As mentioned earlier, we use the DCV-GCMD method [14,18] which combines the MD method in the entire pore system with the grand-canonical Monte Carlo (GCMC) insertions and deletions of the molecules in the CVs. Therefore, to mimic the experimental conditions, the densities, or the corresponding chemical potentials, of the components in the CVs were maintained using a sufficient number of GCMC insertions and deletions. The probability of inserting a particle of component i is given by

$$p_i^+ = \min\left(\frac{Z_i V_c}{N_i+1}\exp(-\Delta E/k_B T), 1\right), \tag{1}$$

where $Z_i=\exp(\mu_i/k_BT)/\Lambda_i^3$ is the absolute activity at temperature T, Λ_i, and μ_i are, respectively, the de Broglie wavelength and chemical potential of component i, ΔE the potential energy change resulting from inserting a particle, and V_c and N_i the volume of the CV and number of atoms of component i in each CV, respectively. The probability of deleting a particle is given by

$$p_i^- = \min\left(\frac{N_i}{Z_i V_c}\exp(-\Delta E/k_B T), 1\right). \tag{2}$$

The two CVs are well mixed and in equilibrium with the two bulk phases that are in direct contact with them. The chemical potentials were converted to equivalent pressures using a LJ equation of state [19].

The molecule-molecule interactions were modeled with the cut-and-shifted LJ 6–12 potential with a cutoff distance, $r_c=4\sigma_1$. To calculate the interactions between the fluids' molecules and the walls, we used the LJ potentional for the interactions between the molecules and the individual carbon atoms on the walls, arranged as in graphite. The cutoff distance between the molecules and the carbon atoms on the walls was $r_c=3.5\sigma_1$. Typically, ten GCMC insertions and deletions in each CV were followed by one MD integration step. The temperature, $T=35$ °C, was held constant in order to eliminate any contribution of the temperature gradient to the transport.

The Verlet velocity algorithm was used to integrate the (dimensionless) equations of motion with a dimensionless time step, $\Delta t^*=5\times10^{-3}$ (i.e., $\Delta t\simeq0.006\,85$ ps). The equations of motion were integrated with up to 1.2×10^7 time steps to ensure that the system was at steady state. Molecules that crossed the outer boundaries of the CVs were removed. The number of such molecules was, however, small, typically about 1% of the total number of molecules that were deleted during the GCMC simulations. In addition, for each

component we allowed for a nonzero streaming velocity (the ratio of the component's flux and concentration) in the pore system, consistent with the presence of a bulk pressure/chemical potential gradient along the x direction. In the CVs, however, the overall streaming velocity was zero. Isokinetic conditions were maintained by rescaling the velocity independently in the three directions.

Two important quantities of interest are the density profile $\rho_i^z(x)$ of component i along the x direction, the direction along which the chemical potential gradient $\nabla\mu$ is imposed on the membrane, and $\rho_i^x(z)$, the density profile in the yz planes that are perpendicular to the direction of $\nabla\mu$. The density profile $\rho_i^z(x)$ was computed by dividing the simulation box in that direction into grids of size, $\ell=1.12\sigma_1$. For each MD step, $\rho_i^z(x)$ was computed by averaging the number of particles of type i over the distance ℓ. A similar procedure was used for computing the density profile $\rho_i^x(z)$ in the yz planes that are perpendicular to the direction of $\nabla\mu$, with the averaging done over asmall distance which were about $0.67\sigma_1$, $0.21\sigma_1$, and $0.09\sigma_1$ for the macropores, mesopores, and nanopores, respectively.

In addition, a most important characteristic property of a membrane is the permeability of a fluid passing through the membrane. Thus, for each component i we calculated its flux J_i in the direction of the applied chemical potential or pressure gradient. The permeability K_i of the component i is then given by Darcy's law

$$K_i = \frac{J_i}{\Delta P_i/L}, \tag{3}$$

where $\Delta P_i = x_i \Delta P$ is the partial pressure drop for species i along the pore system, with x_i being its mole fraction, ΔP the total pressure drop imposed on the system, and L the system's length. We computed the permeabilities for two cases. In one, the upstream condition (higher pressure) was maintained in the CV connected to the macropore, while in the second case the upstream condition was maintained in the nanopore.

III. RESULTS AND DISCUSSION

We first describe the results for pure CO_2, and then present and discuss those for a binary mixture of CO_2 and CH_4. Figure 1 presents a snapshot of the pore system and the distribution of CO_2 molecules in it. The upstream and downstream pressures were 8373 kPa (1215 psi) 4926 kPa (715 psi), respectively. In both cases, the state of CO_2 in the nanopores and mesopores is liquidlike, caused by condensation. The state of CO_2 in the macropore, on the other hand, depends on where the upstream condition is maintained. If the upstream condition is maintained in the CV connected to macropore, then the CO_2 density in the pore is high almost everywhere, resembling a liquidlike state. If, on the other hand, the upstream condition is maintained in the CV connected to the nanopore, the CO_2 density in the macropore near its entrance to the mesopore is high, but decreases somewhat as one gets away from this region towards the CV on the left side of the figure. These are consistent with the time-averaged density profile $\rho^z(x)$ of CO_2 shown in Fig. 2.

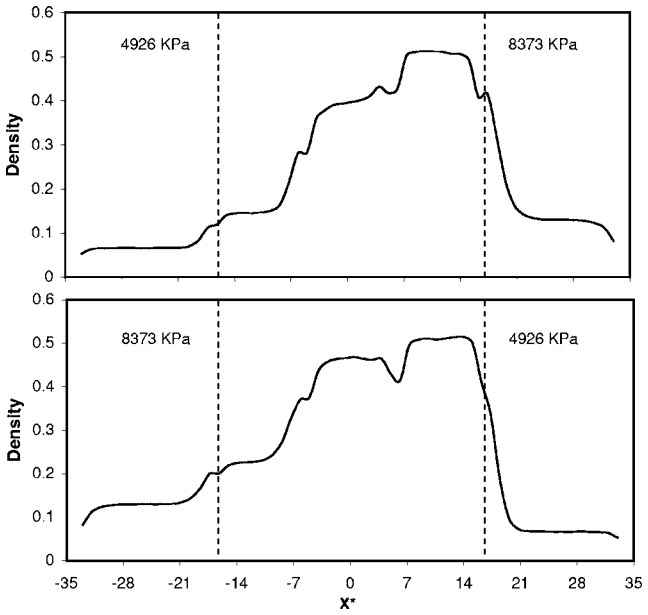

FIG. 2. Time-averaged density profiles $\rho^z(x)$ of pure CO_2 in the transport direction x. The system is at steady state.

Figure 3 presents the CO_2 permeabilities as a function of the upstream pressure, when a pressure drop $\Delta P=3447$ kPa (500 psi) was applied to the pore system. The direction dependence of K is striking, with the permeabilities in the two opposite directions differing by a factor which can be as large as nearly four. Moreover, the trends for the two cases are opposite of each other. Whereas K decreases when the upstream is on the macropore side, it increases when the direction of ΔP is reversed. The reason can be understood by considering Figs. 1 and 2: at a constant overall ΔP, with increasing the upstream pressure on the macropore side, practically the entire pore system is packed with CO_2 molecules. This makes the passage of the molecules from the macropore to the mesopore very difficult, resulting in reduced values of K. On the other hand, at the same overall ΔP, increasing the upstream pressure when applied on the

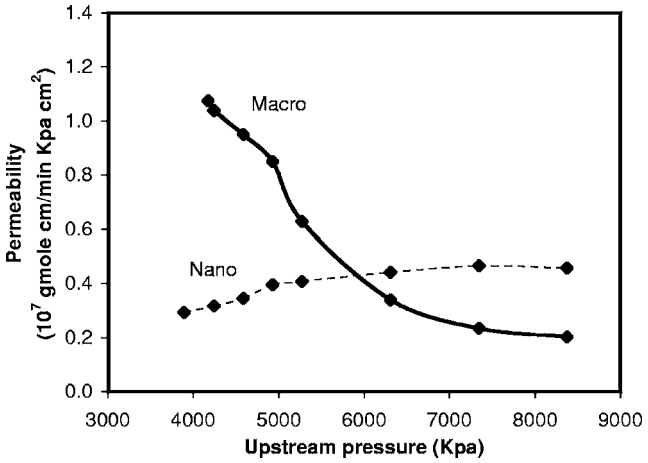

FIG. 3. The permeability of pure CO_2 when a pressure drop $\Delta P=3447$ kPa (500 psi) is applied to the pore system.

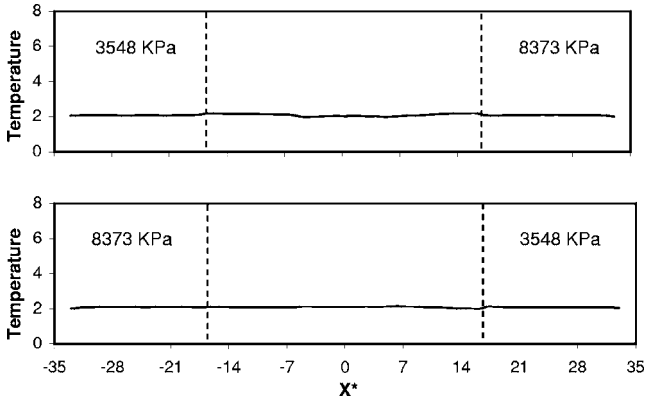

FIG. 4. Time-averaged temperature distribution in the pore system used in the simulation of the CO_2-CH_4 mixture.

nanopore side moves the transition point between a gaslike and liquidlike state to inside the macropore, hence making the passage of the molecules from the mesopore to the macropore easier, which increases K in that direction.

We now present the results for the binary mixture. Figure 4 shows the (dimensionless) temperature (averaged in the yz planes) throughout the pore system, which indicates that it remains constant. Hence, all the possible effects due to a temperature gradient have been eliminated. Figure 5 presents a snapshot of the pore system and the distribution of CO_2 and CH_4 molecules in it, after the steady state was reached, with the upstream and downstream pressures being 1215 psi (8373 kPa) and 515 psi (3548 kPa), respectively. To understand the distributions of the two molecules in the pores better, we present in Figs. 6 and 7 the time-averaged densities $\rho_i^x(z)$ for the two molecules at six different planes that are perpendicular to the direction of ΔP (the coordinates' center is on the centerline that passes through the three pores). Figure 6 shows the density profiles when the upstream condition is maintained in the CV which is connected to the macropore. In plane 1 near the pore mouth connected to the CV, two layers of each type of molecule have been formed. One, with high densities, is near the walls, while the second one with lower densities is closer to the center. In the opposite plane (denoted by 2 in Fig. 6) near the macropore mouth that connects it to the mesopore, the density profiles look chaotic, with several layers of the two molecules forming. This is caused by the entrance effect whereby, due to the size of the mesopore which is much smaller than that of the macropore, a large number of molecules accumulates at the macropore's entrance to the mesopore. But, if we inspect the density profiles just inside the mesopore (denoted by 3 in the figure), we find again that two layers of each type of molecules have been formed inside the mesopore. The molecules' distributions in the region where the mesopore is connected to the nanopore (denoted by 4 in the figure) are qualitatively similar to those in plane 2, and are again dominated by the entrance effects. The very small size of the nanopore allows only monolayer formation. As a result, one obtains the density profiles shown in Fig. 6 for planes 5 and 6 shown in the figure. The same qualitative patterns are obtained when the upstream condition is held in the CV connected to the nanpore (see Fig. 7), but with one difference: Only one layer of each type of molecules has been formed in plane 1, where the macropore is connected to the CV. This is clearly caused by the low downstream pressure which gives rise to a gaslike state in that region, and is also consistent with the snapshot of the pore system shown in Fig. 5.

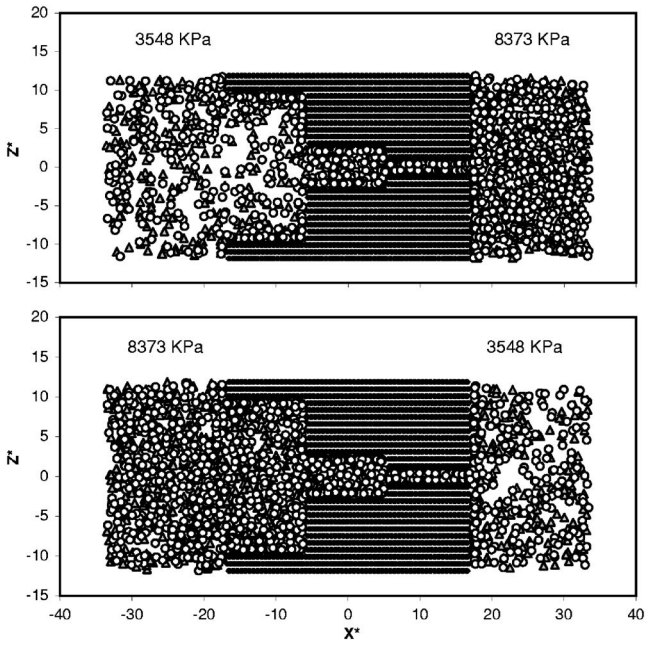

FIG. 5. A snapshot of the pore system with the distributions of CO_2 (circles) and CH_4 (triangles) in an equimolar mixture. The system is at steady state.

Figure 8 presents the time-averaged density profiles $\rho_i^z(x)$ of the two components (averaged in the yz planes) for the two upstream conditions. The mixture is equimolar. The densities in the two bulk regions are constant, as they should be. As one moves from the macropore to mesopore to nanopore, the densities, regardless of the direction of ΔP (or the upstream condition), increase since the pores' sizes decrease. A closer inspection of the densities in the pores indicates that, for the applied ΔP, one has a gaslike (low density) mixture in much of the macropore in both cases, followed by a transition to a liquidlike mixture (due to condensation) which packs the mesopores and nanopores completely at high densities. The position of the transition line from the gaslike to liquidlike mixture depends on the pores' sizes and the direction of ΔP. The density profiles shown in Fig. 8 are consistent with the snapshot of the system shown in Fig. 5, as they should be. At the same time, we should point out that, although we carried out long simulations, the slight increase in the density profile $\rho^z(x)$ of CO_2 (the dashed curve) in the nanopore, when the upstream condition is imposed on this pore (see the upper panel in Fig. 8), could still be due to nonequilibrium effects that may be exceedingly difficult to detect in our simulations.

Figure 9 presents the permeabilities of the two components in an equimolar mixture with ΔP=4825 kPa (700 psi), computed when the pressure drop was applied in the two opposite directions shown in Figs. 1 and 5, and the upstream pressure was varied. The same qualitative patterns are obtained when other values of pressure drops are applied, and

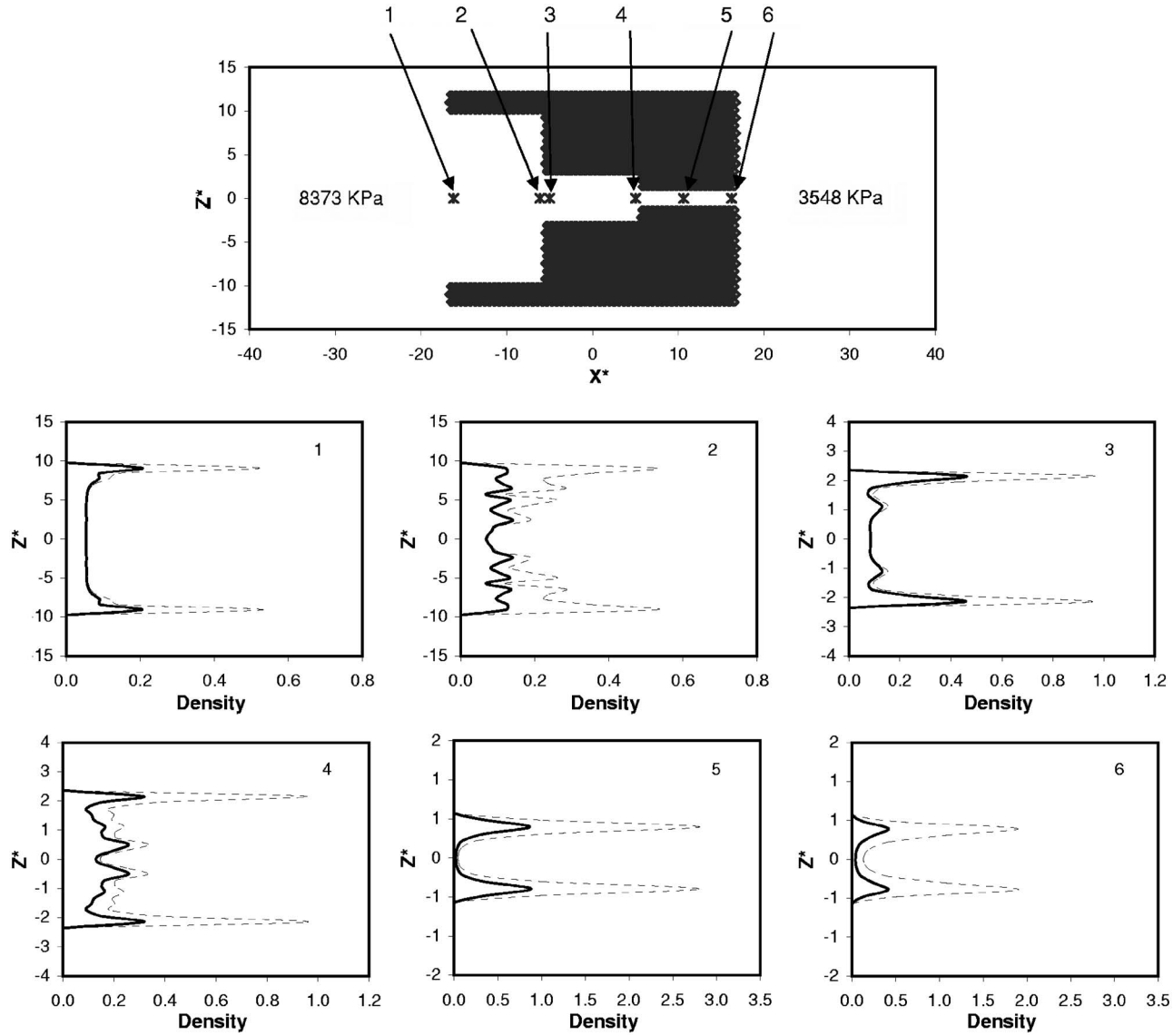

FIG. 6. Time-averaged density profiles $\rho_i^x(z)$ of CO_2 (dashed curves) and CH_4 (solid curves), when the upstream condition is maintained in the control volume connected to the macropore. The mixture is equimolar.

the upstream and downstream conditions are such that one crosses from a subcritical region to a supercritical one (the critical pressure for CO_2 is about 7380 kPa). In addition to the fact that the pressure dependence of K_1 and K_2 is in qualitative agreement with experimental data [10,20], another noteworthy feature of Fig. 9 is that the permeabilities differ significantly, with K_2—that of CO_2—being larger. The reason is that, due to affinity of CO_2 for carbon surfaces, there is significant flow of CO_2 on or near the walls which is not the case for CH_4. This is particularly important, as the nanopores and mesopores are packed with molecules and, therefore, the molecules' motion in the bulk of the pores is exceedingly slow. Hence, surface flow becomes important.

The direction dependence of the permeabilities, for both pure CO_2 and those in the mixture, may be explained based on a continuum model. As is well known, transport in a macropore is dominated by convection, which gives rise to a permeability independent of the direction of the applied pressure gradient. In a mesopore, transport is by a combination of convection and Knudsen diffusion [2,20], whereas in a nanopore, due to its small size and the condensation phenomenon, transport occurs mostly through surface flow. While condensation does play a role in the direction dependence of the effective permeabilities, the most important factor appears to be the composite nature of the system. To see this, we make an analogy between the resistances that the three pores in series offer against transport and that of electrical resistors. Then, because the three pores are in series, the effective permeability K_e of the pore system is given by

$$K_e = L\left[\sum_{i=1}^{3}\left(\frac{K_i}{L_i}\right)\right]^{-1}, \tag{4}$$

where K_i and L_i are, respectively, the overall permeance and length of pore number i. It is now not difficult to show that it is the nonlinear dependence of K_e on K_i that is mostly re-

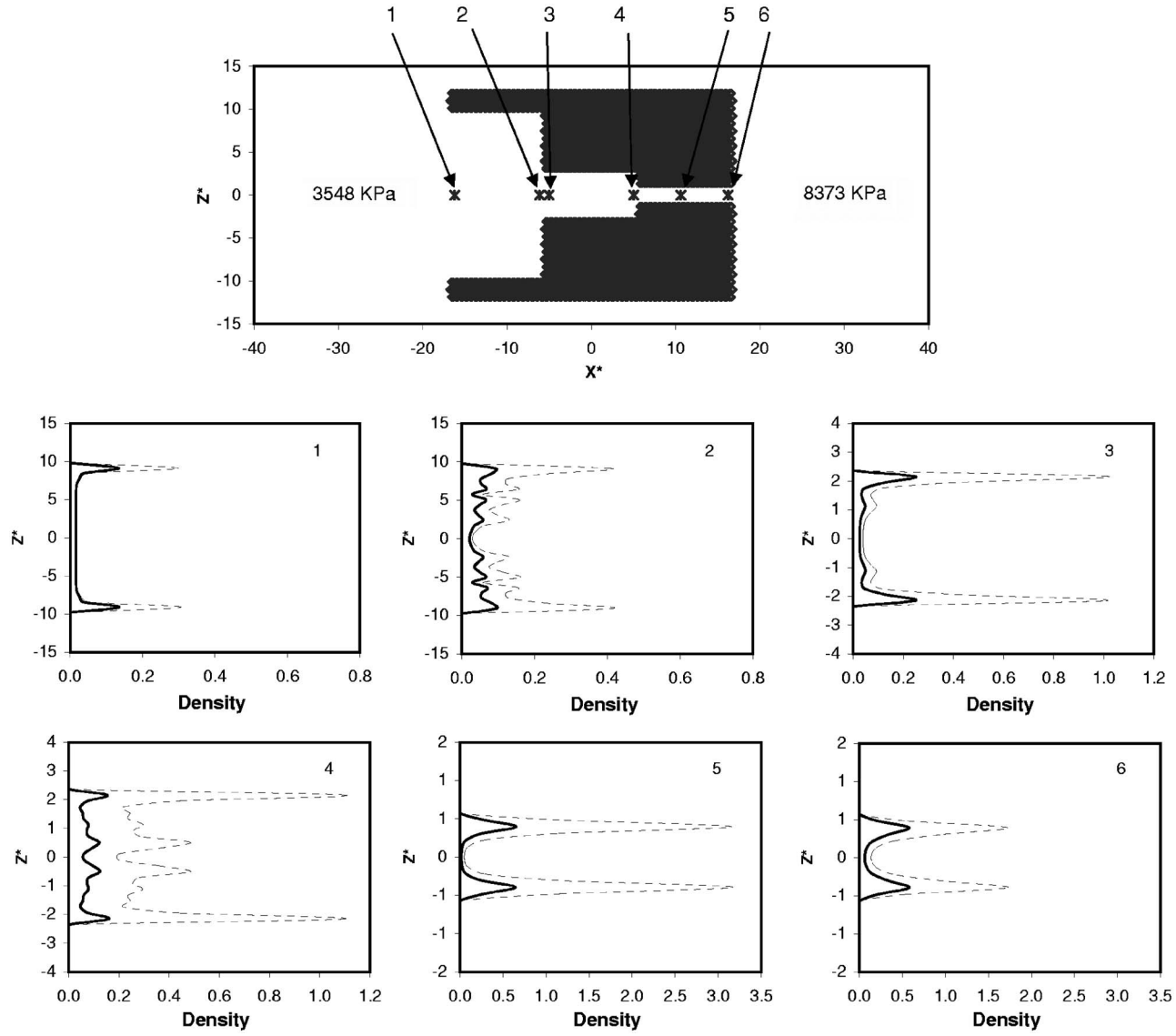

FIG. 7. Same as in Fig. 6, but when the upstream condition is maintained in the control volume connected to the nanopore.

sponsible for its direction dependence. This is true even if one has a gaseous mixture in the composite pore system, as opposed to liquidlike mixtures (caused by condensation) that we deal with in our pore system. To show this, we proceed as follows.

Consider, first, transport of a gas in a single pore and assume that the gas is transported by a combination of convection and Knudsen diffusion. Hence, its flux is given by [2,20,21]

$$J = -\left(D_k \frac{dP}{dx} + K_p P \frac{dP}{dx}\right), \tag{5}$$

where D_K is the Knudsen diffusivity of the gas. K_p is a permeability *coefficient* defined for gases (according to Darcy's law, $K_p P$ is what is usually referred to as the permeability). K_p is independent of the pressure. Assuming, as usual, that D_k is also independent of the pressure, then, since the flux J is constant at steady state, Eq. (4) can be easily integrated to yield

$$J = -L^{-1}\left[D_k(P_2 - P_1) + \frac{1}{2}K_p(P_2^2 - P_1^2)\right], \tag{6}$$

where P_1 and P_2 are the applied pressure at the pores' ends, and L is its length. According to Eq. (6), the magnitude of the flux and, therefore, the effective permeability K_e given by,

$$K_e = D_k + \frac{1}{2}K_p(P_1 + P_2), \tag{7}$$

are independent of the *direction* of the applied pressure drop, $\Delta P = P_2 - P_1$, because the interchanges, $P_1 \to P_2$ and $P_2 \to P_1$ would not alter Eq. (7). Note that, even if we replace the convective term of Eq. (5) by KdP/dx, which is the appropriate form for liquids and the liquidlike mixtures (such as those under supercritical conditions), the conclusion that in a *single pore* K_e does not depend on the direction of ΔP

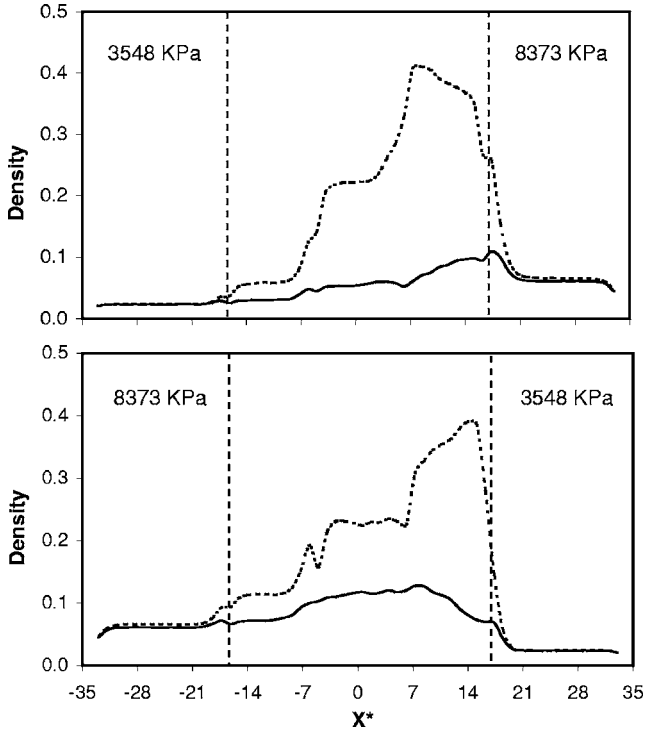

FIG. 8. Time-averaged density profiles $\rho_i^z(x)$ of CO_2 (dashed curves) and CH_4 (solid curves), in an equimolar mixture.

will remain true, since in that case, $K_e=D_k+\frac{1}{2}K$.

Next, consider two pores that are in series, and suppose that the pressure at the interface between them is P_i [21]. We assume that in one pore, say pore 1, convection is the dominant mechanism of transport (as in the macropore), while both convection and Knudsen diffusion contribute to transport in pore 2 (as in the mesopore). Hence, using Eq. (6), we write down the following expressions for the fluxes J_1 and J_2 in the two pores

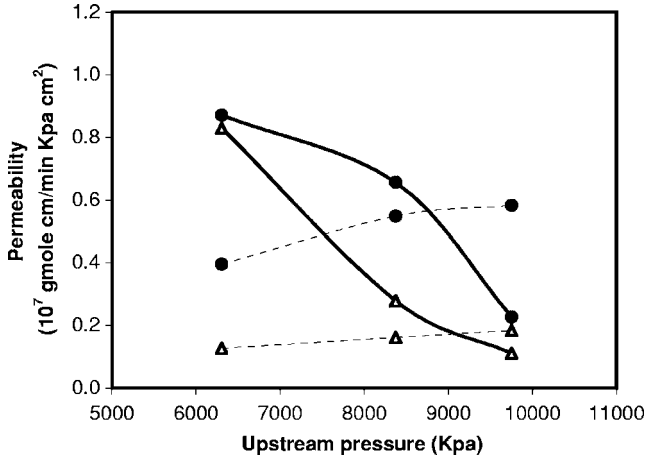

FIG. 9. The dependence of the permeabilities of CO_2 (circles) and CH_4 (triangles) on the upstream pressure, when a pressure drop, $\Delta P=4825$ kPa (700 psi), is applied in the two opposite directions. Continuous and dashed curves show, respectively, the results when the upstream pressure is maintained at entrance to the macropore and nanopore.

$$J_1 = -\frac{1}{2}L_1^{-1}K_p^{(1)}(P_i^2 - P_1^2), \tag{8}$$

$$J_2 = -L_2^{-1}\left[D_k^{(2)}(P_2 - P_i) + \frac{1}{2}K_p^{(2)}(P_2^2 - P_i^2)\right]. \tag{9}$$

At steady state, $J_1=J_2$. Therefore, we only need to determine the pressure P_i, which is obtained by requiring that, $J_1=J_2$, yielding a second-order equation, $aP_i^2+bP_i+c=0$, in which the parameters a, b, and c are given by

$$a = \frac{1}{2}[\alpha K_p^{(1)} + K_p^{(2)}],$$

$$b = D_k^{(2)},$$

$$c = -\left[\frac{1}{2}\alpha K_p^{(1)}P_1^2 + \frac{1}{2}K_p^{(2)}P_2^2 + D_k^{(2)}P_2\right], \tag{10}$$

where $\alpha=L_2/L_1$. It is now not difficult to see that the magnitude of the flux, $J=J_1=J_2$, depends on the *direction* of ΔP by making the interchanges, $P_1 \rightarrow P_2$ and $P_2 \rightarrow P_1$, in agreement with the MD simulations presented above. Clearly, the same approach can be extended to the three-pore system we use in the simulations. Moreover, the conclusion will not change if, for example, Knudsen diffusion is the dominant transport mechanism in one pore, while convection contributes the most to the transport in another pore.

IV. SUMMARY

The results presented in this paper indicate the significance of the pore structure and the fluids' state to their transport through a porous material. In particular, aside from being in qualitative agreement with our preliminary experimental data [22], the results have two important implications:

(1) The classical modeling of transport of fluids through porous membranes, based on a single effective permeability independent of the direction of the applied pressure gradient, is inadequate if they have a composite structure similar to what we use in the present paper. This is usually the case when the membrane has a support structure.

(2) Unlike the popular practice, a single pore is a gross and inadequate model of an actual composite (supported) membrane, which typically consists of several layers, each characterized by their own morphological and transport properties [21].

In practice, supercritical fluid extraction using CO_2 is utilized when the mixture contains heavier hydrocarbons, such as pentane and hexane. In such cases, the molecular structure of the hydrocarbons and their motion through the nanopores give rise to additional complexities, such as *freezing* phenomena whereby the mixture does not move appreciably even over long periods of times. Molecular dynamics simulation of flow and transport of such mixtures through the pore system considered in this paper is underway. The results will be reported in a future paper [23].

ACKNOWLEDGMENTS

We are grateful to the National Science Foundation, the Department of Energy, the Petroleum Research Fund administered by the American Chemical Society, and Media and Process Technology, Inc., for partial support of this work. We would also like to thank the San Diego Supercomputer Center for providing much needed computer time.

[1] *Access in Nanoporous Materials*, edited by T. J. Pinnavaia and M. F. Thorpe (Plenum, New York, 1995).

[2] M. Sahimi, Rev. Mod. Phys. **65**, 1393 (1993); *Flow and Transport in Porous Media and Fractured Rock*, 2nd ed. (VCH, Weinheim, 2006); S. Torquato, *Random Heterogeneous Materials* (Springer, New York, 2002).

[3] M. Sahimi and T. T. Tsotsis, in *Handbook of Computational Nanotechnology*, edited by W. Schommer and M. Reith (American, New York, 2005), Chap. 74; M. Sahimi, *Heterogeneous Materials II* (Springer, New York, 2003), Chap. 9.

[4] E. Kiran and J. M. H. L. Sengers, *Supercritical Fluids-Fundamentals for Applications* (Kluwer, Dordrecht, 1994).

[5] R. K. Roop *et al.*, J. Supercrit. Fluids **1**, 31 (1988); Y. Meguro *et al.*, Radiochim. Acta **75**, 185 (1996).

[6] M. H. Liu *et al.*, Chemosphere **23**, 1088 (1991); A. Firus, W. Weber, and G. Brunner, Sep. Sci. Technol. **32**, 1403 (1997).

[7] L. J. Silva, L. A. Bray, and D. W. Matson, Ind. Eng. Chem. Res. **32**, 2485 (1993).

[8] Z. Novak and Z. Knez, J. Non-Cryst. Solids **221**, 163 (1997); P. Wawrzyniak *et al.*, *ibid.* **225**, 86 (1998).

[9] D. L. Tomasco *et al.*, Environ. Prog. **12**, 208 (1993); D. L. Tomasco *et al.*, Sep. Sci. Technol. **30**, 1901 (1995).

[10] H. Ohya *et al.*, J. Membr. Sci. **84**, 185 (1993); S. Sarrade, G. M. Rios, and M. Carles, *ibid.* **114**, 81 (1996); Y. Tokunaga, T. Fujii, and K. Nakamura, J. Card. Surg. **61**, 1024 (1997).

[11] V. M. Linkov, R. D. Sanderson, and E. P. Jacobs, Mater. Lett. **20**, 43 (1994); T. Steriotis *et al.*, J. Appl. Polym. Sci. **64**, 2323 (1997); M. B. Shiflett and H. C. Foley, Science **285**, 1902 (1999).

[12] M. G. Sedigh, W. J. Onstot, L. Xu, W. L. Peng, T. T. Tsotsis, and M. Sahimi, J. Phys. Chem. A **102**, 8580 (1998); M. G. Sedigh, L. Xu, T. T. Tsotsis, and M. Sahimi, Ind. Eng. Chem. Res. **38**, 3367 (1999); M. G. Sedigh, M. Jahangiri, P. K. T. Liu, M. Sahimi, and T. T. Tsotsis, AIChE J. **46**, 2245 (2000).

[13] T. Düren, S. Jakobtorweihen, F. J. Keil, and N. A. Seaton, Phys. Chem. Chem. Phys. **5**, 369 (2003).

[14] L. Xu, M. G. Sedigh, M. Sahimi, and T. T. Tsotsis, Phys. Rev. Lett. **80**, 3511 (1998); L. Xu, M. G. Sedigh, T. T. Tsotsis, and M. Sahimi, J. Chem. Phys. **112**, 910 (2000); L. Xu, T. T. Tsotsis, and M. Sahimi, *ibid.* **111**, 3252 (1999); L. Xu, M. Sahimi, and T. T. Tsotsis, Phys. Rev. E **62**, 6942 (2000).

[15] S. T. Chung and K. S. Shing, Fluid Phase Equilib. **81**, 321 (1992); C. A. Eckert, B. L. Knutson, and P. G. Debenedetti, Nature (London) **383**, 313 (1996); A. A. Chialvo and P. T. Cummings, Adv. Chem. Phys. **109**, 115 (1999).

[16] D. Nicholson, Carbon **36**, 1511 (1998); T. Shingetta, J. Yoneya, and T. Nitta, Mol. Simul. **16**, 291 (1996); G. K. Papadopoulos, J. Chem. Phys. **114**, 8139 (2001).

[17] M. Firouzi, T. T. Tsotsis, and M. Sahimi, J. Chem. Phys. **119**, 6810 (2004).

[18] G. S. Heffelfinger and F. van Swol, J. Chem. Phys. **100**, 7548 (1994); R. F. Cracknell, D. Nicholson, and N. Quirke, Phys. Rev. Lett. **74**, 2463 (1995); D. M. Ford and G. S. Heffelfinger, Mol. Phys. **94**, 673 (1998).

[19] J. K. Johnson, J. A. Zollweg, and K. E. Gubbins, Mol. Phys. **78**, 591 (1993).

[20] E. Mason and A. P. Malinauskas, *Gas Transport in Porous Media: The Dusty Gas Model* (Elsevier, Amsterdam, 1983).

[21] P. Uchytil, O. Schramm, and A. Seidel-Morgenstern, J. Membr. Sci. **170**, 215 (2000); S. Thomas, R. Schäfer, J. Caro, and A. Seidel-Morgenstern, Catal. Today **67**, 205 (2001).

[22] Kh. Molaai Nezhad, M. Sahimi, and T. T. Tsotsis (unpublished).

[23] M. Firouzi, T. T. Tsotsis, and M. Sahimi (unpublished).

Available online at www.sciencedirect.com
ScienceDirect
Journal of Membrane Science 288 (2007) 290–297
journal of MEMBRANE SCIENCE
www.elsevier.com/locate/memsci

Silicon carbide membranes for gas separation applications

Bahman Elyassi, Muhammad Sahimi, Theodore T. Tsotsis *

Mork Family Department of Chemical Engineering & Materials Science, University of Southern California, Los Angeles, CA 90089-1211, USA

Received 2 October 2006; received in revised form 20 November 2006; accepted 21 November 2006
Available online 25 November 2006

Abstract

SiC microporous membranes were prepared by the pyrolysis of thin allyl-hydridopolycarbosilane (AHPCS) films coated, using a combination of slip-casting and dip-coating techniques, on tubular silicon carbide macroporous supports. Combining slip-casting with dip-coating significantly improved the reproducibility in preparing high quality membranes. The membranes prepared, so far, exhibited an ideal H_2/CO_2 selectivity in the range of 42–96, and a H_2/CH_4 ideal selectivity in the range of 29–78. Separation factors measured with the same membranes, using equimolar binary mixtures of H_2 in CO_2 and H_2 in CH_4, were similar to the ideal selectivity values. Steam stability experiments with the membranes lasting 21 days, using an equimolar flowing mixture of He/H_2O at 200 °C, indicated some initial decline in the permeance of He, after which the permeance became stable at these conditions.

Keywords: Silicon carbide membrane; AHPCS; Slip-coating; Dip-coating; Gas separation

1. Introduction

Growing interest in the hydrogen economy is motivating research on inorganic, hydrogen-permselective membranes, which can be used in processes (related to H_2 production) that take place at high-temperatures and pressures. A promising candidate material for a variety of inorganic membrane applications is SiC due to its many unique properties, such as high thermal conductivity [1], thermal shock resistance [2], biocompatibility [3], resistance in acidic and alkali environments [4], chemical inertness, and high mechanical strength [5,6]. There are relatively few reports discussing the preparation of SiC membranes. Two different approaches have been utilized. One involves the use of chemical-vapor deposition (CVD)/chemical-vapor infiltration (CVI) techniques, while the other approach is based on the pyrolysis of polymeric precursors.

Takeda et al. [7] prepared SiC membranes by CVI, using SiH_2Cl_2 and C_2H_2 diluted with H_2, and γ-Al_2O_3 tubes as supports. Their membrane had a H_2 permeance of 1×10^{-8} mol m^{-2} s^{-1} Pa^{-1} at 350 °C, with an ideal H_2/N_2 selectivity of 3.36, lower than the corresponding Knudsen value. Sea et al. [8] prepared a SiC membrane using an α-alumina tube as support by CVD of $(C_3H_7)_3SiH$ (tri-isopropylsilane or TPS) at 700–800 °C. After CVD, the membrane was calcined at 1000 °C in Ar, then tested with pure gas permeation, and was shown to follow a Knudsen mechanism, with H_2 permeance in the range (5–6) $\times 10^{-7}$ mol m^{-2} s^{-1} Pa^{-1}. A permeation test was also carried out with a H_2–H_2O–HBr gas mixture (molar ratio of 0.49:0.5:0.01) between 200 and 400 °C. In the beginning of the test, the H_2/H_2O separation factor was higher than the Knudsen value (∼5). Exposure of the membrane to the mixture at 400 °C resulted in a decline of the H_2 permeance during the first 50 h (by a factor of ∼2.5); the permeance stabilized after that, remaining constant for the remainder of the run, which lasted 120 h [8]. Pages et al. [9] prepared Si:C:H membranes on alumina supports using plasma enhanced CVD (PECVD) of diethylsilane; the resulting membranes had a permeance in the range of (10^{-7}–10^{-6}) mol m^{-2} s^{-1} Pa^{-1} for H_2, but with an ideal separation factor for H_2/N_2 in the range (3–4).

Our group was the first to report [10] the preparation of microporous SiC membranes using CVD. We utilized $CH_3SiH_2CH_2SiH_3$ (1,3-disilabutane or DSB) to prepare membranes on γ-Al_2O_3 tubular supports. To prepare the membranes, the substrates were exposed to the DSB vapor at temperatures between 650 and 750 °C. Nanoporous membranes were prepared with a He permeance of 3.5×10^{-7} mol m^{-2} s^{-1} Pa^{-1},

* Corresponding author. Tel.: +1 213 740 2069; fax: +1 213 740 8053.
E-mail address: tsotsis@usc.edu (T.T. Tsotsis).

0376-7388/$ – see front matter © 2006 Elsevier B.V. All rights reserved.
doi:10.1016/j.memsci.2006.11.027

and a He/N_2 selectivity of ~55 at 550 °C. The DSB membranes were thermally stable, but did not fare well in the presence of high-temperature steam, being unstable. We have also used CVD of TPS at 700–750 °C to prepare SiC membranes. Depending on the preparation conditions, the He permeance ranged from 8.06×10^{-8} to 1.72×10^{-6} mol m^{-2} s^{-1} Pa^{-1} with a He/N_2 ideal selectivity ranging from 4 to >100. These membranes are also stable in the presence of high-pressure (1–3 bar) and temperature (<750 °C) steam. However, the preparation procedure involves multiple steps, which makes it costly, and requires a high-temperature (1000 °C) treatment, which places a great burden on glass end-seals and membrane housing during the CVD/CVI process. More importantly, the high-temperature post-treatment further modifies the nanoporous structure of the membrane prepared at the lower temperature. Therefore, the final product quality is difficult to predict and control; from a membrane manufacturing standpoint, the advantage of the on-line control of the CVD/CVI technique is, therefore, lost.

To overcome these hurdles, we have pursued, in tandem with TPS CVD/CVI, a dip-coating technique through the pyrolysis of allyl-hydridopolycarbosilane (AHPCS), a partially allyl-substituted hydridopolycarbosilane (HPCS). The choice of AHPCS is because it is curable in the presence of inert Ar gas, rather than oxygen (as are other PCS pre-ceramic polymers). In fact, curing in oxygen introduces Si–O–C linkages in the resulting PCS-derived ceramics, which have proven thermally and hydrothermally unstable. The use of HPCS was first proposed by Interrante et al. [11,12]. The primary pyrolysis product of both HPCS and AHPCS is a SiC ceramic, having a Si–C bond linkage. Increasing the fractions of allyl groups slightly increases the carbon content of the final ceramic, and also makes the polymer cross-linkable at lower temperatures. The membranes we prepared with conventional dip-coating possessed He permeance in the range (10^{-8}–10^{-7}) mol m^{-2} s^{-1} Pa^{-1}, and had an ideal separation factor of about 20 for He/N_2 at 200 °C [10]. They proved thermally stable but, however, did not fare well in the presence of high-temperature steam, proving highly unstable.

Prior to our study, other investigators had reported the pyrolysis of PCS and other polymers for the preparation of SiC membranes. Morooka and coworkers [4,13,14], for example, used a PCS that they cured in oxygen to prepare a Si–O–C membranes on γ- and α-Al_2O_3 tubular substrates with an oxygen content of 13–18 wt%, using polystyrene (PS) as the pore former. A membrane prepared with 1% PS had a H_2 permeance of 4×10^{-8} mol m^{-2} s^{-1} Pa^{-1}, and an ideal H_2/N_2 selectivity of 20 at 773 K. The membrane was unstable in Ar at 1223 K, and also hydrothermally unstable when exposed to a 7.8 wt% H_2O in He mixture at 773 K. Lee and Tsai [15,16] prepared Si–C–O membranes by the pyrolysis of polydimethylsilane (PMS). The PMS undergoes a thermolytic reaction at 733 K for 14 h under 1 atm of Ar, followed by O_2 curing at 473 K for 1 h. The layer was finally pyrolyzed at various temperatures from 523 to 1223 K to produce the membranes. The membrane pyrolyzed at 873 K had the best separation characteristics, exhibiting a He permeance of $\sim 1.4 \times 10^{-9}$ mol m^{-2} s^{-1} Pa^{-1}, a H_2 permeance of $\sim 2.7 \times 10^{-9}$ mol m^{-2} s^{-1} Pa^{-1}, and an ideal H_2/N_2 selectivity of 20 at 473 K. Membranes prepared at the higher pyrolysis temperatures were not microporous. Chen and Tsai [17] prepared PMS-derived SiC membranes in an autoclave under a N_2 atmosphere at low temperatures. Exposure of the membranes to steam increased their permeance, and returned their ideal selectivities to their Knudsen values. Since our study [10], two other groups have prepared membranes by pyrolysis of PCS-type polymers cured in the absence of O_2. Suda et al. [18] prepared SiC membranes by dip-coating PCS on α-alumina tubes (PS was used as the pore-former for some of the membranes). Their membranes exhibited ideal separation factors of 90–150 for H_2/N_2, and H_2 permeance in the range of $(1–3) \times 10^{-8}$ mol m^{-2} s^{-1} Pa^{-1} at 373 K. Nagano et al. [19] prepared SiC membrane by dip-coating of PCS on γ-alumina supports, and reported H_2 permeance $\sim 10^{-7}$ mol m^{-2} s^{-1} Pa^{-1}, and an ideal separation factor of 8–12 for H_2/N_2 at 873 K.

Past studies presented only single gas permeation data; other than the membranes prepared by TPS CVD [10], the rest were shown to be unstable in steam. Membranes prepared by AHPCS pyrolysis [10] showed good separation factors and thermal stability, but also proved unstable in steam. The principal goal of the present study, therefore, was to improve membrane hydrothermal stability. Another important goal was to improve the reproducibility of the fabrication method, since one of the factors that have, so far, hampered the broad application of inorganic membranes is their cost [20]. In this paper, we report significant improvements on the fabrication of high performance SiC membranes using a combination of slip-casting and dip-coating techniques. Membranes are prepared that are stable under conditions that are relevant to the WGS environment. The effect of low temperature oxidation on the properties of these membranes is also reported here.

2. Experimental

Ultra-high purity gases (He, H_2, Ar, CO_2, from Glimore Liquid Air Company, and CH_4 from Specialty Air Technologies, Inc.) were used in the experiments. They were further purified using standard moisture traps. For the CO_2, in addition, we utilized a Hi-EFF® organic trap (Alltech). Porous SiC support tubes were prepared using uniaxial cold-pressing of β-SiC powder (HSC059, by Superior Graphite Co., with an average particle size of 0.6 μm as reported by the manufacturer), together with the appropriate sintering aids. For sintering, the green samples were heated at a temperature of 1800 °C, where they were kept in a furnace (Thermal Technology Inc., Model 1000-4560-FP20) for 3 h in flowing He. After sintering, the samples were cooled down to room temperature (cooling rate of 3 °C/min). The tubes, after sintering, had dimensions of 40 mm × 12 mm, with a thickness of 3 mm. Further details about the sintering characteristics of various SiC powders and the preparation of porous supports were presented elsewhere [21].

The support tubes used in the membrane preparation were treated in air at 450 °C, with the purpose to oxidize any residual carbon that may be introduced during preparation, sonicated several times in acetone, and then dried prior to membrane film deposition. In order to prepare the slip-casting solution, the 0.6 μm SiC powder was mixed with acetone, and the

lighter particles floating on the solution top were separated and dried. Scanning electron microscopy (SEM, Philips, XL3) observations of these particles indicated their size was mostly ~100–200 nm. The dip-coating solution was prepared by dissolving AHPCS (SMP-10, Starfire Systems, Inc.) in hexane (10 wt%). A solution containing 10 wt% of these SiC particles in the dip-coating solution constitutes the slip-casting solution.

Slip-casting was used to coat the first layer on the outer surface of the support tubes. To prepare this layer, the tube was placed in the slip-casting solution for 12 s and, then, drawn out of the solution at a speed of 2 mm/s. The coated tubes were heated in flowing Ar in a tube furnace (Lindberg/Blue, Model STF55433C) at a rate of 2 °C/min, first to 200 °C, where they were kept for 1 h, then to 400 °C, where they were also kept for 1 h, and finally to 750 °C, where they were kept for an additional 2 h. Subsequently, they were cooled down to room temperature in flowing Ar with a cooling rate of 3 °C/min. The reason for the relatively slow heating (and holding at 200 °C) is that we have found (as did others [11,18]), that using such heating rates, and treatment at lower temperatures result, generally, in better cross-linked amorphous SiC materials [11], and membranes with higher hydrogen permeabilities [18].

For membrane preparation, additional layers were deposited on the support tubes, with the slip-casted SiC layer on the top, by dip-coating with the 10 wt% solution of AHPCS in hexane using the same procedure (i.e., 12 s of dipping time, drawing rate of 2 mm/s). The membranes, reported here, were dip-coated four times. After each coating, the new layer was pyrolyzed following the same protocol with the slip-casted layer. Layer-by-layer dip-coating and pyrolysis result in membranes with decreased permeance and higher separation factors. Depositing several thin layers, instead of a single thick layer, provides the advantage of facilitating the release of the gases from the pyrolysis process, and also decreases the chance of defect formation due to film shrinkage.

After coating the final layer, the membranes were typically treated in air for 2 h at 450 °C with the purpose to oxidize potential residual carbon. This, in general, results in higher permeances and lower separation factors (the effect of low temperature air treatment is discussed further later). Although AHPCS has been reported to result in a SiC ceramic with a near stoichiometric Si:C ratio [11], one cannot exclude the possibility that after pyrolysis there may remain trivial amounts of carbon, which may influence membrane performance. Low-temperature air oxidation has been shown effective in removing minute amounts of carbon, for example as a common way for carbon nanotube purification [22–24]. By oxidizing in air the SiC membranes, prior to their use, one ensures that no further variation in membrane properties will occur due to accidental exposure to air.

Surface and cross-section morphologies of the membranes were characterized by SEM. AHPCS-derived powders, pyrolyzed with the same protocol as the membranes, were analyzed by X-ray diffraction analysis (XRD, Rigaku X-ray diffractometer with Cu Kα radiation). Permeation experiments were carried out using a Wicke-Kallenbach-type permeation apparatus previously utilized to measure permeation through flat-disk SiC membranes [10]. In order to use this apparatus for tubular membranes, one end of the membranes is completely sealed using graphite tape and high-temperature non-porous glue (J-B WELD); the other end of the membrane is attached to a flat metal ring using the same glue. The metal ring bearing the membrane is then installed in between the two half-cells of the permeation test-unit using O-rings. Single-gas permeation experiments were carried out by flowing a given gas through the apparatus half-cell facing the membrane dead-end, under constant pressure and temperature, and by measuring the amount of gas that permeates through the membrane to the permeate side which was maintained at atmospheric pressure. In the experiments reported here, the pressure drop across the membranes was kept at 207 kPa (30 psi), and the temperature was varied from room temperature to 200 °C. We report the ideal selectivity for these membranes, which is defined as the ratio of the permeances of the different gases.

Mixed-gas permeation tests were also carried out with select membranes using equimolar binary (H_2/CH_4, and H_2/CO_2) gas mixtures. For the mixed-gas experiments, in addition to the gas flow to the permeate side of the membrane, the composition was also analyzed using a mass spectrometer. During the experiments, the flow of gas permeating through the membrane was less than 0.5 percent of the gas flowing in the feed-side. Therefore, it was assumed that the concentration in the feed-side remained invariant. Steam stability tests, using an equimolar mixture of He and water, were also conducted with the membranes at 200 °C. Water was delivered by a metering micro-pump into a stainless steel steam vessel (vaporizer) in flowing He. The vaporizer was filled with glass beads for better mixing, and its temperature was kept constant at 200 °C.

3. Results and discussion

3.1. Membrane characterization and performance

The quality of the membrane support is known to be important in determining the quality of the membranes that are prepared using these supports. Large defects in the supports are thought to lead to defects in the membranes, resulting in low reproducibility in preparing membranes with high separation factors. The ability to strongly anchor the thin films on the underlying supports is also of key importance. In our prior study [10] we directly dip-coated the membrane films; the resulting membranes had good separation characteristics, but proved to be hydrothermally unstable. In this study we have used slip-casting in order to first condition the surface of supports. Slip-casting results in the formation of a film which strongly adheres onto the underlying support, as manifested by the superior hydrothermal stability of these membranes (see further Section 3), and on which we deposit the subsequent layers by dip-coating. In addition, the success rate in preparing "good" microporous membranes using the porous SiC tubes modified by slip-casting was much higher than when preparing membranes using the original support tubes (a "good" membrane is one with an ideal H_2/CH_4 separation factor ~30 or larger, and with a hydrogen permeance $>10^{-9}$ mol m^{-2} s^{-1} Pa^{-1} at 200 °C).

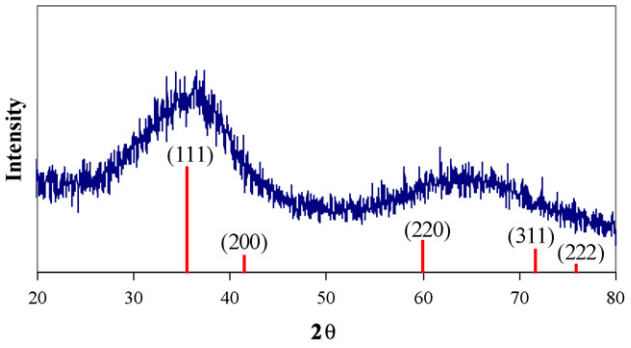

Fig. 1. XRD of an AHPCS-derived amorphous SiC powder pyrolyzed at 750 °C for 2 h along with Joint Committee on Powder Diffraction Standards (JCPDF) card number 29-1129 for crystalline β-SiC.

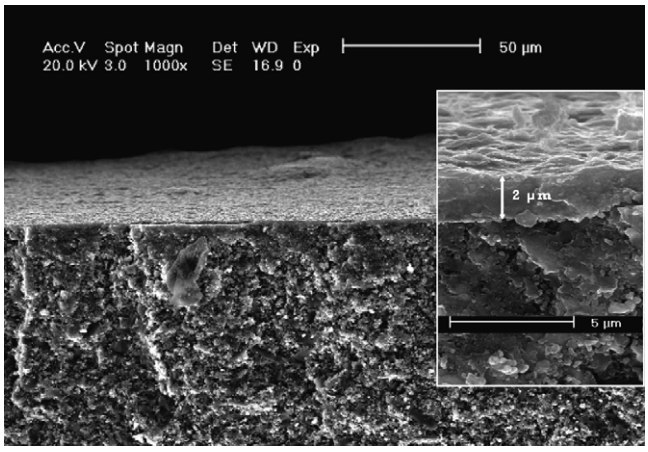

Fig. 2. SEM pictures showing the cross-section and the top view of a SiC membrane.

The type of powder used during slip-casting has also a significant effect on the ability to prepare appropriate top layers, which in turn can be used for further membrane deposition in the preparation of high performance membranes. For example, using a different β-SiC powder with an average size of 30 nm (provided to us by Sumitomo Osaka Cement Co.) did not result in smooth uniform top layers. Instead, after pyrolysis the particles agglomerated on the support tube surface. The difference in behavior could be attributed to the chemical or physical differences between these two SiC powders, which came from two different manufacturers [25–27]. In fact, we found that the Sumitomo powder was more difficult to uniformly disperse in solution and, therefore, to use for producing a homogeneous slip-casting solution. The thickness of the slip-casted film also influences membrane performance. Too thick of a film (prepared, for example, by increasing the residence time in the slip-coating solution) resulted in membranes with poor performance.

In our previous paper, X-ray photoelectron spectroscopy (XPS) analysis and *in situ* diffuse reflectance infrared Fourier transform spectroscopy (DRIFTS) were utilized to follow the various processes that occur during the pyrolysis of AHPCS to produce SiC [10]. We noted that increasing the pyrolysis temperature increases material crystallinity, as indicated both by the XRD and DRIFTS spectra [10]. Fig. 1, for example, shows the XRD of the AHPCS-derived SiC. The broad peaks show that the SiC is still primarily amorphous.

Fig. 2 is the SEM picture of the cross-section and the top surface of one of the membranes. The thickness of the membrane layer is about 2 μm, and sits on top of the SiC support. Energy Dispersive X-ray (EDX) analysis of the membranes revealed the presence of some oxygen in the structure of the membrane. Since the curing and cross-linking of the AHCPS takes place in the presence of Ar, it is unlikely that the oxygen will be introduced during the pyrolysis stage. There are reports, however, indicating the presence of minor amounts of oxygen in the structure of AHPCS-derived SiC (ranging from 3 to 6.7 wt%), and which claimed that the oxygen is introduced into the structure during the polymer preparation or handling stages [12,28,29] (however, the wt% of oxygen in these studies is calculated by difference during elemental analysis, and is not likely to be highly accurate). What is more likely is that the oxygen detected by EDX is the result of membrane exposure to air prior to the analysis; however, elemental analysis of SiC powders before and after low-temperature (450 °C) oxidation in air indicated that the Si:C ratio remains practically invariant, so that any oxygen incorporation, if present, is likely to be limited to the surface region.

Before coating the membranes, the He and Ar permeances (and the ideal selectivity) of the SiC supports were measured at room temperature. The permeance of He was of the order $\sim 10^{-7}$ mol m^{-2} s^{-1} Pa^{-1}, corresponding to an ideal separation factor of 2.6 for He/Ar (below the Knudsen value of 3.16). After deposition of the membrane film on the supports, the permeance of the resulting membranes was again measured at room temperature. Membranes, which exhibited separation factors higher than 6 at room temperature, were selected for further testing at higher temperatures.

Single-gas (H_2, CH_4, and CO_2) membrane permeance, and the corresponding ideal separation factors at 200 °C (for a number of membranes that were previously treated in air at 450 °C) are presented in Table 1. As can be seen, the membranes show relatively high ideal separation factors, ranging between 42–96 for H_2 over CO_2, and 29–78 for H_2 over CH_4. The permeance

Table 1
Range of single-gas permeances and separation factors, measured at 200 °C, prepared by pyrolysis at 750 °C for 2 h

	Single gas		
	H_2	CH_4	CO_2
Permeance ($\times 10^8$ mol m^{-2} s^{-1} Pa^{-1})	0.54–1.18	0.007–0.041	0.006–0.028
S.F. (H_2/gas)		29–78	42–96

Table 2
Single- and mixed-gas permeation properties of two SiC membranes (I and II), measured at 200 °C, prepared by pyrolysis at 750 °C for 2 h. For the mixed gas experiments the membranes were exposed to an equimolar mixture of H_2/CH_4 or H_2/CO_2

	Single gas			Mixed gas		Mixed gas	
	H_2	CH_4	CO_2	H_2	CH_4	H_2	CO_2
Sample I							
Permeance ($\times 10^8$ mol m^{-2} s^{-1} Pa^{-1})	1.18	0.041	0.028	1.01	0.028	0.89	0.018
S.F. (H_2/gas)		29	42		36		50
Sample II							
Permeance ($\times 10^8$ mol m^{-2} s^{-1} Pa^{-1})	0.86	0.026	0.019	0.84	0.023	0.79	0.016
S.F. (H_2/gas)		33	46		37		50

Table 3
Comparison of permeances and ideal separation factors of a SiC membrane before and after oxidation at 450 °C for 2 h

	Before oxidation			After oxidation		
	He	H_2	Ar	He	H_2	Ar
Permeance ($\times 10^8$ mol m^{-2} s^{-1} Pa^{-1})	0.89	0.44	0.006	1.21	0.71	0.014
S.F. (He/gas)		2	147		1.7	89

of H_2 is in the range of (10^{-9}–10^{-8}) mol m^{-2} s^{-1} Pa^{-1}. As expected, membranes with higher separation factors had, typically, lower permeances. The relatively low permeances of our asymmetric membranes are partly due to the relatively low permeance of the support itself, and also of the thick membrane films that are formed. Efforts are currently under way to improve the permeance of these membranes (e.g., through the aid of pore-formers). Extrapolated to a temperature of 500 °C (see Section 3.2), the expected permeance for H_2 is of the order ~10^{-7} mol m^{-2} s^{-1} Pa^{-1}. By comparison, Pd and Pd-alloy membranes exhibited, around 500 °C, permeances in the range of (10^{-7}–10^{-6}) mol m^{-2} s^{-1} Pa^{-1} [30]. However, Pd membranes are known to be sensitive to the presence of H_2S and hydrocarbon impurities; use of Pd-alloy membranes (e.g., Pd–Ag) also faces challenges for long-term usage at temperatures significantly higher than 500 °C.

Table 2 summarizes the single- and mixed-gas experiments with two different membranes using the experimental procedure previously outlined. The mixed-gas H_2 permeances (calculated on the basis of its partial pressure gradient across the membrane) for the H_2/CH_4 mixture are close to the single gas values, while the CH_4 permeance decreases, resulting in mixed-gas separation factor which is ~15–25% higher. The same is true for the H_2/CO_2 mixture with the mixed-gas separation factors being ~10–20% higher than their single-gas counterparts..

3.2. The effect of low temperature oxidation on membrane performance

To understand the effect that low temperature oxidation has on membrane performance, a membrane was prepared without using the final air oxidation step, as previously described in the membrane preparation procedure, and its H_2, He and Ar permeances were measured (see Table 3). Fig. 3 shows H_2 permeances measured at different temperatures with the same membrane (solid line). Hydrogen transport is by an activated diffusion process, as shown in Fig. 3, namely,

$$P_H = P_{H_0} \exp\left(\frac{-E_H}{RT}\right) \quad (1)$$

The calculated activation energy is 12 kJ/mol.

After the permeation experiments were completed, the membrane was subjected to air oxidation at 450 °C and its permeation characteristics were again measured. The H_2, He and Ar permeances of the membrane, after it had been subjected to the oxidation treatment, are also shown in Table 3. The H_2 and He permeances increase substantially; however, the Ar permeance more than doubles, with the net result that the ideal separation (He/Ar) decreases from 147 prior to oxidation to 89 after oxidation. The hydrogen diffusional process is again activated, but the activation energy is somewhat higher, about 17.6 kJ/mol.

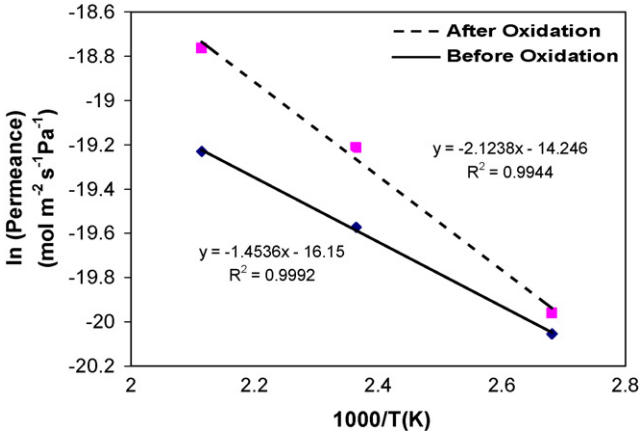

Fig. 3. H_2 permeance as a function of temperature for a SiC membrane. Solid line, membrane without an air oxidation treatment. Broken line, after the membrane had been subjected to a 2 h air oxidation at 450 °C.

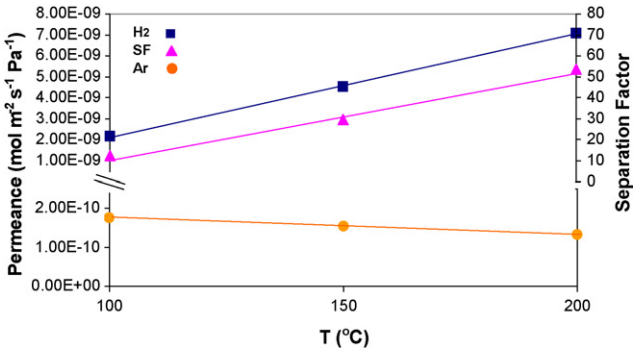

Fig. 4. H_2 and Ar permeance and ideal separation factor as a function of temperature for a SiC membrane at 207 kPa (30 psi) transmembrane pressure.

Though the transport of both He and H_2 is activated, the permeation of Ar is not, as shown in Fig. 4. This indicates, as noted in our prior publication [10], that H_2 (and He) transport through a different set of pores in the membrane than Ar and the other gases with larger kinetic diameter (CH_4 and CO_2). In fact, the permeance of Ar follows a $(1/T)^{0.5}$ dependence on temperature, indicative of Knudsen-type of transport. That air oxidation improves the Ar transport, in our view, means that it removes impurities from the mesoporous region through which Ar transport takes place. That He and H_2 permeances also increase may mean that the same impurities also occupy the pore mouths of the microporous regions. This is based on the fact that oxygen, with a kinetic diameter of 3.46 Å, close to that of CH_4 (3.8 Å) and Ar (3.4 Å), is unlikely to be able to have access to the microporous regions through which He and H_2 transport; however, no other direct experimental evidence exists to support this conjecture, at this point and time.

It is not clear, furthermore, where the likely $(CH)_x$ impurities come from. The AHPCS we utilize has an allyl mole fraction of ∼10% (as reported by the manufacturer), which translates into C:Si ratio of 1.3; it is reported to result in a ceramic with a Si:C ratio very close to 1:1 [12]. Elemental analysis (at Galbraith Laboratories, Inc.) of AHPCS-derived SiC powders that we prepared using the same pyrolysis protocols with the SiC membranes shows a C:Si ratio of 1.2. The air oxidation does very little to change this ratio (in fact, after oxidation the ratio slightly increases to 1.25, but the small increase in the carbon content after oxidation is within the experimental error of the measurement technique). This indicates that air oxidation does not result in bulk oxidation of the material, and that any oxygen incorporation must be limited to the surface region. The elemental analysis also indicates that very little Al or Li is present in the SiC ceramic, a concern since $LiAlH_4$ is used as a catalyst during the preparation of AHPCS. Despite the fact that the air treatment decreases the separation factor, it is considered essential in order to prevent any further changes in membrane performance in case it is exposed accidentally to trace amounts of oxygen during its chemical reactor application.

3.3. Steam stability of the membranes

To test their hydrothermal stability, the membranes were exposed to an equimolar mixture of steam and He at 310 kPa (45 psi) for a number of days at 200 °C (due to the limitations of our experimental system, this is the highest temperature we could expose the membranes to during the hydrothermal test; this temperature is of relevance, however, to the potential future use of such membranes for the water–gas shift reaction). The permeances of He and Ar were measured at the beginning of the experiment, shown as day 0 in Figs. 5 and 6. Subsequently, the membrane was exposed to the He/steam mixture, and the flow rate of He to the permeate side, after condensing the water, was measured on line, see Fig. 7 (the first point in Fig. 7 was measured 2 h after exposure to steam). After 48 h from the point when the membrane was first exposed to steam, the steam flow was turned off. Subsequently, the membrane was exposed to 12 h of He flow under the same pressure and temperature conditions; at the end of this period the He permeance was measured (the second point in Fig. 5). Its value had decreased by 23% from the value measured prior to the exposure to steam. The gas was then

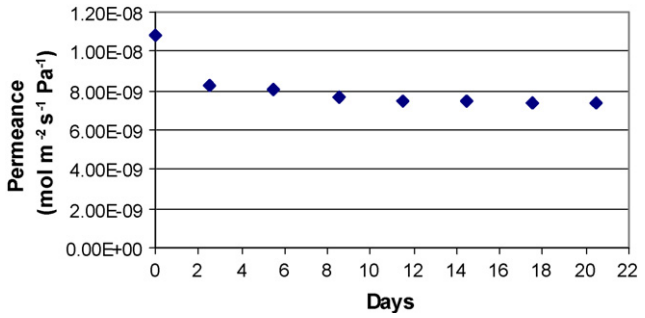

Fig. 5. Single-gas He permeance at a transmembrane pressure of 207 kPa (30 psi) at 200 °C.

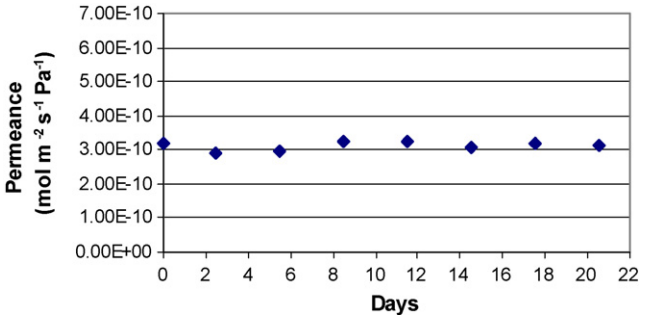

Fig. 6. Single-gas Ar permeance at a transmembrane pressure of 207 kPa (30 psi) at 200 °C.

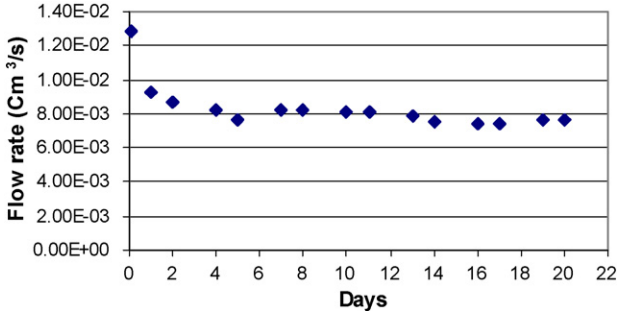

Fig. 7. He flow rate of permeate gas at 200 °C.

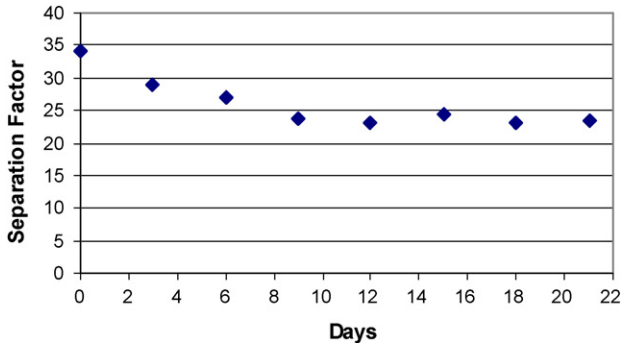

Fig. 8. Ideal selectivity of He/Ar at a transmembrane pressure of 207 kPa (30 psi) at 200 °C.

switched to Ar for an additional 12 h, and at the end of the period the Ar permeance was measured. Then, the He/steam flow was turned on for an additional 48 h, while monitoring on line the dry He flow. Then, the steam was again turned off, and the cycle was repeated, with the entire experiment lasting 21 days, out of which the membrane was exposed to steam for a period of 14 days. It is clear from Figs. 5–7 that exposure to steam has an impact on He permeance. However, the effect saturates out after a period of a few days. The effect, furthermore, is indicative of structural changes rather than reflecting water condensation in the microporous structure, as indicated by measuring the He permeance (Fig. 5) after the membrane had dried out for a period of 12 h.

The Ar permeance, on the other hand, remains totally unaffected; indicating that whatever effect steam has on the membrane is limited only to the surface region, rather than resulting in bulk transformations of the SiC material. The membrane, after 21 days of exposure, still remains microporous as shown in Fig. 8, which shows the ideal He/Ar separation factor. It is not clear what caused the original decline in He permeation. Since the membrane used in the experiments described in Figs. 5–8 had been exposed to the high-temperature air treatment, previously described, it may contain some surface oxygen. Si–O groups are known to be sensitive to the presence of steam [31,32]. Prior research on SiC ceramics indicated that exposure to water-containing air or steam at high-temperatures enhanced the oxidation rates for both crystalline [33,34] and amorphous [35] SiC. These studies were, however, performed at much higher temperatures, and it is not clear whether they relate to any phenomena observed in this study. That He permeation stabilized after a few days on stream is significant for the use of these materials in reactive applications. Results from these studies will be presented in future publications.

4. Conclusions

A new membrane preparation procedure was developed which involves coating, first, the membrane supports by a thin layer using slip-casting, prior to dip-coating additional layers. The resulting membranes exhibited enhanced performance, when compared to membranes prepared using the same supports without slip-casting a top surface layer. The reproducibility in preparing high quality membranes also improved significantly. The membranes reported here are microporous and have good hydrothermal stability, in contrast to membranes prepared previously using the same pre-ceramic polymer. The enhanced hydrothermal stability may be attributed to a different heat-treatment protocol used for AHPCS pyrolysis that leads to better cross-linked SiC membrane.

Small size molecules like H_2 and He permeate through these membranes by activated transport, while Ar and molecules with larger kinetic diameters permeate by Knudsen diffusion. As a result, the separation characteristics of these membranes improve with temperature. Efforts are currently under way to increase the membranes' permeability and investigate their use in reactive applications. The results will be presented in future publications.

Acknowledgements

The support of the US Department of Energy, the National Science Foundation, and NASA is gratefully acknowledged. Superior Graphite Co. and Sumitomo Osaka Cement Co. are acknowledged for kindly providing us the SiC powders. The authors would also like to thank Mr. Tae Kim for assistance in performing the SEM and XRD analyses.

References

[1] Y. Takeda, K. Nakamura, K. Maeda, Y. Matsushita, Effects of elemental additives on electrical resistivity of silicon carbide ceramics, J. Am. Ceram. Soc. 70 (1987) 266–267.
[2] K. Schulz, M. Durst, Advantages of an integrated system for hot gas filtration using rigid ceramic elements, Filtr. Sep. 31 (1994) 25–28.
[3] A.J. Rosenbloom, D.M. Sipe, Y. Shishkin, Y. Ke, R.P. Devaty, W.J. Choyke, Nanoporous SiC: a candidate semi-permeable material for biomedical applications, Biomed. Microdev. 6 (2004) 261–267.
[4] Z. Li, K. Kusakabe, S. Morooka, Preparation of thermostable amorphous Si-C-O membrane and application to gas separation at elevated temperature, J. Membr. Sci. 118 (1996) 159–168.
[5] C.A. Zorman, A.J. Fleischman, A.S. Dewa, M. Mehregany, C. Jacob, S. Nishino, P. Pirouz, Epitaxial growth of 3C–SiC films on 4 in. diam (100) silicon wafers by atmospheric pressure chemical vapor deposition, J. Appl. Phys. 78 (1995) 5136–5138.
[6] S.H. Kenawy, W.M.N. Nour, Microstructural evaluation of thermally fatigued SiC-reinforced Al_2O_3/ZrO_2 matrix composites, J. Mater. Sci. 40 (2005) 3789–3793.
[7] Y. Takeda, N. Shibata, Y. Kubo, SiC coating on porous γ-Al_2O_3 using alternative-supply CVI method, J. Ceram. Soc. Jpn. 109 (2001) 305–309.
[8] B.-K. Sea, K. Ando, K. Kusakabe, S. Morooka, Separation of hydrogen from steam using a SiC-based membrane formed by chemical vapor deposition of triisopropylsilane, J. Membr. Sci. 146 (1998) 73–82.
[9] X. Pages, V. Rouessac, D. Cot, G. Nabias, J. Durand, Gas permeation of PECVD membranes inside alumina substrate tubes, Sep. Purif. Technol. 25 (2001) 399–406.
[10] R.J. Ciora, B. Fayyaz, P.K.T. Liu, V. Suwanmethanond, R. Mallada, M. Sahimi, T.T. Tsotsis, Preparation and reactive applications of nanoporous silicon carbide membranes, Chem. Eng. Sci. 59 (2004) 4957–4965.
[11] L.V. Interrante, C.W. Whitmarsh, W. Sherwood, H.-J. Wu, R. Lewis, G. Maciel, High yield polycarbosilane precursors to stoichiometric SiC. Synthesis, pyrolysis and application, Mater. Res. Soc. Symp. Proc. 346 (1994) 593–603.
[12] L.V. Interrante, C.W. Whitmarsh, W. Sherwood, Fabrication of SiC matrix composites by liquid phase infiltration with a polymeric precursor, Mat. Res. Soc. Symp. Proc. 365 (1995) 139–146.

[13] K. Kusakabe, Z.Y. Li, H. Maeda, S. Morooka, Preparation of supported composite membrane by pyrolysis of polycarbosilane for gas separation at high temperature, J. Membr. Sci. 103 (1995) 175–180.
[14] Z.Y. Li, K. Kusakabe, S. Morooka, Pore structure and permeance of amorphous Si-C-O membranes with high durability at elevated temperature, Sep. Sci. Technol. 32 (1997) 1233–1254.
[15] L.-L. Lee, D.-S. Tsai, A hydrogen-permselective silicon oxycarbide membrane derived from polydimethylsilane, J. Am. Ceram. Soc. 82 (1999) 2796–2800.
[16] L.-L. Lee, D.-S. Tsai, Synthesis and permeation properties of silicon-carbon-based inorganic membrane for gas separation, Ind. Eng. Chem. Res. 40 (2001) 612–616.
[17] C.-L. Chen, D.-S. Tsai, Permeation properties of microporous membranes prepared via coating of evaporated polydimethylsilane, J. Membr. Sci. 237 (2004) 163–165.
[18] H. Suda, H. Yamauchi, Y. Uchimaru, I. Fujiwara, K. Haraya, Preparation and gas permeation properties of silicon carbide-based inorganic membranes for hydrogen separation, Desalination 193 (2006) 252–255.
[19] T. Nagano, K. Sato, T. Saitoh, Y. Iwamoto, Gas permeation properties of amorphous SiC membranes synthesized from polycarbosilane without oxygen-curing process, J. Ceram. Soc. Jpn. 114 (1330) (2006) 533–538.
[20] M. de Vos Renate, H. Verweij, High-selectivity, high-flux silica membranes for gas separation, Science 279 (1998) 1710–1711.
[21] V. Suwanmethanond, E. Goo, P.K.T. Liu, G. Johnston, M. Sahimi, T.T. Tsotsis, Porous silicon carbide sintered substrates for high-temperature membranes, Ind. Eng. Chem. Res. 39 (2000) 3264–3271.
[22] J. Li, Y. Zhang, A simple purification for single-walled carbon nanotubes, Phys. E 28 (2005) 309–312.
[23] S. Osswald, E. Flahaut, Y. Gogotsi, In situ spectroscopy study of oxidation of doubled- and single-wall carbon nanotubes, Chem. Mater. 18 (2006) 1525–1533.
[24] T.-J. Park, S. Banerjee, T. Hemraj-Benny, S.S. Wong, Purification strategies and purity visualization techniques for single-walled carbon nanotubes, J. Mater. Chem. 16 (2006) 141–154.
[25] Y. Shinoda, T. Nagano, F. Wakai, Fabrication of nanograined silicon carbide by ultrahigh-pressure hot isostatic pressing, J. Am. Ceram. Soc. 82 (1999) 771–773.
[26] M.F. Zawrah, L. Shaw, Liquid-phase sintering of SiC in presence of CaO, Ceram. Int. 30 (2004) 721–725.
[27] F. Shojai, A.B.A. Pettersson, T. Mantyla, J.B. Rosenholm, Electrostatic and electrosteric stabilization of aqueous slips of 3Y-ZrO_2 powder, J. Eur. Ceram. Soc. 20 (2000) 277–283.
[28] J. Zheng, M.J. Kramer, M. Akinc, In situ growth of SiC whisker in pyrolyzed monolithic mixture of AHPCS and SiC, J. Am. Ceram. Soc. 83 (2000) 2961–2966.
[29] A.R. Puerta, E.E. Remsen, M.G. Bradley, W. Sherwood, L.G. Sneddon, Synthesis and ceramic conversion reactions of 9-BBN modified allylhydridopolycarbosilane: a new single-source precursor to boron-modified silicon carbide, Chem. Mater. 15 (2003) 478–485.
[30] K.S. Rothenberger, A.V. Cugini, B.H. Howard, R.P. Killmeyer, M.V. Ciocco, B.D. Morreale, R.M. Enick, F. Bustamante, I.P. Mardilovich, Y.H. Ma, High pressure hydrogen permeance of porous stainless steel coated with a thin palladium film via electroless plating, J. Membr. Sci. 244 (2004) 55–68.
[31] J.C.S. Wu, H. Sabol, G.W. Smith, D.L. Flowers, P.K.T. Liu, Characterization of hydrogen-permselective microporous ceramic membranes, J. Membr. Sci. 96 (1994) 275–287.
[32] D.-H. Park, N. Nishiyama, Y. Egashira, K. Ueyama, Enhancement of hydrothermal stability and hydrophobicity of a silica MCM-48 membrane by silylation, Ind. Eng. Chem. Res. 40 (2001) 6105–6110.
[33] E.J. Opila, Variation of the oxidation rate of silicon carbide with water-vapor pressure, J. Am. Ceram. Soc. 82 (1999) 625–636.
[34] K.L. More, P.F. Tortorelli, M.K. Ferber, James R. Keiser, Observations of accelerated silicon carbide recession by oxidation at high water-vapor pressures, J. Am. Ceram. Soc. 83 (2000) 211–213.
[35] B.-Y. Tsui, K.-L. Fang, A novel wafer reclaim method for amorphous SiC and carbon coped oxide films, IEEE Trans. Semicond. Manuf. 18 (2005) 716–721.

ELSEVIER

Chemical Engineering Science 62 (2007) 2777–2789

Chemical Engineering Science

www.elsevier.com/locate/ces

Molecular dynamics simulations of transport and separation of supercritical carbon dioxide-alkane mixtures in supported membranes

Mahnaz Firouzi, Theodore T. Tsotsis, Muhammad Sahimi*

Mork Family Department of Chemical Engineering & Materials Science, University of Southern California, Los Angeles, CA, 90089-1211, USA

Received 29 August 2006; received in revised form 23 January 2007; accepted 17 February 2007
Available online 27 February 2007

Abstract

The results of extensive nonequilibrium molecular dynamics (MD) simulations of flow and transport of several binary mixtures of CO_2 and an *n*-alkane chain, from CH_4 to C_4H_{10}, through a model porous membrane composed of three pores in series with significantly different sizes and in the presence of an external pressure gradient, are reported. The technique that we use for the simulations is a combination of the configurational-bias Monte Carlo method (used for efficient generation of molecular models of *n*-alkane chains) and the dual control-volume grand-canonical MD method. The selectivity of the membrane changes qualitatively as the length of the alkane chain increases, resulting in high separation factors in favor of the alkanes. Moreover, we find that, under supercritical conditions, unusual phenomena occur that give rise to *direction*- and pressure-dependent permeabilities for the fluids. The results, which are also in agreement with a continuum formulation of the problem, indicate that the composite nature of the membrane gives rise to the direction-dependent permeabilities. Hence, modeling flow and transport of supercritical fluid mixtures in porous materials with the type of morphology considered in this paper (such as supported porous membranes) would require using effective permeabilities that depend on *both* the external pressure drop and the direction along which it is applied to the materials.

Keywords: Molecular dynamics; Transport; Separation; Membranes

1. Introduction

Properties and potential use of supercritical fluids—those that are in a thermodynamic state above their critical temperature and /or pressure—have recently attracted much attention. In particular, supercritical fluid extraction (SCFE) utilizing CO_2 has been extensively studied in recent years (for reviews see, for example, Sengers and Sengers, 1986; Kiran and Sengers, 1994), due to its potential utility for the removal of contaminants from water, sludges, soils, spent catalysts, aerogels, and such adsorbents as activated granular carbon. Though other compounds might be better solvents under SC conditions (especially for low-volatility solutes), CO_2 is preferred in environmental applications because it is nontoxic and nonflammable.

A combination of a SC fluid with a porous membrane offers perhaps the most promising SCFE method, as it can continuously and preferentially extract the solute, leaving behind a solute-depleted, recyclable SC solvent stream. Such a separation unit offers significant reductions in the cost of the energy intensive compression/recompression cycle typically associated with the SCFE. Several groups have studied the use of various membranes with SC fluids (see, for example, Muller et al., 1989; Kelley and Chimowitz, 1990; Semenova et al. 1992a,b; Ohya et al., 1993; Nakamura et al., 1994; Afrane and Chimowitz, 1996; Fujii et al., 1996; Sarrade et al., 1996; Tokunaga et al., 1997). Their work indicates that transport of SC fluid mixtures through a membrane gives rise to many complex phenomena, some of which have not yet been understood well. For example, the permeability isotherms exhibited hysteresis at some temperatures, but not at others. They also attain a maximum as a function of the temperature and pressure. Due to the interactions between the highly nonideal, compressible SC mixtures and the complex pore space of a nanoporous membrane, there is currently not much fundamental knowledge on the transport of SC mixtures in membranes.

* Corresponding author. Tel.: +1 213 740 2064; fax: +1 213 740 8053.
E-mail address: moe@iran.usc.edu (M. Sahimi).

0009-2509/$ - see front matter © 2007 Elsevier Ltd. All rights reserved.
doi:10.1016/j.ces.2007.02.026

The goal of this paper is developing a better fundamental understanding of the phenomena that are involved in the transport of CO_2/hydrocarbon mixtures, under SC conditions, in a nanoporous membrane. Since molecular interactions between the fluids' molecules, and between them and the pores' walls, cannot be ignored, one must resort to atomistic models. In a previous paper (Firouzi et al., 2003) we studied the CO_2–CH_4 mixtures in a single nanopore, using MD simulations. In practice, however, most membranes consist of a porous support made of at least two layers of macro- and mesopores, and a nanoporous film deposited on the support. Flow and transport of fluids in such composite porous materials have rarely been studied using atomistic simulations. Thus, another goal of our study is to understand transport and separation of mixtures of CO_2/alkane chains in a membrane under SC conditions. In this paper we present the results of MD simulation of transport of binary mixtures of CO_2 and CH_4, C_2H_6, C_3H_8, and C_4H_{10} under such conditions. To our knowledge, such a study has never been carried out before.

Due to their stability and versatility, carbon molecular-sieve (CMS) membranes have been used by many groups (Koresh and Sofer, 1983; Rao and Sircar, 1993, 1996; Jones and Koros, 1994, 1995, 1996; Chen and Yang, 1994; Linkov et al., 1994; Afrane and Chimowitz, 1996; Sircar et al., 1996; Shusen et al., 1996; Acharya et al., 1997; Petersen et al., 1997; Steriotis et al., 1997; Shiflett and Foley, 1999), as well as our own group (Sedigh et al., 1998, 1999, 2000), in studies of separation of *subcritical* fluid mixtures. Such membranes are prepared with well-controlled porosity and a narrow pore size distribution. The emphasis in our study is on identifying the factors that control the ability of the CMS membranes for separation of SC mixtures.

The rest of this paper is organized as follows. In the next section we describe the details of the model of the membrane that we use. Section 3 describes the molecular models that we utilize for the various components, while Section 4 presents the details of how the alkane chains are grown and inserted in the ore system. Details of the MD simulations are described in Section 5. The results are presented and discussed in Section 6. The paper is summarized in the last section.

2. Atomistic model of a supported membrane

As pointed out by, for example, Seaton et al. (1997), to accurately model a CMS membrane, one must take into account its interconnected pore structure. In previous papers (Ghassemzadeh et al., 2000; Xu et al., 2000b, 2001) we carried out MD studies of transport, adsorption, and separation of simple mixtures under *subcritical* conditions, in three-dimensional (3D) atomistic pore network models of CMS membranes. However, as explained below, carrying out the same type of computations for the mixtures of interest in the present paper under *supercritical conditions* is extremely difficult, especially since we intend to study mixtures that involve relatively long alkane chains. At the same time, MD simulations by Düren et al. (2002, 2003) indicated that transport of fluids in a tight pore is hardly influenced by its shape, so long as the correct average radius, transport length and the applied pressure or chemical potential gradient are used. Therefore, as an intermediate step between a single pore and a 3D pore network model of a CMS membrane, we study transport and separation of SC fluid mixtures in the composite pore model shown in Fig. 7 below. A somewhat similar pore model was utilized by Düren et al. (2002, 2003) in their study of gas transport through a membrane under subcritical conditions.

In the model, each pore represents one layer of a three-layer supported membrane. They all have the same length, with their heights being 77, 23, and 10 Å. The membrane is connected to two control volumes (CVs) that are exposed to bulk fluids at high and low chemical potentials μ or pressures P, with their gradient being in the x direction (parallel to the lines of this page). Periodic boundary conditions are used in the y direction (perpendicular to this page) in the pores, and in the y and z directions in the two CVs.

3. Molecular models of the fluids

We represent CO_2 and CH_4, as well as the C that the pores' walls are made of, by Lennard–Jones (LJ) spheres, characterized by effective LJ size and energy parameters, σ and ε, listed in Table 1. In our previous studies of transport of mixtures through nanopores, we also used a model of CO_2 that consisted of three LJ interaction sites on the three atoms, plus point charges to account for the quadrupole moment of CO_2 molecules, but found no significant effect on the results.

The C_2H_6, C_3H_8, and C_4H_{10} molecules are grown by a configurational-bias Monte Carlo (MC) method, described in the next section. They are represented by a united-atom (UA) model (Ryckaert and Bellemans, 1978), which considers the CH_2 and CH_3 groups as single interaction centers with their own effective potentials. The nonbonded interactions between

Table 1
Values of the molecular parameters used in the simulations

Parameter	Numerical value
σ_{CH_2} (Å)	3.905
σ_{CH_3} (Å)	3.905
σ_{CH_4} (Å)	3.810
σ_{CO_2} (Å)	3.794
σ_C (Å)	3.4
ε_{CH_2}/k_B (K)	59.38
ε_{CH_3}/k_B (K)	88.06
ε_{CH_4}/k_B (K)	148.1
ε_{CO_2}/k_B (K)	225.3
ε_C/k_B (K)	28
Bond length (Å)	1.53
k_θ (K rad^{-2})	62,500
θ_0 (degrees)	112
c_0 (K)	1116
c_1 (K)	1462
c_2 (K)	−1578
c_3 (K)	−368
c_4 (K)	3156
c_5 (K)	−3788

k_B is the Boltzmann's constant.

interaction centers of different molecules are described by a cut-and-shifted LJ potential, with the cut-off distances r_c being, $r_c = 4\sigma_{CH_4} = 15.24$ Å for the CO_2/CH_4 mixtures, and $r_c = 3.5\sigma_{CH_4} = 13.33$ Å for the other three mixtures. No tail corrections were applied to this potential. For simplicity, the total molecular mass of an alkane is equally divided between the C atoms and, therefore, CH_2 and CH_3 groups are assumed to have equal molecular masses. Table 1 lists the size and energy parameters of the CH_2 and CH_3 groups.

The atoms and the UA centers are connected by harmonic potentials. The distance between the atoms was fixed at 1.53 Å. The intramolecular interactions consist of the contributions by bond-bending (BB) and torsional forces. The BB term was represented by the van der Ploeg–Berendsen potential (van der Ploeg and Berendsen, 1982):

$$U_{BB}(\theta) = \tfrac{1}{2}k_\theta(\theta - \theta_0)^2, \tag{1}$$

where θ is the angle between the atomic bonds. The Ryckaert–Bellemans potential (Ryckaert and Bellemans, 1975) was used to represent the torsional potential:

$$U_{\text{tor}}(\phi) = \sum_{k=0}^{5} c_k \cos^k(\phi), \tag{2}$$

where ϕ is the dihedral angle. Numerical values of the potential parameters for all the components are also listed in Table 1.

We used the LJ potential for the interactions between the molecules and the individual carbon atoms on the walls, arranged as in graphite. The cut-off distance between the molecules and the carbon atoms on the walls was $r_c = 3.5\sigma_{CH_4} = 13.33$ Å. For the cross-term LJ parameters the Lorentz–Berthelot combining rules were used, namely, $\varepsilon_{ij} = \sqrt{\varepsilon_i \varepsilon_j}$, and $\sigma_{ij} = \frac{1}{2}(\sigma_i + \sigma_j)$.

4. Configurational-bias and grand-canonical Monte Carlo methods

The configurational-bias Monte Carlo (CBMC) technique (Harris and Rice, 1988; Mooij et al., 1992; Laso et al., 1992; Siepmann and Frenkel, 1992; de Pablo et al., 1992; Frenkel et al., 1992; Smit et al., 1995; Macedonia and Maginn, 1999) was used to grow the alkane chains. In this method one considers the potential energy of an atom as the sum of the internal energy u^{int} which includes parts of the intramolecular interactions, and the external energy u^{ext} which contains the intermolecular interactions, as well as those intramolecular interactions that are not part of the internal energy. The procedure to grow an n-alkane chain atom by atom is as follows (Smit et al., 1995).

(1) The first atom is inserted at a random position and the energy $u_1(n)$ and the quantity, $w_1 = \exp[-\beta u_1(n)]$, are computed, where $\beta = (k_B T)^{-1}$, with k_B being the Boltzmann's constant, T the temperature, and n denoting the new state in which the system is in.

(2) To insert the next atom, k trial orientations (typically five), denoted by $\{\mathbf{b}_k\} = \mathbf{b}_1, \mathbf{b}_2, \ldots, \mathbf{b}_k$, are generated with a probability $p_l^{\text{int}}(\mathbf{b}_i)$, given by

$$p_l^{\text{int}}(\mathbf{b}_i) = \frac{1}{C} \exp[-\beta u_l^{\text{int}}(\mathbf{b}_i)], \tag{3}$$

where C is a normalization factor. For each trial, the *external energy* $u_l^{\text{ext}}(\mathbf{b}_i)$ is also computed, along with, $w_l(n) = \sum_{j=1}^{k} \exp[-\beta u_l^{\text{ext}}(\mathbf{b}_j)]$. One orientation, out of the k trials, is then selected with the probability

$$p_l^{\text{ext}}(\mathbf{b}_i) = \frac{1}{w_l(n)} \exp[-\beta u_l^{\text{ext}}(\mathbf{b}_i)]. \tag{4}$$

This step is repeated $M - 1$ times until the entire alkane molecule is grown, and the Rosenbluth factor (Rosenbluth and Rosenbluth, 1955), $W(n) = \prod_{l=1}^{M} w_l(n)$, is computed. A molecular conformation is generated with the probability,

$$P(n) = \prod_{l=2}^{M} p_l^{\text{int}}(n) p_l^{\text{ext}}(n) = \frac{1}{C^{M-1} W(n)} \exp[-\beta U(n)], \tag{5}$$

with $U = \sum_{l=1}^{M} u_l = \sum_{l=1}^{M} (u_l^{\text{int}} + u_l^{\text{ext}})$.

Next, the alkane chains are inserted into the two CVs in order to generate the necessary pressure or chemical potentials in them, by combining the CBMC method with the grand-canonical Monte Carlo (GCMC) method. The method consists of, (i) generating the chain configurations by the CBMC method, and (ii) computing the Rosenbluth weight W as the alkane is generated, and utilizing it in the acceptance rule of the GCMC method for inserting the chains into the CVs. The probability that a single chain is added to a CV of N_i chains is given by (Macedonia and Maginn, 1999),

$$p^+ = \min\left[1, \frac{\exp(\beta\mu_i)V}{\Lambda_i^3 (N_i + 1)} W(n)\right], \tag{6}$$

where μ_i is the chemical potential of chain i, V is the volume of the CV, and Λ_i is the thermal de Broglie wavelength of component i.

To delete a molecule from the CVs, the Rosenbluth weight is evaluated by *pretending* that the alkane chain is grown into its current position. Thus, one computes, $w_1(o) = \exp[-\beta u_l(o)]$, $w_l(o) = \sum_{j=1}^{k} \exp[-\beta u_l^{\text{ext}}(\mathbf{b}'_j)]$, and $W(o) = \prod_{l=1}^{M} w_l(o)$, using $k-1$ trial orientations, together with the actual current position of the atom l, which form the set $\{\mathbf{b}'_k\}$, where o indicates the molecules' old state. The probability of deleting a chain from a CV is then given by

$$p^- = \min\left[1, \frac{N_i \Lambda_i^3}{\exp(\beta\mu_i)V} \frac{1}{W(o)}\right]. \tag{7}$$

To insert CO_2 in the two CVs, the probabilities p^+ and p^- are computed according to the standard GCMC method, namely,

the Rosenbluth factor W is replaced by $\exp(-\beta\Delta U)$, where ΔU is the potential energy change of the system as a result of adding a molecule to, or removing one from, the CVs.

5. Molecular dynamics simulation

We use the dual control-volume GCMD technique (DCV-GCMD) (Heffelfinger and van Swol, 1994; MacElroy, 1994), which has been used extensively in the past several years by several research groups (Nitta et al., 1993; Cracknell et al., 1995; Furukawa et al., 1996, 1997; Furukawa and Nitta, 1997; Nicholson et al., 1996; Pohl et al., 1996; Heffelfinger and Ford, 1998; Ford and Heffelfinger, 1998; Pohl and Heffelfinger, 1999), as well as our own group (Xu et al., 1998, 1999, 2000a,b; Firouzi et al., 2003, 2004, 2006). Previously, molecular simulations were used for studying SC fluids in the bulk (Shing and Chung, 1987; Nouacer and Shing, 1989; Cummings et al., 1991; Chung and Shing, 1992; Eckert et al., 1996; Martinez et al., 1996; Yoshii and Okazaki, 1997; for a review see Chialvo and Cummings, 1999), very few such studies were devoted to investigating the behavior of SC fluids in small pores (Nicholson, 1998). They were mostly based on the MC method (Nitta and Yoneya, 1995; Shigeta et al., 1996).

The Verlet velocity algorithm was used to integrate the (dimensionless) equations of motion with a (dimensionless) time step, $\Delta t = 5\times10^{-3}$, with up to 1.2×10^{7} time steps to ensure that the system reached the steady state. Such long computations are essential for simulating the behavior of SC fluids in tight pores, and indicate the difficulty that one encounters in studying the same mixtures in a fully 3D pore network. Molecules that crossed the outer boundaries of the CVs (typically about 1% of the total number of molecules that were deleted during the GCMC simulations) were removed. The overall streaming velocity (the ratio of the component's flux and concentration) was zero in the two CVs, but not in the pores.

Iso-kinetic conditions were maintained by rescaling the velocity independently in all the three directions. To maintain the densities of each component in the two CVs at some fixed values, they, or the corresponding chemical potentials of each component in the two CVs, were maintained by carrying out a sufficient number of GCMC insertions and deletions of the molecule, with the probabilities of inserting and deleting a molecule of component i given by Eqs. (6) and (7) (or their modified form, as described above, for the cases of CO_2 and CH_4), respectively. Typically, 50 GCMC insertions and deletions in each CV were followed by 5 MD integration steps. The chemical potentials were converted to equivalent pressures using a LJ equation of state (Johnson et al., 1993).

The density profile $\rho_i^z(x)$ of component i along the x-direction, the direction along which the chemical potential gradient $\nabla\mu$ is imposed on the membrane, and $\rho_i^x(z)$, the density profile in the yz planes that are perpendicular to the direction of $\nabla\mu$ are computed. $\rho_i^z(x)$ was computed by dividing the simulation box in that direction into grids of size, $\ell = 1.12\sigma_{CH_4}$, and averaging for each MD step the number of molecules of type i over the distance ℓ. A similar procedure was used for computing $\rho_i^x(z)$ in the yz planes, with the averaging done over small distances which were about $0.67\sigma_{CH_4}$, $0.21\sigma_{CH_4}$, and $0.09\sigma_{CH_4}$ for the largest pore, the middle pore, and the smallest one, respectively. For each component i we also calculate its flux J_i in the direction of the applied $\nabla\mu$. The permeability K_i of component i is then given by Darcy's law,

$$K_i = \frac{J_i}{\Delta P_i/L}, \tag{8}$$

where $\Delta P_i = x_i \Delta P$ is the partial pressure drop for species i along the pore system, with x_i being its mole fraction, ΔP the total pressure drop imposed on the system, and L the system's length. We computed the permeabilities for two cases. In one, the upstream condition (higher pressure) was maintained in the CV connected to the largest pore, while in the second case the upstream condition was maintained in the smallest pore. Finally, the dynamic separation factor S is defined by

$$S_{21} = \frac{K_2}{K_1}, \tag{9}$$

where K_1 and K_2 are, respectively, the permeabilities of the components such that $K_2 > K_1$, so that, $S_{21} > 1$.

6. Results and discussions

We first describe the results for pure CO_2, and then present and discuss those for binary mixtures of CO_2 and the n-alkanes.

6.1. Pure CO_2

Fig. 1 presents the CO_2 permeability K at $T = 50\,^{\circ}C$ as a function of the upstream pressure, if a pressure drop $\Delta P = 3447$ KPa (500 psi) is applied to the membrane. The direction-dependence of K is strong, with the permeabilities in the two opposite directions differing by a factor as large as four. Moreover, the trends for the two cases are opposite of one another. Whereas K decreases when the upstream is on the side of the largest pore, it increases when the direction of ΔP is reversed. The reason

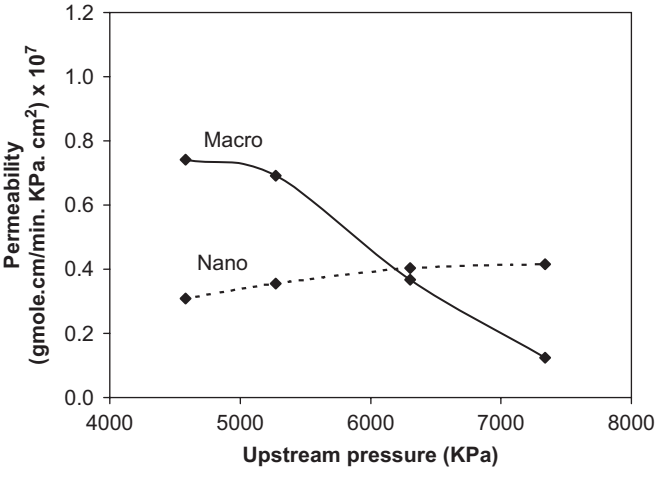

Fig. 1. The permeability of pure CO_2 at $T = 50\,^{\circ}C$, when a pressure drop $\Delta P = 3447$ KPa (500 psi) is applied to the pore system.

is that, at a constant overall ΔP, with increasing the upstream pressure on the largest pore side, practically the entire membrane is packed with CO_2 molecules. This makes their passage from the largest pore to the middle one very difficult, resulting in reduced values of K. But, at the same overall ΔP, increasing the upstream pressure, when applied on the side of the smallest pore (representing the membrane layer), moves the transition point between a gas-like and liquid-like state to inside the largest pore, which allows easier passage of CO_2 from the middle pore to the largest one, hence increasing K in that direction.

6.2. CO_2–CH_4 *mixtures*

Fig. 2 presents the permeabilities of the two components in two different mixtures, in which the CO_2 mole fraction x_{CO_2} is 0.5 and 0.9. The pressure drop is, $\Delta P = 4825$ KPa (700 psi), and the permeabilities were computed when ΔP was applied in the two opposite directions, and the upstream pressure was varied. The same qualitative patterns are obtained when other values of pressure drops are applied, and the upstream and downstream conditions are such that one crosses from a subcritical region to a supercritical one (the critical pressure of CO_2 is 7383 KPa, or 72.86 atm). In addition to the pressure-dependence of K_1 and K_2 being in qualitative agreement with the experimental data (Ohya et al., 1993; Sarrade et al., 1996; Tokunaga et al., 1997), another noteworthy feature of Fig. 2 is that the permeabilities differ significantly, with K_2—that of CO_2—being larger. The reason is the affinity of CO_2 for carbon surfaces. Hence, unlike CH_4, there is significant flow of CO_2 on or near the walls. This is particularly important, as the smallest pore and the middle one are packed with molecules and, therefore, their motion in the bulk of the pores is exceedingly slow. Hence, surface flow becomes important.

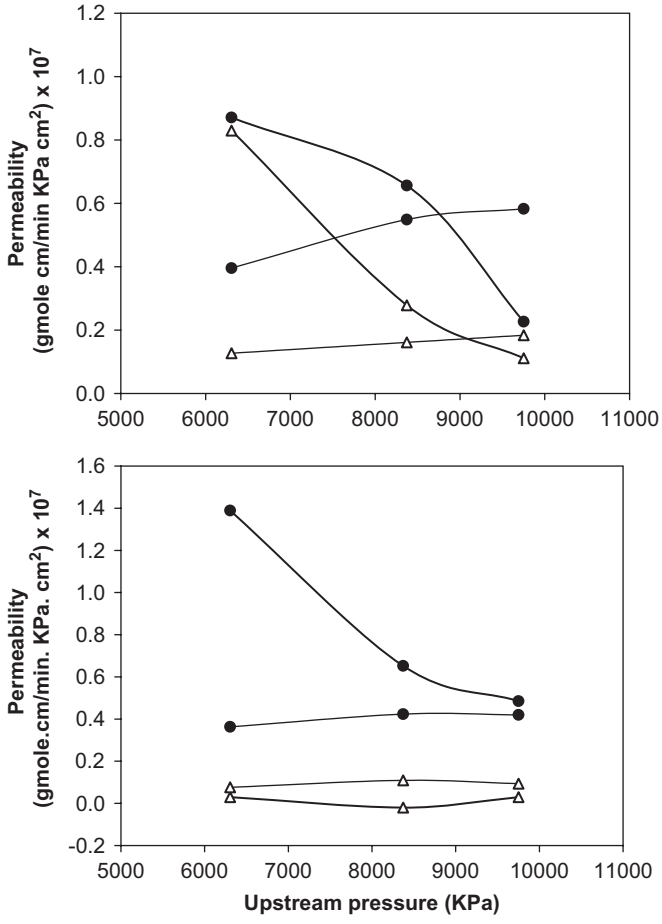

Fig. 2. The dependence of the permeabilities of CO_2 (circles) and CH_4 (triangles) at $T = 35\,^{\circ}C$ on the upstream pressure, when a pressure drop of 4825 KPa (700 psi) is applied in the two opposite directions. The top and bottom panels show, respectively, the results for $x_{CO_2} = 0.5$ and 0.9. Continuous and dashed curves show, respectively, the results when the upstream pressure is maintained at the entrance to the largest pore and smallest pore.

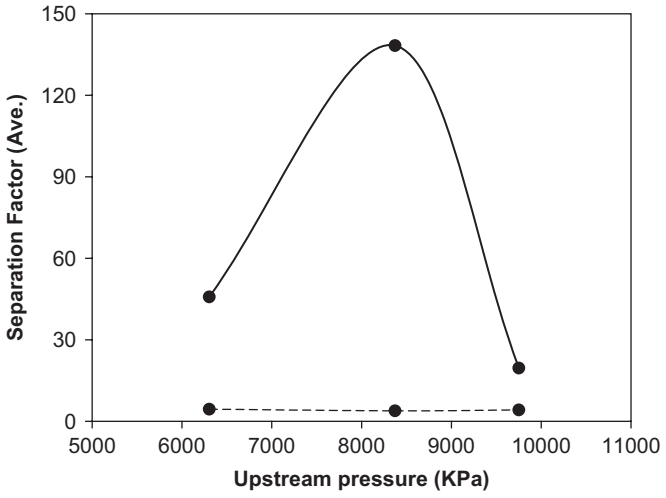

Fig. 3. The separation factors, $S = K_{CO_2}/K_{CH_4}$, with, $x_{CO_2} = 0.9$. The rest of the conditions are the same as those of Fig. 2.

Since, as far as practical applications are concerned, the separation factors are a quantitative measure of the performance of a membrane, we show in Fig. 3 the separation factors for the case in which, $x_{CO_2} = 0.9$, at $T = 35\,^{\circ}C$. Clearly, the direction-dependence of the permeabilities creates an asymmetric membrane, such that the separation factors are roughly 50% higher when the smallest pore (the membrane layer) is at the upstream condition.

6.3. CO_2–C_2H_6 *mixtures*

Fig. 4 presents the pressure-dependence of the permeabilities for a CO_2/C_2H_6 mixture at $T = 35\,^{\circ}C$ in which, $x_{CO_2} = 0.9$. Unlike the CO_2/CH_4 mixtures, the permeabilities seem to have simple functional dependence on the pressure. When the upstream condition is imposed on the CV connected to the smallest pore, the permeabilities are very small. This is caused by relatively large size of C_2H_6 molecules and the pore's small size, and the fact that, unlike CH_4 which is represented by a LJ sphere, they possess chain-like structure. The corresponding dynamic separation factors are shown in Fig. 5. It indicates that there is an optimal upstream pressure for the separation of the two components at which the separation factor S_{21} is

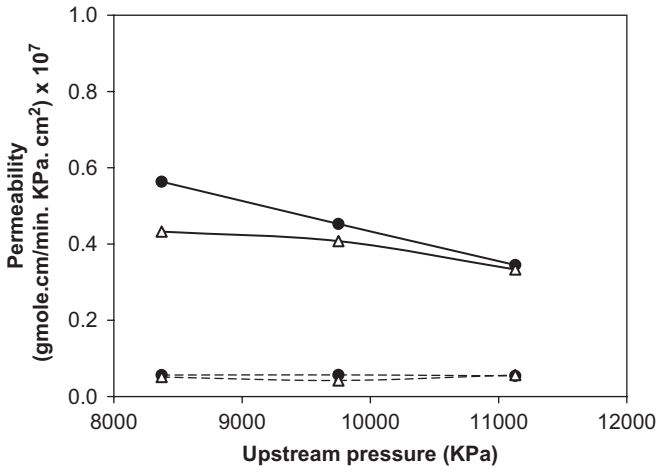

Fig. 4. Dependence of the permeabilities of CO_2 (circles) and C_2H_6 (triangles) at $T = 35\,^{\circ}C$ on the upstream pressure, when a pressure drop of 4825 KPa is applied in the two opposite directions, and $x_{CO_2} = 0.9$. Continuous and dashed curves show, respectively, the results when the upstream pressure is maintained at the entrance to the largest pore and smallest pore.

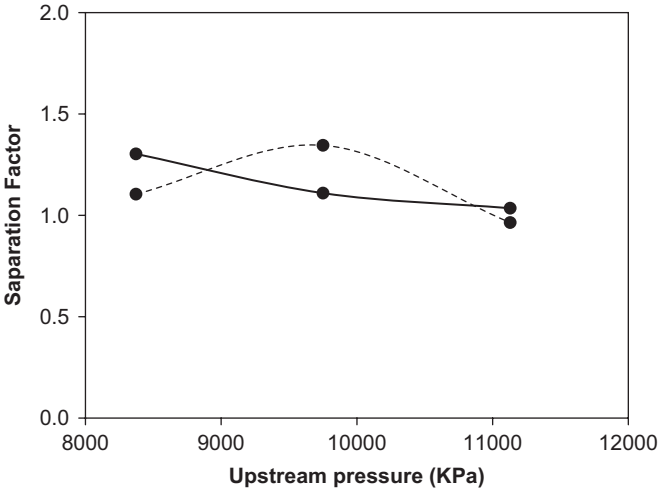

Fig. 5. The separation factors that correspond to the permeabilities shown in Fig. 4.

maximum. The physical reason for this important result may be as follows.

The overall pressure drop is fixed at $\Delta P = 4825$ KPa (700 psi), and the upstream pressure is varied in such a way that it is always above the critical pressures of both CO_2 and C_2H_6. But, the downstream pressure P_2 varies over a range of values that includes both the supercritical and subcritical conditions for C_2H_6. At the lowest upstream pressure, P_2 is below the critical pressure of C_2H_6 which is about 4872 KPa (48.08 atm). Since the CO_2 mole fraction is much larger than that of C_2H_6 and it is in a liquid-like state (condensation), convective transport helps carrying it in the pores in amounts that are much larger than C_2H_6, as a result of which the separation of the two fluids improves and, hence, the separation factor increases. The maximum separation factor corresponds to a downstream pressure (about 4900 KPa) which is just about the critical pressure of C_2H_6. Beyond this point, the upstream pressure is above the critical pressures of both components, while the downstream pressure is above the critical pressure of C_2H_6. These conditions create liquid-like states of the two components and, therefore, the separation factor decreases. This phenomenon will not be as effective in larger pores, where there is less condensation. The existence of an optimal pressure drop for which the separation of the two components is most efficient has very important consequences for practical applications involving SCFE with CO_2.

6.4. CO_2–C_3H_8 *mixtures*

As the alkane chains become longer, the behavior of their mixtures with CO_2 also becomes more complex. When the upstream and downstream pressures are high enough, the state of CO_2 in the smallest pore and the middle one is liquid-like (condensation). The state of CO_2 in the largest pore, on the other hand, depends on where the upstream condition is maintained. If the upstream condition is maintained in the CV connected to largest pore itself, then the CO_2 density in that pore is high everywhere, resembling a liquid-like state. If, on the other hand, the upstream condition is maintained in the CV connected to the smallest pore, the CO_2 density in the largest pore near its entrance to the middle pore is high, but decreases somewhat as one gets away from this region towards the CV on the left side

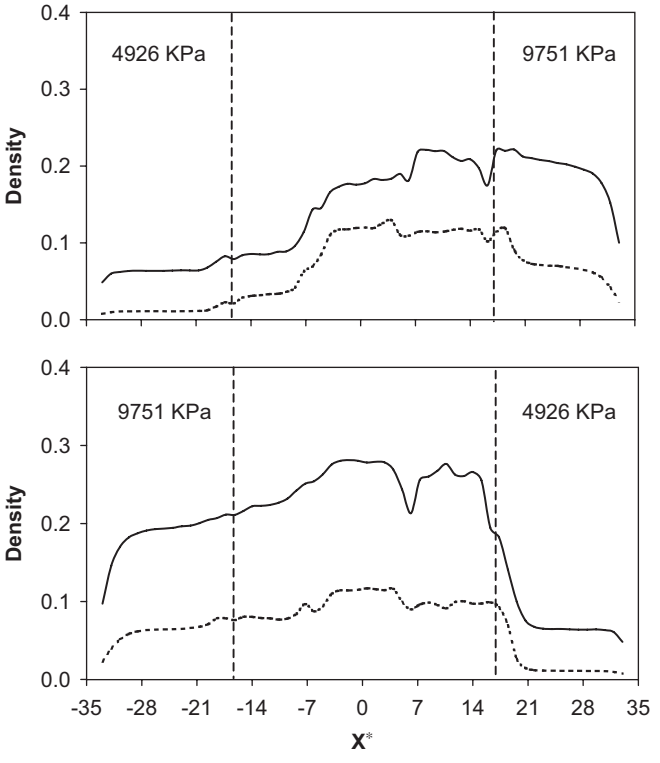

Fig. 6. Time-averaged density profiles $\rho_i^z(x)$ of CO_2 (solid curves) and C_3H_8 (dashed curves) in a mixture with, $x_{CO_2} = 0.9$, at $T = 35\,^{\circ}C$. Dashed vertical lines indicate the boundaries of the pore system.

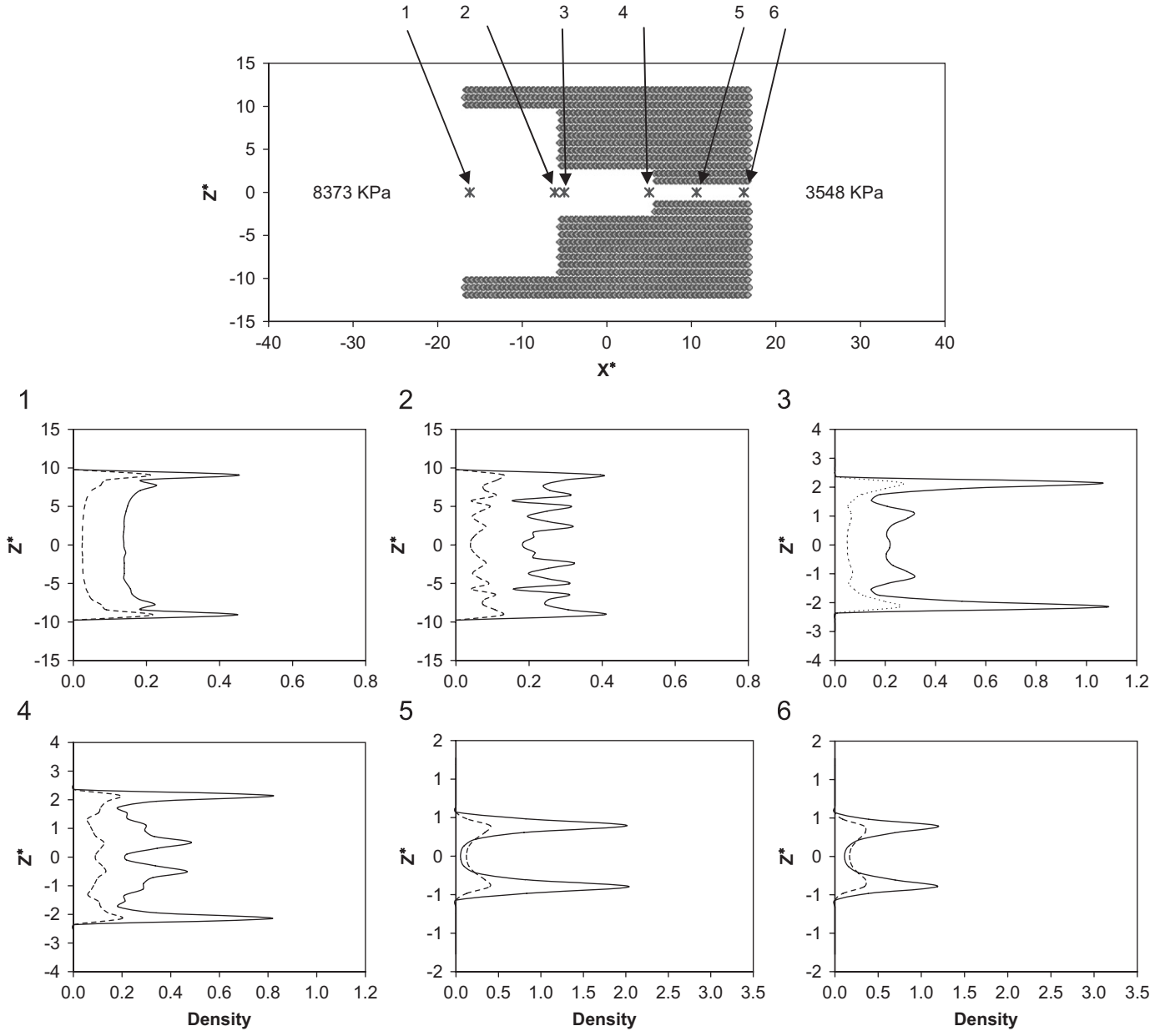

Fig. 7. Time-averaged density profiles $\rho_i^x(z)$ of CO_2 (solid curves) and C_3H_8 (dashed curves) at $T = 35\,^{\circ}C$, when the upstream condition is maintained in the control volume connected to the largest pore, in a mixture with $x_{CO_2} = 0.9$.

of the system. Similar statements may be made for C_3H_8. Under such conditions, maintaining a constant temperature throughout the pore system is both important and difficult.

To understand better the distributions of the two components in the pores, we present in Fig. 6 their time-averaged density profiles $\rho_i^z(x)$ (averaged in the yz planes) at $T = 35\,^{\circ}C$ with $x_{CO_2} = 0.9$, for the two upstream conditions, computed by averaging the results over the last 200,000 time steps of the simulations. The dashed lines indicate the boundaries of the pore region with the two CVs. The densities in the two bulk regions are essentially constant, as they should be. The numerical values of the densities in the two CVs match those obtained by the GCMC method at the same conditions, indicating that the chemical potentials in the two CVs have been properly maintained during the MD simulations. The small downward curvature at (dimensionless) $X^* = \pm 33.5$ is due to the "leakage" of the molecules out of the two CVs, which are those that, as described in Section 5, cross the outer boundaries of the CVs and leave the system. However, such deviations from a flat profile are insignificant. Note that, due to the large pressure drop applied to the pore system, the density profiles are not linear, as the total flux is the sum of the diffusive and convective parts.

As one moves from the left to right, the densities, regardless of the direction of the applied ΔP (the upstream condition), increase since the pores' sizes decrease. A closer inspection of the densities in the pores indicates that, for the applied ΔP,

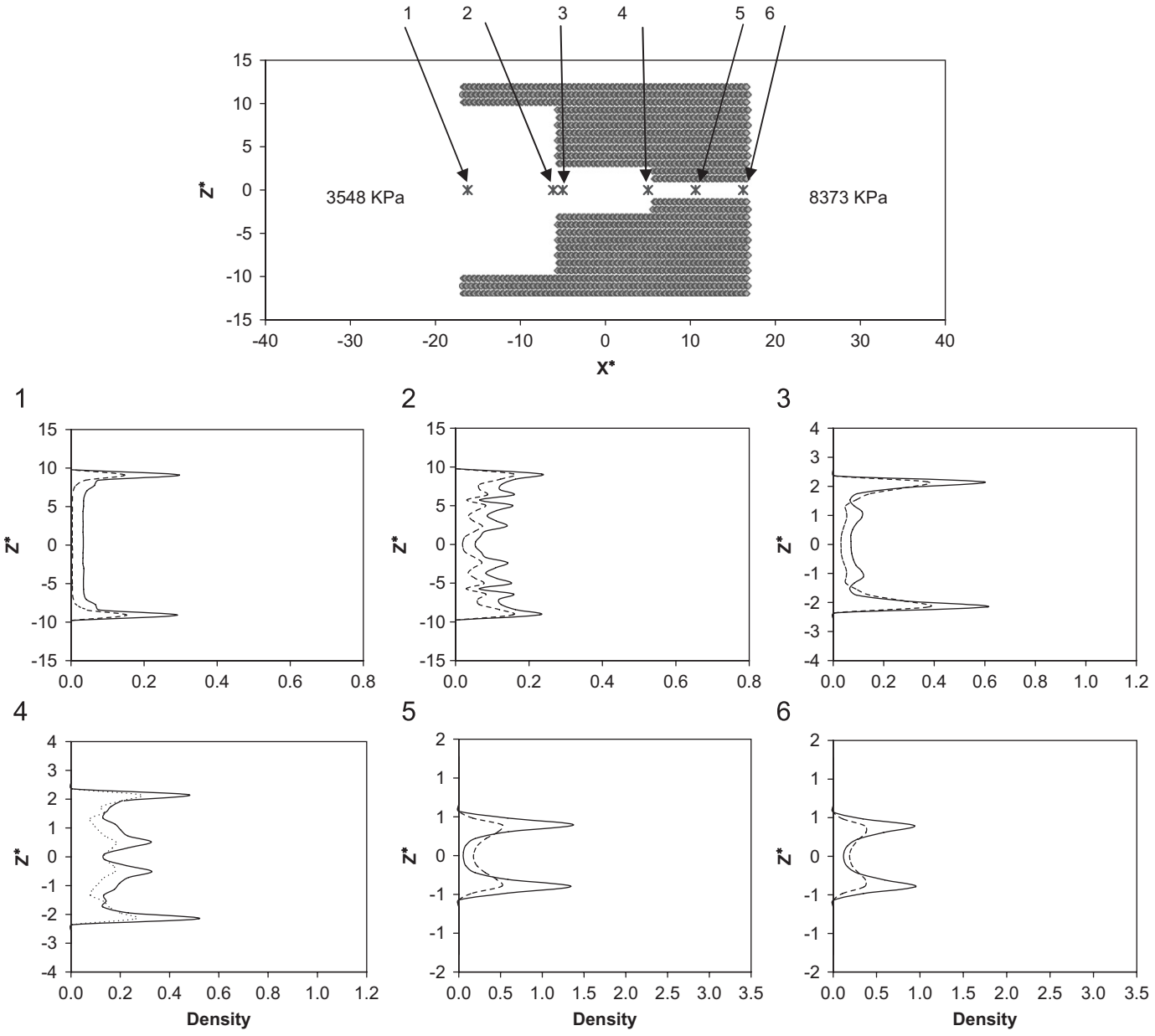

Fig. 8. Same as in Fig. 7, but when the upstream condition is maintained in the control volume connected to the smallest pore.

one has a gas-like (low density) mixture in the largest pore when the upstream condition is imposed on the smallest pore, followed by a transition to a liquid-like mixture (condensation) which packs completely the two smallest pores at high densities. The position of the transition line from the gas-like to liquid-like mixture depends on the pores' sizes and the direction and magnitude of ΔP.

We present in Figs. 7 and 8 the time-averaged densities $\rho_i^x(z)$ for the two components in six different planes that are perpendicular to the direction of the applied ΔP (the coordinates' center is on the centerline that passes through the three pores). Fig. 7 shows the density profiles when the upstream condition is maintained in the CV which is connected to the largest pore. The SC fluid mixture forms several liquid-like layers, packing the pore almost completely. In plane 1 near the pore mouth connected to the CV, two layers of each component have been formed. One, with high densities, is near the walls, while the second one with lower densities is closer to the center. In the opposite plane (denoted by 2 in Fig. 7) near the largest pore's mouth that connects it to the middle pore, the density profiles look chaotic and several layers of the two components have formed. This is an entrance effect whereby, due to the size of the middle pore being much smaller than that of the largest pore and the relative large size of C_3H_8, a large number of molecules accumulates at the entrance between the two pores. But, if we inspect the density profiles just inside the middle pore (denoted by 3 in the figure), we find again that two layers of each component have been formed. The molecules'

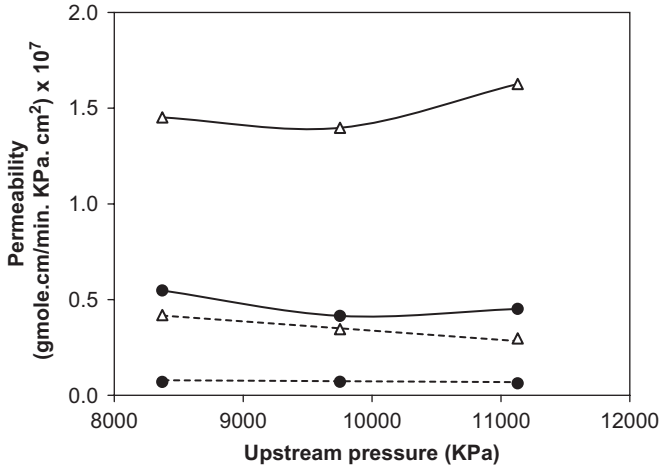

Fig. 9. Dependence of the permeabilities of CO_2 (circles) and C_3H_8 (triangles) on the upstream pressure, in a mixture at $T = 35\,^{\circ}C$ with $x_{CO_2} = 0.9$. The applied pressure drop is 4825 KPa (700 psi). Continuous and dashed curves represent the results for, respectively, when the upstream condition is maintained at the entrance to the largest pore and smallest pore.

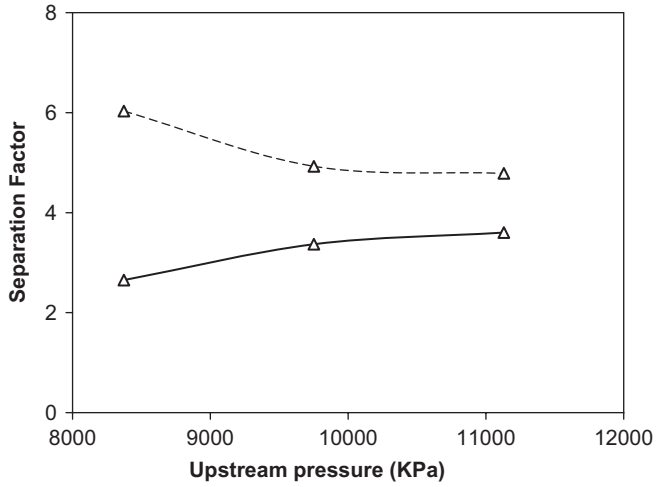

Fig. 10. The separation factors for the CO_2/C_3H_8 mixture that correspond to Fig. 9.

distributions in the region where the two smallest pores are connected (denoted by 4 in the figure) are qualitatively similar to those in plane 2, and are again dominated by the entrance effects. The size of the smallest pore and the relatively large size of C_3H_8 allow only monolayer formation. As a result, one obtains the density profiles shown in Fig. 7 for the planes 5 and 6. The same qualitative patterns are obtained when the upstream condition is held in the CV connected to the smallest pore (see Fig. 8).

These features should be compared with those encountered with subcritical gases in small pores that form only two adsorbed layers near a pore's walls, leaving its middle region sparsely populated. Multilayer formation persists in the entire pore system so long as the downstream pressure is high enough for the mixture to exit the system under, or close to, supercritical conditions. If, however, the downstream pressure is low, then multilayer formation occurs only near the upstream region of the pore. As the molecules approach the downstream region, only two layers, one near each wall, survive, hence signaling a phase transition from a liquid-like state to a gaseous one.

Fig. 9 presents the permeabilities of the two components under the two upstream conditions at $T = 35\,^{\circ}C$, with $x_{CO_2} = 0.9$. The applied pressure drop is, $\Delta P = 4825$ Kpa (700 psi). A comparison of these results with those shown in Figs. 2 and 4 for, respectively, CO_2/CH_4 and CO_2/C_2H_6 mixtures, indicates qualitative changes, or a type of transition, as the *n*-alkane becomes larger: the permeability of CO_2 is distinctly larger than that of CH_4 in their binary mixtures; the permeabilities are roughly equal for CO_2/C_2H_6 mixtures, whereas Fig. 9 indicates that the permeability of C_3H_8 is larger than CO_2. As a result, the separation process turns in favor of C_3H_8. The fact that the strength of adsorption of alkanes on the carbon walls increases with increasing molecular weight (or their chain's length) also contributes to the improved separation. This is shown in Fig. 10 .These are all new results, at least so far as MD simulations of CO_2–*n*-alkane mixtures under SC conditions are concerned.

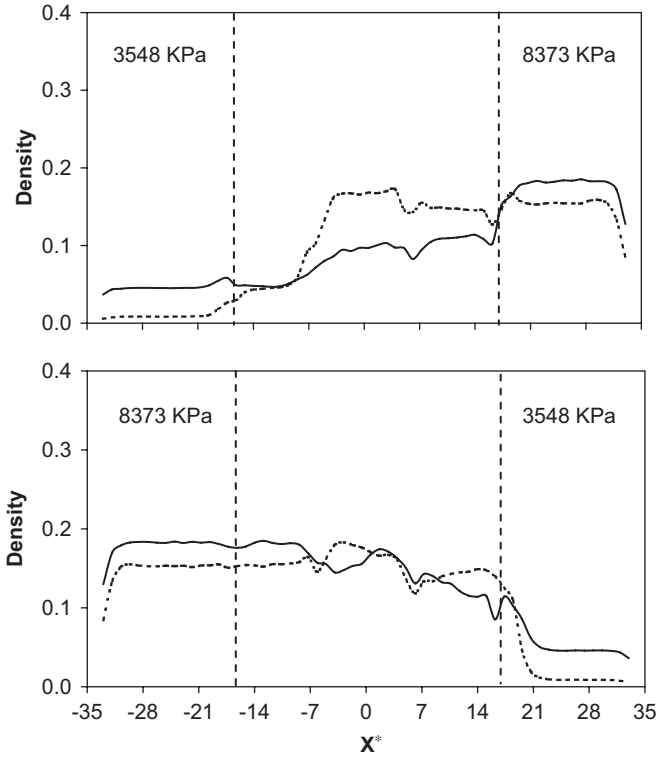

Fig. 11. Time-averaged density profiles in the transport direction x in the pore system for a mixture of CO_2 (continuous curves) and C_4H_{10} (dashed curves) with, $x_{CO_2} = 0.9$, at $T = 35\,^{\circ}C$. Dashed vertical lines indicate the boundaries of the pore region.

6.5. CO_2–C_4H_{10} *mixtures*

Fig. 11 presents the density profiles $\rho_i^z(x)$ for the two components and under the two upstream conditions, at $T = 35\,^{\circ}C$, with $x_{CO_2} = 0.9$. Note that the critical pressure of C_4H_{10} is about 3796 KPa (37.46 atm). Due to its large size and the sizes of the two smallest pores, the density of C_4H_{10} in the two pores

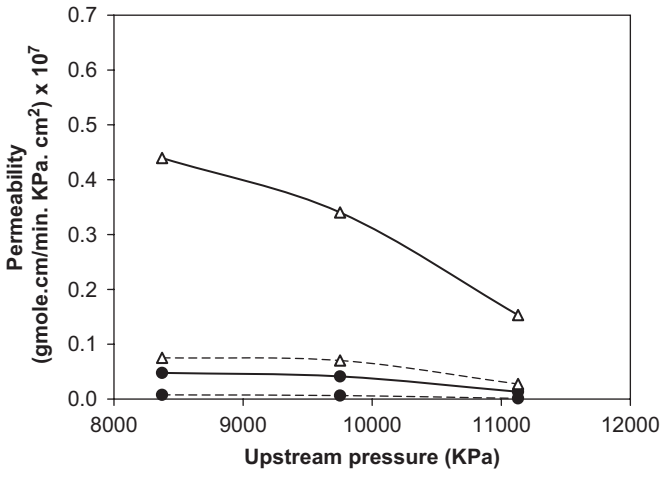

Fig. 12. Dependence of the permeabilities of CO_2 (circles) and C_4H_{10} (triangles) on the upstream pressure, for a mixture with $x_{CO_2} = 0.9$, at $T = 35\,^{\circ}C$. The applied pressure drop is 4825 KPa. Continuous and dashed curves show, respectively, the results for when the upstream condition is maintained at the entrance to the largest pore and smallest pore.

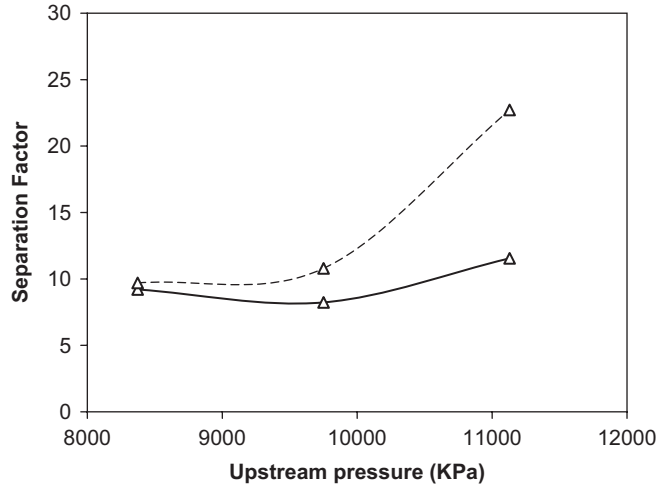

Fig. 13. The separation factors of the CO_2/C_4H_{10} mixture that corresponds to the permeabilities shown in Fig. 12.

is larger than that of CO_2, when the upstream conditions are maintained at the CV which is connected to the smallest pore. This is unlike the binary mixtures of CO_2 with the lighter *n*-alkanes. The same is more or less true about the case when the upstream conditions are imposed on the CV connected to the largest pore, except that the difference between the two densities is smaller. Qualitatively, the two components' density profiles $\rho_i^x(z)$ are similar to those shown in Fig. 7 for the CO_2/C_3H_8 mixture.

Fig. 12 shows the pressure dependence of the two components' permeabilities at $T = 35\,^{\circ}C$, with $x_{CO_2} = 0.9$. The pressure drop is $\Delta P = 4825$ KPa. Consistent with the pattern of the permeabilities described above, the permeabilities of C_4H_{10} are larger than those of CO_2. As a result, as Fig. 13 indicates, the separation process turns in favor of C_4H_{10}, with separation factors that are as large as 25. In addition, with increasing upstream pressure, the separation factors also increase. In practice, one cannot, of course, increase the upstream pressure to very large values, since it can damage the membrane.

6.6. Continuum basis for the direction-dependence of the permeabilities

Although the MD simulations provided convincing molecular-based evidence for the direction-dependence of the permeabilities for all the components, one might be tempted to attribute it to the small thickness of the membrane, and the resulting large pressure gradient applied to it. However, in addition to the fact that our own preliminary experimental data with real CMS membranes also agree with this result, the direction dependence may also be explained based on a simple continuum model, independent of the thickness of the membrane used in the simulations. As is well known, transport of molecules in a macropore (to which a pressure drop has been applied) is dominated by convection, which gives rise to a permeability independent of the direction of the applied pressure gradient. In a mesopore, transport of molecules is by a combination of convection and Knudsen diffusion (Mason and Malinauskas, 1983; Sahimi, 1993, 1995), if the loading is not high (i.e., if the fluid–fluid interactions are not strong), whereas, due to its small size and condensation phenomenon, transport through a nanopore occurs mostly through surface flow (if the fluid–surface interactions are favorable and strong). While condensation plays a role in the direction-dependence of the permeabilities, the most important factor that contributes to this dependence is the composite nature of the membrane.

To show this, we make an analogy between the resistances that the three pores in series offer against transport and that of electrical resistors. Then, the effective permeability K_e of the model membrane is given by

$$K_e = L\left[\sum_{i=1}^{3}\left(\frac{K_i}{L_i}\right)\right]^{-1}, \tag{10}$$

where K_i and L_i are, respectively, the permeance and length of pore i. It is now not difficult to show that it is the nonlinear dependence of K_e on K_i which is mostly responsible for its direction-dependence. This is true even if one has a gaseous mixture in the membrane (under subcritical conditions), as opposed to liquid-like mixtures (condensation) that we deal with in our pore system. To show this, we proceed as follows.

Consider, first, transport of a gas in a single pore and assume that the gas is transported by a combination of convection and Knudsen diffusion. Hence, its flux is given by (Mason and Malinauskas, 1983; Uchytil et al., 2000; Thomas et al., 2001),

$$J = -\left(D_k\frac{\mathrm{d}P}{\mathrm{d}x} + K_pP\frac{\mathrm{d}P}{\mathrm{d}x}\right), \tag{11}$$

where D_K is the Knudsen diffusivity of the gas. Here, K_p is a permeability *coefficient* defined for gases (if we were to use the Darcy's law, K_pP would be what is usually referred to as the

permeability). K_p is independent of the pressure. Assuming, as usual, that D_k is also independent of the pressure, then, since the flux J is constant at steady state, Eq. (11) can be easily integrated to yield

$$J = -L^{-1}[D_k(P_2 - P_1) + \tfrac{1}{2}K_p(P_2^2 - P_1^2)], \tag{12}$$

where P_1 and P_2 are the applied pressure at the pore's ends, and L is its length. According to Eq. (12), the magnitude of the effective permeability K_e, given by

$$K_e = D_k + \tfrac{1}{2}K_p(P_1 + P_2) \tag{13}$$

is independent of the *direction* of the applied pressure drop, $\Delta P = P_2 - P_1$, because the interchanges, $P_1 \to P_2$ and $P_2 \to P_1$ would not alter Eq. (13). This also implies that the magnitude of J is direction-independent. Note that, even if we replace the convective term of Eq. (11) by $K\,\mathrm{dP}/\mathrm{d}x$, which is the appropriate form for liquids and liquid-like mixtures (such as those under supercritical conditions), the conclusion that in a *single pore* K_e does not depend on the direction of ΔP will remain true, but with, $K_e = D_k + \frac{1}{2}K$.

Consider two pores that are in series, and suppose that the pressure at the interface between them is P_i (the following analysis was first advanced by Thomas et al., 2001). For simplicity, we assume that in one pore, say pore 1, convection is the dominant mechanism of transport (as in a macropore), while both convection and Knudsen diffusion contribute to the transport process in pore 2 (as in a mesopore). Hence, using Eq. (12), we write down the following expressions for the fluxes J_1 and J_2 in the two pores:

$$J_1 = -\tfrac{1}{2}\,L_1^{-1}K_p^{(1)}(P_i^2 - P_1^2), \tag{14}$$

$$J_2 = -L_2^{-1}[D_k^{(2)}(P_2 - P_i) + \tfrac{1}{2}\,K_p^{(2)}(P_2^2 - P_i^2)]. \tag{15}$$

At steady state, $J_1 = J_2$, which yields a second-order algebraic equation, $a\,P_i^2 + b\,P_i + c = 0$, for the pressure P_i, in which the parameters a, b, and c are given by

$$a = \tfrac{1}{2}\,[\alpha K_p^{(1)} + K_p^{(2)}],$$
$$b = D_k^{(2)},$$
$$c = -[\tfrac{1}{2}\,\alpha K_p^{(1)}P_1^2 + \tfrac{1}{2}K_p^{(2)}P_2^2 + D_k^{(2)}P_2], \tag{16}$$

where $\alpha = L_2/L_1$. According to Eqs. (16), the magnitude of the flux, $J = J_1 = J_2$, depends on the *direction* of ΔP. Such a direction dependence, which can be seen by making the interchanges, $P_1 \to P_2$ and $P_2 \to P_1$, is in agreement with the results of the MD simulations presented above. Clearly, the same approach can be extended to the three-pore system that we use in the MD simulations. Moreover, the conclusion will not change if, for example, Knudsen diffusion is the dominant transport mechanism in one pore, while convection contributes the most to the transport in a second pore connected in series to the first one.

7. Summary

The results presented in this paper indicate the significance of the pore structure and the fluids' thermodynamic states to their transport through a porous material, such as a supported membrane. In particular, the results have the following important implications:

(1) the permeabilities of all the components depend on the pressure;
(2) due to the composite nature of a supported membrane, the permeabilities also depend on the direction of the applied pressure gradient;
(3) with heavier alkanes one can obtain high separation factors for the alkane chains, which is the intention for practical application of SCFE using a supported membrane; and
(4) the classical modeling of transport of fluids through porous membranes, based on a single effective permeability independent of the applied pressure gradient's direction, is inadequate if they have a composite structure similar to what we use in the present paper. This is usually the case for supported membranes.

In practice, SCFE using CO_2, when utilized with heavier hydrocarbons, such as pentane and hexane, may give rise to additional complexities, such as *freezing* phenomena whereby the mixture does not move appreciably even over long periods of times. The results for such mixtures will be reported in a future paper.

Acknowledgments

We are grateful to the National Science Foundation, the Department of Energy, and Media & Process Technology for partial support of this work. We thank the San Diego Supercomputer Center for providing us with much needed computer time.

References

Acharya, M., Raich, B.A., Foley, H.C., Harold, M.P., Lerou, J.J., 1997. Metal-supported carbogenic molecular sieve membranes: synthesis and applications. Industrial & Engineering Chemistry Research 36, 2924.

Afrane, G., Chimowitz, E.H., 1996. Experimental investigation of a new supercritical fluid-inorganic membrane separation process. Journal of Membrane Science 116, 293.

Chen, Y.D., Yang, R.T., 1994. Preparation of carbon molecular sieve membrane and diffusion of binary mixtures in the membrane. Industrial & Engineering Chemistry Research 33, 3146.

Chialvo, A.A., Cummings, P.T., 1999. Molecular-based modeling of water and aqueous solutions at supercritical conditions. Advances in Chemical Physics 109, 115.

Chung, S.T., Shing, K.S., 1992. Multiphase behavior of binary and ternary systems of heavy aromatic hydrocarbons with supercritical carbon dioxide: Part I. Experimental results. Fluid Phase Equilibria 81, 321.

Cracknell, R.F., Nicholson, D., Quirke, N., 1995. Direct molecular dynamics simulation of flow down a chemical potential gradient in a slit-shape micropore. Physical Review Letters 74, 2463.

Cummings, P.T., Cochran, H.D., Simonson, J.M., Mesmer, R.E., 1991. Simulation of supercritical water and of supercritical aqueous solutions. Journal of Chemical Physics 94, 5606.

de Pablo, J.J., Bonnin, M., Prausnitz, J.M., 1992. Vapor-liquid equilibria for polyatomic fluids from site-site computer simulations: pure hydrocarbons and binary mixtures containing methane. Fluid Phase Equilibria 73, 187.

Düren, T., Keil, F.J., Seaton, N.A., 2002. Composition dependent transport diffusion coefficients of CH_4/CF_4 mixtures in carbon nanotubes by

non-equilibrium molecular dynamics simulations. Chemical Engineering Science 57, 1343.

Düren, T., Jakobtorweihen, S., Keil, F.J., Seaton, N.A., 2003. Grand canonical molecular dynamics simulations of transport diffusion in geometrically heterogeneous pores. Physical Chemistry Chemical Physics 5, 369.

Eckert, C.A., Knutson, B.L., Debenedetti, P.G., 1996. Supercritical fluids as solvents for chemical and materials processing. Nature 383, 313.

Firouzi, M., Tsotsis, T.T., Sahimi, M., 2003. Nonequilibrium molecular dynamics simulations of transport and separation of supercritical fluid mixtures in nanoporous membranes. I. Results for a single carbon nanopore. Journal of Chemical Physics 119, 6810.

Firouzi, M., Molaai Nezhad, Kh., Tsotsis, T.T., Sahimi, M., 2004. Molecular dynamics simulations of transport and separation of carbon dioxide-alkane mixtures in carbon nanopores. Journal of Chemical Physics 120, 8172.

Firouzi, M., Sahimi, M., Tsotsis, T.T., 2006. Supercritical fluids in porous composite materials: direction-dependent flow properties. Physical Review E 73, 036312.

Ford, D.M., Heffelfinger, G.S., 1998. Massively parallel dual control volume grand canonical molecular dynamics with LADERA II. Gradient driven diffusion through polymers. Molecular Physics 94, 673.

Frenkel, D., Mooij, G.C.A.M., Smit, B., 1992. Novel scheme to study structural and thermal properties of continuously deformable molecules. Journal of Physics: Condensed Matter 4, 3053.

Fujii, T., Tokunaga, Y., Nakamura, K., 1996. Effect of solute adsorption properties on its separation from supercritical carbon dioxide with a thin porous silica membrane. Bioscience Biotechnology and Biochemistry 60, 1945.

Furukawa, S., Nitta, T., 1997. Computer simulation studies on gas permeation through nanoporous carbon membranes by non-equilibrium molecular dynamics. Journal of Chemical Engineering of Japan 30, 116.

Furukawa, S., Shigeta, T., Nitta, T., 1996. Non-equilibrium molecular dynamics for simulating permeation of gas mixtures through nanoporous carbon membrane. Journal of Chemical Engineering of Japan 29, 725.

Furukawa, S., Hayashi, K., Nitta, T., 1997. Effect of surface heterogeneity on gas permeation through slit-like carbon membranes by non-equilibrium molecular dynamics simulations. Journal of Chemical Engineering of Japan 30, 1107.

Ghassemzadeh, J., Xu, L., Tsotsis, T.T., Sahimi, M., 2000. Statistical mechanics and molecular simulation of adsorption of gas mixtures in microporous materials: pillared clays and carbon molecular sieve membranes. Journal of Physical Chemistry B 104, 3892.

Harris, J., Rice, S.A., 1988. A lattice model of a supported monolayer of amphiphile molecules: Monte Carlo simulations. Journal of Chemical Physics 88, 1298.

Heffelfinger, G.S., Ford, D.M., 1998. Massively parallel dual control volume grand canonical molecular dynamics with LADERA I. Gradient driven diffusion in Lennard–Jones fluids. Molecular Physics 94, 659.

Heffelfinger, G.S., van Swol, F., 1994. Diffusion in Lennard–Jones fluids using dual control volume grand canonical molecular dynamics dimulation (DCV-GCMD). Journal of Chemical Physics 100, 7548.

Johnson, J.K., Zollweg, J.A., Gubbins, K.E., 1993. The Lennard–Jones equation of state revised. Molecular Physics 78, 591.

Jones, C.W., Koros, W.J., 1994. Carbon molecular sieve gas separation membranes-II. Regeneration following organic exposure. Carbon 32, 1427.

Jones, C.W., Koros, W.J., 1995. Characterization of ultramicroporous carbon membranes with humidified feeds. Industrial & Engineering Chemistry Research 34, 158.

Jones, C.W., Koros, W.J., 1995. Carbon composite membranes: a solution to adverse humidity effects. Industrial & Engineering Chemistry Research 34, 164.

Kelley, F.D., Chimowitz, E.H., 1990. Near-critical phenomena and resolution in supercritical fluid chromatography. A.I.Ch.E. Journal 36, 1163.

Kiran, E., Sengers, J.M.H.L., 1994. Supercritical Fluids-Fundamentals for Applications. Kluwer, Dordrecht.

Koresh, J.E., Sofer, A., 1983. Molecular sieve carbon permselective membrane. Part I. Presentation of a new device for gas mixture separation. Separation Science and Technology 18, 723.

Laso, M., de Pablo, J.J., Suter, U.W., 1992. Simulation of phase equilibria for chain molecules. Journal of Chemical Physics 97, 2817.

Linkov, V.M., Sanderson, R.D., Jacobs, E.P., 1994. Highly asymmetrical carbon membranes. Journal of Membrane Science 95, 93.

Macedonia, M.D., Maginn, E.J., 1999. A biased grand canonical Monte Carlo method for simulating adsorption using all-atom and branched united atom models. Molecular Physics 96, 1375.

MacElroy, J.M.D., 1994. Non-equilibrium molecular dynamics simulation of diffusion and flow in thin microporous membranes. Journal of Chemical Physics 101, 5274.

Martinez, H.L., Ravi, R., Tucker, S.C., 1996. Characterization of solvent clusters in a supercritical Lennard–Jones fluid. Journal of Chemical Physics 104, 1067.

Mason, E., Malinauskas, A.P., 1983. Gas Transport in Porous Media: The Dusty Gas Model. Elsevier, Amsterdam.

Mooij, G.C.A.M., Frenkel, D., Smit, B., 1992. Direct simulation of phase equilibria of chain molecules. Journal of Physics: Condensed Matter 4, L255.

Muller, A., Martinet, J.M., Vignet, P., 1989. Gas liquid and supercritical carbon dioxide permeability through a 5 nm port radius alumina membrane. In: Proceedings of the 1st International Conference on Inorganic Membranes. p. 337.

Nakamura, K., Hoshino, T., Morita, A., Hattori, M., Okamoto, R., 1994. In: Yano, T., Matsuno, R., Nakamura, K. (Eds.), Developments in Food Engineering. Blackie, Glasgow, p. 820.

Nicholson, D., 1998. Simulation studies of methane transport in model graphite micropores. Carbon 36, 1511.

Nicholson, D., Cracknell, R.F., Quirke, N., 1996. Transition in the diffusivity of adsorbed fluid through micropores. Langmuir 12, 4050.

Nitta, T., Yoneya, J., 1995. Computer simulations for adsorption of benzene diluted in supercritical carbon dioxide. Journal of Chemical Engineering of Japan 28, 31.

Nitta, T., Nozawa, M., Hishikawa, Y., 1993. Monte Carlo simulation of adsorption of gases in carbonaceous slitlike pores. Journal of Chemical Engineering of Japan 26, 266.

Nouacer, M., Shing, K.S., 1989. Grand canonical Monte Carlo simulation for solubility calculation in supercritical extraction. Molecular Simulation 2, 55.

Ohya, H., Higashijima, T., Tsuchiya, Y., Tokunaga, H., Nogishi, Y., 1993. Separation of supercritical carbon dioxide and isooctane mixtures with an asymmetric polyimide membrane. Journal of Membrane Science 84, 185.

Petersen, J., Matsuda, M., Haraya, K., 1997. Capillary carbon molecular sieve membranes derived from Kapton for high temperature gas separation. Journal of Membrane Science 131, 85.

Pohl, P.I., Heffelfinger, G.S., 1999. Massively parallel molecular dynamics simulation of gas permeation across porous silica membranes. Journal of Membrane Science 155, 1.

Pohl, P.I., Heffelfinger, G.S., Smith, D.M., 1996. Molecular dynamics computer simulation of gas permeation in thin silicalite membranes. Molecular Physics 89, 1725.

Rao, M.B., Sircar, S., 1993. Nanoporous carbon membranes for separation of gas mixtures by selective surface flow. Journal of Membrane Science 85, 253.

Rao, M.B., Sircar, S., 1996. Performance and pore characterization of nanoporous carbon membranes for gas separation. Journal of Membrane Science 110, 109.

Rosenbluth, M.N., Rosenbluth, A.W., 1955. Monte Carlo calculation of the average extension of molecular chains. Journal of Chemical Physics 23, 356.

Ryckaert, J.-P., Bellemans, A., 1975. Molecular dynamics of liquid *n*-butane near its boiling point. Chemical Physics Letters 30, 123.

Ryckaert, J.-P., Bellemans, A., 1978. Molecular dynamics of liquid alkanes. Faraday Discussions Chemical Society 66, 95.

Sahimi, M., 1993. Flow phenomena in rocks: from continuum models to fractals, percolation, cellular automata, and simulated annealing. Reviews of Modern Physics 65, 1393.

Sahimi, M., 1995. Flow and Transport in Porous Media and Fractured Rock. VCH, Weinheim, Germany.

Sarrade, S., Rios, G.M., Carles, M., 1996. Nanofiltration membrane behavior in a supercritical medium. Journal of Membrane Science 114, 81.

Seaton, N.A., Friedman, S.P., MacElroy, J.M.D., Murphy, B.J., 1997. The molecular sieving mechanism in carbon molecular sieves: a molecular dynamics and critical path analysis. Langmuir 13, 1199.

Sedigh, M.G., Onstot, W.J., Xu, L., Peng, W.L., Tsotsis, T.T., Sahimi, M., 1998. Experiments and simulation of transport and separation of gas mixtures in carbon molecular sieve membranes. Journal of Physical Chemistry A 102, 8580.

Sedigh, M.G., Xu, L., Tsotsis, T.T., Sahimi, M., 1999. Transport and Morphological Characteristics of Polyetherimide-Based Carbon Molecular Sieve Membranes. Industrial & Engineering Chemistry Research 38, 3367.

Sedigh, M.G., Jahangiri, M., Liu, P.K.T., Sahimi, M., Tsotsis, T.T., 2000. Structural characterization of polyetherimide-based carbon molecular sieve membranes. A.I.Ch.E. Journal 46, 2245.

Semenova, S.I., Ohya, H., Higashijima, T., Negishi, Y., 1992a. Dependence of permeability through polyimide membranes on state of gas, vapor, liquid and supercritical fluid at high temperature. Journal of Membrane Science 67, 29.

Semenova, S.I., Ohya, H., Higashijima, T., Negishi, Y., 1992b. Separation of supercritical carbon dioxide and ethanol mixtures with an asymmetric polyimide membrane. Journal of Membrane Science 74, 131.

Sengers, J.V., Sengers, J.M.H.L., 1986. Thermodynamic behavior of fluids near the critical point. Annual Reviews of Physical Chemistry 37, 189.

Shiflett, M.B., Foley, H.C., 1999. Ultrasonic deposition of high-selectivity nanoporous carbon membranes. Science 285, 1902.

Shigeta, T., Yoneya, J., Nitta, T., 1996. Monte Carlo simulation study of adsorption characteristics in slit-like micropores under supercritical conditions. Molecular Simulations 16, 291.

Shing, K.S., Chung, S.T., 1987. Computer simulation methods for the calculation of solubility in supercritical extraction systems. Journal of Physical Chemistry 91, 1674.

Shusen, W., Meiyun, Z., Zhizhong, W., 1996. Asymmetric molecular sieve carbon membranes. Journal of Membrane Science 109, 267.

Siepmann, J.I., Frenkel, D., 1992. Configurational bias Monte Carlo: a new sampling scheme for flexible chains. Molecular Physics 75, 59.

Sircar, S., Golden, T.C., Rao, M.B., 1996. Activated carbon for gas separation and storage. Carbon 34, 1.

Smit, B., Karaborni, S., Siepmann, J.I., 1995. Computer simulations of vapor–liquid phase equilibria of *n*-alkanes. Journal of Chemical Physics 102, 2126.

Steriotis, Th., Beltsios, K., Mitropoulos, A.Ch., Kanellopoulos, N., Tennison, S., Wiedenman, A., Keiderling, U., 1997. On the structure of an asymmetric carbon membrane with a novolac resin precursor. Journal of Applied Polymer Science 64, 2323.

Thomas, S., Schäfer, R., Caro, J., Seidel-Morgenstern, A., 2001. Investigation of mass transfer through inorganic membranes with several layers. Catalysis Today 67, 205.

Tokunaga, Y., Fujii, T., Nakamura, K., 1997. Separation of caffeine from supercritical carbon dioxide with a zeolite membrane. Bioscience Biotechnology and Biochemistry 61, 1024.

Uchytil, P., Schramm, O., Seidel-Morgenstern, A., 2000. Influence of the transport direction on gas permeation in two-layer ceramic membranes. Journal of Membrane Science 170, 215.

van der Ploeg, P., Berendsen, H.J.C., 1982. Molecular dynamics simulation of a bilayer membrane. Journal of Chemical Physics 76, 3271.

Xu, L., Sedigh, M.G., Sahimi, M., Tsotsis, T.T., 1998. Non-equilibrium molecular dynamics simulation of transport of gas mixtures in nanopores. Physical Review Letters 80, 3511.

Xu, L., Tsotsis, T.T., Sahimi, M., 1999. Nonequilibrium molecular dynamics simulation of transport and separation of gases in carbon nanopores. I. Basic results. Journal of Chemical Physics 111, 3252.

Xu, L., Sedigh, M.G., Tsotsis, T.T., Sahimi, M., 2000a. Nonequilibrium molecular dynamics simulation of transport and separation of gases in carbon nanopores. II. Binary and ternary mixtures and comparison with the experimental data. Journal of Chemical Physics 112, 910.

Xu, L., Tsotsis, T.T., Sahimi, M., 2000b. Nonequilibrium molecular dynamics simulations of transport and separation of gas mixtures in nanoporous materials. Physical Review E 62, 6942.

Xu, L., Tsotsis, T.T., Sahimi, M., 2001. Statistical mechanics and molecular simulation of adsorption of ternary gas mixtures in nanoporous membranes. Journal of Chemical Physics 114, 7196.

Yoshii, N., Okazaki, S., 1997. A large-scale and long-time molecular dynamics study of supercritical Lennard–Jones fluid. An analysis of high temperature clusters. Journal of Chemical Physics 107, 2020.

Molecular dynamics simulation of diffusion of gases in a carbon-nanotube–polymer composite

Seong Y. Lim, Muhammad Sahimi,* Theodore T. Tsotsis, and Nayong Kim
Mork Family Department of Chemical Engineering & Materials Science, University of Southern California, Los Angeles, California 90089-1211, USA

(Received 28 October 2006; revised manuscript received 23 April 2007; published 31 July 2007)

Extensive molecular dynamics (MD) simulations were carried out to compute the solubilities and self-diffusivities of CO_2 and CH_4 in amorphous polyetherimide (PEI) and mixed-matrix PEI generated by inserting single-walled carbon nanotubes into the polymer. Atomistic models of PEI and its composites were generated using energy minimizations, MD simulations, and the polymer-consistent force field. Two types of polymer composite were generated by inserting (7,0) and (12,0) zigzag carbon nanotubes into the PEI structure. The morphologies of PEI and its composites were characterized by their densities, radial distribution functions, and the accessible free volumes, which were computed with probe molecules of different sizes. The distributions of the cavity volumes were computed using the Voronoi tessellation method. The computed self-diffusivities of the gases in the polymer composites are much larger than those in pure PEI. We find, however, that the increase is not due to diffusion of the gases *through* the nanotubes which have smooth energy surfaces and, therefore, provide fast transport paths. Instead, the MD simulations indicate a squeezing effect of the nanotubes on the polymer matrix that changes the composite polymers' free-volume distributions and makes them more sharply peaked. The presence of nanotubes also creates several cavities with large volumes that give rise to larger diffusivities in the polymer composites. This effect is due to the repulsive interactions between the polymer and the nanotubes. The solubilities of the gases in the polymer composites are also larger than those in pure PEI, hence indicating larger gas permeabilities for mixed-matrix PEI than PEI itself.

DOI: 10.1103/PhysRevE.76.011810 PACS number(s): 61.25.Hq, 02.70.Ns, 61.82.Pv, 81.07.De

I. INTRODUCTION

Nanoporous media constitute an important class of materials with a wide variety of applications. They include catalysts, membranes, adsorbents, and thin flims that are used not only in surface coating, but also as low-dielectric-constant materials, sensors, and insulators. In particular, membranes have been advocated for many years as a promising tool for the separation and purification of fluids [1–3], while biological membranes are also of immense importance to a variety of biological activities and functions. For example, separation by membranes of oxygen from air, enrichment of methane in the gas mixtures that landfills produce, and separation of H_2 and CO_2 from coal gasification processes have attracted considerable attention. In addition, an important impedement to the use of fuel cells has been the production of hydrogen with high degree of purity, which certain nanoporous membranes may be able to provide by separating H_2 from various gas mixtures.

Among many nanoporous membranes that have been prepared and advocated for various applications, carbon-molecular-sieve membranes (CMSMs), which are prepared by carbonization of a variety of polymeric precursors, have recently been studied as a promising alternative to both inorganic and polymeric membranes [4–8]. In particular, we have been using polyetherimide (PEI)—a high-temperature, glassy, amorphous polymer [8]—as the polymeric precursor in the preparation of CMSMs. The average pore size of CMSMs is typically less than 5 Å, because of which the molecular interactions between the gases that pass through the membranes' nanopores are important and cannot be ignored. Therefore, accurate studies of such nanoporous materials and sorption and transport of gases and liquids in them require detailed molecular modeling [9,10]. Over the past few years, we have been developing [11–13] atomistic models of CMSMs and of sorption and transport of low-molecular-weight gasess in them, using molecular dynamics (MD) simulations. Our models and studies have provided not only estimates of the macroscopic properties of interest, such as the effective diffusivity and solubility of various gases, but also detailed information on the mechanisms of transport processes in such materials. Since we have been using PEI as a polymeric precursor for the preparation of CMSMs [7,14], one goal of our study, in addition to being important and interesting on its own, has been gaining better understanding of the similarities and differences between transport and sorption in PEI—the precursor material—and CMSMs—the final nanoporous material made from the precursor.

Recent experiments indicated [14] that mixed-matrix membranes, composed of polyimide and CMSMs pyrolyzed from polyimide, exhibit much improved permeance and selectivity for the separation of various gas mixtures, such as CO_2/CH_4. At the same time, recent atomistic simulations of gases in single-walled carbon nanotubes [15,16] indicated very high gas permeances, rates of transport, and excellent separation properties. The purpose of the present paper is to report the preliminary results of a study for investigating the possibility of improving the performance of a polymeric membrane by inserting carbon nanotubes in its matrix. Using MD simulations, we study diffusion and solubility of CO_2 and CH_4 in PEI and in its composites, which we generate by inserting carbon nanotubes in PEI. Such a study is important not only on its own, as it explores the possibility of developing better polymeric membranes and composites, but can

*Corresponding author. moe@iran.usc.edu

also provide insight into improving the performance of CMSMs for which PEI is a precusor. Our study has been made possible by recent advances in computing and molecular simulation techniques that enable us to construct models of glassy amorphous polymers, such as PEI, with accurate interatomic potentials.

Only a relatively small number of studies has been devoted in the past to molecular modeling of diffusion (and sorption) in polymers, most of which have dealt with flexible polymeric chains composed of repeating units with a relatively simple structure, such as poly(dimethylsiloxane) (PDMS), poly(isobutylene), polyethylene (PE), and polypropylene [17–23]. Moreover, very few studies have focused on polymers that consist of stiff chains [24–26], as well as membrane materials, such as polyelectrolytes [27,28]. Mooney and MacElroy [28] studied, for example, diffusion of small molecules in semicrystalline aromatic polymers. There have been only a few papers using MD simulations to study the transport mechanism(s) in polymeric materials. For example, Tamai *et al.* [17] and Fritz and Hofmann [18] utilized MD simulations to study the diffusion and sorption of methane, water, and ethanol in PDMS and PE using a united-atom model in the bulk region, while Muller-Plathe [19] carried out MD simulation of diffusion of water in poly(vinyl alcohol), used as packaging materials. Very few studies have focused on the transport of small molecules through glassy polymers [28], calculating both the molecules' solubility and diffusivity. Generally speaking, while good qualitative agreement between simulation and experimental values of the diffusion coefficients and the solubilities has been obtained, only a few models have produced quantitative agreement with the experimental data. While tuning the parameters of the force field that represents the polymers improves the agreement between the computed and measured values, it has been shown that the size of the simulation cell itself [23] and the method of polymer generation [22] significantly affect the calculated molecular solubility in a polymer glass. The only work that we are aware of that investigates the properties of nanotube-polymer composites is that of Wei *et al.* [29] who used MD simulations to study the thermal expantion and transport characteristics of carbon nanotube-polyethylene composites. In addition, MD simulations were very recently utilized by Han and Elliot [30] to compute the elastic properties of polymer-canbon nanotube composites.

The rest of this paper is organized as follows. In Sec. II we present the details of the molecular modeling, including the atomistic models of PEI, its composites, MD simulation of gas diffusion in the materials, and computation of the free-volume distributions and the gases' solubilities. Section III contains the results of the study and their implications, while Sec. IV presents an in-depth discussion of the results. The last section summarizes the paper.

II. MOLECULAR MODELING AND SIMULATION

The MD simulations consist of two steps. First, we generate molecular models of PEI and also a mixed-matrix polymer (MMP) composite, consisting of PEI and carbon nanotubes, by the methods described below and compute the free-volume distributions and the solubilities. The next step is carrying out equilibrium MD simulations of the diffusion of CO_2 and CH_4 in PEI and MMP composites. In what follows, we describe the details of the computational techniques employed in our studies.

A. Generation of the polymer and its mixed-matrix composites

The PEI microstructure was generated using a modified version [31,32] of the self-avoiding walk (SAW) method of Theodorou and Suter [33]. Polymer generation starts by inserting three atoms in the backbone of the polymer, connected together by the bonds, in a cubic unit cell in a random orientation. The length of the backbone chain is then increased stepwise by adding one atom at a time to the growing polymer chain, using the modified SAW method. During the growth of the polymer, the allowed rotational states of successive bonds between adjacent atoms are determined from the probability distribution functions that are governed by energy considerations. The probability that a bond assumes a given orientation relative to an adjacent bond depends on the rotational state of the adjacent bond. Therefore, although an atom can be added to the growing polymer in a number of different orientations, only the particular orientation that results in the smallest increase in the potential energy of the polymer has the highest probability of forming. In this way polymers of a given length are constructed. The PEI structure was constructed using 40 repeating units, and a single polymer chain was inserted into the simulation cell in order to eliminate chain-end effects.

We used single-walled carbon nanotubes (SWCNTs) in order to generate nanotube–PEI-polymer composites. Two types of composite were generated using open-ended zigzag (7,0) and (12,0) nanotubes. (Use of other types of carbon nanotubes is currently being studied.) We refer to the two types of polymer composites as MMP7 and MMP12, respectively. The length of both nanotubes was about 14.4 Å, whereas their open-end diameters were 7 and 10.5 Å, respectively. In each case three nanotubes were inserted at randomly selected positions within the polymer matrix (without allowing overlap with the polymer's atoms) and their dangling ends were saturated with hydrogen atoms. Their final locations within the polymer were determined using energy minimization and MD simulations (see below). The weight fractions of the (7,0) and (12,0) nanotubes in the composites were 0.13 and 0.22, respectively. Figure 1 presents the structure of a repeating unit of PEI, together with that of the (7,0) nanotube. Minimum-image periodic boundary conditions were imposed on the cubic simulation cell in order to eliminate the boundary effects. The entire procedure for generating the structures of the materials and computing the various properties of interest was as follows.

In the case of pure PEI [13], the initial packing density in the simulation cell was set at 0.1 g/cm^3 (using a large simulation cell). The energy of the system was then minimized using conjugate-gradient algorithms [9]. The resulting structure was then compressed using MD simulation in a (*NPT*) ensemble under a pressure of 0.6 GPa for 10 ps in order to increase the polymer density to be as close to the experimen-

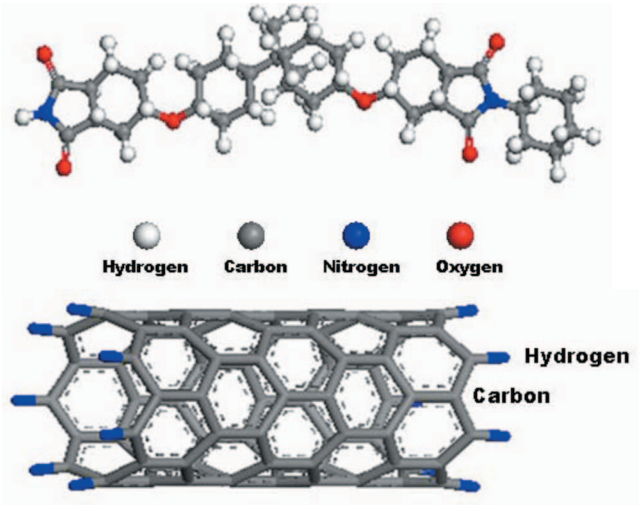

FIG. 1. (Color online) Repeating units of the PEI (top) structure and the zigzag (7,0) carbon nanotube (bottom).

tal value of 1.27 g/cm^3 as possible. Energy minimization and short-duration MD simulations in the (*NVT*) ensemble at 1000 K were then followed in order to further relax the material. Then, MD simulations were carried out in the (*NPT*) ensemble for several ns at 1 atm and 300 K. The gases' solubility and the free-volume distribution of the polymer were then computed. To compute the effective self-diffusivities of CO_2 and CH_4 in the PEI structure we followed the same procedure as above, except that, after generating the initial PEI structure by the SAW method, we inserted the gas molecules in the simulation cell (without allowing overlaps of the gases with the atoms of the PEI structure) and followed the energy-minimization–MD simulation procedure. We estimated the diffusivities by using both the (*NPT*) and (*NVT*) ensembles and, as discussed below, discovered some differences between the results obtained with the two ensembles.

In the case of MM PEI, after generating the polymer at low density, we inserted the SWCNTs at randomly selected points within the simulation cell, disallowing overlap with the atoms of the PEI structure. The same energy minimization, compression, and further relaxation steps as above were then followed. The gases' solubilities and the composites' free-volume distributions were then computed. To compute the self-diffusivities of the gases, insertion of the nanotubes was followed by insertion of the gases' molecules into the simulation cell at randomly selected points (without allowing overlaps), followed by energy minimization, compression, and further structural relaxation. In all the cases, ten molecules of each gas were utilized in the diffusion simulations. During all MD simulations, the time step was 1 fs. The temperature was held constant by the Nosé-Hoover method [34], while pressure was fixed by the Andersen method [35]. All softwares used in the simulations have been developed in our group.

B. Force field

All interaction potentials for pure PEI were computed based on the polymer-consistent (PC) force field [36]. The details of the force fields were given previously [13,36], but for completeness are briefly described here. The potential energy associated with bond stretching is given by

$$E_s = \sum_{i=2}^{4} k_i (\ell - \ell_0)^i, \tag{1}$$

where ℓ_0 is the equilibrium length of the bond, ℓ its length during the simulations, and k_i a force constant. The potential energy associated with the deviations of bonds' angles from their equilibrium values is determined by

$$E_\theta = \sum_{i=2}^{4} h_i (\theta - \theta_0)^i, \tag{2}$$

where θ_0 is the equilibrium bond angle, θ its angle during the simulations, and h_i the corresponding force constant. The dihedral (torsional) potential energy of the bonds is given by

$$E_\phi = \sum_{i=2}^{4} d_i (1 - \cos i\phi), \tag{3}$$

with d_i being a force constant and ϕ the dihedral angel. The nonbonded interactions were estimated using a sum of a 6–9 Lennard-Jones (LJ) potential and the standard expression for the Coulombic interactions:

$$E_{nb}(r_{ij}) = \sum_{ij} \epsilon_{ij} \left[2\left(\frac{\sigma_{ij}}{r_{ij}}\right)^9 - 3\left(\frac{\sigma_{ij}}{r_{ij}}\right)^6 \right] + \sum_{ij} \frac{q_i q_j}{r_{ij}}, \tag{4}$$

with

$$\sigma_{ij} = \left(\frac{\sigma_i^6 + \sigma_j^6}{2}\right)^{1/6}, \quad \epsilon_{ij} = 2\sqrt{\epsilon_i \epsilon_j} \frac{\sigma_i^3 \sigma_j^3}{\sigma_i^6 + \sigma_j^6}, \tag{5}$$

where σ_i and ϵ_i are the usual LJ size and energy parameters for atom i, r_{ij} is the distance between atoms i and j, and q_i and q_j are their partial electrical charges. In the present study, the potential energy function E_{nb} for the nonbonded interactions was cut off at an interatomic distance of 11 Å. This was based on our previous molecular simulations of the diffusion and sorption of various gases in other nanoporous materials [37,38]. In those studies we used the Ewald summation technique [37] and the multipole expansion method [38,39] in order to account for the Coulombic interactions. Our studies [37,38] indicated that a relatively large cut off distance for computing the contributions of the Coulombic interactions yields reasonably accurate results, while being much simpler than either of the other two methods. Table I lists the force field parameters of CO_2 and CH_4 used in the simulations.

We are not aware of any classical force fields that have been designed for a polymer composite of the type that we are considering in the present paper. If the radius of a SWCNT is large, its properties must be closely related to carbons in graphite, which have sp^2 valence orbital hybridization. Quantum mechanical studies [40] indicate that as the radius decreases, the curvature structure of a nanotube changes valence orbital hybridization and the effective bond order. This leads to hybridization which is close to sp^3, which influences the dynamic fluctuations of the SWCNTs out of their smooth cylindrical structure at zero temperature.

TABLE I. Values of the PC force field for CH_4 and CO_2.

	CH_4			CO_2		
	C	H	C-H	C	O	C-=O
σ (Å)	4.010	2.995		4.010	3.530	
ϵ (kcal/mol)	0.054	0.020		0.064	0.060	
q (electron)	−0.0530	0.01325		0.120	−0.06	
l_0 (Å)			1.101			1.160

Consequently, the potential interaction between gas molecules and the SWCNTs may also be affected. Therefore, it is reasonable to expect that adsorption and diffusion of gas molecules *inside* SWCNTs may also be affected by the change in hybridization. Indeed, this has been found to be the case by Mao *et al.* [16] and others [29,41]. These groups used a variety of classical force fields based on the Brenner potential and its extensions [42]. One may also develop a classical force field for SWCNTs by interpolating between sp^2 and sp^3 values, using the data for sp^2 and sp^3 carbons provided by the self-consistent force field [43].

However, the above results were obtained for diffusion and adsorption *inside* SWCNTs. Our preliminary simulations for the MM PEI structure with SWCNTs indicated that, regardless of the force field used, the gas molecules hardly ever pass *through* the nanotubes. Instead, as described below, the main effect of the nanotubes on the composite polymers is inducing large fluctuations in their accessible free volumes and increasing them, which, in turn, affects diffusion and sorption of gas molecules in the composite polymers. Given that (a) the nanotubes are also composed of carbon atoms and that (b) the PC force field is supposed to be able to represent a variety of polymers and carboneous materials, we used the PC force field to also generate the atomistic models of MM PEI composites. While a more detailed force field would be desirable using, for example, the technique of Ref. [43], we do not believe that such a force field would change the essence of the results that are presented below.

We also point out that the partial charges that are listed in Table I are smaller than those reported previously in the literature and that the carbon van der Waals radius listed in Table I is about 20% larger than what has been reported previously [10–13,44–47]. The reason for the difference is as follows. According to Eqs. (4) and (5), a 6–9 LJ potential, as opposed to the classical 6–12 LJ potential utilized in previous studies, is used in the present work. Moreover, the mixing rules, Eqs. (5), are different from the usual Lorentz-Berthelot rules (arithmetic and geometric averages for the size and energy parameters, respectively) used in most of previous studies. Since the LJ parameters are typically estimated by using experimental data for some properties of a material to fit the parameters of a force field which is used in atomistic simulations, the difference between what is listed in Table I and the previously reported values is natural. This is particularly true if we recall that the parameters of the PC force field represent *optimal values*, designed to reproduce reasonably accurately the morphology of the PEI. As such, they are necessarily not the same as those reported in the literature, even if we had used the 6–9 LJ potential with the Lorentz-Berthelot mixing rules.

C. Estimation of the self-diffusivities

As mentioned above, to estimate the self-diffusivities of CO_2 and CH_4 in the PEI and MM PEI structures, ten molecules of each gas were added to the simulation cell that contains the PEI or MM PEI structure, after which energy minimization, compression, and further relaxation of the system were carried out. The self-diffusivities were then estimated from the mean-square displacements of the gas molecules using the Einstein relation

$$D = \lim_{t\to\infty} \frac{1}{6t}\langle|\mathbf{R}(t) - \mathbf{R}(0)|^2\rangle. \tag{6}$$

Here, $\langle\cdot\rangle$ indicates averages over all gas molecules and over all possible time origins for the motion of the gas molecules and $\mathbf{R}(t)$ is the Cartesian position vector of a gas molecule at time t. The time intervals between the origins were selected to be 100 fs apart.

D. Accessible free volumes and solubilities

To compute the free-volume distributions of the PEI and MM PEI structures, MD simulations in the (*NPT*) ensemble were carried out in the absence of gas molecules. Twenty configurations each of the PEI, MMP7, and MMP12 PEI structures were taken from the simulation trajectories at every 100 fs. The accessible free volumes of the PEI and MM PEI structures were then computed using the following method based on a hard-sphere probe.

(i) The cubic simulation cell was partitioned into a three-dimensional mesh of $100\times100\times100$ subcells.

(ii) A probe molecule (hard sphere) of a given diameter was inserted at the center of each subcell, and the distance to the nearest atom of the material was computed. If the distance turned out to be larger than the sum of the van der Waals radii of the penetrant molecule and the material's atom, the subcell was considered as contributing to the accessible free volume. The cavity size distributions of the PEI and MMP structures were then computed using a Voronoi tessellation of the space based on the algorithm of Tanemura *et al.* [48]. The vectors connecting (the centers of) the atoms in the system were perpendicularly bisected and a large number of intersecting planes were generated. The polyhedra associated with the atoms were then constructed using the al-

gorithm. As a Voronoi polyhedron around an atom identifies its own available space, it can be related to the void volume of the dense amorphous polymer, which was then used to study the evolution of the free volume.

The particle insertion method of Widom [49] was used to estimate the solubility S_0 of the gases in the PEI and MM PEI structures. S_0 is defined as the gas concentration in a volume element of the polymer which is in equilibrium with a given outside reservoir pressure of the same gas. Following the energy minimization, compression, and MD simulation procedure described above, 20 PEI and MM PEI configurations at 20 different times, with intervals of 100 fs in between, were extracted from the MD simulations and used in the simulations with a test particle. The potential parameters for the test particle was also taken from the PC force field. The insertion procedure was then followed by calculating the interaction energy E of the system, consisting of the test particle and the polymers. In the (NPT) ensemble the excess chemical potential μ_e is computed via

$$\mu_e = -k_B T \ln S_0 = -k_B T \ln\langle f_v V \exp(-E/k_B T)/\langle V\rangle\rangle, \quad (7)$$

where T is the temperature, k_B is Boltzmann's constant, f_v is the accessible free-volume fraction, V is the cell's volume during the simulations with $\langle V\rangle$ being its ensemble average, and $\langle\cdots\rangle$ denotes an ensemble average over all the polymers' configurations extracted during the MD simulations. The relation between the solubility S_0 in Eq. (7) and the actual solubility coefficient S in units of cm^3 (STP)/(cm^3 atm) is given by

$$S = \frac{T_0}{T}\frac{1}{P}S_0, \quad (8)$$

with T_0=273.15 K and P_0=1.0 atm.

III. RESULTS

The cell length was about 31 Å for the PEI and 33 and 35 Å for the MMP7 and MMP12 structures, respectively. The density of the materials, after energy minimization, compression, and further relaxation, was about 1.15 g/cm^3 for the MMP7 PEI, 1.1 g/cm^3 for the MMP12 (we are not aware of any data for the densities of the MMP7 and MMP12), and 1.27 g/cm^3 for the PEI structures which is the same as the experimental value. Given the void space that the SWCNTs generate in the MM polymers (see below), their densities appear reasonable, as they are lower than that of PEI.

A typical morphology of the MM polymer in a simulation cell is shown in Fig. 2. To understand the morphology better, we make a rough analogy between the SWCNTs in the PEI structure, on the one hand, and a polymer near a rigid wall, on the other hand (the analogy is not exact, because the nanotubes' walls are not completely rigid and also have curvature). Then, in analogy with the phenomenon of polymer depletion near a rigid wall, one may also expect polymer depletion normal to the long axis of the nanotubes, a phenomenon induced by entropic effects, but also affected by the flexibility of the nanotubes normal to their long axis. Figure 2 indicates this effect.

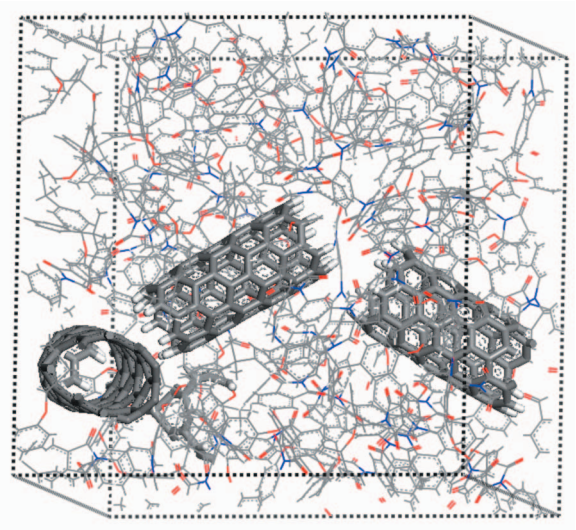

FIG. 2. (Color online) Calculated radial distribution functions of PEI and its composites.

The computed radial distribution functions $g(r)$, defined as the probability of finding atoms at a distance r from another atom compared to the ideal gas distribution, are presented in Fig. 3. The first sharp peak at 1.3 Å is due to the C-H bonding, while the second sharp peak at 1.4 Å is contributed by the C-C bonding in the phenyl rings. Note that, due to the phenyl groups of the nanotubes, the second peaks of the radial distribution functions of the composite polymers are higher than that of PEI. As is well known, the difference between a liquid state and an amorphous polymer is that short-range order in polymers is dominated by the fixed bond lengths associated with the backbone atoms. The radial distribution functions shown in Fig. 3 indicate clearly the amorphous nature of the three polymers—i.e., the complete absence of long-range order.

The time dependence of the free-volume fractions f_v for a probe of size σ=2.5 Å, averaged over 20 configurations taken from the MD simulation in the (NPT) ensemble, is shown in Fig. 4. During the MD simulation in the (NPT) ensemble, fluctuations of f_v were very small. In general, in glassy polymers such as PEI, the characteristic times are so long that the accessible free volumes undergo very small fluctuations. As Fig. 4 indicates, fluctuations of the accessible free volumes in MMP7 and MMP12 are somewhat larger than those in PEI, which is due to the presence of nanotubes and the fluctuations that they induce in the free volume of the polymer chain. These features indicate that the atomistic models that we have generated for PEI and its composites should be quite reasonable.

Figure 5 presents the accessible free-volume fractions f_v, calculated based on a hard-sphere probe and plotted as a function of the probe's diameter (which is represented by its LJ size parameter σ) for PEI and its composites. We took into account the effect of the different densities of PEI and its composites. The values of f_v decrease rapidly with increasing probe diameters. The free-volume fractions are the largest for MMP12, while those of PEI are the smallest. In PEI and MMP7, the accessible free-volume fractions are less

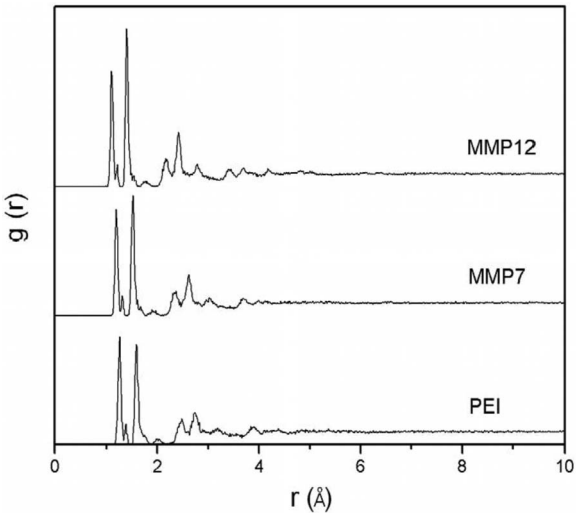

FIG. 3. Fluctuations with the time of the accessible free-volume fractions of PEI and its composites. The probe size is 2.5 Å.

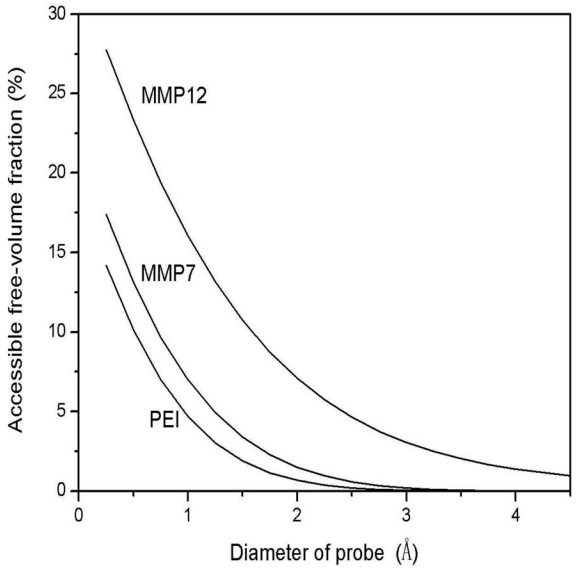

FIG. 5. Three-dimensional view of the mixed-matrix PEI structure within the simulation cell.

than 1% when the probe size is only 3 Å. One might then conclude that the empty volume of the nanotubes contributes significantly to f_v. However, since the difference between values of f_v for PEI and its composites for the smallest probe size is somewhat larger than the empty volumes of the (7,0) and (12,0) nanotubes, we recognize that the increase in f_v in the two polymer composites relative to PEI is, in fact, due to a variety of factors. The most important of such factors is the repulsive interactions between the nanotubes and the polymers' chain, and the fluctuations that such interactions induce in the polymers' morphologies. Figure 5 also indicates that permeation of gas molecules through the polymer composites must be easier than that in PEI, hence already indicating a possible improvement in the separation and transport properties of the composites over pure PEI.

As described earlier, the Voronoi tessellation method was utilized to compute the distributions of the cavity sizes (volumes) for the unit cells of the PEI, MMP7, and MMP12 structures, taking all the atoms into account. The resulting distributions of the cavity sizes (volumes) at three different times are shown in Fig. 6. The shape of the cavity size distribution in the PEI structure is somewhat different from those of its composites, exhibiting distinct "shoulders" that are not seen in the polymer composites. On the other hand, there are small numbers of high-volume cavities in the polymer composites that are not seen in the PEI structure. This is particularly true of MMP12 which has a small, but significant, fraction of cavities with volumes larger than 40 $Å^3$. These features are caused by the absence of the nanotubes in pure PEI and their presence in the polymer composites. The nanotubes squeeze the PEI matrix, hence making the cavity size distributions in the composites more sharply peaked. But they also make it possible to generate a small number of large cavities in the polymer composites, hence opening the way for their improved performance as membranes for gas separation and as composites for other applications. The squeezing effect may be atributed to the repulsive interaction between the polymer and the nanotubes, and is also consistent with the depletion of a polymer near a rigid wall described above. Consistent with Fig. 4, the cavity size distributions do not vary widely with time. Figure 7 presents the ensemble-averaged cavity size distributions at long times.

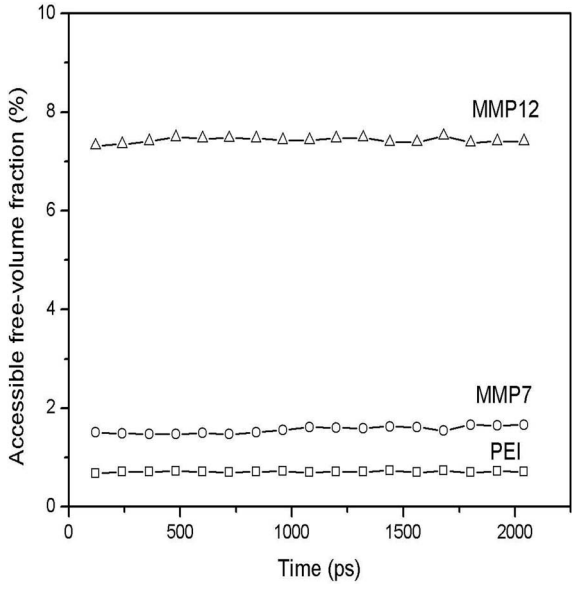

FIG. 4. The distributions of the free-volume fractions of PEI and its composites, averaged over 20 configurations.

As mentioned earlier, the test particle insertion method [49] was used to compute the excess chemical potentials of CH_4 and CO_2 in PEI, MMP7, and MMP12 at 300 K and 1 atm. Figure 8 presents the results. Due to their high free-volume fractions, the excess chemical potentials of the gases in the composite polymers are lower than those in PEI, with the excess chemical potentials in MMP12 being the lowest. In all cases, the excess chemical potentials of CO_2 in the materials are lower than those of CH_4, presumably due to the van der Waals energy and Coulombic charges for

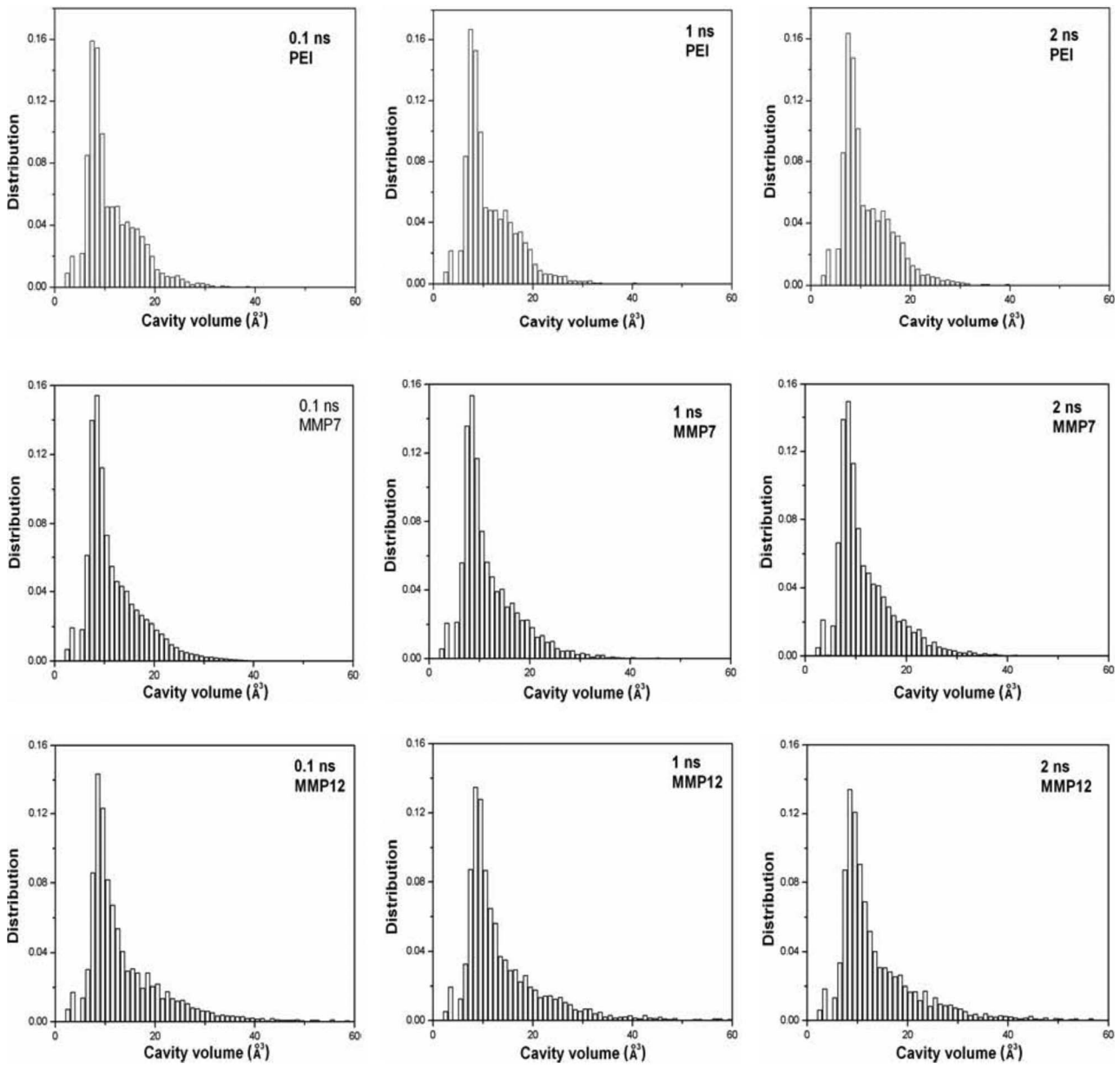

FIG. 6. Time evolution of the cavity volume distributions in PEI and its composites.

CO_2, which are larger than those of CH_4. The fluctuations in the excess chemical potentials are clearly correlated with those of the free-volume fractions shown in Fig. 5.

The computed solubility coefficients are presented in Table II, where, in the case of PEI, they are also compared with the experimental data [50]. In the case of PEI, the computed solubility of CO_2 is about one order of magnitude larger than the measured value, while the computed CH_4 solubility is about a factor of 6 larger the corresponding experimental measurement. The computed ratio is $S_{CO_2}/S_{CH_4} \simeq 8.0$, which should be compred with the measured value of about 3.7. Note that there are some experimental uncertainties in the experimental values of the solubilities, as Henry's law constant, which is derived from fitting experimental sorption isotherm data to the so-called dual-mode sorption model [51], is taken as the experimental value of the solubility. Note also that the difference between the computed and measured solubilities that we are reporting here is about the same as those reported previously [18,19,29].

There are currently no experimental data for MMP7 and MMP12 to compare with our computed values, but as Table II indicates, the polymer composites have much higher gas solubilities than PEI. If we assume that the difference between the computed gases solubilities in MMP7 and MMP12 and the true experimental data (if they were available) are of the same order of magnitude as those for PEI, the results shown in Table II would still indicate gas solubilities in polymer composites that are larger than those in PEI. Since the permeability K of a gas through a membrane is usually defined in terms of its self-diffusivity and solubility, the higher solubilities of the gases in the polymer composites indicate

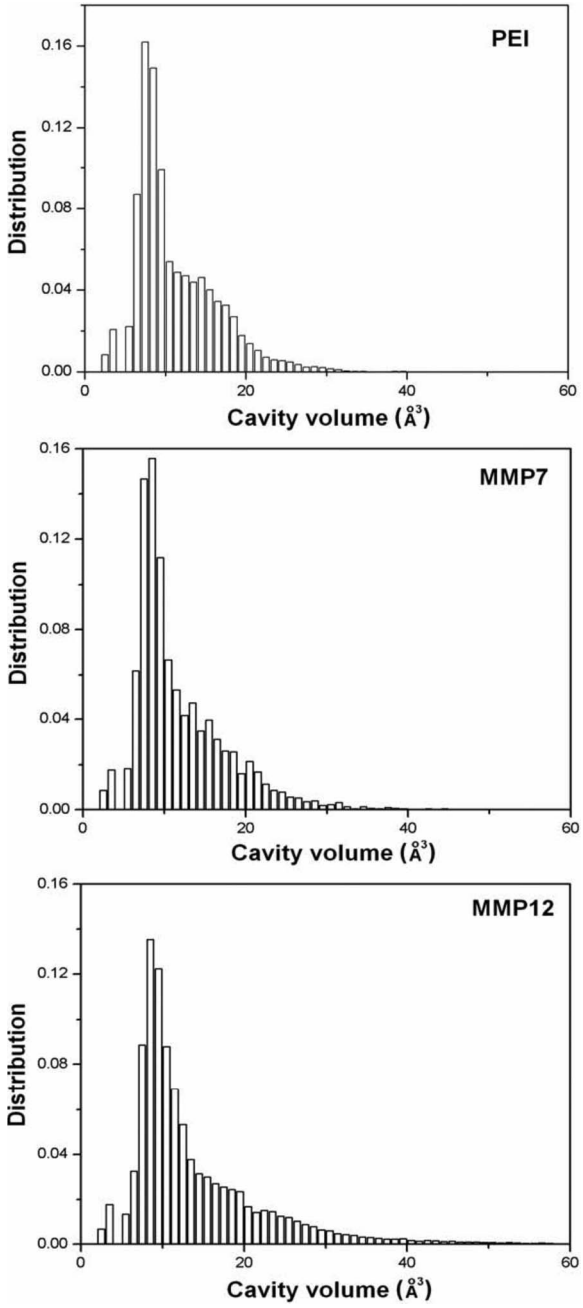

FIG. 7. The distributions of the cavity volumes in PEI and its composites, averaged over 20 realizations.

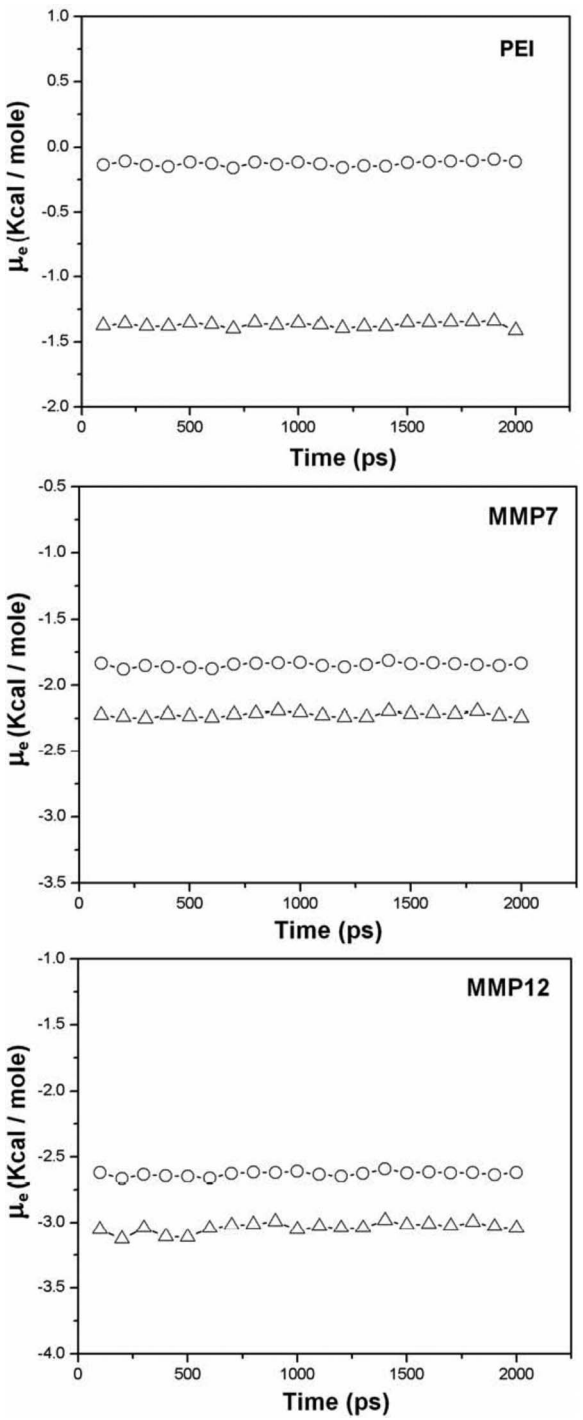

FIG. 8. The excess chemical potentials of CH_4 (circles) and CO_2 (triangles) in the three materials.

that they may also have higher gas permeabilities. We shall return to this point shortly.

We now turn to presenting the results for the self-diffusivities of CO_2 and CH_4. We first note that, in a polymer composite made of one SWCNT and the PEI structure, one would expect the accessible free volume for the diffusion of small gas molecules to be distributed *inhomogeneously* about the long axis of the nanotube. In such a material, the diffusion coefficients may vary *locally*. That is, they will be different if computed for different parts of a polymer composite. The dependence of the diffusivities on the local free-volume fraction may then be described by Doolitles' law

$$D = A \exp\left(-\frac{B}{\eta_{\max} - \eta}\right), \tag{9}$$

or a modification of it [52], where η is the packing fraction of the material with $\eta_{\max}$ being its maximum value, and A and B are constant. In the present work three SWCNTs have been inserted at random into the PEI-structure matrix, which decrease the degree of inhomogeneity about the long axis of any one of them. Therefore, the effective self-diffusivities

TABLE II. Computed and measured solubilities of CH_4 and CO_2.

	PEI		MM7		MM12	
	CO_2	CH_4	CO_2	CH_4	CO_2	CH_4
S (computed)	9.05	1.12	39.05	20.14	149.6	74.95
S (measured)	0.76	0.21				

that we calculate from the slope of the plots of the mean-square displacements (MSDs) versus time should be reasonable indicator of the effect of polymer composites' morphologies on diffusion of small gas molecules through them.

Figures 9 and 10 display, respectively, the ensembles of the gases' trajectories in the simulations cells in the PEI and MMP7 structures, over the length of the simulations. Compared with PEI, the ensemble of the CO_2 trajectories in the MMP7 appears in the form of a large and elongated part of the space which is *around* the nanotubes, rather than a part of the space that include the nanotubes themselves. This is caused by (a) the presence of nanotubes and the squeezing effect that they have on the polymer's morphology (see above) and (b) the depletion phenomenon near the nanotubes. There are also striking differences between the ensembles of the CH_4 trajectories in PEI and MMP7. The enlarged sets of trajectories for both gases also indicate that their effective self-diffusivities in MMP7 (and, hence, MMP12) must be larger than the corresponding values in PEI. As discussed below, this is indeed the case.

To better understand the differences between the trajectories of the two gases in PEI and its composites, we present in Figs. 11 and 12 the time dependence of the displacements $R(t)$ of the two gases in PEI and MMP7, respectively. The fluctuations of $R(t)$ for CO_2 in MMP7 are larger than those in pure PEI by a factor of about 2. Equally striking are the differences between the displacements of CH_4 in PEI and MMP7. While displacements of CH_4 in PEI fluctuate mostly in a narrow band around 3 Å, they vary widely anywhere between 1 and 9 Å in MMP7. The differences are clearly indicative of the restricted morphology of PEI for diffusion of the gases.

These features are all consistent with the hopping mechanism which is often invoked to explain diffusion of small gas

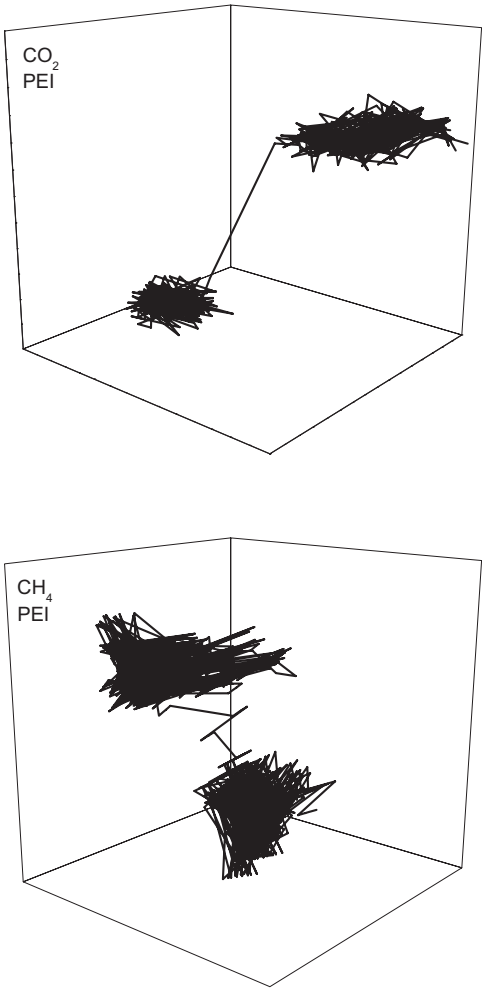

FIG. 9. The ensemble of the trajectories of CO_2 and CH_4 in the PEI structure.

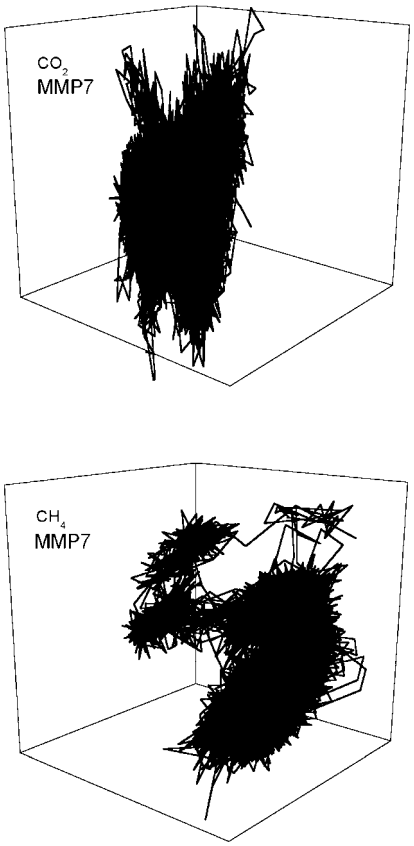

FIG. 10. Same as in Fig. 9, but in the MMP7 structure.

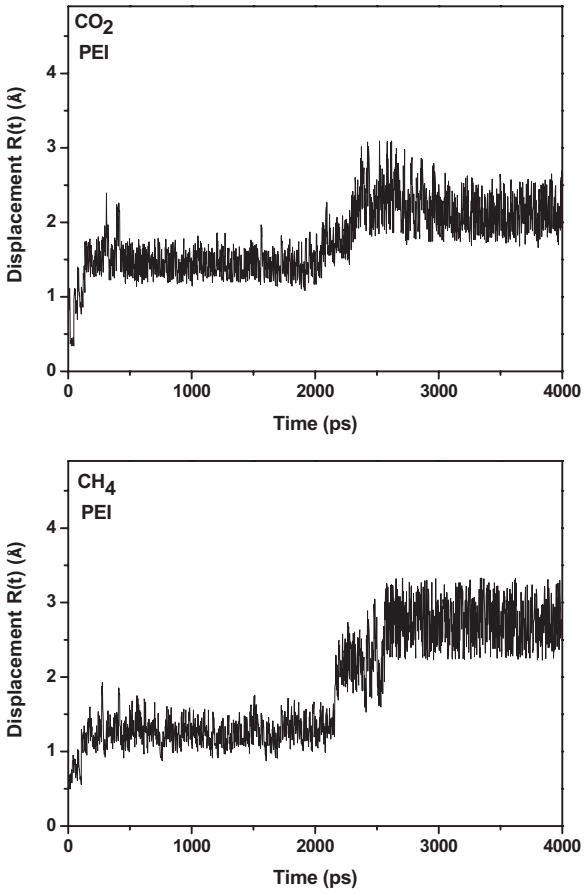

FIG. 11. Time dependence of the displacements of CO_2 and CH_4 from their initial positions in the PEI structure.

molecules in amorphous polymers. According to the hopping mechanism, the gas molecules oscillate in a cavity until the "tunnels" between adjacent cavities are opened, which allows them to hop to the neighboring cavities, provided that they are not already occupied by other gas molecules. The magnitude of the oscillations and the frequency of the hops from one cavity to another depend on the polymer's density and the flexibility of its morphology. In the MD simulations the nanotubes were allowed to be deformable, rather than being rigid structures. Therefore, fluctuations in the deforming nanotubes give rise to increased fluctuations in the PEI chain, hence leading to more frequent hops or jumps of the gas molecules between the cavities. Such fluctuations then explain the larger oscillations and the jump frequencies of the gases in MMP7 (and still larger in MMP12) than those in PEI.

Figures 13 and 14 present the time dependence of the MSDs of the two gases in PEI. In the Fickian regime of diffusion, a plot of log(MSD) versus log(t) must be linear with a slope of 1. Figures 13 and 14 also present such plots, and in both cases the slopes are $\simeq 1$. Moreover, in both cases, the diffusion of the gases reaches the Fickian regime relatively quickly.

The computed self-diffusivities of the two gases in PEI are listed in Table III, along with the experimental data. The computed self-diffusivity of CH_4 is within a factor of 6 of the measured value. As for CO_2, the reported measured self-

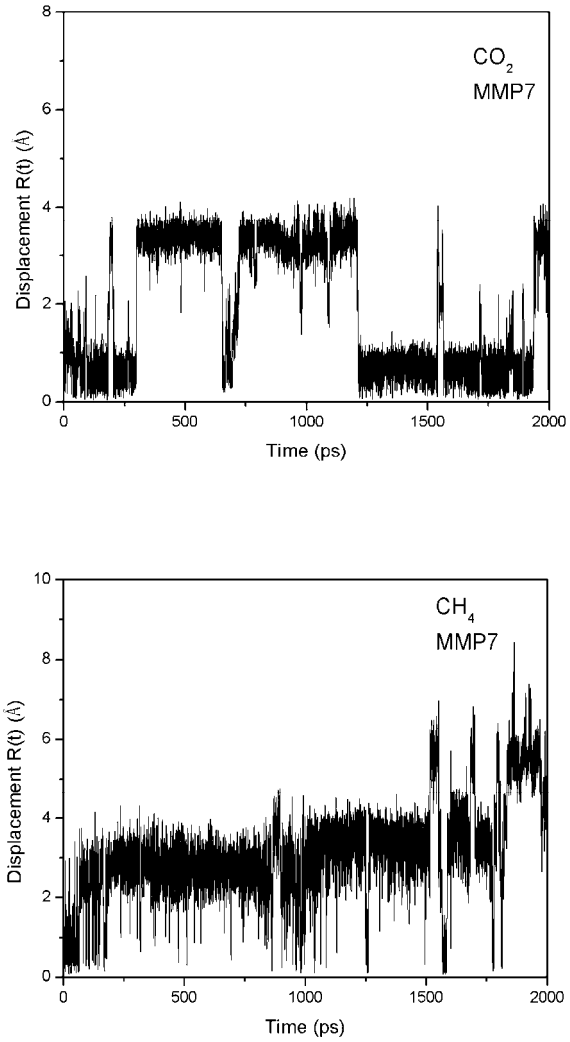

FIG. 12. Same as in Fig. 11, but in the MMP7 structure.

diffusivity of CO_2 in PEI varies by as much as one order of magnitude, ranging (all in cm^2/s) from 11.4×10^{-9} [50] to 7.5×10^{-9} [51] and 1.3×10^{-9} [53]. Therefore, the computed self-diffusivity of CO_2, 5.5×10^{-9} cm^2/s, is just in the middle of the range of the measured values. Given that the parameters of the PC force field have been optimized for accurate representation of the morphology of a class polymers, but not for the transport properties of the gases in them, the agreement between the computed and measured diffusivities of the gases in the PEI is reasonable.

We note one possible qualitative difference between the computed and measured self-diffusivities of the two gases. Whereas the computed self-diffusivities indicate that $D_{CO_2} < D_{CH_4}$, the measured values do not indicate a clear pattern. The two lower measured self-diffusivities reported in the literature [51,53] (see above) are consistent with the pattern of the computed diffusivities, but the highest reported measured self-diffusivity of CO_2 indicates the opposite pattern: namely, that $D_{CO_2} > D_{CH_4}$. This calls for more accurate measurements of the diffusivities in PEI.

As mentioned earlier, we also estimated the self-diffusivities of the two gases in PEI using the (NPT) ensemble. This means that during the MD simulation of the

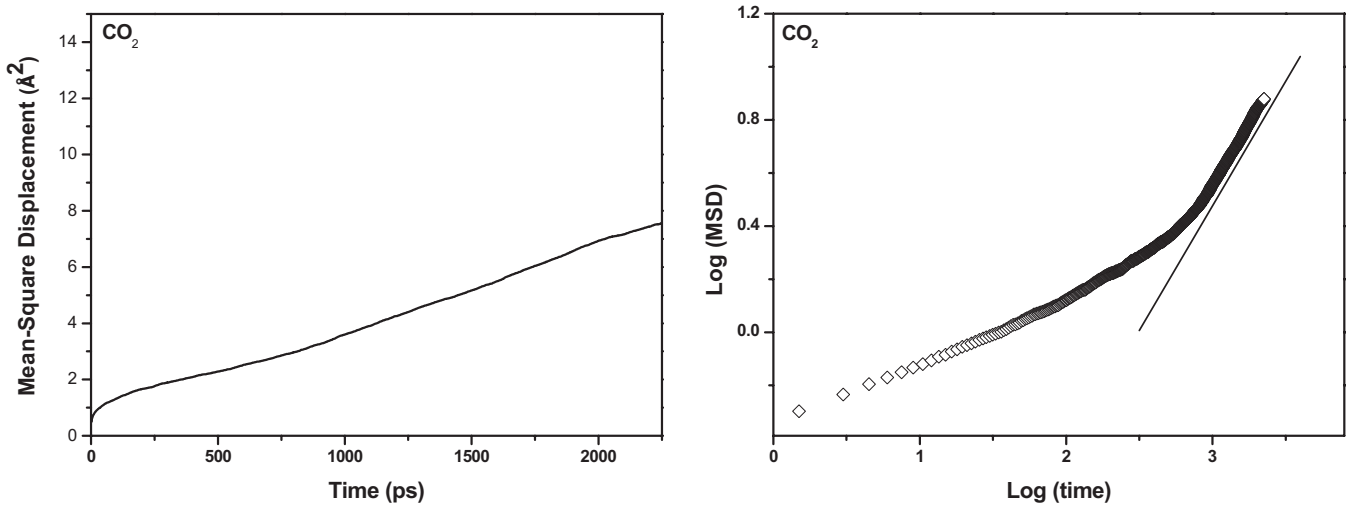

FIG. 13. Time dependence of the MSDs of CO_2 in the PEI structure (left) and its logarithmic plot (right), computed using the (*NPT*) ensemble.

diffusion process the polymer can expand and attain a lower density. Indeed, the density of PEI, which was initially fixed at its experimental value of 1.27 g/cm^3, decreased to, and settled at, 1.19 g/cm^2 after some time, when we carried out the simulations with the (*NPT*) ensemble. Figure 15 presents the resulting MSDs for the two gases obtained with the (*NPT*) ensemble. They result in self-diffusivities that are larger than those reported above, obtained with the (*NVT*) ensemble which holds the volume (and, therefore, the density) of the polymer fixed during the simulations. Such self-diffusivities also indicate that $D_{CO_2} > D_{CH_4}$. One might argue that in an actual experiment in which CO_2 or CH_4 diffuses in a polymer, the volume of the polymer may increase (unless it is somehow prevented from doing so) and, thus, the simulations with the (*NPT*) ensemble might correspond more closely with such an experiment. However, practically all previous MD simulations of the diffusion of gases in various polymers have been carried out in the (*NVT*) ensemble. Moreover, recall that (see above) during the energy minimization and MD simulations of the polymer and the gases' molecules the system is allowed to expand. Thus, we believe that the simulations in the (*NVT*) ensemble are appropriate.

Figure 16 present the time dependence of the MSDs of CO_2 and CH_4 in the two polymer composites, obtained with the (*NVT*) ensemble. The resulting self-diffusivities are also listed in Table III. We are aware of no experimental data for diffusion of the two gases in the two polymer composites. As Table III indicates, the self-diffusivities of both CO_2 and CH_4 in the polymer composites are larger than those in PEI. In particular, the estimated self-diffusivity of CO_2 in MMP12 is larger than in PEI by a factor of more than 2, while that of CH_4 is larger by a factor of about 7. Note that, consistent with the computed self-diffusivities of the two gases in PEI, the ratio D_{CH_4}/D_{CO_2} for the polymer composites is greater than 1. Given the relative accuracy of the gases' effective self-diffusivities in PEI, the results for the polymer composites should also be reasonably accurate.

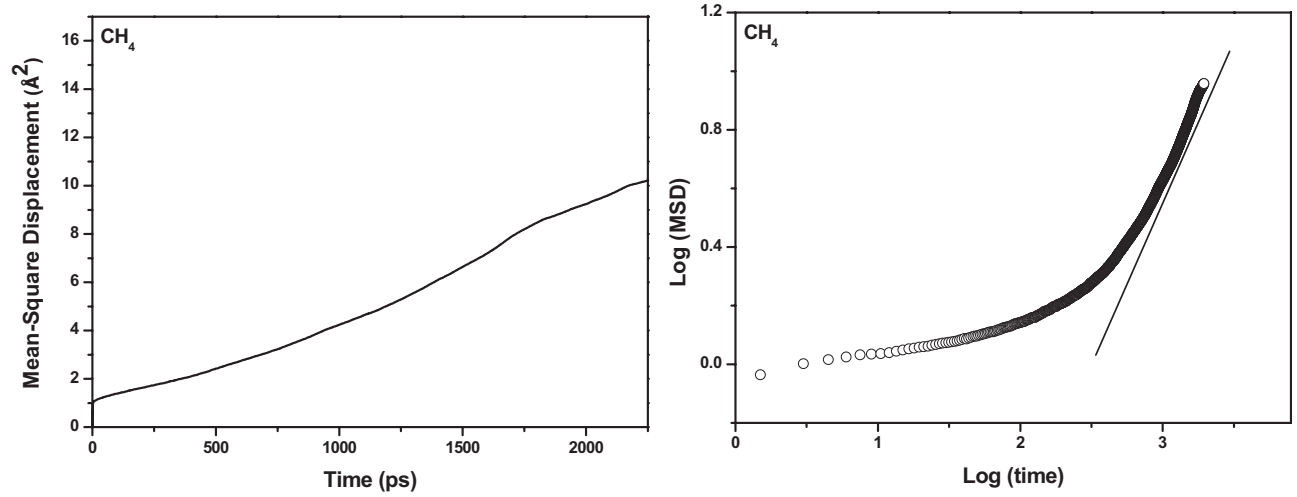

FIG. 14. Same as in Fig. 13, but for CH_4.

TABLE III. Computed and measured self-diffusivities of CH_4 and CO_2, obtained with the (*NVT*) ensemble. All numbers are in cm^2/cs.

	PEI		MM7		MM12	
	CO_2	CH_4	CO_2	CH_4	CO_2	CH_4
$D \times 10^9$ (computed)	5.5	8.0	7.35	16.27	13.73	57.2
$D \times 10^9$ (measured)	1.3–11.4	1.13				

Recall that, as our simulations indicate, the gases' solubilities in the polymer composites, even when we take into account the uncertainties in the computed and measured values, are higher than those in pure PEI (see Fig. 8 and Table II). Then, since the permeability K of a gas through a polymer is defined by

$$K = DS, \tag{10}$$

we may conclude that the polymer composites generated with the carbon nanotubes should have gas permeabilities that are larger than those in PEI by at least a factor of 2–3, when we take into account the uncertainties indicated by Tables II and III. While there are currently no experimental data to compare with our results for polymer composites to confirm our contention, we believe that the results do indicate clearly the possibility of designing MM polymeric membranes, using carbon nanotubes, for gas separation with much improved permeabilities and separation properties than pure polymeric membranes.

It should also be pointed out that in a graphene sheet the conduction and valence bands touch each other at the six corner points of the first Brillouin zone, filled with electrons at the Fermi (highest-)energy level [54,55]. Thus, in general, the sheet behaves as a semimetallic material with a zero band gap. If a nanotube is infinitely long, its electronic states will be parallel lines in the Fourier space. The lines are quantized along the circumference, but continuous along the tube's axis. A (m,n) nanotube can behave as a metallic material if $m=n$, since in this case there are always electronic lines (states) that cross the corner points of the first Brillouin zone. If m-n is *not* a multiple of 3, the electronic states will not pass through the corner points, in which case the nanotube acts as a semiconducting material. But if m-n is a multiple of 3, certain electronic states cross the corner points of the first Brillouin zone, implying that the tube should be semimetallic [55].

Since we have used zigzag $(m,0)$ SWCNTs, the two nanotubes have the two distinct types of electronic properties described above. That is, in the case of the (12,0) nanotube,

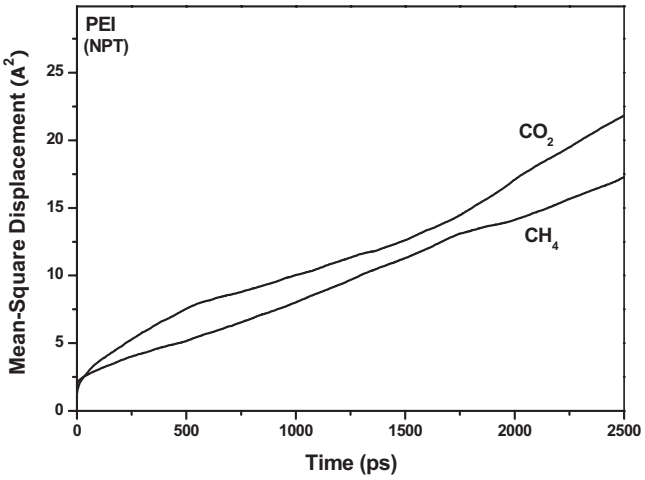

FIG. 15. Time-dependence of the mean-square displacements of CO_2 and CH_4 in the PEI structure, computed using the (*NPT*) ensemble.

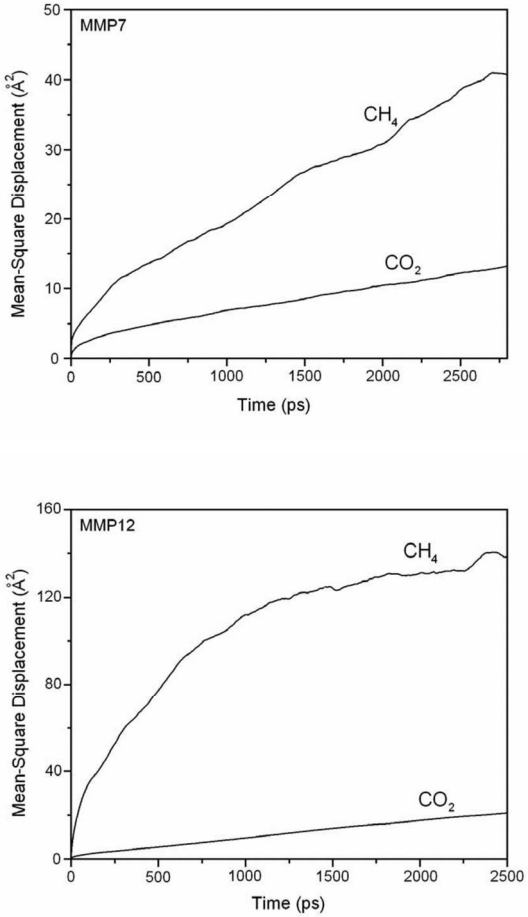

FIG. 16. Time dependence of the MSDs of the two gases in the polymer composites, computing using the (*NVT*) ensemble.

the material is semimetallic, while the (7,0) nanotube should be semiconducting. Thus, it may be that the differences in the diffusion properties of the MM7 and MM12 composites might partly be attributable to the difference between the electronic properties of the two nanotubes. To check this possibility more precisely, one must have a more accurate force field than what we have used in this work. Work in this direction is in progress.

IV. DISCUSSION

In general, one might expect the simple insertion of nanotubes in to a polymer to improve the transport properties of gases through the material, because one might intuitively expect the gas molecules to pass *through* the nanotubes which have smooth potential energy surfaces (provided that their walls are more or less rigid) that give rise to fast transport. However, attributing higher diffusivities to only passages through the nanotubes is naive. The phenomenon is, in fact, far more complex.

First, the nanotubes must have open ends with diameters that are large enough to accomodate the gas molecules. For example, in the present study, the MMP12 material can accomodate both CO_2 and CH_4, as does MMP7 but with somewhat more difficulty.

Second, passage through the nanotube can facilitate transport of the gases through the polymer composite only if either the tubes themselves form percolating paths through the polymer or do so jointly with large cavities (which, however, fluctuate in time). In the present study, we inserted only three SWCNTs in the polymer, hardly enough to form percolating paths for gas transport (see Fig. 2).

Third, if the nanotubes are inserted in the polymer matrix in such a way that the gas molecules can hardly access them (a percolation effect), then no significant improvement in the performance of the MM polymer should be expected, unless the nanotubes can induce creation of larger accessible free volume fraction in the polymer, which is the case here.

The fourth, and perhaps most important, aspect of this phenomenon is that the gas molecules may become essentially trapped in the cavities dispersed in the polymer matrix that originate from entanglement of a polymer chain for periods of time that can be quite long (see Figs. 11 and 12). Therefore, improvement in the performance of the polymer matrix for gas transport depends (in addition to the polymer's density and morphology) on how much the nanotubes can squeeze the polymer matrix to induce fluctuations in its morphology, leading to the creation of large cavities (see above).

It is well known that the transport and solubility of small-size gas molecules are significantly affected by the free-volume distribution in amorphous polymers. It is, of course, of great interest to correlate the free volumes with the self-diffusivities and solubilities. There have been many efforts in the past to determine the free-volume distributions by experimental techniques, such as positron annihilation lifetime spectroscopy (PALS) and photochromic and spin probe methods. In particular, PALS has emerged as a powerful technique, since it provides one with direct and detailed information on the free volume. For example, Hofmann *et al.* [56] compared the results of molecular simulations with the PALS measurements of highly permeable poly(1-(trimethylsilyl)-1-propyne) and moderately permeable polystyrene derivatives, while Nagel *et al.* [57] made the same comparison for polyimide. Dong and Jacob [58] investigated the effect of molecular orientation on the free volume of polyethylene using the Voronoi tessellation technique described above, while Dammert *et al.* [59] studied the relation between the tacticity and free volume of polystyrene by PALS and Voronoi tessellation. It would be of great interest to prepare polymer composites of the type modeled in the present paper and measure the self-diffusivities and solubilities of gases in them in order to confirm the results of the MD simulations reported here.

V. SUMMARY

Atomistic simulations were used to generate models of amorphous polyetherimide and mixed-matrix PEI by inserting carbon nanotubes into a pure polymer. The self-diffusivities of CO_2 and CH_4 in PEI and its mixed-matrix composites at 300 K were estimated using molecular dynamics simulations. In the presence of nanotubes and their repulsive interactions with PEI, there are larger fluctuations in the free-volume distributions of the composites. This is partly reflected in the distributions of the cavity sizes in the PEI, when carbon nanotubes are inserted into it, which take on sharply peaked shapes, but with a few large cavities created in the polymer. As a result, the self-diffusivities of the gases in the mixed-matrix polymers are higher than those in pure PEI.

The solubility coefficients of CO_2 and CH_4 in PEI and its mixed-matrix versions were also computed using molecular simulations. The polymer composites also have higher gas solubilities than PEI, hence indicating that a mixed-matrix polymer that consists of a polymer and carbon nanotubes will have much improved gas permeabilities and separation properties for gaseous mixtures than the original polymer itself.

Clearly, more extensive simulations are needed in order to draw more quantitative conclusions. In particular, one should systematically change the number of nanotubes and also use chiral nanotubes, as opposed to the zigzag ones used in the present study, in order to study their effects. The use of a more accurate force field for representing the nanotubes would also be desirable, as would a study of the diffusion of gases of various sizes in composites. Work on these aspects is in progress.

We note, however, that a recent theoretical study by Hill [60] also indicated that the gases' permeabilities and diffusivities in composite polymeric membranes should be larger than those in a pure polymer. Hill attributed this effect, as we do, to the replusive interactions between the polymer and the

inserted particles. Thus, we believe that the qualitative aspects of our results will remain unchanged, even if more acurate force fields are used. But this assertion remains to be confirmed.

ACKNOWLEDGMENTS

We are grateful to the National Science Foundation, the Department of Energy, and the California Energy Commission for partial support of the work reported in this paper.

[1] *Access in Nanoporous Materials*, edited by T. J. Pinnavaia and M. F. Thorpe (Plenum, New York, 1995).
[2] R. T. Yang, *Gas Separation by Adsorption Processes* (Butterworths, Boston, 1987).
[3] M. Sahimi, Rev. Mod. Phys. **65**, 1393 (1993); *Flow and Transport in Porous Media and Fractured Rock* (VCH, Weinheim, 1995).
[4] J. E. Koresh and A. Sofer, Sep. Sci. Technol. **18**, 723 (1983); C. Bourgerette, A. Oberlin, and M. Inagaki, J. Mater. Res. **7**, 1158 (1992); Y. Hishyama, A. Yoshida, Y. Kaburagi, and M. Inagaki, Carbon **30**, 333 (1992).
[5] C. W. Jones and W. J. Koros, Carbon **32**, 1427 (1994); Ind. Eng. Chem. Res. **34**, 158 (1994); **34**, 164 (1994).
[6] M. B. Shiflett and H. C. Foley, Science **285**, 1902 (1999).
[7] M. G. Sedigh, W. J. Onstat, L. Xu, W. L. Peng, T. T. Tsotsis, and M. Sahimi, J. Phys. Chem. A **102**, 8580 (1998); M. G. Sedigh, L. Xu, T. T. Tsotsis, and M. Sahimi, Ind. Eng. Chem. Res. **38**, 3367 (1999); M. G. Sedigh, M. Jahangiri, P. K. T. Liu, M. Sahimi, and T. T. Tsotsis, AIChE J. **46**, 2245 (2000).
[8] H. Qariouh, R. Schue, F. Schue, and C. Bailly, Polym. Int. **48**, 171 (1999).
[9] M. Sahimi and T. T. Tsotsis, in *Handbook of Theoretical and Computational Nanotechnology*, edited by M. Rieth and W. Schommers (American Scientific, New York, 2006), Chap. 10.
[10] L. D. Gelb, K. E. Gubbins, R. Radhakrishna, and M. Sliwinska-Bartkowiak, Rep. Prog. Phys. **62**, 1573 (1999).
[11] J. Ghassemzadeh, L. Xu, T. T. Tsotsis, and M. Sahimi, J. Phys. Chem. B **104**, 3892 (2000); J. Ghassemzadeh and M. Sahimi, Mol. Phys. **102**, 1447 (2004).
[12] L. Xu, M. Sahimi, and T. T. Tsotsis, Phys. Rev. E **62**, 6942 (2000); L. Xu, T. T. Tsotsis, and M. Sahimi, J. Chem. Phys. **114**, 7196 (2001).
[13] S. Y. Lim, T. T. Tsotsis, and M. Sahimi, J. Chem. Phys. **119**, 496 (2003).
[14] D. Q. Vu, W. J. Koros, and S. J. Miller, J. Membr. Sci. **211**, 311 (2003); **211**, 335 (2003); R. Mahajan and W. J. Koros, Polym. Eng. Sci. **42**, 1420 (2002).
[15] Q. Wang, S. R. Challa, D. S. Sholl, and J. K. Johnson, Phys. Rev. Lett. **82**, 956 (1999); S. R. Challa, D. S. Sholl, and J. K. Johnson, Phys. Rev. B **63**, 245419 (2001); J. Chem. Phys. **116**, 814 (2002).
[16] Z. Mao, A. Garg, and S. B. Sinnott, Nanotechnology **10**, 273 (1999); A. I. Skoulidas, D. M. Ackerman, J. K. Johnson, and D. S. Sholl, Phys. Rev. Lett. **89**, 185901 (2002).
[17] Y. Tamai, H. Tanaka, and K. Nakanishi, Macromolecules **27**, 4498 (1994); **28**, 2544 (1995).
[18] L. Fritz and D. Hofmann, Polymer **38**, 1035 (1997).
[19] F. Muller-Plathe, J. Membr. Sci. **141**, 147 (1998).
[20] S. G. Charati and S. A. Stern, Macromolecules **31**, 5529 (1998).
[21] T. R. Cutherbert, N. J. Wagner, M. E. Paulatis, G. Murgia, and B. D'Auanno, Macromolecules **32**, 5017 (1999).
[22] N. F. A. van der Vergt, W. J. Briels, M. Wessling, and H. Strathmann, J. Chem. Phys. **105**, 8849 (1996).
[23] P. V. Krishna Pant and R. H. Boyd, Macromolecules **26**, 679 (1993); R. K. Bharadwaj and R. H. Boyd, Polymer **40**, 4229 (1999).
[24] R. Zhang and W. L. Mattice, J. Membr. Sci. **108**, 15 (1995).
[25] D. Hofmann, L. Fritz, J. Ulbrich, and D. Paul, Polymer **38**, 6145 (1997); D. Hofmann, L. Fritz, J. Ulbrich, and C. Scherpers, Macromol. Theory Simul. **9**, 293 (2000).
[26] J. R. Fried, M. Sadad-Akhavi, and J. E. Mark, J. Membr. Sci. **149**, 115 (1998); J. R. Fried and D. K. Goyal, J. Polym. Sci., Part B: Polym. Phys. **36**, 519 (1998).
[27] F. Muller-Plathe and W. F. van Gunsteren, J. Chem. Phys. **103**, 4745 (1995); F. Muller-Plathe, H. Liu, and W. F. van Gunsteren, Comput. Theor. Polym. Sci. **139**, 1 (1998).
[28] D. A. Mooney and J. M. D. MacElroy, J. Chem. Phys. **110**, 11087 (1999).
[29] C. Wei, D. Srivastava, and K. Cho, Nano Lett. **2**, 647 (2002).
[30] Y. Han and J. Elliot, Comput. Mater. Sci. **39**, 315 (2007).
[31] E. Tocci, D. Hofmann, D. Paul, N. Russo, and E. Drioli, Polymer **42**, 521 (2001).
[32] M. M. Ostwal, T. T. Tsotsis, and M. Sahimi, J. Chem. Phys. **126**, 124903 (2007).
[33] D. N. Theodorou and U. W. Suter, Macromolecules **18**, 1467 (1985).
[34] S. Nosé, J. Chem. Phys. **81**, 511 (1984); W. G. Hoover, Phys. Rev. A **31**, 1695 (1985).
[35] H. C. Andersen, J. Chem. Phys. **72**, 2384 (1980).
[36] H. Sun, S. J. Mumby, J. R. Maple, and A. T. Hagler, J. Am. Chem. Soc. **116**, 2978 (1994).
[37] N. Kim, Y. Kim, T. T. Tsotsis, and M. Sahimi, J. Chem. Phys. **122**, 214713 (2005); N. Kim, A. Harale, T. T. Tsotsis, and M. Sahimi, *ibid.* (to be published).
[38] A. R. Mehrabi and M. Sahimi, Phys. Rev. Lett. **82**, 735 (1999).
[39] L. Greengard and V. I. Rokhlin, Chem. Scr. **29A**, 139 (1989); H.-Q. Ding, N. Karasawa, and W. A. Goddard III, J. Chem. Phys. **97**, 4309 (1992).
[40] H. Cheng, G. P. Pez, and A. C. Cooper, J. Am. Chem. Soc. **123**, 5845 (2001).
[41] Z. Mao and S. B. Sinnott, J. Phys. Chem. B **104**, 4618 (2000); **105**, 6916 (2001).
[42] D. W. Brenner, Phys. Rev. B **42**, 9458 (1990); J. Che, T. Cagin, and W. A. Goddard III, Theor. Chem. Acc. **102**, 346 (1999).
[43] M. K. Kostov, H. Cheng, A. C. Cooper, and G. P. Pez, Phys. Rev. Lett. **89**, 146105 (2002).
[44] M. J. Hwang, T. P. Stockfisch, and A. T. Hagler, J. Am. Chem. Soc. **116**, 2515 (1994).
[45] W. A. Steele, Langmuir **12**, 145 (1996).

[46] J. Vrabec and J. Fischer, AIChE J. **43**, 212 (1997).
[47] L. Xu, M. G. Sedigh, M. Sahimi, and T. T. Tsotsis, Phys. Rev. Lett. **80**, 3511 (1998); L. Xu, T. T. Tsotsis, and M. Sahimi, J. Chem. Phys. **111**, 3252 (1999); L. Xu, M. G. Sedigh, T. T. Tsotsis, and M. Sahimi, *ibid.* **112**, 910 (2000).
[48] M. Tanemura, T. Ogawa, and N. Ogita, J. Comput. Phys. **51**, 191 (1983).
[49] B. Widom, J. Chem. Phys. **39**, 2808 (1963).
[50] T. A. Barbari, W. J. Koros, and D. R. Paul, J. Polym. Sci., Part B: Polym. Phys. **26**, 709 (1988); **26**, 729 (1988).
[51] H. Kumazawa, J. S. Wang, T. Fukuda, and E. Sada, J. Membr. Sci. **93**, 53 (1994).
[52] J. Budzien, J. D. McCoy, and D. B. Adolf, J. Chem. Phys. **119**, 9269 (2003). One may also consider the Cohen-Turnbull statistical mechanical theory according to which $D=A\exp(-Bv_m/v_f)$, where A and B are constants, v_m is the minimum free volume required for a diffusing molecule to escape its cage of neighboring atoms, and v_f is the available free volume per volume of occupying element; see M. H. Cohen and D. Turnbull, *ibid.* **31**, 1164 (1959).
[53] C. Uriarte, J. Alfageme, and J. J. Iruin, Eur. Polym. J. **34**, 1405 (1998).
[54] M. S. Dresselhaus, G. Dresselhaus, and P. C. Ekland, *Science of Flurenes and Carbon Nanotubes* (Academic Press, San Diego, 1996).
[55] N. Hamada, S.-I. Sawada, and A. Oshiyama, Phys. Rev. Lett. **68**, 1579 (1992); X. Blase, L. X. Benedict, E. L. Shirley, and S. G. Louie, *ibid.* **72**, 1878 (1994).
[56] D. Hofmann, M. Heuchel, Y. Yampolskii, V. Khotimskii, and V. Shantarovich, Macromolecules **35**, 2129 (2002).
[57] C. Nagel, E. Schimidtke, K. Gönther-Schade, D. Hofmann, D. Fritsch, T. Strunskus, and F. Faupel, Macromolecules **33**, 2242 (2000).
[58] H. Dong and K. I. Jacob, Macromolecules **36**, 8881 (2003).
[59] R. M. Dammert, S. L. Maunu, F. H. K. Maurer, I. M. Neelov, S. Nielmelä, F. Sundholm, and C. Wästlund, Macromolecules **32**, 1930 (1999).
[60] R. J. Hill, Phys. Rev. Lett. **96**, 216001 (2006).

Available online at www.sciencedirect.com
ScienceDirect
Journal of Membrane Science 316 (2008) 73–79
journal of MEMBRANE SCIENCE
www.elsevier.com/locate/memsci

A novel sacrificial interlayer-based method for the preparation of silicon carbide membranes

Bahman Elyassi, Muhammad Sahimi, Theodore T. Tsotsis *

Mork Family Department of Chemical Engineering & Materials Science, University of Southern California, Los Angeles, CA 90089-1211, USA

Received 3 July 2007; received in revised form 14 September 2007; accepted 18 September 2007
Available online 29 September 2007

Abstract

A novel method is presented based on the use of sacrificial interlayers for the preparation of nanoporous silicon carbide membranes. It involves periodic and alternate coatings of polystyrene sacrificial interlayers and silicon carbide pre-ceramic layers on the top of slip-casted tubular silicon carbide supports. Membranes prepared by this technique exhibit single gas ideal separation factors of helium and hydrogen over argon in the ranges 176–465 and 101–258, respectively, with permeances that are typically two to three times higher than those of silicon carbide membranes prepared previously by the more conventional techniques. Mixed-gas experiments with the same membranes indicate separation factors as high as 117 for an equimolar H_2/CH_4 mixture. We speculate that the improved membrane characteristics are due to the sacrificial interlayers filling the pores in the underlying structure and preventing their blockage by the pre-ceramic polymer. The new method has good promise for application to the preparation of a variety of other inorganic microporous membranes.

Keywords: Silicon carbide membrane; AHPCS; Slip-coating; Dip-coating; Gas separation; Polystyrene sacrificial interlayers

1. Introduction

The increased interest in the efficient production of hydrogen, and in environmentally benign power generation, is driving current development efforts on the preparation of microporous, hydrogen-permselective, inorganic membranes, which can be used in the processes (related to H_2 production and power generation) that take place at high temperatures and pressures. The preparation of a promising new type of microporous membrane with a –[Si–C]– backbone has attracted much attention [1–14]. Such membranes show promise for overcoming some of the challenges faced by the current inorganic membranes, which include questionable hydrothermal stability (e.g., SiO_2 and zeolite membranes), high cost and sensitivity to sulfur poisoning (Pd and Pd-alloys), and poor resistance to oxidizing environments (carbon molecular-sieve membranes). Two different approaches have been utilized for the preparation of such membranes, the first involving the use of chemical-vapor deposition (CVD)/chemical-vapor infiltration (CVI) techniques, the other involving the pyrolysis of polymeric, pre-ceramic precursors.

Ciora et al. [1] were the first to report on the preparation of microporous SiC membranes using CVD. Prior to their effort other researchers also reported the preparation of porous SiC membranes by deposition from the vapor phase. They included Takeda et al. [2] who prepared such membranes by CVI, using SiH_2Cl_2 and C_2H_2 diluted with H_2, and γ-Al_2O_3 tubes as supports, Pages et al. [3] who prepared Si:C:H membranes on alumina supports using plasma-enhanced CVD of diethylsilane, and Sea et al. [4] who prepared a SiC membrane (using an α-alumina tube as support) by CVD of $(C_3H_7)_3SiH$ (tri-isopropylsilane or TPS) at 700–750 °C. The membranes from these groups showed mostly Knudsen-type transport and no permselectivity towards hydrogen, however. In our own studies [1], we utilized two different precursors to prepare membranes on γ-Al_2O_3 tubular supports, namely, $CH_3SiH_2CH_2SiH_3$ (1,3-disilabutane or DSB) and TPS. Both precursors produced microporous, hydrogen permselective membranes. The DSB-derived membranes, though thermally stable, did not fare well in the presence of high-temperature steam, proving unstable. The TPS-derived SiC membranes, on the other hand, in addition to

* Corresponding author. Tel.: +1 213 740 2069; fax: +1 213 740 8053.
E-mail address: tsotsis@usc.edu (T.T. Tsotsis).

0376-7388/$ – see front matter © 2007 Elsevier B.V. All rights reserved.
doi:10.1016/j.memsci.2007.09.044

having a high He/N_2 ideal selectivity, proved also stable in the presence of high-pressure (1–3 bar) and temperature (<750 °C) steam. However, the preparation procedure using TPS involves multiple steps, and requires a high temperature (1000 °C) post-treatment [1], which is costly and places stringent requirements on the end-seals and membrane housing during the CVD/CVI process. Furthermore, the high temperature post-treatment modifies the membrane pore structure, making it difficult to predict and to control final product quality; from the membrane manufacturing standpoint, this diminishes the advantage of the on-line control of the CVD/CVI technique.

In tandem with the TPS CVD/CVI method, we also pursued [1] a dip-coating technique through the pyrolysis of allylhydridopolycarbosilane (AHPCS), a partially allyl-substituted hydridopolycarbosilane (HPCS). HPCS and AHPCS both produce a SiC-based ceramic [15,16]. AHPCS was chosen because it is curable in the presence of inert gases, rather than oxygen, as required for other PCS polymers (the allyl groups also make the polymer cross-linkable at lower temperatures). This is important, since curing in oxygen introduces Si–O–C linkages in the resulting ceramics, which have proven to be thermally and hydrothermally unstable. Prior to our report, other investigators had reported the preparation of SiC-based membranes by the pyrolysis of PCS and polysilanes. In an early effort, Morooka and co-workers [6,7] pyrolyzed PCS, cured in oxygen, to prepare Si–O–C membranes on alumina substrates, using polystyrene (PS) as a pore former. A membrane prepared with 1% PS in PCS had a H_2 permeance of 4×10^{-8} mol m^{-2} s^{-1} Pa^{-1}, and an ideal H_2/N_2 selectivity of 20 at 773 K, but proved unstable when heated in Ar at 1223 K, or exposed to steam at 773 K. Lee and Tsai [8,9] prepared Si–O–C membranes by the pyrolysis of polydimethylsilane (the PMS layer was subjected to a thermolytic reaction at 733 K in Ar, followed by O_2 curing at 473 K, and finally pyrolyzed at various temperatures from 523 to 1223 K). Membranes pyrolyzed at 873 K had the highest separation characteristics (membranes prepared at the higher temperatures were not microporous), exhibiting a H_2 permeance of $\sim 2.7 \times 10^{-9}$ mol m^{-2} s^{-1} Pa^{-1}, and an ideal H_2/N_2 selectivity of 20 at 473 K. PMS-derived membranes prepared in an autoclave under a N_2 atmosphere at low temperatures were also microporous, but proved unstable to the exposure to steam [10]. Most recently, Wach et al. [11,12] prepared Si–O–C membranes by the pyrolysis of a blend of PCS and polyvinylsilane on porous alumina substrates by radiation curing in the presence of oxygen. Their membrane indicated a H_2 permeance of $\sim 3 \times 10^{-9}$ mol m^{-2} s^{-1} Pa^{-1} and ideal (H_2/N_2) and (He/N_2) selectivities of 206 and 241 at 250 °C, respectively [11].

The membrane prepared by AHPCS pyrolysis possessed a H_2 permeance in the range 10^{-8}–10^{-7} mol m^{-2} s^{-1} Pa^{-1}, and had an ideal separation factor of about 20 for He/N_2 at 200 °C [1]. They proved thermally stable, but the AHPCS-derived membranes did not fare well in the presence of high temperature steam, proving unstable. Since that early study [1], two other groups also prepared membranes by pyrolysis of PCS-type pre-ceramic polymers cured in the absence of O_2. Suda et al. prepared [13] SiC membranes by dip-coating PCS on α-alumina tubes (for cross-linking they used *p*-diethynylbenzene and 1-3 divinyltetramethyldisiloxane and, as in the earlier studies by Morooka and co-workers [6,7], PS was also used as the pore former for some of the membranes). Their cross-linked PCS-derived SiC membranes exhibited ideal separation factors of 90–150 for H_2/N_2, and H_2 permeance in the range of $(1–3) \times 10^{-8}$ mol m^{-2} s^{-1} Pa^{-1} at 373 K. Nagano et al. [14] prepared SiC membranes by dip-coating of PCS on γ-alumina supports, and reported H_2 permeance of about 10^{-7} mol m^{-2} s^{-1} Pa^{-1}, and an ideal separation factor of 8–12 for H_2/N_2 at 873 K.

The studies discussed so far reported only single-gas permeation data, and (other than the membranes prepared by CVD of TPS [1]) when tested in steam, the membranes were shown to be unstable. In a recent paper [17], we reported significant improvements in the preparation of amorphous SiC-based membranes by the pyrolysis of AHPCS films coated on tubular SiC porous supports, using a combination of slip-casting and dip-coating techniques. Combining slip-casting with dip-coating significantly improved the reproducibility in preparing high quality membranes. The membranes prepared had ideal H_2/CO_2 and H_2/CH_4 selectivities in the ranges 42–96 and 29–78, respectively. Mixed-gas separation factors measured using equimolar binary mixtures were close to the ideal selectivities. Steam-stability experiments with the membranes lasting 21 days, using an equimolar flowing mixture of He/H_2O at 200 °C, indicated some initial decline in the permeance of He, after which the permeance became stable at such conditions.

In this paper, we report further progress in the development of AHPCS-derived amorphous SiC membranes. We have utilized in the preparation of these membranes PS sacrificial interlayers with the goal of increasing the membrane permeance, but without negatively impacting the membrane separation characteristics. As noted above, previously, other researchers employed PS as a pore-forming agent (mixed in the PCS prior to layer formation) to increase the hydrogen permeance [6,7,13]. This was attributed to phase separation and formation of PS domains during pyrolysis [7,13,18] to form mesoporous and macroporous regions, and potentially membrane defects. The resulting membranes had, as a result, a lower separation factor. On the other hand, the membranes reported in the present study have both an improved membrane permeance and also a higher separation factor.

Sacrificial layers to prepare microporous inorganic membranes have been previously utilized to prepare silica and zeolite membranes. Gavalas and co-workers, for example, formed [19,20] a carbon barrier layer (by polymerization and carbonization of furfuryl alcohol) inside the support pores during the preparation of silica and zeolite ZSM-5 membranes. Hedlund et al. used [21,22] wax as a masking layer against infiltration of precursors into the support for preparing MFI membranes. In these studies, the stated role of the sacrificial layer was to prevent infiltration of the membrane layer into the underlying porous support in order to reduce the membrane thickness, and also to prevent crack formation. Though preventing film penetration into the underlying porous structure is also one of the roles that the PS sacrificial layers potentially play during SiC membrane preparation, their role during membrane formation is likely more

complex, as PS has been shown previously [18] to impact not only the cross-linking process, but also the formation of the three-dimensional (3D) pore structure during PCS pyrolysis. The key goal of this paper is to introduce this new preparation technique, which could potentially be used to prepare other asymmetric inorganic membranes.

2. Experimental

Ultra-high purity gases (He, H_2, Ar, CO_2, from Glimore Liquid Air Company, and CH_4 from Specialty Air Technologies, Inc.) were used in the experiments. Porous SiC support tubes were prepared using uniaxial cold-pressing of β-SiC powder (HSC059, provided by Superior Graphite Co., with an average particle size of 0.6 μm), together with appropriate sintering aids. For sintering, the green samples were heated at a temperature of 1700 °C, where they were kept in a furnace (Thermal Technology Inc., Model 1000-3060-FP20) for 3 h in flowing He. After sintering, the samples were cooled down to room temperature (with a cooling rate of 3 °C/min). The resulting tubes, shown in Fig. 1, had dimensions of 40 mm × 12 mm, with a thickness of 3 mm. The Archimedes method was used to measure the porosities of the supports, and their average pore size was estimated through permeation measurements. Further details about the sintering characteristics of various SiC powders, and the preparation and characterization of porous membrane supports were presented elsewhere [17,23].

The support tubes used in the membrane preparation were treated in flowing synthetic air at 450 °C (with the purpose of oxidizing any potential contaminants present), sonicated several times in acetone, and then dried prior to membrane film deposition. The dip-coating solution was prepared by dissolving 10 wt% of AHPCS (SMP-10, Starfire Systems, Inc.) in hexane. In order to prepare the slip-casting solution, the 0.6 μm SiC powder was mixed with acetone, and the lighter particles floating on the solution top were separated and dried. Scanning electron microscopy (SEM, Cambridge 360) observations of the particles indicated that their size was mostly in the range of 100–200 nm, which is close to the mean pore diameter of the support, as obtained from the permeation data (see Section 3.1). The slip-casting solution consisted of 5 wt% of the SiC particles intermixed in the dip-coating solution. In our prior paper [17], the slip-casting solution contained a larger concentration of particles (10% vs. 5%). We found, however, that decreasing the concentration of the particles in the slip-casting solution down to this lower level did not impact adversely the quality of the final membrane layers using the sacrificial layer approach.

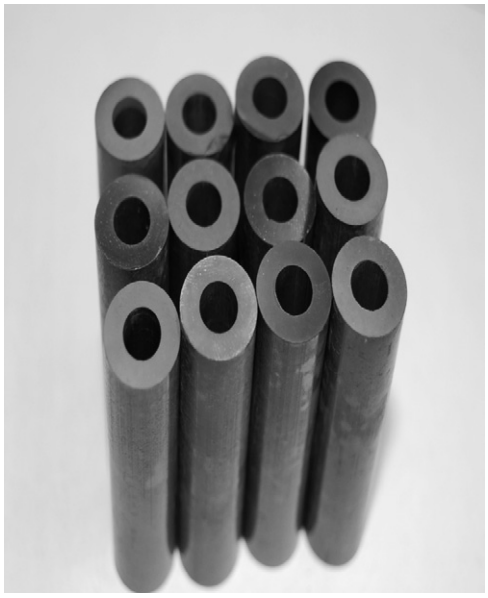

Fig. 1. SiC tubular supports sintered at 1700 °C for 3 h.

Slip-casting was used to coat the first layer on the outer surface of the support tubes. To prepare this layer, the tubes were placed in the slip-casting solution for 12 s and, then, drawn out of the solution at a speed of 0.25 mm/s. The coated tubes were heated in flowing Ar in a tube furnace (Lindberg/Blue, Model STF55433C) at a rate of 2 °C/min, first to 200 °C, where they were kept for 1 h, then to 400 °C, where they were also kept for 1 h, and finally to 750 °C, where they were kept for an additional 2 h. Subsequently, they were cooled down to room temperature in flowing Ar with a cooling rate of 3 °C/min. The reason for the relatively slow heating (and holding at 200 °C) is that we have found [17], as have others [13,15], that using such heating rates and treatment at lower temperatures result, generally, in better cross-linked amorphous SiC materials [15], and membranes with higher hydrogen permeabilities [13].

Subsequently, the membranes were dip-coated in a solution of 1 wt% of polystyrene (GPC grade, $M_w = 2500$, Scientific Polymers Products, Inc.) in toluene. For the PS coating, a dip-coating time of 12 s and a drawing rate of 0.58 mm/s were applied. After drying the PS layer at 100 °C for 1 h, the membranes were dip-coated in a 10 wt% of AHPCS in hexane solution, with a dip-coating time of 12 s and a drawing rate of 2 mm/s. In order to prevent significant dissolution of the formed polystyrene barrier layer into the AHPCS dip-coating solution, the solvent utilized for the solution must not dissolve the PS layer neither during dip-coating nor afterwards. The choice of hexane as the solvent for AHPCS was, therefore, due to polystyrene showing no substantial solubility in hexane.

Following the coating of the AHPCS solution, the membranes were pyrolyzed at 750 °C for 2 h in Ar, following the same heat treatment protocol used for the preparation of the slip-casted tubes. A schematic of the preparation process is shown in Fig. 2. After the pyrolysis, three additional layers of PS and AHPCS were coated on the support (first the PS layer, followed by the AHPCS layer, etc.) with the same dipping protocol. After each dual layer (PS + AHPCS) deposition, the membrane was pyrolyzed under the same conditions used for the pyrolysis of the first dual-layer.

After coating and pyrolysis of the final dual-layer, the membranes were treated in flowing synthetic air for 2 h at 450 °C, with the purpose of oxidizing any potential carbon-based residues resulting from the preparation process (low-temperature air oxidation has been shown to be effective in removing minute amounts of carbon, for example as a common way for carbon nanotube purification [24–26]). Though AHPCS has been shown

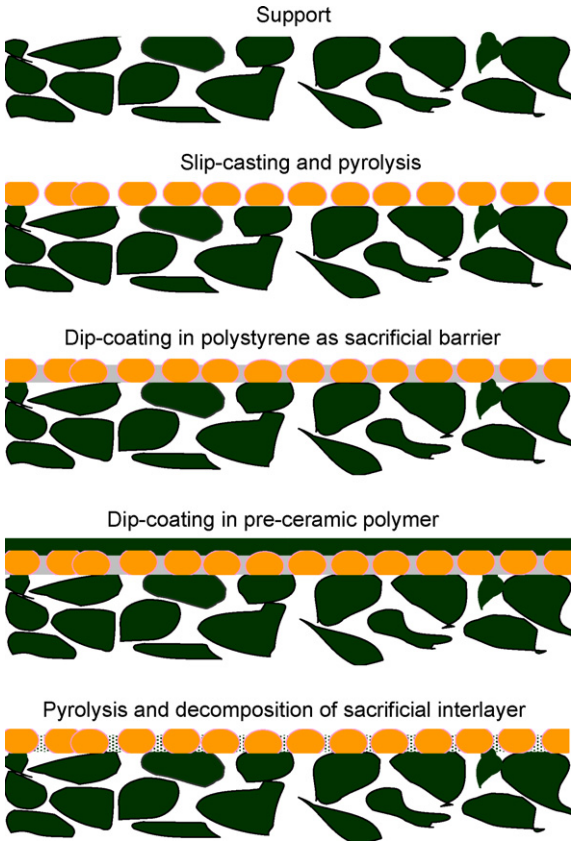

Fig. 2. A schematic of the new preparation technique.

to result in a SiC ceramic with a near stoichiometric Si:C ratio [15], one cannot exclude the possibility that after pyrolysis there may still remain trivial amounts of carbon-based residues, which may influence overall membrane performance. We showed previously [17] with AHPCS-derived SiC membranes that the mild temperature air oxidation results in higher permeances but lower separation factors. This is an undesirable outcome, of course, but by oxidizing the SiC membranes in air, prior to their use, one ensures that no further variation in the membrane properties will occur due to accidental exposure to air. Moreover, in the potential use of these materials in membrane reactors (e.g., in steam reforming of hydrocarbons), if carbon deposits form during the reaction and affect the membranes, one possible means of recovering their performance would be by mild temperature air oxidation. Using such an oxidation treatment during the membrane preparation phase, one can hopefully ensure that no dramatic changes in the membrane properties will occur during regeneration.

The morphology of the membranes (top surface and cross-sections) were characterized by SEM. Permeation experiments were carried out using a Wicke–Kallenbach type permeation apparatus previously utilized to measure permeation through flat-disk and tubular SiC membranes [1,17,23]. In the apparatus for tubular membranes, one end of the membrane is completely sealed using graphite tape and high temperature non-porous glue (J-B WELD); the other end of the membrane is attached to a flat metal ring using the same glue. The metal ring bearing the membrane is then installed in between the two half-cells of

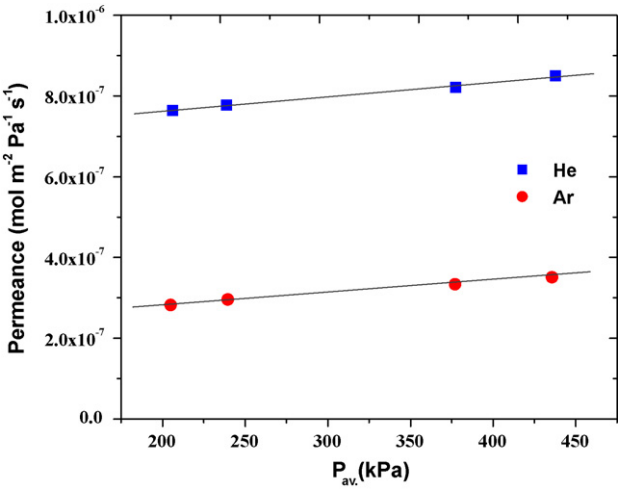

Fig. 3. Permeance vs. average pressure across the membrane for He and Ar.

the permeation test-unit using O-rings. Single-gas permeation experiments were carried out by flowing a given gas through the apparatus half-cell facing the membrane dead-end, under constant pressure and temperature, and by measuring the amount of gas that permeates through the membrane to the permeate side, which was maintained at atmospheric pressure. In the experiments reported here, the pressure drop across the membranes was kept at 207 kPa (30 psi), while the temperature was varied from room temperature to 200 °C. We report the ideal selectivity for the membranes, which is defined as the ratio of the permeances of the different gases. Mixed-gas permeation tests were also carried out with select membranes using equimolar binary (H_2/CH_4, and H_2/CO_2) gas mixtures. For the mixed-gas experiments, in addition to the gas flow to the permeate side of the membrane, the composition was also measured using a mass spectrometer.

3. Results and discussion

3.1. Support characterization

As noted above, the porosity of the membrane supports was obtained by the Archimedes method (details about the technique and its use for the characterization of SiC macroporous substrates can be found in ref. [23]). The porosities of the various supports were 26.5 (±1%). For membrane applications, higher porosity for supports is more desirable, and we are currently working to increase the porosity of the supports without unduly impacting their mechanical properties. Fig. 3 shows the measured He and Ar single-gas permeances for one of the supports. Clearly, the support is macroporous and the two permeances are a linear function of $P_{av.}$. One can express the permeance of the support for species j as (see, e.g., ref. [27])

$$\text{Permeance} = \frac{N_j}{\Delta P} = \frac{1}{r_o \ln(r_o/r_i) RT}\left[\frac{B_o}{\mu} P_{av.} + \frac{4}{3} K_o \sqrt{\frac{8RT}{\pi M_j}}\right] \quad (1)$$

where

$$\frac{\varepsilon}{\tau} = \frac{K_o^2}{2B_o} \quad (2)$$

$$d_p = \frac{4K_o}{\varepsilon/\tau} \quad (3)$$

In the above equations N_j is the molar flux of species j (calculated with respect to the outside support surface), ΔP the pressure gradient across the support, r_o the support outside radius, r_i the support inside radius, R the universal gas constant, T the temperature, ε the porosity, τ the tortuosity, μ the gas viscosity, $P_{av.}$ the arithmetic average pressure across the support, M_j the molecular weight of species j, B_o the viscous flow parameter, and K_o the Knudsen flow parameter.

Using the permeation data in Fig. 3 and Eqs. (1)–(3), we calculate an average pore size of ∼130 nm for the support (and a tortuosity of 2); this is within the range of average particle size measured (from SEM images) of the powder used in our slip-casting solution (100–200 nm). We expect, therefore, most of these particles to sit on the top of the support, rather than propagate and be lodged deep into the membrane structure during slip-casting.

3.2. Membrane characterization and performance

The quality of the membrane support is known to be important in determining the quality of the membranes that are prepared using these supports. Large defects in the supports are thought to lead to defects in the membranes themselves, thus resulting in low reproducibility in preparing membranes with high separation factors. Previously, we showed that putting a first layer on the support by slip-casting improved not only the performance of the membranes, but also increased the success rate in preparing high quality membranes [17]. Therefore, in this study, we continued placing a first layer by slip-casting as a means of conditioning the membrane support surface.

In order to gain some insight into what role the sacrificial PS layer plays in the membrane preparation process, SEM pictures were taken of the membrane's cross-section after coating the last PS layer and before coating the final layer of the pre-ceramic polymer. A SEM picture of such a cross-section is shown in Fig. 4, where within the SEM's resolution one cannot discern a distinguishable uniform PS top layer on the membrane, meaning that the PS layer is either very thin or that it has potentially infiltrated inside the porous structure, or both, thus forming a barrier prior to the deposition of the final AHPCS layer. That the PS polymer chains would potentially infiltrate into the underlying pyrolyzed AHPCS layer is not totally unexpected since we selected a PS with a low average molecular weight of 2500 with a corresponding radius of gyration of ∼1 nm [28].

The fact that the PS sacrificial interlayer acts as an effective barrier is also supported by other experimental evidence. We observed, for example, that when using the sacrificial interlayer technique, the amount of dip-coating solution that is being uptaken is less than what is used when using the conventional technique without sacrificial layers coated on the supports, implying, likely, that the presence of the sacrificial interlayer allows for less AHPCS polymer to infiltrate within the underlying pores during coating. Using the sacrificial interlayer technique, the formation of a visible top SiC layer can be observed from the beginning of the membrane formation process, typically after a couple of coatings. Thicker membrane films also form, despite the fact that less AHPCS is being utilized. As seen in Fig. 4, the thickness of the membrane layer, even before the final SiC layer coating, is ∼7 μm, which is larger than the thickness of membranes formed (typically ∼2 μm [17]), without the aid of PS interlayers.

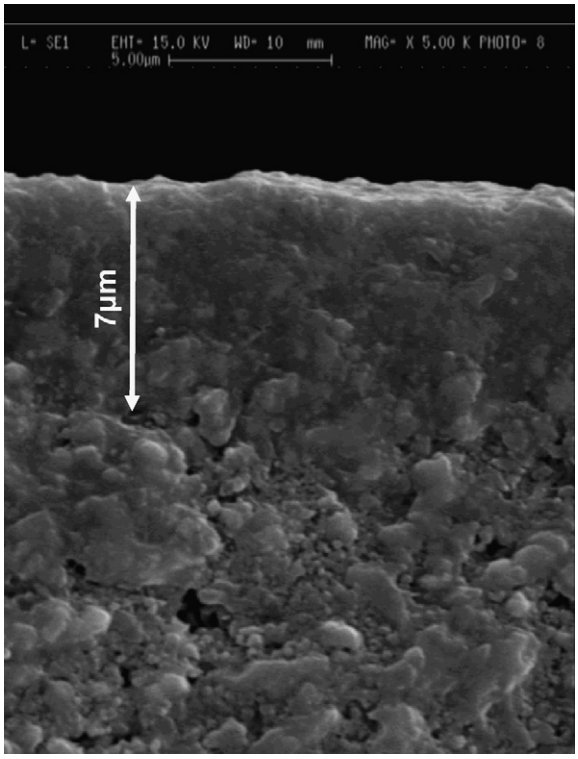

Fig. 4. SEM picture showing the cross-section of a SiC membrane after three dual (PS + AHPCS) coatings, and one additional coating of PS.

Despite the fact that the new technique prepares thicker membranes, their permeances are significantly higher than those of the membranes prepared by the conventional technique, as discussed below. Why this happens is not entirely clear at this point, since the presence of the PS sacrificial layers implies the onset of a set of complex phenomena during the membrane preparation process. For instance, the PS layer has a melting point of ∼240 °C [29] and its decomposition starts at temperatures higher than 350 °C [30]; we expect cross-linking of AHPCS to be taking place within the same temperature range during pyrolysis. Also relevant here is the recent investigation by Suda et al. [18],

Table 1
Range of single-gas permeances and separation factors, measured at 200 °C, for membranes prepared by pyrolysis at 750 °C for 2 h

	He	H_2	Ar
Permeance ($\times 10^8$ mol m^{-2} s^{-1} Pa^{-1})	1.8–4.3	1.05–2	0.01
S.F. (gas/Ar)	176–465	101–258	

Table 2
Mixed-gas permeation properties of SiC membranes, measured at 200 °C, prepared by pyrolysis at 750 °C for 2 h

	H_2 permeance ($\times 10^8$ mol m^{-2} s^{-1} Pa^{-1})	S.F. (H_2/CH_4)	H_2 permeance ($\times 10^8$ mol m^{-2} s^{-1} Pa^{-1})	S.F. (H_2/CO_2)
Sample I	1.54	104	1.47	93
Sample II	1.55	117	–	–

For the mixed-gas experiments the membranes were exposed to an equimolar mixture of H_2/CH_4 or H_2/CO_2.

in whose studies PS was used as a pore former (rather than as a sacrificial barrier layer used in our studies) mixed with regular polycarbosilane which, unlike AHPCS, needs to be cross-linked by the addition of chemical cross-linking agents. PS appeared to actively participate in the formation of the 3D pore structure. How the AHPCS layer interacts with the PS sacrificial layer during pyrolysis, and the impact on the membrane characteristics definitely need more in-depth research.

The permeation properties of three different single gases (He, H_2, and Ar) through the membranes were measured at 200 °C. The range of permeances and the corresponding ideal separation factors are presented in Table 1. The H_2 permeance of the membranes, varying in the range $(1.05–2.0) \times 10^{-8}$ mol m^{-2} s^{-1} Pa^{-1}, is significantly higher than the H_2 permeances reported previously with membranes prepared with the same exact protocol (number of AHPCS layers, deposition conditions, pyrolysis temperature, etc.) but without the use of sacrificial PS layers [17]. This is so, despite the fact, as previously noted, that the thickness of the membranes prepared by the use of sacrificial layers, is ~3 times larger than the corresponding thickness of the membranes prepared by the technique without the use of sacrificial layers. The corresponding ideal separation factors are also significantly higher. For example, for the He/Ar pair the ideal separation factors varied between 176 and 465. The He/Ar ideal separation factor reported previously was 89 [17].

The permeances of He, H_2, and Ar, as a function of temperature, for one of the membranes prepared by the sacrificial layer method, are shown in Fig. 5. Small molecules, such as H_2 and He, permeate through the SiC membranes by activated transport, while Ar and other molecules with larger kinetic diameters permeate following a Knudsen diffusion mechanism. For

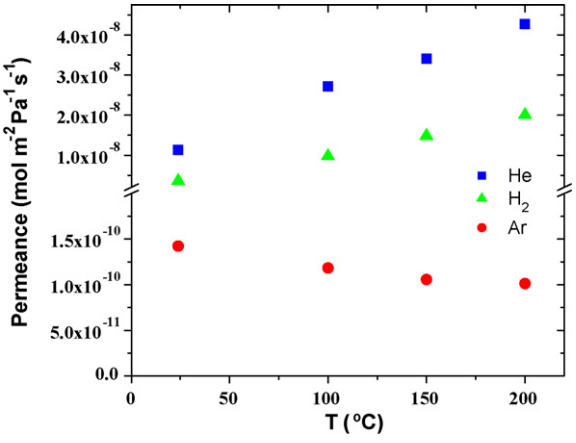

Fig. 5. He, H_2, and Ar permeance as a function of temperature for a SiC membrane at 207 kPa (30 psi) transmembrane pressure.

He the activation energy for transport is 8.9 kJ/mol, while for H_2 the corresponding value is 11.7 kJ/mol, which is close to the values measured previously [12,17]. As a result, the separation characteristics of the membranes improve with temperature. The permeance of H_2 at 200 °C is 2×10^{-8} mol m^{-2} s^{-1} Pa^{-1}. Extrapolated to a temperature of 500 °C, the expected permeance for H_2 should be 6.5×10^{-8} mol m^{-2} s^{-1} Pa^{-1}. By comparison, Pd and Pd-alloy membranes, around 500 °C, typically exhibit permeances in the range 10^{-7}–10^{-6} mol m^{-2} s^{-1} Pa^{-1} [31]. However, Pd membranes are known to be sensitive to the presence of H_2S and hydrocarbon impurities; use of Pd-alloy membranes (e.g., Pd–Ag) also faces challenges for long-term usage at temperatures significantly higher than 500 °C.

As noted in the introduction, a key potential application for these SiC-based membranes is in hydrogen production, through methane steam reforming where such membranes are integrated in membrane reactors. Another key potential application is in modern IGCC power generation systems, where such membranes may potentially be useful in producing a CO_2-free H_2 stream for further use in turbines or fuel cells. The permeation characteristics of two of these membranes towards an equimolar H_2/CH_4 mixture were tested using the experimental procedure previously outlined, and also described in greater detail in ref. [17] (the permeation characteristics of one of the membranes were also tested with an equimolar H_2/CO_2 mixture). The membranes exhibited good selectivity towards hydrogen (see Table 2) with H_2/CH_4 separation factors that are significantly higher than those reported previously with membranes that were prepared without the use of sacrificial PS layers [17].

4. Conclusions

A new procedure was developed for the preparation of SiC-based membranes which involves the periodic coating of sacrificial polystyrene interlayers in between pre-ceramic AHPCS layers. Applying this technique, we have been able to prepare membranes with significantly enhanced performance when compared to the membranes we prepared previously without using sacrificial interlayers. The mechanism by which the sacrificial PS layers participate in the membrane formation process is likely to be very complex. We have selected to form the sacrificial interlayers using a low molecular weight (~2500) PS with a corresponding small radius of gyration of ~1 nm [28]. The idea here was that the low molecular weight PS chains would be able to penetrate the underlying –[Si–C]– type pores, thus preventing the AHPCS chains, during the recoating, from re-entering these pores. The phenomena are likely to be more complex, however. As previously noted, the PS layer has a

melting point of ∼240 °C [29], and begins to decompose at temperatures higher than 350 °C [30], where we expect cross-linking of AHPCS to be also taking place. As noted in the recent study by Suda et al. [18], PS plays an important role as a pore-former through the release of various low molecular weight gases but also, in addition, actively participates during the cross-linking and 3D pore-structure formation process. It is the ability of PS to directly influence the 3D structure of the resulting SiC-based ceramic that makes the technique different from previous efforts using sacrificial layers [19–22], where the barrier layer did not directly participate in the zeolite membrane formation process.

There is still, of course, a lot that is not understood about the preparation technique, and additional studies are currently in progress. For example, the thickness of the PS barrier appears to be a key factor; too thick barrier layers, for example, are undesirable, as they result in peeling of the SiC layer after pyrolysis. The methodology employing sacrificial barrier layers, such as polystyrene, which decompose in inert or oxidizing environments is potentially of general applicability for the formation of other microporous inorganic thin films and membranes.

Acknowledgements

The support of the U.S. Department of Energy, the National Science Foundation, and NASA is gratefully acknowledged. Superior Graphite Co. is acknowledged for kindly providing us the SiC powders. The authors would also like to thank Mr. Li-Chung Lai and Mr. Tae Wook Kim for performing the SEM analysis.

References

[1] R.J. Ciora, B. Fayyaz, P.K.T. Liu, V. Suwanmethanond, R. Mallada, M. Sahimi, T.T. Tsotsis, Preparation and reactive applications of nanoporous silicon carbide membranes, Chem. Eng. Sci. 59 (2004) 4957–4965.

[2] Y. Takeda, N. Shibata, Y. Kubo, SiC coating on porous γ-Al_2O_3 using alternative-supply CVI method, J. Ceram. Soc. Jpn. 109 (2001) 305–309.

[3] X. Pages, V. Rouessac, D. Cot, G. Nabias, J. Durand, Gas permeation of PECVD membranes inside alumina substrate tubes, Sep. Purif. Technol. 25 (2001) 399–406.

[4] B.-K. Sea, K. Ando, K. Kusakabe, S. Morooka, Separation of hydrogen from steam using a SiC-based membrane formed by chemical vapor deposition of triisopropylsilane, J. Membr. Sci. 146 (1998) 73–82.

[5] K. Kusakabe, Z.Y. Li, H. Maeda, S. Morooka, Preparation of supported composite membrane by pyrolysis of polycarbosilane for gas separation at high temperature, J. Membr. Sci. 103 (1995) 175–180.

[6] Z. Li, K. Kusakabe, S. Morooka, Preparation of thermostable amorphous Si—C—O membrane and its application to gas separation at elevated temperature, J. Membr. Sci. 118 (1996) 159–168.

[7] Z.Y. Li, K. Kusakabe, S. Morooka, Pore structure and permeance of amorphous Si—C—O membranes with high durability at elevated-temperature, Sep. Sci. Technol. 32 (1997) 1233–1254.

[8] L.-L. Lee, D.-S. Tsai, A hydrogen-permselective silicon oxycarbide membrane derived from polydimethylsilane, J. Am. Ceram. Soc. 82 (1999) 2796–2800.

[9] L.-L. Lee, D.-S. Tsai, Synthesis and permeation properties of silicon–carbon-based inorganic membrane for gas separation, Ind. Eng. Chem. Res. 40 (2001) 612–616.

[10] C.-L. Chen, D.-S. Tsai, Permeation properties of microporous membranes prepared via coating of evaporated polydimethylsilane, J. Membr. Sci. 237 (2004) 163–165.

[11] R.A. Wach, M. Sugimoto, M. Yoshikawa, Formation of silicone carbide membrane by radiation curing of polycarbosilane and polyvinylsilane and its gas separation up to 250 °C, J. Am. Ceram. Soc. 90 (2007) 275–278.

[12] R.A. Wach, M. Sugimoto, A. Idesaki, M. Yoshikawa, Molecular sieve SiC-based membrane for hydrogen separation produced by radiation curing of preceramic polymers, Mater. Sci. Eng. B 140 (2007) 81–89.

[13] H. Suda, H. Yamauchi, Y. Uchimaru, I. Fujiwara, K. Haraya, Preparation and gas permeation properties of silicon carbide-based inorganic membranes for hydrogen separation, Desalination 193 (2006) 252–255.

[14] T. Nagano, K. Sato, T. Saitoh, Y. Iwamoto, Gas permeation properties of amorphous SiC membranes synthesized from polycarbosilane without oxygen-curing process, J. Ceram. Soc. Jpn. 114 (2006) 533–538.

[15] L.V. Interrante, C.W. Whitmarsh, W. Sherwood, H.-J. Wu, R. Lewis, G. Maciel, High yield polycarbosilane precursors to stoichiometric SiC. Synthesis, pyrolysis and application, Mater. Res. Soc. Symp. Proc. 346 (1994) 593–603.

[16] L.V. Interrante, C.W. Whitmarsh, W. Sherwood, Fabrication of SiC matrix composites by liquid phase infiltration with a polymeric precursor, Mater. Res. Soc. Symp. Proc. 365 (1995) 139–146.

[17] B. Elyassi, M. Sahimi, T.T. Tsotsis, Silicon carbide membranes for gas separation applications, J. Membr. Sci. 288 (2007) 290–297.

[18] H. Suda, H. Yamauchi, Y. Uchimaru, I. Fujiwara, K. Haraya, Structural evolution during conversion of polycarbosilane precursor into silicon carbide-based microporous membranes, J. Ceram. Soc. Jpn. 114 (2006) 539–544.

[19] S. Jiang, Y. Yan, G.R. Gavalas, Temporary carbon barriers in the preparation of H_2-permselective silica membranes, J. Membr. Sci. 103 (1995) 211–218.

[20] Y. Yan, M.E. Davis, G.R. Gavalas, Use of diffusion barriers in the preparation of supported zeolite ZSM-5 membranes, J. Membr. Sci. 126 (1997) 53–65.

[21] J. Hedlund, J. Sterte, M. Anthonis, A.-J. Bons, B. Carstensen, N. Corcoran, D. Cox, H. Deckman, W. de Gijnst, P.-P. de Moor, F. Lai, J. McHenry, W. Mortier, J. Reinoso, J. Peters, High-flux MFI membranes, Microporous Mesoporous Mater. 52 (2002) 179–189.

[22] J. Hedlund, F. Jareman, A.-J. Bons, M. Anthonis, A masking technique for high quality MFI membranes, J. Membr. Sci. 222 (2003) 163–179.

[23] V. Suwanmethanond, E. Goo, P.K.T. Liu, G. Johnston, M. Sahimi, T.T. Tsotsis, Porous silicon carbide sintered substrates for high-temperature membranes, Ind. Eng. Chem. Res. 39 (2000) 3264–3271.

[24] J. Li, Y. Zhang, A simple purification for single-walled carbon nanotubes, Physica E 28 (2005) 309–312.

[25] S. Osswald, E. Flahaut, Y. Gogotsi, In situ spectroscopy study of oxidation of doubled- and single-wall carbon nanotubes, Chem. Mater. 18 (2006) 1525–1533.

[26] T.-J. Park, S. Banerjee, T. Hemraj-Benny, S.S. Wong, Purification strategies and purity visualization techniques for single-walled carbon nanotubes, J. Mater. Chem. 16 (2006) 141–154.

[27] H.W.J.P. Neomagus, W.P.M. van Swaaij, G.F. Versteeg, The catalytic oxidation of H_2S in a stainless steel membrane reactor with separate feed of reactants, J. Membr. Sci. 148 (1998) 147–160.

[28] K. Huber, S. Bantle, P. Lutz, W. Burchard, Hydrodynamic and thermodynamic behavior of short-chain polystyrene in toluene and cyclohexane at 34.5 °C, Macromolecules 18 (1985) 1461–1467.

[29] J. Brandrup, E.H. Immergut, E.A. Grulke, Polymer Handbook, Wiley, New York, 1999.

[30] A. Marcilla, M. Beltran, Kinetic study of the thermal decomposition of polystyrene and polyethylene-vinyl acetate graft copolymers by thermogravimetric analysis, Polym. Degrad. Stab. 50 (1995) 117–124.

[31] K.S. Rothenberger, A.V. Cugini, B.H. Howard, R.P. Killmeyer, M.V. Ciocco, B.D. Morreale, R.M. Enick, F. Bustamante, I.P. Mardilovich, Y.H. Ma, High pressure hydrogen permeance of porous stainless steel coated with a thin palladium film via electroless plating, J. Membr. Sci. 244 (2004) 55–68.

Available online at www.sciencedirect.com
ScienceDirect
Journal of Membrane Science 315 (2008) 48–57
journal of MEMBRANE SCIENCE
www.elsevier.com/locate/memsci

Pore network model of transport and separation of binary gas mixtures in nanoporous membranes

Feng Chen, Rayan Mourhatch, Theodore T. Tsotsis, Muhammad Sahimi *

Mork Family Department of Chemical Engineering & Material Science, University of Southern California, Los Angeles, CA 90089-1211, USA

Received 21 November 2007; received in revised form 25 January 2008; accepted 4 February 2008
Available online 13 February 2008

Abstract

We develop a pore network model of transport and separation of a binary gaseous mixture through a nanoporous membrane. A three-dimensional network is used to represent the membrane's pore space, in which the effective pores' radius is distributed according to a pore size distribution (PSD). The connectivity of the pores, as well as the broadness of the PSD, are varied in order to study their effect on the transport and separation processes. The Maxwell–Stefan equations are used for describing the pore-level transport processes, which include Knudsen and hindered diffusion, as well as viscous flow. The simulations indicate that Knudsen diffusion is the dominant mechanism of transport in pores as small as 7 Å. In smaller pores it is hindered diffusion that controls the rate of the molecular transport. Excellent agreement is found between the simulation results and our experimental data for the single-gas permeances and the ideal selectivity of a silicon–carbide membrane for a helium–argon system, if the thickness of the network and its average pore size are adjusted. The results also indicate the fundamental significance to the permselectivity of a membrane of the tail of the PSD, as well as the percolation effect which is manifested through the interconnectivity of the pores that are accessible to the gases.

Keywords: Nanoporous membranes; Knudsen diffusion; Configurational diffusion; Pore network model

1. Introduction

Equilibrium and nonequilibrium properties of fluids and their mixtures in confined media are of much current interest. Examples of such media include nano- and mesoporous materials, such as catalysts, adsorbents, and synthetic and natural (biological) membranes (see, for example, [23]). For practical applications, it is important to understand how transport of mixtures occur in the pore space of nanoporous materials. To develop such understanding, one must have an accurate model of the pore space, as well as including in the model the correct mechanism(s) by which molecules and their mixtures are transported through the pore space.

An important class of porous materials consists of nanoporous membranes that have been under active investigations, both experimentally and by computer simulations, for separation of gaseous and liquid mixtures into their constituent components, and as potential sensors that can detect trace amounts of certain chemical compounds. Our group (as well as others) has been preparing a variety of amorphous nanoporous membranes for separation of gaseous mixtures, which include carbon molecular-sieve (CMS) [38–40] and silicon–carbide membranes [42,8,12,13]. Optimizing the performance of such membranes, and in particular their selectivity, entails developing deeper understanding of how transport of gaseous (or liquid) mixtures through them is affected by the morphology of the pore space, and in particular its pore size distribution (PSD) and pore connectivity.

One approach to modelling of gas transport through nanoporous materials is phenomenological, which relies on the continuum equations of transport of mixtures. It ignores important information about the porous material's morphology, including its PSD and the interconnectivity of the pores. An example of such an approach was described in our recent paper [7].

Due to the small pore sizes, molecular interactions between the molecules, and between them and the nanopores' walls, are important. Therefore, another approach to understanding trans-

* Corresponding author. Tel.: +1 213 740 2064; fax: +1 213 740 8053.
E-mail address: moe@iran.usc.edu (M. Sahimi).

0376-7388/$ – see front matter © 2008 Elsevier B.V. All rights reserved.
doi:10.1016/j.memsci.2008.02.005

port and separation of mixtures through nanoporous materials has been based on atomistic models of both the molecules and the materials (for recent reviews see, for example, [14,36]). Most of such models are based on atomistic simulation of flow and transport of a fluid mixture through a *single* nanopore.

In practice, however, the pore space of a membrane layer (as well as its support) consists of a network of interconnected pores, the sizes of which are distributed according to a PSD. The network is typically three dimensional (3D), or quasi-2D if the membrane layer is thin. As pointed out by, for example, [37], to accurately model any membrane and the phenomena that take place there, one must take into account the effect of its interconnected pore structure. In previous papers [15,44,45] we carried out atomistic studies of transport, adsorption, and separation of several mixtures in 3D atomistic pore network models of membranes. Such simulations require, however, highly intensive computations [35], which explains why there have been very few attempts in this direction.

The third approach is based on utilizing pore network models of porous materials (for reviews and extensive discussions see, for example, [33,29,31,25,26,16]). Any porous medium can, in principle, be mapped onto an equivalent network of pore throats (bonds) and pore bodies (nodes). For brevity, we refer to pore throats and pore bodies simply as pores and nodes. The pores' sizes are distributed according to a PSD that can be measured by a variety of techniques. Since the network's pores are interconnected, the effect of their connectivity, which greatly influences transport and separation of molecules through the network, is also automatically taken into account. Thus, one has a realistic model of a nanoporous membrane which can be used to study the effect of a variety of factors on the transport and separation of gaseous mixtures through it.

In this paper, we develop a pore network model for a nanoporous membrane that we have prepared in our laboratory (see below), and study transport and separation of a binary mixture of gases *A* (argon, Ar) and *B* (helium, He) through it. The results are then compared with our own experimental data for transport and separation of the same binary mixture through a SiC nanoporous membrane. The model is, however, general and applicable to a variety of nanoporous membranes, including the CMS membranes. The present work represents the first step toward our long-term goal of developing predictive pore network models of amorphous nanoporous membranes and the transport and separation of multicomponent gaseous mixtures through them.

Although pore network models have been used extensively in the past (for reviews see, for example, [33,29,31,16]) for studying transport and reaction processes in porous catalysts and several other types of porous media, they have not been used, to our knowledge, for modelling of transport and separation of gaseous mixtures in nanoporous membranes. [5], Sotirchos and Burganos, 1988, and [41] did study transport of multicomponent gaseous mixtures in pore networks, but their study was in the context of the effective-medium approximation. [22] used a network model to study gas transport in a bidisperse porous adsorbent, while [4] used a pore network model to study Knudsen diffusion of a single gas in porous materials. Knudsen diffusion in randomly oriented capillary structures was studied by [6]. An interesting approach to the transport of gaseous mixture through membranes was developed by [18,37,46], based on combining atomistic simulations and the critical-path analysis (CPA). The CPA [1] is a technique according to which, for a sufficiently broad PSD, the transport process is dominated by a pore of size r_c, such that pores with sizes much larger or smaller than r_c do not make significant contributions to the overall rate of the transport in the membrane. The original CPA was developed for hopping conduction in amorphous semiconductors, but has since been applied to a wide variety of transport processes in disordered materials (see, for example, [28,29,32]).

The plan of this paper is as follow. In the next section we describe the pore network model that we used to model a nanoporous membrane. Section 3 describes the model of multicomponent gas transport through the network's pores, while Monte Carlo simulation of gas transport and separation through the pore network is described in Section 4. The results are presented and discussed in Section 5. The paper is summarized in the last section, where we describe its extension to more complex mixtures.

2. The pore network model

We represent a nanoporous membrane by a simple-cubic network. The coordination number of the network – the number of pores that are connected to each node – is six. To study the effect of the pore connectivity, we also use networks with an *average* coordination number Z_p which we construct by randomizing the simple-cubic network. That is, we select at random a fraction p_b of the pores given by

$$p_b = 1 - \frac{1}{6}Z_p, \tag{1}$$

and remove them from the network (i.e., we set their radii equal to zero).

Molecular dynamics simulations of [10,11] indicated that the transport of fluids in a pore is hardly influenced by its shape, so long as the correct average radius, transport length, and the applied pressure (or concentration) gradient are used. Therefore, the pores are assumed to be cylindrical with smooth internal surface, to each of which we assign an effective radius. The pores' effective radii are distributed according to a PSD $f(r_p)$. We used two PSDs. One, the shape of which is qualitatively similar to the experimental PSD for many membranes, is given by

$$f(r_p) = \frac{r_p - r_{min}}{(r_a - r_{min})^2} \exp\left[-\frac{1}{2}\left(\frac{r_p - r_{min}}{r_a - r_{min}}\right)^2\right], \tag{2}$$

where r_a and r_{min} are the average and minimum pore radius, respectively. r_{min} is set to the molecular size of helium, which is 0.257 nm. As for r_a, we used a value that corresponds to that of the SiC membrane prepared in our laboratory, but we also varied r_a in order to study its effect (see below) on the results. Fig. 1 shows examples of the PSD that Eq. (1) generates.

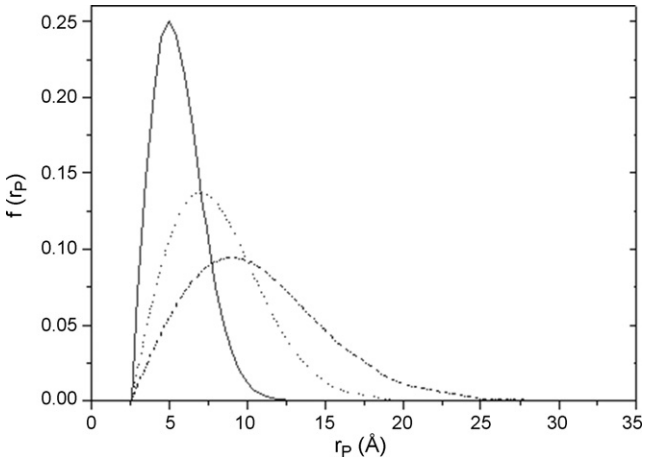

Fig. 1. Three pore size distributions generated by Eq. (2), with $r_a = 5$ Å (continuous curve), 7 Å (dotted curve), and 9 Å (dashed-dotted curve).

The second PSD that we utilized was a Gaussian distribution with the same average pore sizes as those of Eq. (2),

$$f(r_p) = \frac{1}{\sqrt{2\pi}\sigma}\exp\left[-\frac{(r_p - r_a)^2}{2\sigma^2}\right], \tag{3}$$

in which we varied the variance σ^2 in order to study the effect of the PSD's broadness on the results.

3. Pore-level description of transport of multicomponent mixtures

Transport of multicomponent mixtures in porous materials consists of a complex set of phenomena that cannot be described by Fick's law of diffusion. The modelling is usually based on the dusty-gas (DG) (model [19]; for a comprehensive review see, for example, [17]). The DG model itself is based on the Maxwell–Stefan (MS) equations [43,17], which is an approximation of the Boltzmann's equations for dilute gas mixtures. In a membrane in which the pore sizes vary anywhere from a few angstroms to a few tens of angstroms, the important mechanisms of transport are: (i) Knudsen diffusion, which is dominant when the collisions between the molecules and the pores' walls are important (which is the case when the molecules' mean-free paths are larger than the pore radius); (ii) hindered or configurational diffusion, which is significant when the pore size is small enough that $\lambda = R_k/r_p$, the ratio of the molecular size R_i of component k and the pore size r_p, is not small; and (iii) the viscous flow contribution. However, although we included the contribution of viscous flow in the formulation (see below), we found that its contribution to the transport process, over the range of the pore sizes that we consider in this paper, is negligible. Naturally, if we use a broader PSD, then, the contribution of the viscous flow might become significant, in which case the pore network model that we have developed takes its effect into account. Moreover, if there is significant sorption on the pores' walls, surface diffusion can also be important. However, due to the particular binary (Ar/He) mixture that we consider in this paper, the contribution of surface diffusion is negligible.

Therefore, the total flux $\mathbf{J}$ in any pore is given by,

$$\mathbf{J} = \mathbf{J}^V + \mathbf{J}^D \tag{4}$$

where $\mathbf{J}^V$ and $\mathbf{J}^D$ are, respectively, the viscous and diffusive fluxes. If z denotes the axial direction in each pore, $\mathbf{J}^V$, the viscous flux, is given by

$$\mathbf{J}^V = -\alpha\mathbf{C}. \tag{5}$$

Here $\mathbf{C} = [C_A, C_B]^T$, and $\alpha = [ZRTr_p^2/(8\mu)]\mathrm{d}C/\mathrm{d}z$, with z being the compressibility factor, R the gas constant, T the temperature, r_p the pore's radius, μ the viscosity, and $C = C_A + C_B$. The diffusive flux $\mathbf{J}^D$, according to the DG-MS equations, is given by

$$\mathbf{J}^D = -\mathbf{D}^{-1}\frac{\mathrm{d}\mathbf{C}}{\mathrm{d}z}, \tag{6}$$

where the entries of the matrix $\mathbf{D}$ are given by

$$D_{ij} = \begin{cases} -\dfrac{x_i}{D_i} & i \neq j \\ \dfrac{1}{D_i^K} + \displaystyle\sum_{k=1,\,k\neq i}^{2}\frac{x_k}{D_k} & i = j \end{cases} \tag{7}$$

where D_i^K is the Knudsen diffusivity of component i, x_k the mole fraction of component k, and D_k the hindered or configurational diffusivity of component k. The Knudsen diffusivity is given by,

$$D_i^K = \frac{4}{3}r_p\sqrt{\frac{2RT}{\pi M_i}}, \tag{8}$$

with M_i being the molecular weight of component i. The diffusivity D_k is given by

$$D_k = D_k^\infty(\lambda), \tag{9}$$

where $\lambda = R_k/r_p$, with R_k being the molecular size of gas k, D_k^∞ the bulk diffusivity, and $h(\lambda)$ a function that has been determined both theoretically and semi-empirically (for a review see [9]). D_k^∞ was estimated using the well-known expressions for diffusion coefficients of gases [2]. Hindered diffusion of a single gas in pore network models of porous materials was studied previously by [34,27], and [47]. For $\lambda \leq 0.3$ [3] derived the follwing expression,

$$h(\lambda) = (1 - 1.539\lambda + 1.125\lambda\ln\lambda + \ldots)(1-\lambda)^{-2}, \tag{10}$$

while for $\lambda \geq 0.9$ [20] obtained

$$h(\lambda) = 0.984(1-\lambda)^{4.5}. \tag{11}$$

[21] and [24] proposed a semi-emprirical correlation for $h(\lambda)$ which is as follows,

$$h(\lambda) = (1-\lambda)^2(1 - 2.104\lambda + 2.09\lambda^3 - 0.95\lambda^5). \tag{12}$$

We used all the above three expressions in our computations.

Assuming steady state, within each pore and for component i of the mixture one has, $\nabla\mathbf{J}_i = 0$, where $\mathbf{J}_i$ is the total flux of component i. We assume that transport in each pore is 1D (so

that the concentrations represent averages over the pore's cross-sectional area) in the axial direction. Therefore, within each pore one has

$$\frac{dJ_i}{dz} = \frac{d}{dz}(J_i^V + J_i^D) = 0, \tag{13}$$

where J_i^V and J_i^D are given by Eqs. (5)–(9). At every node j of the pore network, one must have mass balance for each component of the gaseous mixture:

$$\sum_{jl}^{Z_j} S_{jl} J_i^{(jl)} = 0, \quad i = 1, 2 \tag{14}$$

where $J_i^{(jl)}$ is the total flux of component i in pore jl that reaches node j, S_{jl} is the cross-sectional area of pore jl, Z_j is the coordination number of node j, and the sum is over all the pores jl that are connected to node j. Eqs. (13)nd (14) govern the transport of a gaseous mixture throughout the nodes and pores of a network.

4. Monte carlo simulation

If we use Eqs. (5)–(9), together with Eqs. (10)nd (12), to substitute for J_i^V and J_i^D in Eqs. (13)nd (14), we obtain a set of coupled nonlinear equations that govern the concentrations C_A and C_B of the two gases in every pore and node of the network. To solve the equations, we first discretized them using the finite-difference (FD) approximation. We then numbered the grid points within each pore from 0 to n. Then, for a grid point k inside a pore, we used

$$\frac{dC_i}{dz} \simeq \frac{C_i^{k+1} - C_i^{k-1}}{2\Delta z}, \tag{15}$$

$$\frac{d^2C_i}{dz^2} \simeq \frac{C_i^{k+1} - 2C_i^k + C_i^{k-1}}{\Delta z^2}, \tag{16}$$

whereas at the two ends of each pore we used the one-sided FD discretization,

$$\frac{dC_i}{dz}|_{z=0} \simeq \frac{-3C_i^0 + 4C_i^1 - C_i^2}{2\Delta z}, \tag{17}$$

$$\frac{dC_i}{dz}|_{z=\ell} \simeq \frac{-3C_i^{n-2} + 4C_i^{n-1} - C_i^n}{2\Delta z}, \tag{18}$$

all of which are accurate to $\mathcal{O}(\Delta z^2)$, where Δz is the distance between two neighboring grid points, with ℓ being the length of each pore. We assumed complete mixing in every node of the network, so that the concentrations at the two ends of each pore coincide with those in the two nodes that are connected to the pore. Similar FD approximations were used for discretizing the equations that govern the gas concentrations in the nodes of the pore network. Note that, in all the pores for which, $r_{min} < r_p < R_{Ar}$, only helium contributes to the rate of gas transport, whereas for $r_p > R_{Ar}$ both gases diffuse (and flow). Therefore, so far as argon is concerned, there is a percolation effect at work, namely, a fraction q of the pores, given by,

$$q = \int_{r_{min}}^{R_{Ar}} f(r_p) dr_p, \tag{19}$$

cannot be accessed by it. Clearly, if $q > p_c$, where p_c is the bond percolation threshold of the network, no macroscopic transport of argon can take place in the pore network. For a 3D network of average coordination number Z_p, one has [30], $p_c \simeq 1.5/Z_p$. The discretized equations, when written for every grid point in each pore and for every interior node of the network, yield a large set of nonlinear algebraic equations that govern the two gases' concentrations in the network. The size of the set depends on the size of the network, and the number of grid points used inside each pore. If the network contains n nodes, and we use M grid points inside each pore, then the number of equations to be solved is of the order of $2N(3M + 1)$, which requires a very efficient and accurate numerical technique. To speed up the computations, we guess the concentration distribution for one of the gases, say A, throughout the pore network and solve the set for the concentration distribution of the second gas, B. We use the biconjugate-gradient method to solve the set. The solution is then used to obtain a new approximate solution for A. If it agrees with the initial guess, then the numerical calculations stop. If not, the new solution is used to obtain a new spatial distribution of the concentration C_B throughout the network. The iteration process between C_A and C_B is continued until we obtain converged solutions for both. The boundary conditions, used in the macroscopic ($z-$) direction, are

$$\begin{cases} C_A = C_{feed} x_A \\ C_B = C_{feed} x_B \end{cases} \tag{20}$$

for the feed side of the membrane, where C_{feed} is the total feed concentration, and

$$C_A = C_B = 0, \tag{21}$$

for the permeate side (as if a sweep gas is used there). We also used a no-flux boundary condition (impermeable surfaces) for the other four surfaces, namely,

$$\mathbf{J} = \mathbf{0}. \tag{22}$$

We used networks of size $L_x \times L_y \times L_z$, where L_z is the thickness of the network (feed-to-permeate side), and L_x, L_y, and L_z are measured in units of ℓ, the length of the pores (assumed to be the same for all the pores). In most of the calculations we used $L_x = L_y = 30$, but also investigated the effect of the thickness on the results (see below). We also made several realizations of each network, and averaged the results over all of them. The molecular sizes of He and Ar were taken to be, respectively, R_{He}=0.257 nm and R_{Ar}=0.343 nm.

Let us point out that, the pore space of a real membrane has a very large number of pores. Modelling such a pore space using a pore network with the appropriate PSD, porosity, and about the same number of pores as that of a real membrane is very difficult, if not impossible. In our simulations, we use a large network (see above) and maintain realistic values for the pore sizes. If the network's thickness and the number of pores L_z in

the macroscopic direction are specified, the length ℓ of the pores is easily estimated. At the same time, as mentioned above, we also generate many realizations of the network, and average the results over all of them. Moreover, the macroscopic properties of pore networks become independent of their linear size (see also below), once they are larger than a certain size.

For each component i we compute the total flux J_i in the macroscopic ($z-$)direction. The permeability K_i of component i is then given by,

$$K_i = \frac{J_i}{\Delta P_i / L_z}, \tag{23}$$

where $\Delta P_i = x_i \Delta P$ is the partial pressure drop for component i in the macroscopic direction, with x_i being its mole fraction, $P = C_{\text{feed}} ZRT$ the pressure imposed on the system on the feed side, and L_z the pore network's thickness. The dynamic selectivity, or the separation factor, S is defined by,

$$S = \frac{K_{\text{He}}}{K_{\text{Ar}}}. \tag{24}$$

Since, $K_{\text{He}} > K_{\text{Ar}}$, one has, $S > 1$. We also carried out single-gas calculations, i.e., studied the case in which each of the two gases was transported in the network alone, in order to compute their permeabilities K_i^0 and the *ideal* separation factor,

$$S_i = \frac{K_{\text{He}}^0}{K_{\text{Ar}}^0}. \tag{25}$$

The goal is to see whether S_i and S are equal.

5. Results and discussion

We first describe the single-gas results for the case in which Eq. (2) represented the PSD of the pore network. We then describe and discuss the results for the binary gas mixture, computed using both PSDs (2)nd (3). Unless otherwise specified, all the results presented are for $L_z = 30$.

5.1. Results for transport of single gases

Shown in Fig. 2 are the permeances of He and Ar, obtained with single-gas simulations. The pore network's connectivity is $Z_{\text{p}} = 6$. The He permeance is virtually unaffected by the decreases in the average pore size, since the minimum pore size is the molecular radius of He and, therefore, all the pores are open and accessible to He. In contrast, the Ar permeance decreases by a factor of about 5 when the average pore size decreases by a factor of about 2. The reason is the percolation effect, which we now describe in more details.

The percolation effect is demonstrated in Fig. 3 where we present the fraction q of the pores that are smaller than the molecular size of argon [see Eq. (19)] and, hence, are inaccessible to it. As the average pore size decreases, the fraction of pores that are inaccessible to Ar increases rapidly. For a pore network with an average pore size r_{a}=0.375 nm, the fraction q of the pores that are inaccessible to Ar is, $q > p_{\text{c}} \simeq 0.25$, where p_{c} is the bond percolation threshold of the simple-cubic network that we

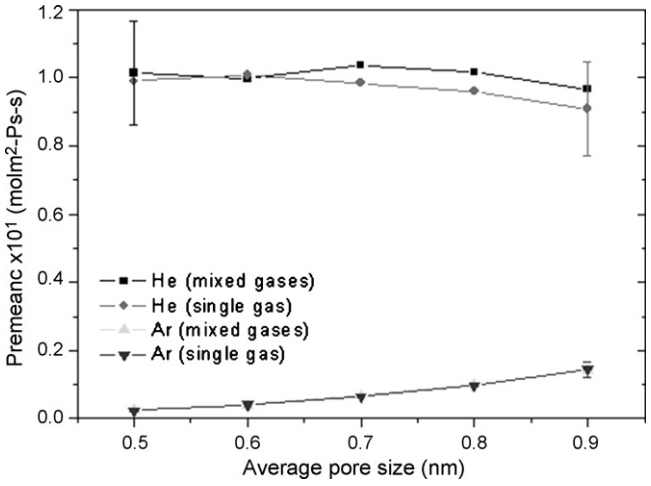

Fig. 2. Comparison of the single- and mixed-gas permeances and their dependence on the average pore size. The PSD is given by Eq. (2), and the connectivity is $Z_{\text{p}} = 6$.

used in the simulations. The bond percolation threshold is the minimum fraction of the open pores for macroscopic transport [30]. Therefore, for a pore network with an average pore size, r_{a}=0.375 nm (which is larger than the molecular radius of Ar which is 0.343 nm), there is no sample-spanning cluster of the pores that are accessible to Ar and, hence, the pore network is effectively closed to argon.

Fig. 4 presents the dependence of the gases' permeances on the thickness L_z of the network. If we keep the cross-sectional area of the network constant, but increase its thickness, the permeance of the two gases decreases by about the same factor. The reason for the decrease in the permeances is again due to the percolation effect. Increasing the thickness while keeping the cross-sectional area constant implies that the pore network becomes elongated. As L_z increases, the network resembles increasingly a two-dimensional system (with lower connectivity), and it is well-known [31] that reducing the dimensionality and connectivity of a network results in reduced permeances.

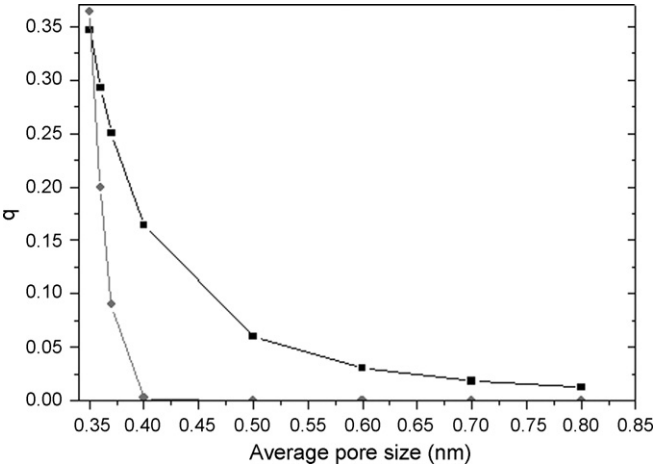

Fig. 3. Dependence of the fraction q of the pores that are closed to Ar, on the average pore size. Squares and circles denote, respectively, the results with Eqs. (2)nd (3).

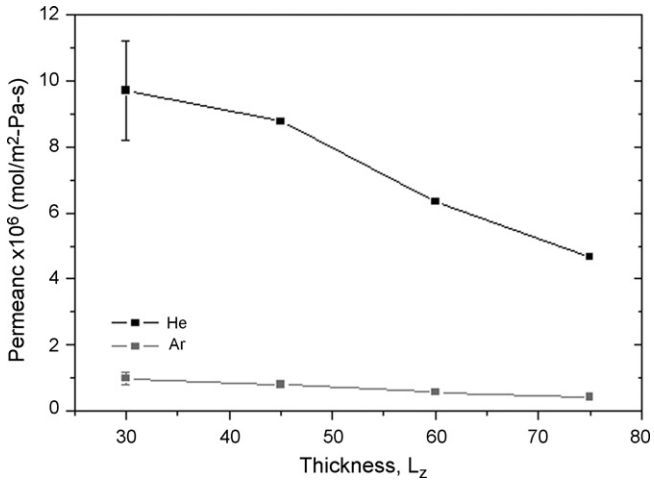

Fig. 4. Dependence of the permeances of the single gases on the network's thickness. The PSD is given by Eq. (2), the average pore size is 0.8 nm, and the connectivity is, $Z_p = 6$.

Since the two permeances decrease by about the same factor, the ideal selectivity remains independent of the thickness. Thus, it is the average pore size (and, hence, the percolation effect) that influences the selectivity and permeances.

The dependence of the ideal selectivity on the average pore size is shown in Fig. 5. Consistent with the results shown in Fig. 2, the selectivity increases as the average pore size decreases. Since the ideal selectivity of the pore network is independent of its thickness L_z, we assume that the network has the same thickness L_z as that of the SiC membrane prepared in our laboratory. Thus, adjusting L_z to be about 1.6 μm, Fig. 2 then indicates that, with an average pore size of 0.8 nm, the permeances of the two gases are (in mol/m^{2}Pa s), $K_{He} \simeq 1.0 \times 10^{-7}$ and, $K_{Ar} \simeq 1.0 \times 10^{-8}$. The experimental values of the two permeances for the SiC membrane are precisely the same [7]. In effect, this is a two-parameter fit of the data, but needs further checking, which is provided by Fig. 5. This figure indicates that, with an average pore size, $r_a = 0.8$ nm, the ideal selectivity is about 10, the same as our experimental data for the ideal selectivity of the nanoporous SiC membrane [7].

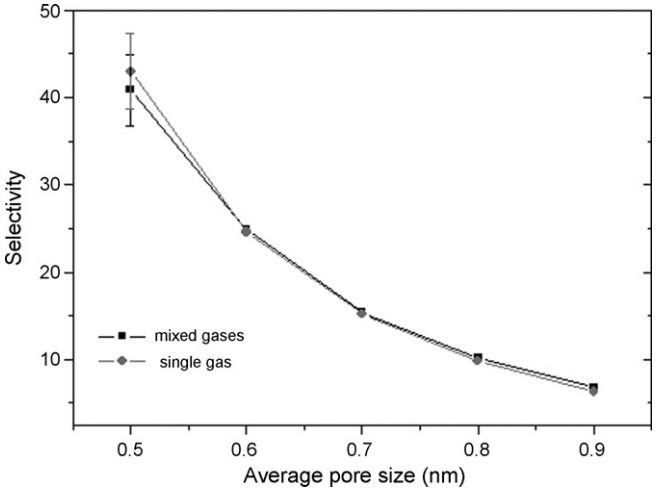

Fig. 5. Comparison of the ideal and mixed-gas selectivities and their dependence on the average pore size. The simulations parameters are the same as those of Fig. 2.

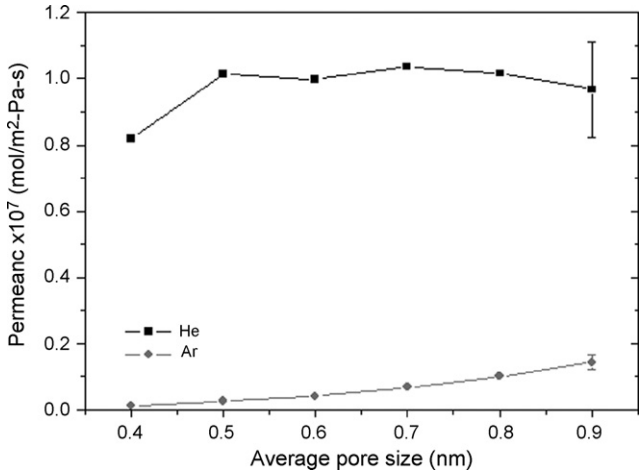

Fig. 6. Dependence of the gases' permeances in the binary mixture on the average pore size. The PSD is given by Eq. (2), and the connectivity is $Z_p = 6$.

5.2. Results for the binary mixture

All the results for the binary mixture were computed for the mole fractions, $x_{He} = x_{Ar} = 0.5$. We also assumed that the network thickness is, $L_z = 1.6$ μm. Fig. 6 presents the effect of the average pore size r_a on the permeance of the two gases in their mixture. The connectivity of the pore network was fixed at $Z_p = 6$. In all the cases, the He permeance is about one order of magnitude larger than that of argon. As the average pore size decreases, so also does the permeance to argon, becoming very small for small r_a, while the He permeance remains more or less constant over much of the range of r_a. Similar to the single-gas results, the near constancy of the He permeance is due to the fact that, so long as the pore sizes are larger than the molecular size of He, there is always a percolating path for helium to flow through the network, whereas the same is not true for Ar.

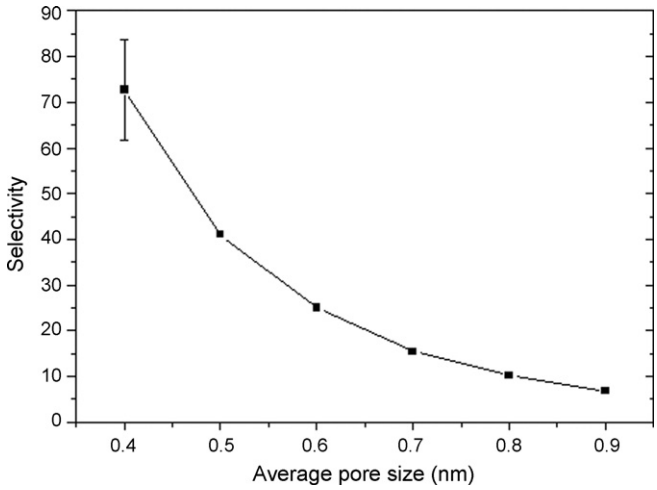

Fig. 7. Dependence of the selectivity of the pore network on the average pore size. The PSD is given by Eq. (2), and the connectivity is $Z_p = 6$.

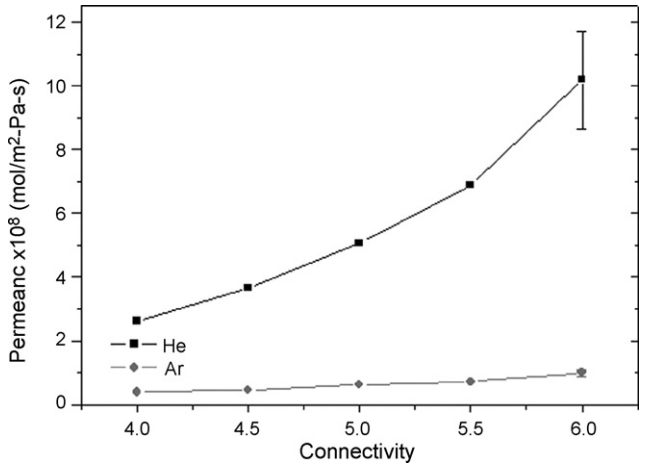

Fig. 8. Effect of pore network connectivity on the gases' permeances in their binary mixture. The PSD is given by Eq. (2) with an average pore size, r_a = 0.8 nm.

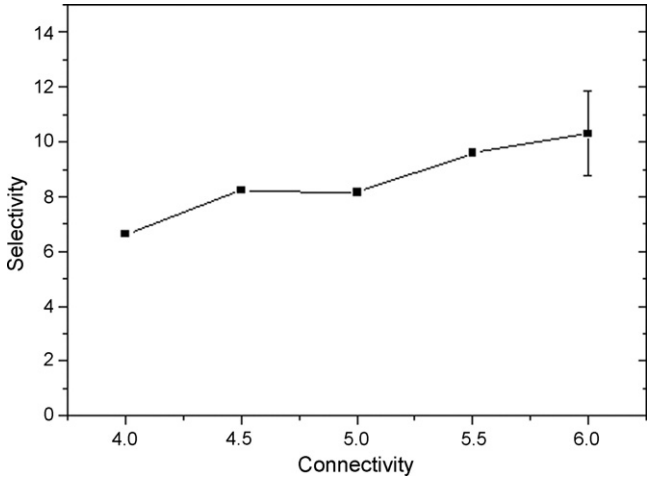

Fig. 9. Dependence of the selectivity on the pore network connectivity. The PSD is given by Eq. (2) with an average pore size, $r_a = 0.8$ nm.

The corresponding selectivities S are shown in Fig. 7. As one might expect, decreasing the average pore size increases the selectivity, as Ar finds it increasingly more difficult to find a percolating path of the accessible pore to pass through the pore network. Fig. 7 indicates that, for $r_a = 0.8$ nm – which is what we identified (see above) to be about the same as the average pore size of our SiC membrane – the selectivity is about 10.3, which is essentially identical with the ideal selectivity of the pore network, as well as that of the membrane.

How do the results for the binary mixture compare with those for the single gases? Figs. 2 and 5 compare the gases' permeances in the mixture with those of the single gases alone, as well as the selectivity for the binary mixture with the ideal selectivity. There is virtually no difference between the permeances for the two cases. As a result, the actual and ideal selectivities, defined by Eqs. (24)nd (25), are also virtually identical. This result is presumably due to the fact that He and Ar do not interact with each other, and do not also adsorb on the pores' surface. As a result, the presence of one gas does not strongly affect the transport of the other.

Next, we studied the effect of the connectivity Z_p on the permeance and selectivity. Fig. 8 presents the results. The average pore size has been fixed at $r_a = 0.8$ nm. The He permeance is much more affected by the average connectivity than that of Ar because, as discussed above, for a fixed connectivity all the pores are larger than the molecular size of He and, therefore, all the pores remain open to it. It is only through reducing the connectivity, i.e., setting the size of some pores to zero (or to a value smaller than the molecular size of He) that He begins to experience the percolation effect and K_{He} starts to decrease. In contrast, as discussed above, since a fraction q of the pores, given by Eq. (19), is always closed to argon, the loss of connectivity has a much weaker effect on K_{Ar}.

The corresponding dependence of the selectivity on the connectivity is shown in Fig. 9. Consistent with Fig. 8, as the connectivity decreases, so also does the selectivity, because reducing the connectivity makes it more difficult for He to pass through the network, while it affects the transport of Ar in a much weaker way. Note that for a connectivity of 6, the selectivity is about 10.2, about the same as the experimental value for the ideal selectivity of both the pore network and the SiC membrane, which is 10. This represents further confirmation of the accuracy of the two-parameter fit of the single-gas results to the experimental data. All the single-gas simulations were carried out for a network connectivity of 6, and the selectivity for the binary gas mixture with an average pore size of 0.8 nm and connectivity 6 is also about 10.2. Thus, we may conclude that, not only is the model self-consistent, but also that the average connectivity of the membrane is about 6.

Next, we study the effect of the network's thickness L_z on the results. Fig. 10 presents the dependence of the two gases' permeances on L_z. The mean pore size is $r_a = 0.8$ nm, and the connectivity, $Z_p = 6$. Both permeances decrease by a factor which is a little over 2, as the thickness is also increased by about the same factor. The reason for the decrease in the permeances is, once again, the percolation effect: increasing the thickness, while keeping the cross-sectional area constant, has the effect of reducing the effective dimensionality of the network. In fact,

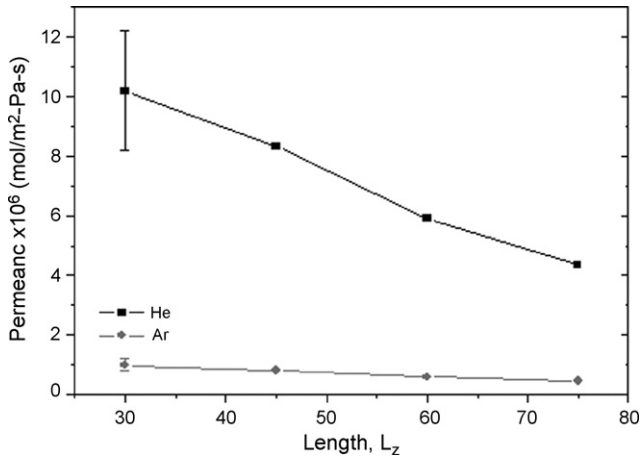

Fig. 10. The dependence of the gases' permeances in their binary mixture on the thickness of the pore network. The PSD is given by Eq. (2) with an average pose size, $r_a = 0.8$ nm. The connectivity is $Z_p = 6$.

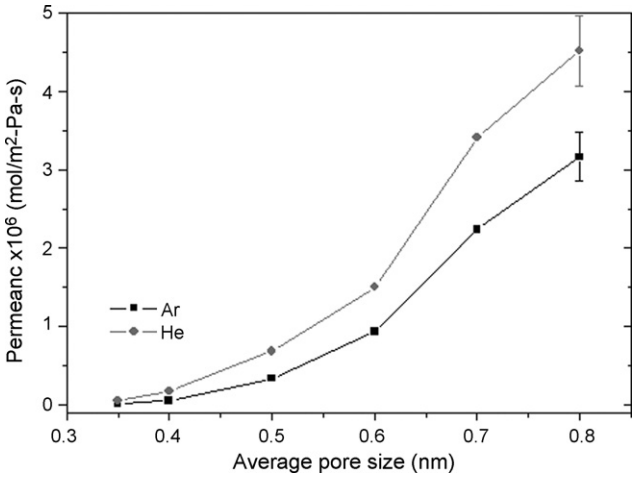

Fig. 11. Dependence of the gases' permeances in their mixture on the average pore size, when only hindered diffusion is the meachism of gas transport. The PSD is given by Eq. (2), and the connectivity is $Z_p = 6$.

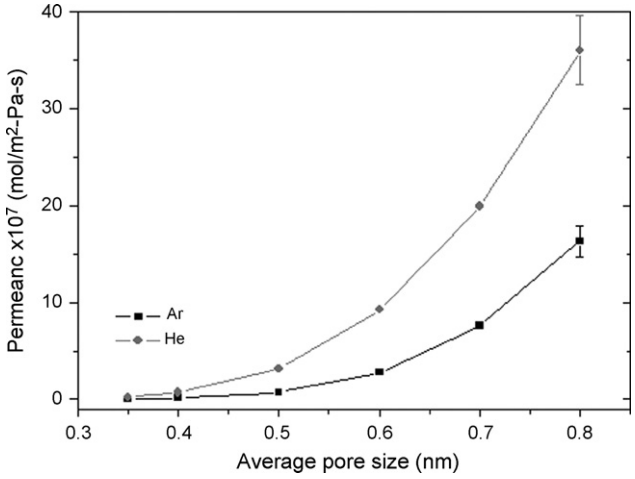

Fig. 13. Same as in Fig. 11, except that the PSD is given by Eq. (3). The standard deviation of the distribution is, $\sigma = 0.02$, and the pore network connectivity is $Z_p = 6$.

if L_z becomes large, the network becomes effectively 2D with reduced connectivity, and as is well known [31], the effective permeability of 2D porous materials with reduced connectivity is smaller than that of 3D materials, even if they both have the same PSD. As a result, selectivity remains essentially independent of the thickness, since the gases' permeances decrease by roughly the same amount as the network thickness increased.

How can we separate the contributions of the three mechanisms of transport of the gases (Knudsen and hindered diffusion, and viscous flow), in order to understand the significance of each? As mentioned above, our simulations indicated that the contribution of viscous flow to the overall rate of the transport is negligible. Therefore, in what follows we do not discuss the effect od viscous flow any further. To discern the contributions of Knudsen and hindered diffusion, we carried out a series of simulations in which only hindered diffusion was included in the computation; Knudsen diffusion was eliminated altogether. The results for the permeances and selectivity are presented in Figs. 11 and 12. The network connectivity was $Z_p = 6$. A comparison between Fig. 11 and Figs. 2 and 6 indicates a drastic difference between the two sets of results. When both Knudsen and hindered diffusion contribute to the transport of the two gases (Figs. 2 and 6), there is an order of magnitude difference between the permeances of the two gases, whereas with hindered diffusion alone (Fig. 11) the two permeances follow very similar dependence on the mean pore size. Moreover, with hindered diffusion alone, the gases' permeances are significantly larger than the case when both Knudsen and hindered diffusion contribute to the transport process. As a result, the selectivity for the binary mixture remains low when only hindered diffusion is the main mechanism of gas transport process, given the PSD, r_a and Z_p values that we used. Note that, as Fig. 12 indicates, even when the average pore size is about 0.35 nm, the selectivity is only about 6.

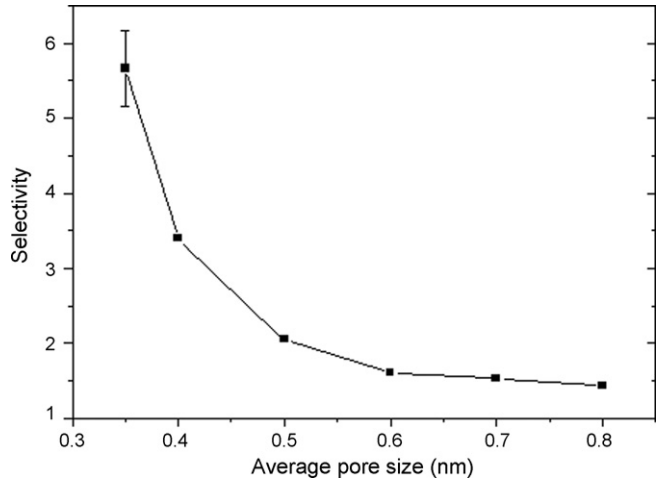

Fig. 12. The selectivities that correspond to the permeances shown in Fig. 11.

This rather surprising result can be explained based on the percolation effect. According to Eq. (19) and Fig. 3, when the average pore size is 0.8 nm, over 90% of all the pores have a size larger than the molecular size of argon, if the PSD (2) (see Fig. 1) is used. This is due to the long tail of the PSD (2), which gives rise to a significant number of relatively large pores. Under such conditions, it is Knudsen diffusion which is the dominant mechanism of gas transport and, therefore, in its absence the selectivity is low. Only when the average pore size decreases to very low values, and the percolation effect begins to have a strong influence on the Ar transport, do we see a mild rise in the selectivity, shown in Fig. 12.

To understand this better, we used the Gaussian PSD given by Eq. (3), and carried out a series of simulations in which only hindered diffusion contributed to the transport of the gases in the network. We used a standard deviation, $\sigma = 0.02$ nm, and a connectivity $Z_p = 6$. Due to the symmetry of the distribution, there are as many pores with $r_p < r_a$ as there are with $r_p > r_a$ and, therefore, the effect of the long tail of the PSD (2) is eliminated. The results are shown in Figs. 13 and 14. As Fig. 13 indicates, there is a larger difference between the two permeances than what is indicated by Fig. 11. Moreover, as Fig. 14 indicates, as the average pore size is reduced to 0.35 nm, the selectivity rises sharply to about 20, which is in contrast with Fig. 11.

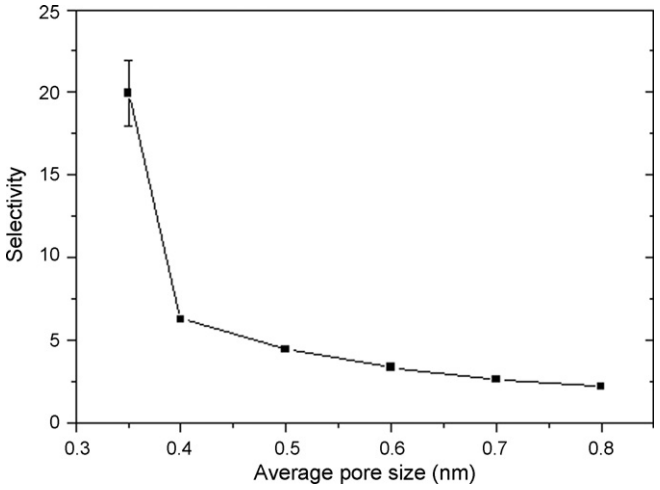

Fig. 14. The selectivities that correspond to the permeances shown in Fig. 13.

These results indicate that: (i) Knudsen diffusion is still very important in pores as small as 7 Å; (ii) the tail of the PSD distribution has a strong effect on the separation process; and (iii) the percolation effect, manifested through the connectivity of the accessible pores, plays a role in a membrane's selectivity which is at least as important as that of the PSD.

6. Summary and conclusions

A three-dimensional pore network model was developed for studying transport and separation of a binary gas mixture through a nanoporous membrane. The sizes of the pores were distributed according to a PSD, for which we used two different distributions. The connectivity of the network and its thickness were also varied in order to study their effect on the transport of the gases. Knudsen and hindered diffusion, as well as viscous flow, were included in the model as the mechanisms of mass transport, although our simulations indicated that the contribution of viscous flow, over the range of the pore sizes that we considered, is negligible. However, with a broader PSD and larger pores, the effect of viscous flow may become important, in which case the model can take its effect into account.

It was demonstrated that, provided that the network is large enough, adjusting the thickness of the network and its average pore size – a two-parameter fit of the simulation result – provide estimates for the permselective properties of the network that are in excellent agreement with the experimental data. Moreover, the model demonstrates the fundamental importance of two factors to the permselectivity of a membrane, namely, the tail of the PSD, and the percolation effect manifested through the connectivity of the pores that are accessible to the gas molecules. In addition, the results indicate that Knudsen diffusion is the dominant mechanism of gas transport in pores as small as 0.7 nm.

Acknowledgments

We are grateful to the National Science Foundation, the Department of Energy, and Media & Process Technology for partial support of this work. We would like to thank Raudel Sanchez for very helpful discussions regarding the numerical solution of the governing equations.

References

[1] V. Ambegaokar, B.I. Halperin, J.S. Langer, Hopping conduction in disordered systems, Phys. Rev. B 4 (1971) 2612.
[2] R.B. Bird, W.E. Stewart, E.N. Lightfoot, Transport Phenomena, 2nd revised ed., Wiley, New York, 2007.
[3] H. Brenner, L.J. Gaydos, The constrained Brownian movement of spherical particles in cylindrical pores of comparable radius, J. Colloid Interf. Sci. 58 (1977) 312.
[4] V.N. Burganos, A.C. Payatakes, Knudsen diffusion in random and correlated networks of constricted pores, Chem. Eng. Sci. 47 (1992) 1383.
[5] V.N. Burganos, S.V. Sotirchos, Diffusion in pore networks. Effective medium theory and smooth-field approximation, AIChE J. 33 (1987) 1678.
[6] V.N. Burganos, S.V. Sotirchos, Knudsen diffusion in parallel multidimensional or randomly oriented capillary structures, Chem. Eng. Sci. 44 (1989) 2451.
[7] F. Chen, R. Mourhatch, T.T. Tsotsis, M. Sahimi, Experimental studies and computer simulation of preparation of nanoporous silicon–carbide membranes by chemical-vapor deposition and infiltration techniques, Chem. Eng. Sci. 63 (2008) 1470.
[8] R.J. Ciora, B. Fayyaz, P.K.T. Liu, V. Suwanmethanond, R. Mallada, M. Sahimi, T.T. Tsotsis, Preparation and reactive applications of nanoporous silicon carbide membranes, Chem. Eng. Sci. 59 (2004) 4957.
[9] W.M. Deen, Hindered transport of large molecules in liquid-filled pores, AIChE J. 33 (1987) 1409.
[10] T. Duren, F.J. Keil, N.A. Seaton, Composition dependent transport diffusion coefficients of CH_4/CF_4 mixtures in carbon nanotubes by non-equilibrium molecular dynamics simulations, Chem. Eng. Sci. 57 (2002) 1343.
[11] T. Duren, S. Jakobtorweihen, F.J. Keil, N.A. Seaton, Grand canonical molecular dynamics simulations of transport diffusion in geometrically heterogeneous pores, Phys. Chem. Chem. Phys. 5 (2003) 369.
[12] B. Elyassi, M. Sahimi, T.T. Tsotsis, Silicon carbide membranes for gas separation applications, J. Membr. Sci. 288 (2007) 290.
[13] Elyassi, B., Sahimi, M., Tsotsis, T.T., A novel sacrificial interlayer-based method for the preparation of silicon carbide membranes, J. Membr. Sci., in press.
[14] L.D. Gelb, K.E. Gubbins, R. Radhakrishna, M. Sliwinska-Bartkowiak, Phase separation in confined systems, Rep. Prog. Phys. 62 (1999) 1573.
[15] J. Ghassemzadeh, L. Xu, T.T. Tsotsis, M. Sahimi, Statistical mechanics and molecular simulation of adsorption of gas mixtures in microporous materials: pillared clays and carbon molecular sieve membranes, J. Phys. Chem. B 104 (2000) 3892.
[16] F.J. Keil, Diffusion and reaction in porous networks, Catal. Today 53 (1999) 245.
[17] R. Krishna, J.A. Wesselingh, The Maxwell–Stefan approach to mass transfer, Chem. Eng. Sci. 52 (1997) 861.
[18] J.M.D. MacElroy, N.A. Seaton, S.P. Friedman, Sorption rate processes in carbon molecular sieves. Equilibria and Dynamics of Gas Adsorption in Heterogeneous Solid Surfaces, vol. 104, Elsevier, Amsterdam, 1997, p. 837.
[19] E. Mason, A.P. Malinauskas, Gas Transport in Porous Media The Dusty Gas Model, Elsevier, Amsterdam, 1983.
[20] G.M. Mavrovouniotis, H. Brenner, Hindered sedimentation, diffusion, and dispersion coefficients for Brownian spheres in cylindrical pores, J. Colloid Interf. Sci. 124 (1988) 269.
[21] J.R. Pappenheimer, E.M. Renkin, L.M. Barrero, Filtration, diffusion, and molecular sieving through peripheral capilliary membranes pores, Am. J. Physiol. 67 (1951) 13.
[22] J.H. Petropoulos, J.K. Petrou, A.I. Liapis, Network model inverstigation of gas transport in bidisperse porous adsorbents, Ind. Eng. Chem. Res. 30 (1991) 1281.
[23] T.J. Pinnavaia, M.F. Thorpe (Eds.), Access in Nanoporous Materials, Plenum, New York, 1995.

[24] E.M. Renkin, Filtration, diffusion, and molecular sieving through porous cellulose membranes, J. Gen. Physiol. 38 (1954) 225.
[25] C. Rieckmann, F.J. Keil, Multicomponent diffusion and reaction in three-dimensional networks: general kinetics, Ind. Eng. Chem. Res. 36 (1997) 3275.
[26] C. Rieckmann, F.J. Keil, Simulation and experiment of multicomponent diffusion and reaction in three-dimensional networks, Chem. Eng. Sci. 54 (1999) 3485.
[27] M. Sahimi, Transport of macromolecules in porous media, J. Chem. Phys. 96 (1992) 4718.
[28] M. Sahimi, Nonlinear transport processes in disordered media, AIChE J. 39 (1993) 369.
[29] M. Sahimi, Flow phenomena in rocks: from continuum models to fractals, percolation, cellular automata, and simulated annealing, Rev. Mod. Phys. 65 (1993) 1393.
[30] M. Sahimi, Applications of Percolation Theory, Taylor and Francis, London, 1994.
[31] M. Sahimi, Flow and Transport in Porous Media and Fractured Rock, VCH, Weinheim, Germany, 1995.
[32] M. Sahimi, Heterogeneous Materials I Linear Transport and Optical Properties, Springer, New York, 2003.
[33] M. Sahimi, G.R. Gavalas, T.T. Tsotsis, Statistical and continuum models of fluid–solid reactions in porous media, Chem. Eng. Sci. (1990) 1443.
[34] M. Sahimi, V.L. Jue, Diffusion of large molecules in porous media, Phys. Rev. Lett. 62 (1989) 629.
[35] M. Sahimi, T.T. Tsotsis, Molecular pore network models of nanoporous materials, Physica B 338 (2003) 291.
[36] M. Sahimi, T.T. Tsotsis, M. Rieth, W. Schommers, in: Handbook of Theoretical and Computational Nanotechnology, American Scientific, New York, 2006, Chapter 10.
[37] N.A. Seaton, S.P. Friedman, J.M.D. MacElroy, B.J. Murphy, The molecular sieving mechanism in carbon molecular sieves: a molecular dynamics and critical path analysis, Langmuir 13 (1997) 1199.
[38] M.G. Sedigh, W.J. Onstot, L. Xu, W.L. Peng, T.T. Tsotsis, M. Sahimi, Experiments and simulation of transport and separation of gas mixtures in carbon molecular sieve membranes, J. Phys. Chem. A 102 (1998) 8580.
[39] M.G. Sedigh, L. Xu, T.T. Tsotsis, M. Sahimi, Transport and morphological characteristics of polyetherimide-based carbon molecular sieve membranes, Ind. Eng. Chem. Res. 38 (1999) 3367.
[40] M.G. Sedigh, M. Jahangiri, P.K.T. Liu, M. Sahimi, T.T. Tsotsis, Structural characterization of polyetherimide-based carbon molecular sieve membranes, AIChE J. 46 (2000) 2245.
[41] S.V. Sotirchos, Multicomponent diffusion and convection in capillary structures, AIChE J. 35 (1989) 1953.
[42] V. Suwanmethanond, E. Goo, P.K.T. Liu, G. Johnston, M. Sahimi, T.T. Tsotsis, Porous silicon carbide sintered substrates for high-temperature membrane, Ind. Eng. Chem. Res. 39 (2000) 3264.
[43] R. Taylor, R. Krishna, Multicomponent Mass Transfer, Wiley, New York, 1993.
[44] L. Xu, T.T. Tsotsis, M. Sahimi, Nonequilibrium molecular dynamics simulations of transport and separation of gas mixtures in nanoporous materials, Phys. Rev. E 62 (2000) 6942.
[45] L. Xu, T.T. Tsotsis, M. Sahimi, Statistical mechanics and molecular simulation of adsorption of ternary gas mixtures in nanoporous membranes, J. Chem. Phys. 114 (2001) 7196.
[46] A.M. Vieira-Linhares, N.A. Seaton, Pore network connectivity effects on gas separation in a microporous carbon membrane, Chem. Eng. Sci. 58 (2003) 5251.
[47] L. Zhang, N.A. Seaton, Prediction of the effective diffusivity in pore networks close to a percolation threshold, AIChE J. 38 (1992) 1816.

ELSEVIER

Chemical Engineering Science 63 (2008) 1460–1470

Chemical Engineering Science

www.elsevier.com/locate/ces

Experimental studies and computer simulation of the preparation of nanoporous silicon-carbide membranes by chemical-vapor infiltration/chemical-vapor deposition techniques

Feng Chen, Rayan Mourhatch, Theodore T. Tsotsis, Muhammad Sahimi*

Mork Family Department of Chemical Engineering and Material Science, University of Southern California, Los Angeles, CA 90089-1211, USA

Received 9 July 2007; received in revised form 26 November 2007; accepted 3 December 2007
Available online 5 December 2007

Abstract

Preparation of asymmetric nanoporous silicon-carbide membranes using chemical-vapor infiltration/chemical-vapor deposition (CVI/CVD) is described. We use macroporous SiC disks and tubes as supports, and tri-isopropylsilane as the precursor. Experimental data for the permeation and selectivity of the membranes are presented. We also develop two dynamic models to describe the preparation of the membranes. The models are shown to provide accurate predictions for the experimental data for the permeation characteristics of the membranes, as a function of the preparation conditions.

Keywords: Nanoporous membranes; Knudsen diffusion; Hindered diffusion; Chemical-vapor deposition; Chemical-vapor infiltration; Numerical simulation

1. Introduction

Inorganic membranes have been attracting much attention for industrial separations of mixtures into their constituent components, since they can be effective at the high temperatures at which the polymeric membranes are not capable of functioning (see, for example, Sanchez and Tsotsis, 2002). As a result, considerable efforts have been devoted in recent years to producing high-temperature ceramic (alumina, silica, and zeolite) and metal (Pd, Ag, and their alloys) membranes, which exhibit much improved properties over the polymeric membranes. They have, however, proven, unsatisfactory in terms of their performance and/or material stability in high-temperature applications, particularly in the presence of steam.

Over the past few years, we have been developing a new inorganic membrane which overcomes such difficulties. It is made of silicon carbide, a promising material with high fracture toughness and thermal shock resistance, which is also capable of withstanding high temperatures and corrosive environments. Various aspects of preparation of such membranes have been reported by our group (Suwanmethanond et al., 2000; Ciora et al., 2004; Elyassi et al., 2007a, b), as well as others (for brief reviews see, for example, Elyassi et al., 2007a, b). Two distinct approaches may be used to prepare SiC membranes. One is based on the use of chemical-vapor infiltration (CVI)/chemical-vapor deposition (CVD), while the second one utilizes pyrolysis of a polymeric precursor. The first method has been used by several groups. For example, Takeda et al. (2001) prepared SiC membranes by the CVI using SiH_2Cl_2 and C_2H_2, diluted with H_2, and γ-Al_2O_3 tubes as supports. Sea et al. (1998) prepared a SiC membrane using an α-alumina tube as the support, and used CVD of $(C_3H_7)_3SiH$ at 700–800 °C.

Our group was the first (Ciora et al., 2004) to report preparation of nanoporous SiC membranes using the CVD technique. We utilized tri-isopropylsilane (TPS), $(C_3H_7)_3SiH$, as the precursor to form the SiC nanoporous layer on porous alumina substrates. The membranes were characterized for their permeance, selectivity, and hydrothermal stability. Depending on the preparation conditions, their He permeance ranged from 8×10^{-8} to 1.7×10^{-6} mol/m^2 s Pa, with a He/N_2 selectivity ranging from 4 to larger than 100. More recently, we have prepared improved nanoporous SiC membrane using the technique

* Corresponding author. Tel.: +1 213 740 2064; fax: +1 213 740 8053.
E-mail address: moe@iran.usc.edu (M. Sahimi).

0009-2509/$ - see front matter © 2007 Elsevier Ltd. All rights reserved.
doi:10.1016/j.ces.2007.12.001

of sacrificial layers (Elyassi et al., 2007b) and have obtained membranes with very high selectivity.

In this paper we report the results of our ongoing investigations of the preparation of asymmetric nanoporous SiC membranes using CVI/CVD of the TPS. We utilize porous SiC disks and tubes as the supports (Suwanmethanond et al., 2000). Using SiC porous substrates, instead of such materials as porous alumina, to prepare the nanoporous membranes minimizes difficulties that may potentially arise due to the mismatch in the thermal expansion coefficients between the thin membrane layers and the underlying porous support. The current focus of our work is on understanding the CVI/CVD processes themselves, and the effect of the various preparation parameters that determine the rate of deposition of the SiC film, and the transport characteristics of the resulting membranes. A better fundamental understanding of the various physicochemical processes that take place during formation of the SiC film is of vital importance to optimizing the preparation conditions and controlling the final characteristics of the resulting membranes.

The present work combines theory and experiments in order to study the various phenomena that take place during the membrane formation. We describe the development of dynamic models of the membrane fabrication process, for both the disk-shaped and tubular membranes, using the CVI/CVD technique, which we show to properly account for the reaction, fluid mechanics, and the transport processes that take place inside the reactor and membranes. As described below, the numerical solutions of the models correctly predict key characteristics of the membranes, such as their permeance and the evolution of their porosity as functions of the deposition time and other experimental conditions.

Considerable efforts have been devoted in the past to modelling of the CVD process of solid materials inside porous substrates. For example, Lin and Burggraaf (1991) developed a phenomenological continuum model for the CVI/CVD preparation of reinforced ceramic-matrix composites. Tsapatis and Gavalas (1992) developed a model in order to describe reaction and diffusion in, and evolution of, a porous structure made of porous Vycor tubes during deposition of silica and alumina by the CVD process. Lin and Burggraaf (1992) and Brinkman et al. (1993) developed models for the analysis of the fabrication of various ceramic membranes by the CVD process. Jensen et al. (1991), Komiyama et al. (1999), and Dollet (2004) reviewed the state-of-the-art of the modelling of the CVD processes for the growth of thin films.

The rest of this paper is organized as follows. In the next section we describe the preparation of the disk-shaped and tubular SiC membranes and present the experimental data. Section 3 describes a dynamic model for the phenomena that take place during preparation of the disk-shaped membrane by the CVI/CVD and presents its predictions for the permeance of argon through the membrane, while Section 4 does the same, but for the tubular membrane. The paper is summarized in Section 5, where we also describe possible future directions in this area of research.

2. Preparation of the membranes

Fig. 1 presents the schematic of our CVI/CVD apparatus. In the experiments we utilized SiC porous disks with a diameter of 1.2 cm and thickness of 0.2 cm as the support for the membrane preparation. The disks had an average pore size (radius) of 28 nm and were prepared by the techniques described in an earlier paper (Suwanmethanond et al., 2000). We also used 5 cm-long tubular supports, the outside and inside diameters of which were, respectively, 1.27 and 0.63 cm.

Prior to using the supports for membrane preparation, they were treated in flowing air at 450 °C, in order to remove any excess carbon that could be present. The TPS (purchased from the Aldrich Company) was used without any further purification. Ultra-high pure Ar and He (both with 99.999% purity) were used as the carrier gases, and their flow rates were controlled by mass-flow controllers (Brooks 5850E). The diameter and length of the hot-wall CVI reactor, shown in Fig. 1, were, respectively, 3.8 and 73 cm, with the length of the hot zone being 20 cm. Prior to the deposition, the porous support disk was sealed on top of a quartz tube (1 cm ID) using a glass powder (No. 7740, purchased from the Corning Company) as the sealant. The quartz tube, with the SiC on its top surface, was then coaxially inserted into the center of the reactor, and the two were connected with the aid of a Cajon™ Utra-Torr fitting. A ceramic cylindrical heater was used to heat up the reactor with the temperature being controlled by an OMEGA controller (CN 9000). A syringe pump (Harvard, PHD2000) was used to inject the TPS precursor into the carrier gas at a pre-determined rate. The feed lines from the pump to the furnace were heat-traced and kept at 140 °C at all times, in order to ensure that the TPS was in the vapor phase before entering the reactor. In the experiments reported here, the pressure inside the larger tube (the reactor) was kept constant at $\sim$ 1.2 atm, while the pressure of the inside (quartz) tube was kept at $\sim$ 1.0 atm, both of which were monitored with the aid of pressure (or vacuum) gauges. The reactor and the quartz tube could also be operated under vacuum conditions with the aid of mechanical pumps. The flow rate of the TPS was varied between 1×10^{-8} and 5×10^{-8} mol/s, while the Ar flow rate changed from 2×10^{-5} to 9×10^{-5} mol/s. The deposition time was between 5 and 30 h.

The membrane characteristics—permeance and permselectivity—were measured on-line during the CVI/CVD processes. In the temperature range, 760–800 °C, the Ar permeance, K_{Ar}, varied from 4×10^{-8} to 1×10^{-6} mol/Pa s m^2. Figs. 2 and 3 present the typical data obtained with one of the SiC disks with an initial porosity of $\varepsilon_0 = 0.3$ which, prior to the deposition, had an Ar permeance of 1.8×10^{-7} mol/Pa s m^2. In these experiments the flow rate of the TPS was set at 4.3×10^{-8} mol/s, and the deposition temperature in the hot zone at 1033 K. The permeances of Ar and He, measured in situ during the CVI/CVD deposition experiments, are shown in Fig. 2. During the first 13 h of the experiment, the permeances of both He and Ar decreased as the deposition proceeded. However, the He permeance decreased more slowly than that of Ar and, as a result, as shown in Fig. 3, the ideal selectivity, $S = K_{He}/K_{Ar}$, increased steadily. This behavior may be explained as follows. Since the

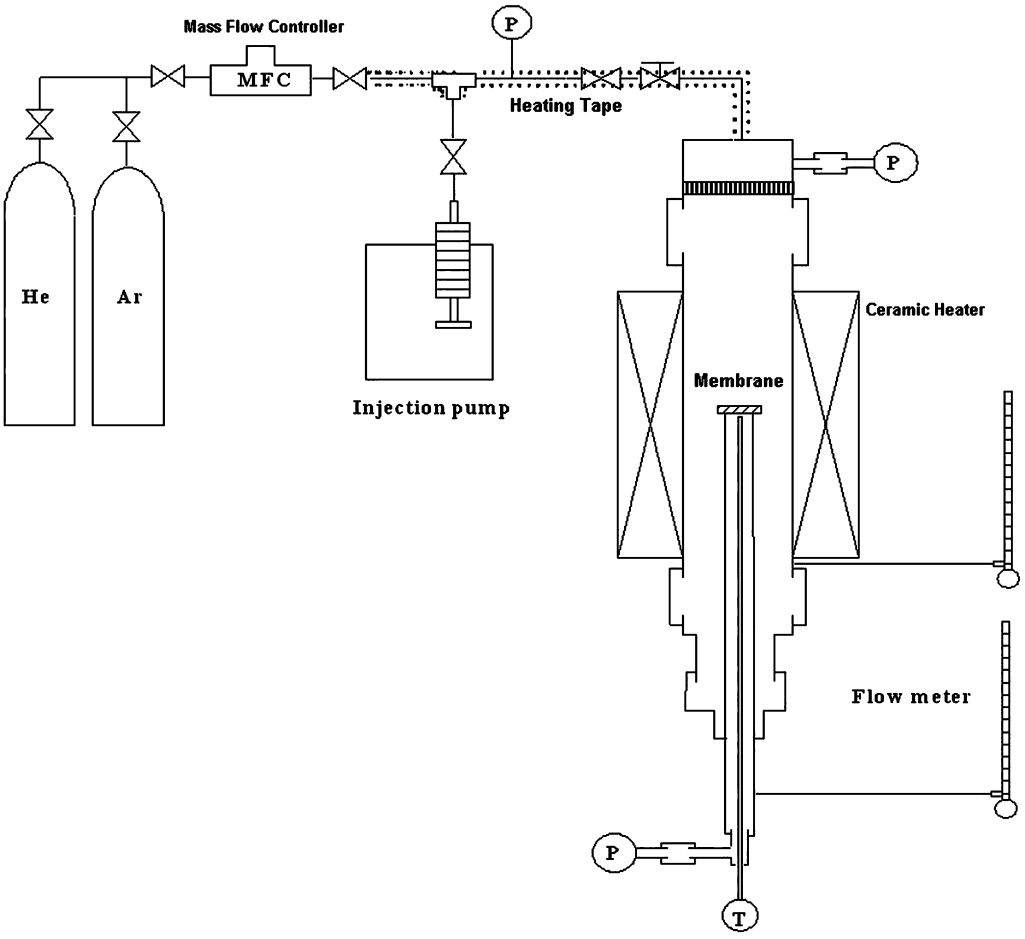

Fig. 1. Schematic of the apparatus used for the preparation of the disk-shaped membrane.

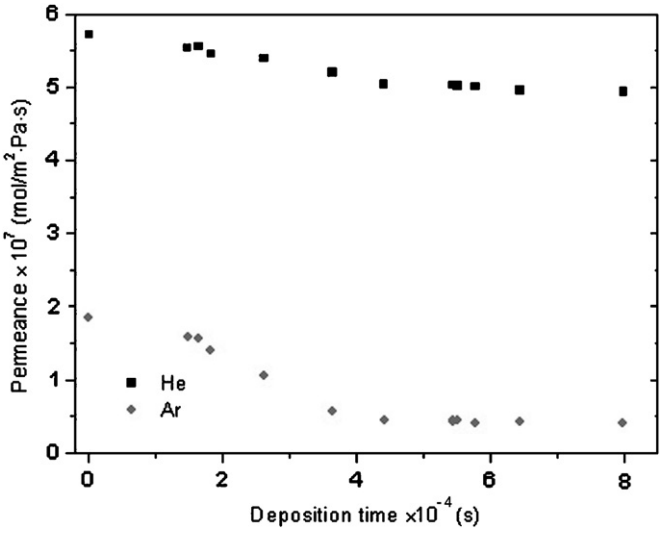

Fig. 2. Dependence of the gases permeances on the deposition time in the disk-shaped membrane.

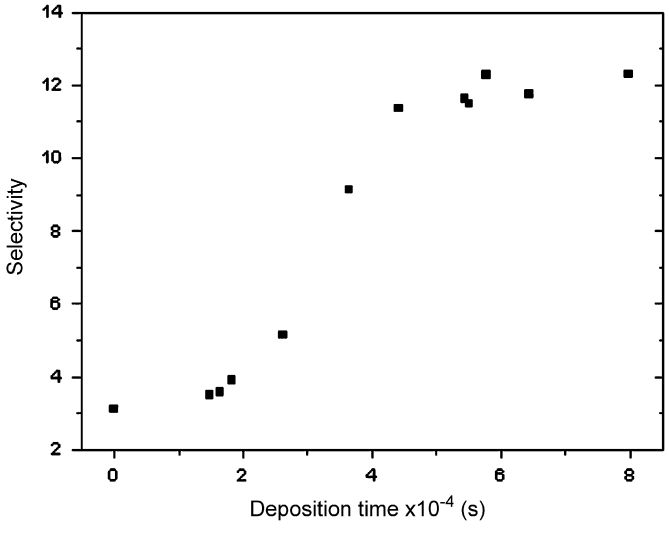

Fig. 3. Ideal selectivity of the disk-shaped membrane as a function of the deposition time.

disk is a mesoporous material at the beginning of the experiments, Ar and He were both transported by Knudsen diffusion. As the TPS decomposed into SiC and gradually filled the membrane pores, the average pore size decreased, which resulted in decreasing the permeance for both He and Ar. Since He is the smaller of the two molecules, it can penetrate through a

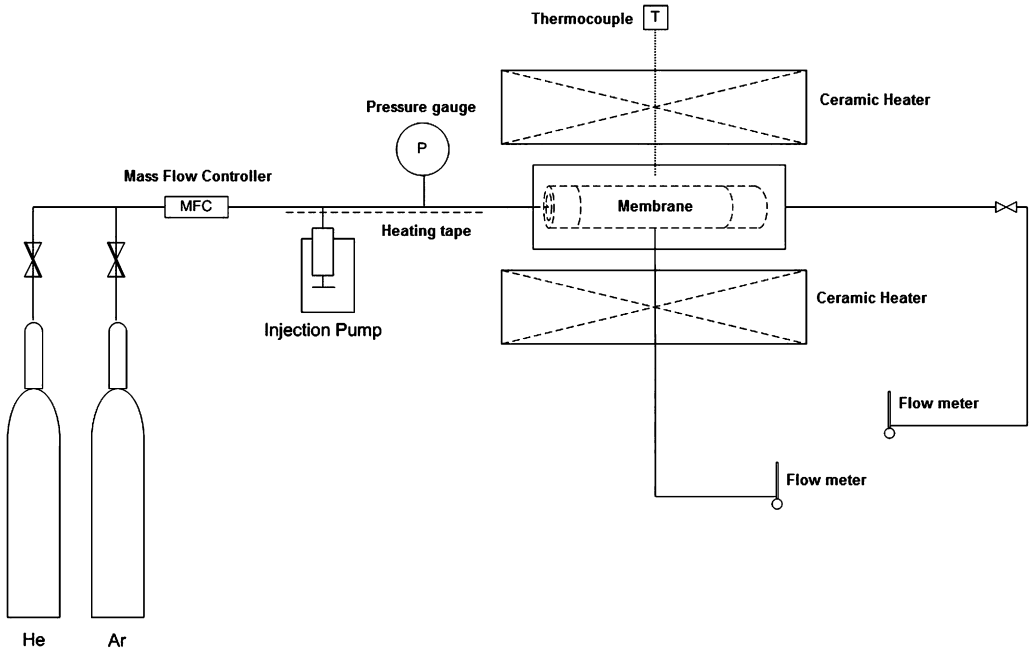

Fig. 4. Schematic of the apparatus used for the preparation of the tubular membrane.

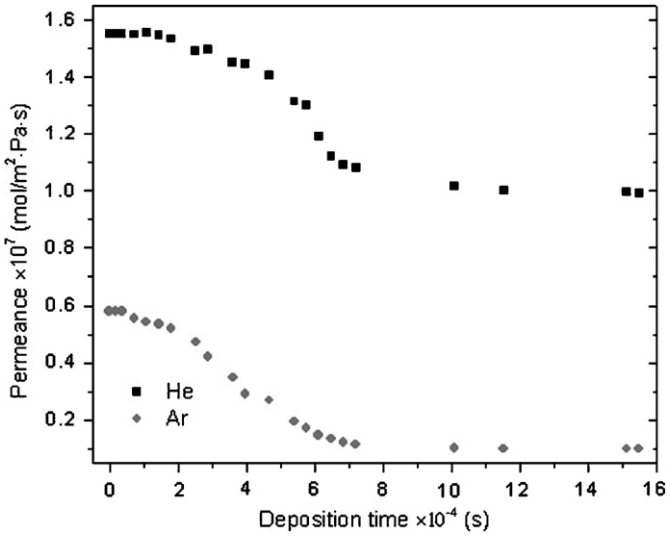

Fig. 5. Dependence of the gases' permeances on the deposition time in the tubular membrane.

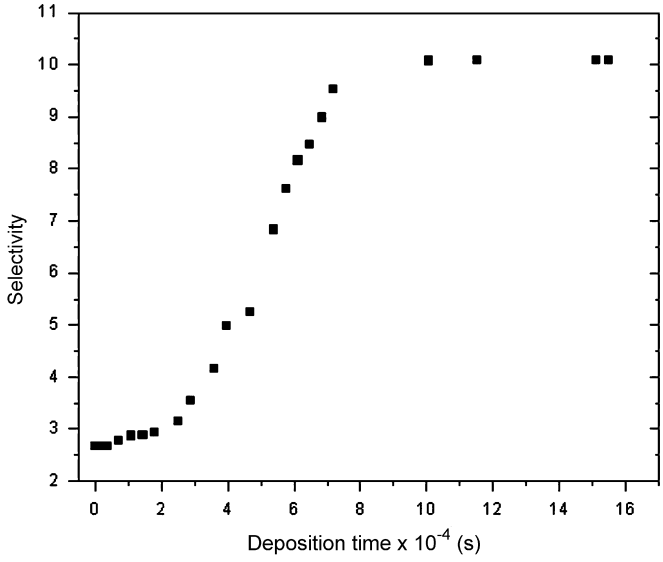

Fig. 6. Ideal selectivity of the tubular membrane as a function of the deposition time.

larger fraction of small unplugged pores than Ar, by an activated diffusion mechanism and, therefore, plugging of the pore space affected its permeance less than that of Ar.

The experiments for the preparation of the tubular membrane were similar to those for the pellet membrane described above, except that the reactor geometry was different. Fig. 4 presents the schematic of the apparatus used in the experiments.

Fig. 5 presents the permeance of Ar and He in the tubular membrane, as the deposition proceeded. During the first 22 h the two permeances decreased with the deposition time, after which they became stable and constant. Another way of seeing this is by inspecting how the membrane's ideal selectivity varies with the deposition time. This is shown in Fig. 6 which indicates that the selectivity became constant after about 22 h. The selectivity of the tubular reactor, which is about 10, is similar to that of the disk-shaped membrane shown in Fig. 3, hence indicating that the two different sets of experiments and different geometries actually follow the same mechanisms of SiC deposition and formation of the membranes' nanopore space.

Fig. 7 presents the temperature dependence of the He and Ar permeances in the tubular membrane. Raising T from the room temperature to about 750 °C changes the He permeance

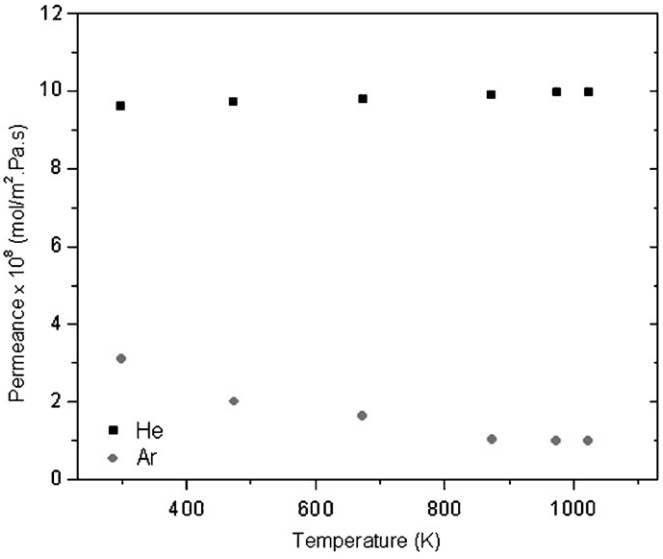

Fig. 7. Temperature dependence of the gases' permeances in the tubular membrane.

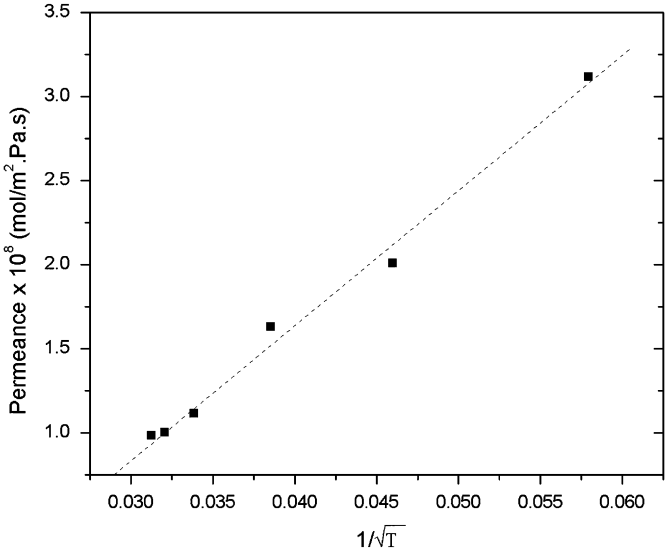

Fig. 8. Plot of the Ar permeance versus $1/\sqrt{T}$, indicating that Knudsen diffusion is the main mechanism of transport.

only slightly, which is indicative of the dominance of the activated diffusion. On the other hand, the Ar permeance, which has a kinetic diameter larger than that of He, increased as the temperature decreases, which is indicative of the significance of Knudsen diffusion. As Fig. 8 indicates, a plot of the Ar permeance versus $1/\sqrt{T}$ produces a straight line, the expected behavior for the temperature dependence of the Knudsen diffusion.

3. Theoretical modelling and computer simulation of the CVI/CVD preparation of the disk-shaped membranes

Fig. 9 presents the schematic of the phenomena that are likely to occur during the formation of the SiC membrane (Kusakabe et al., 1996). The TPS is carried by Ar into the support's pore space, where it reacts to form SiC on the pores' surface which gradually shrinks the pores and reduces the membrane's permeance. Our own experiments, as well as those of several other groups, indicated that the gas-phase reaction is insignificant. For example, Boo et al. (2000) found a very high sticking coefficient for the SiC source growth on the SiC substrate. Park et al. (2000) and Valente et al. (2004) reported that the SiC surface has a very strong reaction potential for the SiC source. Therefore, we assume that the main reaction occurs on the pores' solid surface.

A gas is transported through a porous membrane by four main mechanisms, namely, molecular, Knudsen, and hindered or configurational diffusion, and viscous flow. In principle, surface flow might also play a role in transport through very small pores. It is very difficult, however, to quantify the effect of surface flow without introducing several empirical parameters. Moreover, in small pores where the ratio of the molecules and the pores' sizes is close to 1, it is difficult, and indeed not clear, how to distinguish surface flow from hindered transport that we include in the modelling. Therefore, we ignored the effect of surface flow.

Molecular diffusion and viscous flow occur only in large pores. Since the support that we used has an average pore size which is smaller than the mean-free paths of He and Ar, we only include hindered and Knudsen diffusion in our model. Because the disk's radius is much larger than its thickness, a one-dimensional (1D) system should suffice for modelling the phenomena. Thus, the continuity equations for two species A and B are given by

$$\frac{\partial[\varepsilon_p(q)C_A]}{\partial t}+\frac{\partial q}{\partial t}=\frac{\partial}{\partial z}\left[\frac{\varepsilon_p(q)}{\tau}D_{eA}\frac{\partial C_A}{\partial z}\right], \tag{1}$$

$$\frac{\partial[\varepsilon_p(q)C_B]}{\partial t}=\frac{\partial}{\partial z}\left[\frac{\varepsilon_p(q)}{\tau}D_{eB}\frac{\partial C_B}{\partial z}\right]. \tag{2}$$

Here, C_A represents the molar concentration of the intermediate species responsible for the SiC growth, C_B the molar concentration of the carrier gas (Ar), $\varepsilon_p(q)$ the local porosity with q being the amount of deposited SiC (mol Si/m^3), and τ the tortuosity factor. We assume that while the local porosity changes as a result of the SiC deposition, the tortuosity factor remains invariant.

The effective diffusivity for both species A and B is given by

$$\frac{1}{D_e}=\frac{1}{D_K}+\frac{1}{D_H}, \tag{3}$$

where D_K and D_H represent, respectively, the Knudsen and hindered diffusivities. In general, the expression that relates D_e to D_K and D_H is more complex than Eq. (3), and involves the concentrations (or mole fractions) of the gases in the mixture (Chen et al., 2007). We find, however, that Eq. (3) provides adequate estimates of D_e (see below). The Knudsen diffusion coefficient of B (Ar) is described by

$$D_{BK}=\frac{8}{3}R_p\left(\frac{R_gT}{2\pi M_{\mathrm{Ar}}}\right)^{1/2}, \tag{4}$$

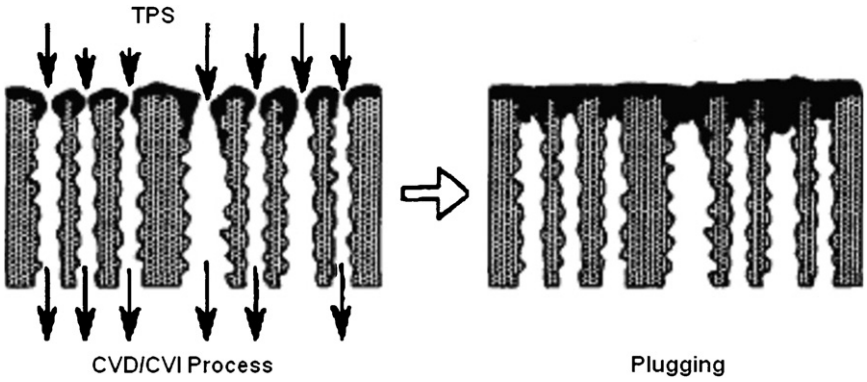

Fig. 9. Schematic of the deposition process, and shrinkage and plugging of the membrane's pores (after Kusakabe et al., 1996).

where T is the temperature, R_g the gas constant, M_{Ar} the molecular weight of Ar, and R_p the pore size which is described by

$$\frac{R_p^2}{R_{p0}^2} = \frac{\varepsilon_p(q)}{\varepsilon_{p0}}. \tag{5}$$

Here, R_{p0} and ε_{p0} are the initial pore size and porosity of the substrate, prior to deposition. The Knudsen diffusivity of A is given by an equation similar to Eq. (4), written down for the reactants. The local porosity $\varepsilon_p(q)$ that appears in that equation varies as a function of the deposition process according to the following equation:

$$\varepsilon_p(q) = \varepsilon_{p0} - \frac{M_{\mathrm{SiC}}}{\rho} q, \tag{6}$$

where M_{SiC} and ρ are, respectively, the molecular weight and density of SiC.

The hindered diffusivity is usually written as

$$D_H = D_\infty f(\lambda), \tag{7}$$

where λ is the ratio of the molecules' radius and the pore size, and D_∞ the bulk diffusivity. Several theoretical and semi-empirical expressions have been proposed in the past. For $\lambda \leqslant 0.3$, Brenner and Gaydos (1977) derived the following expression:

$$f(\lambda) = (1-\lambda)^2(1 - \tfrac{9}{8}\lambda \ln \lambda^{-1} - 1.539\lambda + \cdots). \tag{8}$$

For $\lambda > 0.3$, we used the semi-empirical expression due to Renkin and co-workers (Pappenheimer et al., 1951; Renkin, 1954)

$$f(\lambda) = (1-\lambda)^2(1 - 2.104\lambda + 2.09\lambda^3 - 0.95\lambda^5). \tag{9}$$

The bulk diffusivities were computed using the known relations for the diffusivity of gases (Bird et al., 2007).

We must now specify an expression for the rate of deposition of SiC. We assume that the rate is described by the following equation (Chang et al., 1997; Yamaguchi et al., 2000; Beyne and Froment, 2001; Birakayala and Evans, 2002):

$$\frac{\partial q}{\partial t} = K_d C_A \sigma_v^{\eta}(\varepsilon), \tag{10}$$

which is consistent with the assumption of having a high sticking coefficient for the SiC precursor on the pore surface of the SiC membrane. Here, K_d is an effective deposition rate constant, σ_v the local internal pore surface area per unit volume, which depends on the porosity $\varepsilon_p(q)$, and η the surface reaction exponent. We also assume that (Beyne and Froment, 2001)

$$\sigma_v = A\varepsilon_p(q)^{1/n}, \tag{11}$$

where A is a constant, and $n = 2$ for a pore space consisting of (parallel) cylindrical pores ($n = \frac{2}{3}$ if the pore space consists of spherical cavities).

Therefore, putting everything together, we obtain the following set of equations that govern the evolution of the system:

$$\frac{\partial[\varepsilon_p(q)C_A]}{\partial t} + KC_A\varepsilon_p(q)^{\eta/2} = \frac{\partial}{\partial z}\left[\frac{\varepsilon_p(q)}{\tau} D_{eA}\frac{\partial C_A}{\partial z}\right], \tag{12}$$

$$\frac{\partial[\varepsilon_p(q)C_B]}{\partial t} = \frac{\partial}{\partial z}\left[D_{eB}\frac{\varepsilon_p(q)}{\tau}\frac{\partial C_B}{\partial z}\right], \tag{13}$$

$$\frac{\partial \varepsilon_p(q)}{\partial t} = -\frac{M_{\mathrm{SiC}}K}{\rho} C_A[\varepsilon_p(q)]^{\eta/2}, \tag{14}$$

where $K = AK_d$. The parameters K and η are used to fit the results of the numerical solution of Eqs. (12)–(14) to our experimental data. In a series of preliminary simulations, we also treated the molecular weight of the reactants A as a fitting parameter. However, the fitted molecular weight turned out to be about 150, very close to that of the TPS which is 158 which, interestingly, implies that the reactant reaches and penetrates the pores nearly intact. Thus, we set the molecular weight of the reactants A to be the same as that of the TPS and did not treat it as an adjustable parameter.

To solve Eqs. (12)–(14), we used the following initial conditions, which are consistent with the way the deposition experiments were carried out. At $t = 0$ and for $|z| \leqslant z_0$, we set

$$C_A = 0, \quad C_B = C_{Bi}(z) \tag{15}$$

and

$$\varepsilon_p(q) = \varepsilon_{p0}, \tag{16}$$

where $C_{Bi}(z)$ is computed by solving the steady-state form of Eq. (13) *prior to* the deposition, i.e., $C_{Bi}(z)$ is the solution of the following equation:

$$0 = D_{BK}\frac{\varepsilon_{p0}}{\tau}\frac{\mathrm{d}}{\mathrm{d}z}\left[\frac{\mathrm{d}C_{Bi}(z)}{\mathrm{d}z}\right]. \tag{17}$$

The solution of Eq. (17) is a linear profile for $C_{Bi}(z)$. We must also specify the boundary conditions in order to solve Eqs. (12)–(14). For the pellet's top surface at z=0, the following boundary conditions were used for times $t \leqslant t_{TP}$,

$$C_A = C_{A0}, \quad C_B = C_{B0}, \tag{18}$$

whereas for times $t > t_{TP}$ we used

$$\frac{\partial C_A}{\partial z} = 0 \tag{19}$$

(the no-flux condition) and

$$C_B = C_{B0}. \tag{20}$$

Here, t_{TP} is the time at which a turning point in the porosity is reached, i.e., when the local porosity at the disk's top surface reaches a value such that the corresponding average pore radius is close to the molecular diameter of the TPS. At the bottom surface, $z = L$, we set

$$C_A = 0, \quad C_B = \frac{P}{ZR_gT}, \tag{21}$$

where Z is the gas compressibility factor. L, the thickness of the disk, was taken to be 2 mm. Boundary conditions (21) were utilized for both $t < t_{\mathrm{TPS}}$ and $t > t_{\mathrm{TPS}}$. Moreover, we neglect the concentration of the reaction products that result from the decomposition of the precursor A.

The finite-element method (Finlayson, 1980) was utilized in order to solve Eqs. (12)–(14) and their associated initial and boundary conditions. Linear basis functions were utilized, and the time-dependent terms were discretized as

$$\frac{\partial C_A}{\partial t} \simeq \frac{C_{Ai}^{n+1} - C_{Ai}^{n}}{\Delta t}, \tag{22}$$

where Δt is the size of the time step, and C_{Ai}^{n} is the concentration at grid point i after n time steps. Adaptive time step, as well as adaptive computational grid, was used in order to ensure accurate solutions. When the quantities of interest varied rapidly, a smaller time step was used, whereas when they varied relatively slowly, a larger Δt was utilized. Thus, in the intervals $0 < t \leqslant 9.7$ h and $10.5 < t < 22$ h we used, $\Delta t = 20$ s, while in between the two intervals $\Delta t = 5$ s was utilized since, as the results presented below indicate, the most significant changes in the quantities of interest occur in the middle time interval. As for the computational grid, in the intervals $0 < z < 1$ and $2\,\mu\mathrm{m} < z < 2$ mm the grid was unform with the distance between the grid points being, respectively, 25 and 0.15 nm. The grid in between the two intervals was adaptive in order to ensure flexibility in the computations and accuracy of the solutions. The Newton–Raphson method was used to linearize the equations, and the linearized equations were solved using the biconjugate-gradient method.

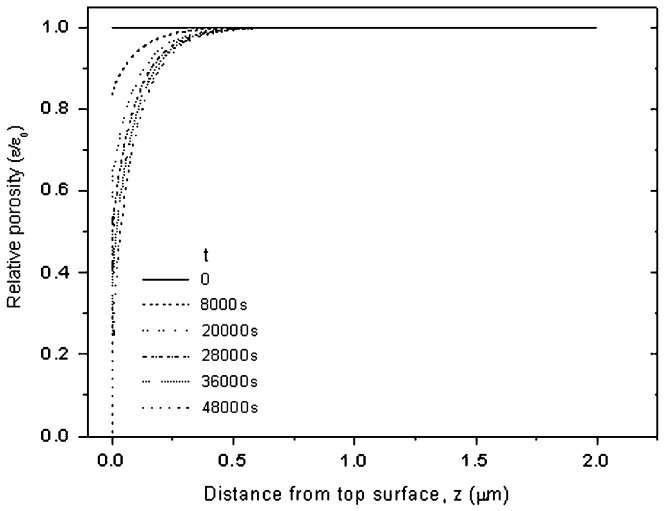

Fig. 10. Dependence of the relative porosity of the disk-shaped membrane on the distance z from the support's top surface, at several times t. The experimental parameters were, $T = 1033$ K, $P_{\mathrm{in}} = 1.2$ atm, and $P_{\mathrm{out}} = 1$ atm, and the flow rates of the TPS and Ar were, respectively, 4.3×10^{-8} and 9×10^{-5} mol/s.

Fig. 10 presents the computed relative porosity, $\varepsilon/\varepsilon_0$, at the membrane's centerline as a function of the distance z from the membrane's top surface, at various deposition times. The most significant changes in the porosity happen very near the top surface ($z = 0$) of the support that faces the precursor flow. As the pore volume decreases, the corresponding average pore size also decreases, eventually reaching the value corresponding to the kinetic diameter of the TPS, taken to be ~ 0.5 nm in the simulations. To obtain the results of the simulations shown in Fig. 10, this happens after about 13 h of deposition. Beyond this time, the TPS is no longer able to infiltrate into the support while Ar, with a kinetic diameter of ~ 0.34 nm, still permeates through. Therefore, after about 13 h, very little additional deposition can happen inside the disk support and, hence, the Ar permeance becomes stable.

The porosity variations shown in Fig. 10 are in qualitative agreement with the electron microscopy observations of the membranes prepared by the CVD/CVI of the TPS. Shown in Fig. 11 is a scanning-electron microscopy image of the cross section of a membrane, indicating a relatively uniform membrane layer (the darker part of the image at the top), followed by a relatively intact portion, consistent with the simulations results.

Fig. 12 presents a comparison between the experimental data for the Ar permeance as a function of the deposition time, and the computed permeance obtained by fitting the parameters K and η of Eqs. (12)–(14). The fitting yielded, $K = 22,000$ s^{-1} and $\eta \simeq 1.3$. As Fig. 12 indicates, the model with only two adjustable parameters is capable of providing reasonably accurate predictions for the Ar permeance and how it varies with the deposition time, over a relatively long period of time.

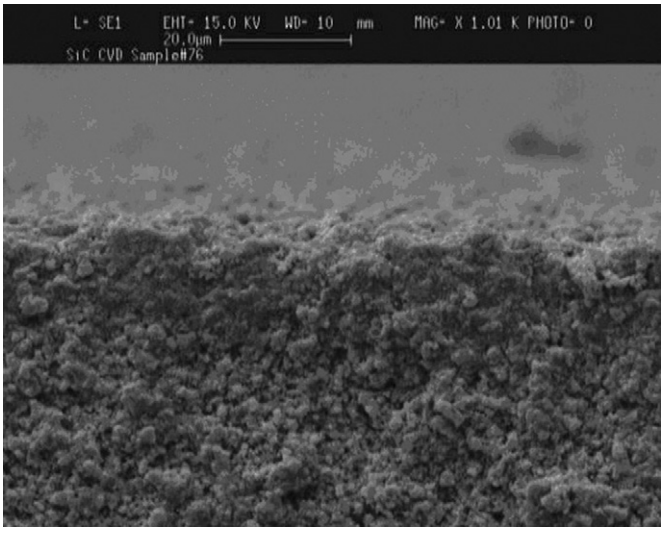

Fig. 11. A SEM image of the cross section of the disk-shaped membrane. The darker area near the top surface is the membrane layer.

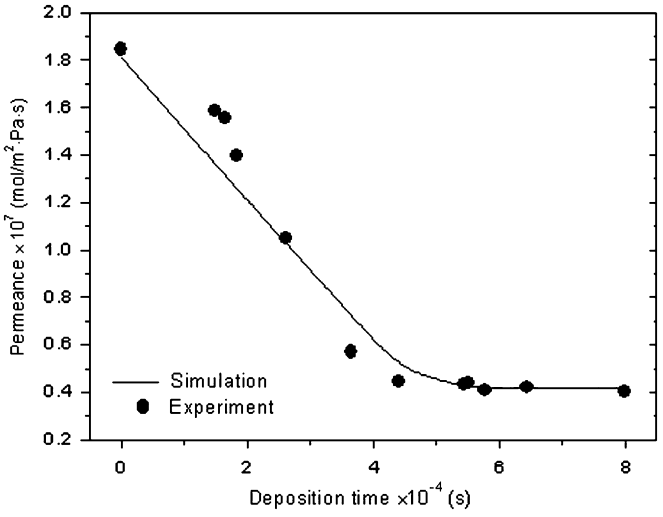

Fig. 12. Comparison of the experimental data for the Ar permeance in the disk-shaped membrane with the results of the numerical simulations. The experimental parameters are the same as those in Fig. 10.

4. Theoretical modelling and computer simulation of the CVI/CVD preparation of the tubular membranes

Fig. 13 depicts the schematic of the system in which the CVI/CVD is used to prepare the tubular membranes. We assume that, compared to the convective flow, the pressure drop along the axial direction is negligible. Moreover, we assume that in the membrane part, diffusion along its length is negligible compared with the radial diffusion, and that the pressure along the reactor length is uniform, both for the tube and shell sides.

Inside the membrane: This part of the model is similar to what we developed for the disk-shaped membrane, but with two differences. One is that the transport-reaction equations are now solved in the radial (r-)direction (instead of the z-direction for

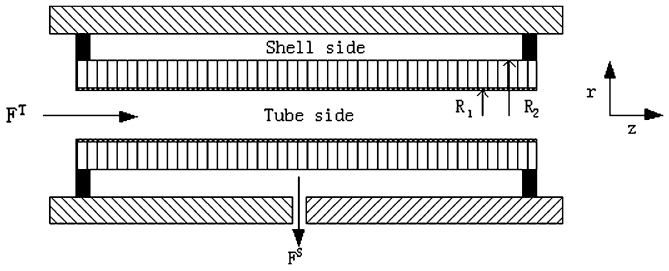

Fig. 13. Schematic of the model for the tubular membrane.

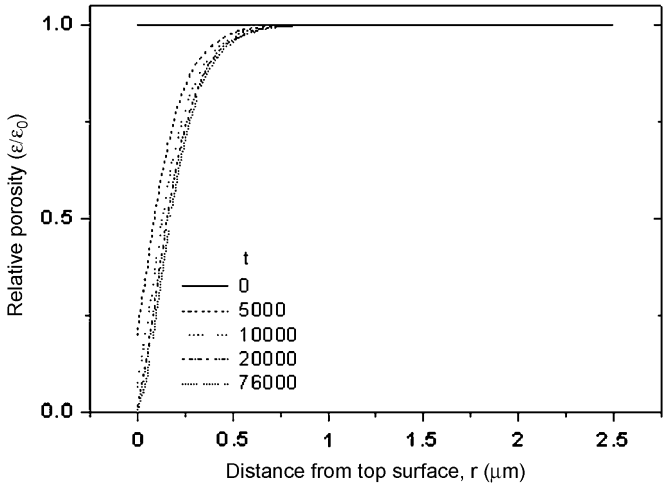

Fig. 14. Dependence of the relative porosity of the tubular membrane on the distance r from the support's top surface, at several deposition times t. The experimental parameters were, $T = 1023$ K, $P_{\text{in}} = 1.2$ atm, $P_{\text{out}} = 1$ atm ($\Delta P = 0.3$ atm $= 2.94$ psi), and the flow rates of the TPS and Ar were, respectively, 6.8×10^{-9} and 4.5×10^{-5} mol/s.

the disk-shaped membranes). The second difference is in the boundary conditions for the model. On the tubular membrane surface at $r = R_1$ (see Fig. 13) and at times $t \leqslant t_{TP}$, we set

$$C_A = y_A^T C_t^T, \quad C_B = y_B^T C_t^T, \tag{23}$$

where C_t is the total concentration, and superscript T indicates the tube side. For times $t > t_{TP}$ we used

$$\frac{\partial C_A}{\partial r} = 0 \tag{24}$$

and

$$C_B = y_B^T C_t^T. \tag{25}$$

On the surface at $r = R_2$ (see Fig. 13)—the shell side denoted by the superscript S—and for times $t > 0$, we set

$$C_A = y_A^S C_t^S, \quad C_B = y_B^S C_t^S. \tag{26}$$

In practice, however, C_A nearly vanishes on the surface at $r = R_2$.

On the tube side: The system is described by the following equations for the species A and B:

$$\frac{\mathrm{d}F_A^T}{\mathrm{d}z} = -2\pi D_{eA} r \left(\frac{\partial C_A}{\partial r}\right)_{r=R_1} \tag{27}$$

and

$$\frac{dF_B^T}{dz} = -2\pi D_{eB} r \left(\frac{\partial C_B}{\partial r}\right)_{r=R_1}. \quad (28)$$

The boundary condition at $z = 0$ was set to be

$$F_A^T = F_{A0}^T = F_0^T y_{A0}^T \quad (29)$$

and

$$F_B^T = F_{B0}^T = F_0^T y_{B0}^T. \quad (30)$$

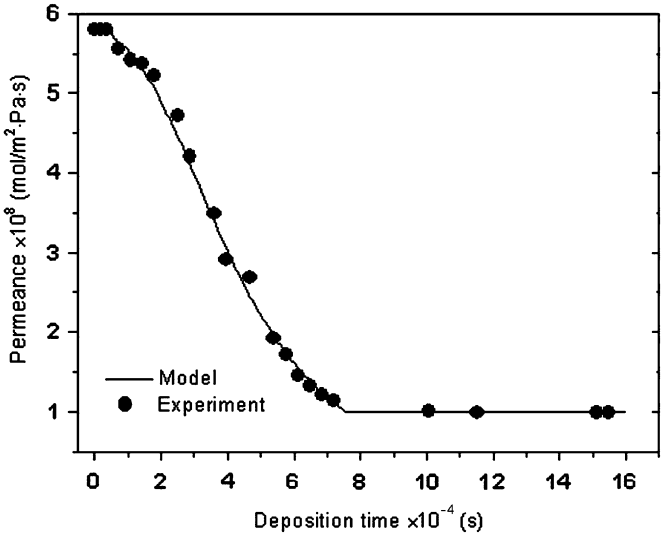

Fig. 15. Same as in Fig. 12, but for the tubular membrane. The experimental parameters are the same as those in Fig. 14.

Here, F_A^T and F_B^T are, respectively, the molar flow rates of Argon and the TPS, F_{A0}^T and F_{B0}^T the corresponding inlet molar flow rates, F_0^T the total molar flow rate, and y_{A0}^T and y_{B0}^T the inlet mole fractions.

On the shell side: The corresponding equations, and the boundary conditions at $z = 0$, for F_A^S and F_B^S are similar to those for the tube side, except that the right sides of the equations must be evaluated at $r = R_2$. The permeate molar flow rate in this case is F_0^S.

To solve the equations numerically, we divide the length of the system into a number of grid blocks. We used 10, 20, 30, and 40 grid blocks, but the accuracy of the solution with 10 blocks was comparable to those obtained with the denser grids. The total length of the reactor was 5 cm. The initial average pore size of the membrane (support) was 65 nm, while its initial porosity was 0.3. The governing equations for the membrane in the radial direction, adjacent to the first block in the z-direction, were then solved by the same method that we described for the numerical simulation of the model for the disk-shaped membrane. The TPS consumption rates, namely, $-D_{eA}\partial C_A/\partial r$, and the flux of argon, $-D_{eB}\partial C_B/\partial r$, both evaluated at $r = R_1$, were then computed for the first block. Eqs. (27) and (28) for the tube side, together with their boundary conditions, Eqs. (29) and (30) were then solved analytically for the first grid block in the z-direction (the advancing-front method). Similarly, the governing equations for the shell side were also solved. The fluxes of A and B in the first block were then used as the boundary conditions for the second block. The governing equations for the membrane in the r-direction were then solved, the flux of Ar and the consumption rate of the TPS were computed, and Eqs. (27)–(30) for the tube side, and similar equations for the

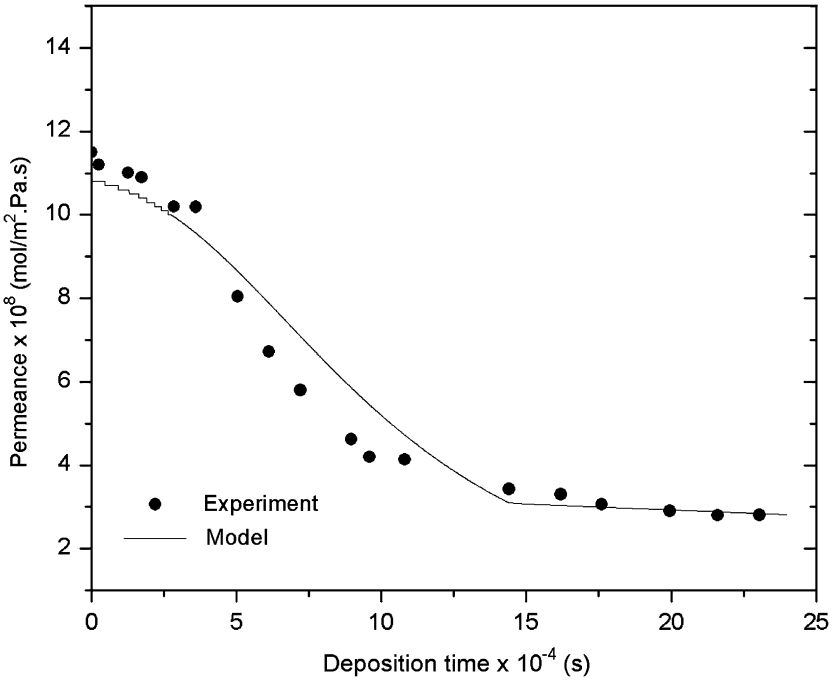

Fig. 16. Same as in Fig. 12, but with, $\Delta P = 1.0$ psi, and an Ar flow rate of 2 ml/s at $T = 1013$ K. The flow rate of the TPS is the same as in Fig. 12.

shell side, were solved. The procedure was repeated until the solution for the entire system was obtained.

Fig. 14 presents the dependence of the relative porosity (the ratio of the membrane's porosity and the initial porosity) on the distance r from the top surface, at several deposition times. A comparison between Figs. 10 and 14 indicates that the TPS penetrates the tubular support deeper than the disk-shaped one. This is due to the fact that, in the disk-shaped support, the pores' mouths that are directly connected to the top surface are bombarded directly by the TPS hitting the surface. As a result, the pores near the surface undergo very rapid changes, whereas with the tubular support, due to the geometry that causes deeper penetration of the TPS, the changes are more gradual. As a result, the rate of change of the relative porosity with r is slower in the tubular membrane than what is indicated by Fig. 10 for the disk-shaped system. The difference indicates that a tubular support results in a more uniform distribution of the porosity in the membrane.

Fig. 15 compares our experimental data for the Ar permeance during the deposition process with the computed permeances, obtained by the numerical simulations of the governing equations. We used the same values of K and η that we obtained for the disk-shaped membrane. The agreement between the data and the numerical results is excellent, hence indicating the accuracy of the model.

To further test the model, we carried out a third set of experiments with a pressure drop, $\Delta P = 1$ psi (as opposed to 2.94 psi used above), and Ar flow rate of 2 ml/s (as opposed to 1 ml/s used above), at $T = 1013$ K (as opposed to 1023 K used above). The TPS injection rate was the same as above. Fig. 16 presents the experimental data and compares them with the fit of the numerical solution of the governing equations, using the same values as before of the adjustable parameters K and η. The agreement is reasonable, hence indicating the accuracy of the model.

5. Summary and conclusions

The results of a comprehensive experimental study, as well as computer simulation, of preparation of SiC membranes by chemical-vapor deposition and infiltration techniques were presented, for both tubular and disk-shaped membranes. The two membranes exhibit very similar deposition behavior. The study indicates that the CVI/CVD process of the TPS on the SiC support continues only so long as the pore sizes are larger than the molecular radius R_{TPS} of the TPS. Once the pores shrink to a size smaller than (or equal to) R_{TPS}, the permeance of argon no longer changes, even if one continues the deposition. Moreover, significant porosity changes occur mostly in the region very close to the top surface. Two dynamic models were developed for describing the CVI/CVD processes. Using only two adjustable parameters, the models provided accurate predictions for the membranes' permeances.

Therefore, given their accuracy, the models may be used for optimizing the experimental parameters, such as the deposition rates, the reactants' concentration, and other operating parameters. In a future paper we will demonstrate this.

Acknowledgments

We are grateful to the National Science Foundation, the Department of Energy, and Media and Process Technology for partial support of this work.

References

Beyne, A.O.E., Froment, G.F., 2001. The effect of pore blockage on the diffusivity in ZSM5: a percolation approach. Chemical Engineering Journal 82, 281.

Birakayala, N., Evans, E.A., 2002. A reduced reaction model for carbon CVD/CVI processes. Carbon 40, 675.

Bird, R.B., Stewart, W.E., Lightfoot, E.N., 2007. Transport Phenomena, second revised ed. Wiley, New York.

Boo, J.H., Lee, S.B., Yu, K.S., Sung, M.M., Kim, Y., 2000. High vacuum chemical vapor deposition of cubic SiC thin films on Si(0 0 1) substrates using single source precursor. Surface and Coating Technology 131, 147.

Brenner, H., Gaydos, L.J., 1977. The constrained Brownian movement of spherical particles in cylindrical pores of comparable radius. Journal of Colloids and Interface Science 58, 312.

Brinkman, H.W., Cao, G.Z., Meijerink, J., de Vries, K.J., Burggraaf, A.J., 1993. Modelling and analysis of CVD processes for ceramic membrane preparation. Solid State Ionics 63–65, 37.

Chang, H.-C., Morse, T.F., Sheldon, B.W., 1997. Minimizing infiltration times during isothermal chemical vapor infiltration with methyltrichlorosilane. Journal of the American Ceramic Society 80, 1805.

Chen, F., Mourhatch, R., Tsotsis, T.T., Sahimi, M., 2007. Pore network model of transport and separation of binary gas mixtures in nanoporous membranes. Journal of Membrane Science, submitted for publication.

Ciora, R.J., Fayyaz, B., Liu, P.K.T., Suwanmethanond, V., Mallada, R., Sahimi, M., Tsotsis, T.T., 2004. Preparation and reactive applications of nanoporous silicon carbide membranes. Chemical Engineering Science 59, 4957.

Dollet, A., 2004. Multiscale modeling of CVD film growth—a review of recent works. Surface and Coating Technology 245, 177–178.

Elyassi, B., Sahimi, M., Tsotsis, T.T., 2007a. Silicon carbide membranes for gas separation applications. Journal of Membrane Science 288, 290.

Elyassi, B., Sahimi, M., Tsotsis, T.T., 2007b. A novel sacrificial interlayer-based method for the preparation of silicon carbide membranes. Journal of Membrane Science, in press.

Finlayson, B.A., 1980. Nonlinear Analysis in Chemical Engineering. McGraw-Hill, New York.

Jensen, K.F., Einset, E.O., Fotiadis, D.I., 1991. Flow phenomena in chemical vapor deposition of thin films. Annual Reviews of Fluid Mechanics 23, 197.

Komiyama, H., Shimogaki, Y., Egashira, Y., 1999. Chemical reaction engineering in the design of CVD reactors. Chemical Engineering Science 54, 1941.

Kusakabe, K., Yokoyama, S., Morooka, S., Hayashi, J., Nagata, H., 1996. Development of supported thin palladium membrane and application to enhancement of propane aromatization on Ga-silicate catalyst. Chemical Engineering Science 51, 3027.

Lin, Y.S., Burggraaf, A.J., 1991. Modeling and analysis of CVD processes in porous media for ceramic composite preparation. Chemical Engineering Science 46, 3067.

Lin, Y.S., Burggraaf, A.J., 1992. CVD of solid oxides in porous substrates for ceramic membrane modification. A.I.Ch.E. Journal 38, 445.

Pappenheimer, J.R., Renkin, E.M., Barrero, L.M., 1951. Filtration, diffusion, and molecular sieving through peripheral capillary membranes pores. American Journal of Physiology 67, 13.

Park, S.-C., Kang, H., Lee, S.B., 2000. Reaction intermediate in thermal decomposition of 1,3-disilabutane to silicon carbide on Si(1 1 1): comparative study of Cs^+ reactive ion scattering and secondary ion mass spectrometry. Surface Science 450, 117.

Renkin, E.M., 1954. Filtration diffusion and molecular sieving through porous cellulose membranes. Journal of General Physiology 38, 225.

Sanchez, J., Tsotsis, T.T., 2002. Catalytic Membranes and Membrane Reactors. Wiley-VCH, Berlin.

Sea, B.-K., Ando, K., Kusakabe, K., Morooka, S., 1998. Separation of hydrogen from steam using a SiC-based membrane formed by chemical vapor deposition of triisopropylsilane. Journal of Membrane Science 146, 73.

Suwanmethanond, V., Goo, E., Liu, P.K.T., Johnston, G., Sahimi, M., Tsotsis, T.T., 2000. Porous silicon carbide sintered substrates for high-temperature membrane. Industrial and Engineering Chemistry Research 39, 3264.

Takeda, Y., Shibata, N., Kubo, Y., 2001. SiC coating on porous γ-Al_2O_3 using alternative-supply CVI method. Journal of the Ceramic Society of Japan 109, 305.

Tsapatis, M., Gavalas, G.R., 1992. A kinetic model of membrane formation by CVD of SiO_2 and Al_2O_3. A.I.Ch.E. Journal 38, 847.

Valente, G., Wijesundara, M.B.J., Maboudian, R., Carraro, C., 2004. Single-source CVD of 3C-SiC films in a LPCVD reactor: reactor modeling and chemical kinetics. Journal of Electrochemical Society 151, C215.

Yamaguchi, T., Ying, X., Tokimasa, Y., Nair, B.N., Sugawara, T., Nakao, S.-I., 2000. Reaction control of tetraethyl orthosilicate (TEOS) and tetramethyl orthosilicate (TMOS) counter diffusion chemical vapour deposition for preparation of molecular-sieve membranes. Physical Chemistry Chemical Physics 2, 4465.

Journal of Membrane Science 335 (2009) 5–12

Contents lists available at ScienceDirect

Journal of Membrane Science

journal homepage: www.elsevier.com/locate/memsci

Molecular pore-network model for nanoporous materials. I: Application to adsorption in silicon-carbide membranes

Nafiseh Rajabbeigi, Bahman Elyassi, Theodore T. Tsotsis, Muhammad Sahimi*

Mork Family Department of Chemical Engineering & Materials Science, University of Southern California, Los Angeles, CA 90089-1211, USA

ARTICLE INFO

Article history:
Received 11 November 2008
Received in revised form 21 February 2009
Accepted 23 February 2009
Available online 13 March 2009

Keywords:
Nanoporous membranes
Molecular dynamics simulation
Voronoi tessellation
Silicon carbide
Adsorption

ABSTRACT

We develop a new model for nanoporous materials and inorganic membranes, the pore space of which consists of interconnected pores of irregular shapes and sizes. The model is based on the Voronoi tessellation of the atomistic structure of the crystalline or amorphous materials, of which the membrane is made. It generates three-dimensional molecular pore networks with pore size distributions (PSDs) that resemble those of real inorganic nanoporous materials. In addition to being interconnected and having irregular shapes and distributed sizes, the pores also have rough internal surface, which is what one may expect to exist in most real nanoporous materials. To test the validity of the model, we utilize it to compute the adsorption isotherms of nitrogen in three distinct silicon-carbide (SiC) membranes at 77 K, using equilibrium molecular dynamics simulations. Using *at most* one adjustable parameter, the simulated isotherms and the experimental data are found to be in very good agreement.

1. Introduction

Equilibrium and nonequilibrium properties of fluids and their mixtures in nano- and mesoporous materials, such as catalysts, adsorbents, and synthetic and natural (biological) membranes, are of much current interest. In particular, adsorption, flow, and transport of fluids and their mixtures in such porous materials have been studied for a long time [1–4]. To be used efficiently in any practical application, it is crucial to understand how such equilibrium and nonequilibrium processes occur in the pore space of nanoporous materials. Development of such an understanding is greatly facilitated, if one has an accurate model of the materials' pore space. Such understanding may then help one to address fundamental issues, such as the design of the best mode of operation for a membrane.

An important class of nanoporous materials consists of membranes that have been studied, both experimentally and by computer simulations, for separation of gaseous and liquid mixtures into their constituent components. In particular, inorganic nanoporous membranes have recently received much attention, due to their high permeability and thermochemical stability in harsh environments. Due to their high potential for gas separation, several groups have developed various inorganic membranes, such as silica, zeolite, and carbon molecular-sieve (CMS) membranes.

Our group (as well as other groups) has been preparing a variety of amorphous nanoporous membranes for separation of gaseous mixtures, including the CMS [5–7] and silicon-carbide (SiC) membranes [8–11]. Optimizing the performance of such membranes, and in particular their selectivity, entails developing much deeper understanding of how adsorption and transport of gaseous (or liquid) mixtures through them is affected by the morphology of the pore space, and in particular the pore size distribution (PSD), pore connectivity, surface roughness, and other controlling factors.

Several approaches have already been developed for modeling of the pore space of a membrane. One approach is phenomenological. It relies on the continuum equations of transport of gases (or liquids) through the pore space, and ignores important information about the porous material's morphology, including its PSD and the pores' connectivity. An example of such an approach was described in our recent paper [12].

Another approach is based on utilizing pore-network models of porous materials [4,13–18], using the idea that any porous medium can, in principle, be mapped onto an equivalent network of interconnected pores. The pores' sizes are distributed according to the measured PSD of the membrane. Since the network's pores are interconnected, the effect of their connectivity, which greatly influences transport and separation of molecules through the pore network, is also automatically taken into account. Thus, one has a realistic model of a nanoporous membrane which can be used to study the effect of a variety of factors on the transport and separation of gaseous mixtures through it.

Due to the pores' nanoscale size, molecular interactions between the guest molecules in the pore space, and between them and the

* Corresponding author. Tel.: +1 213 740 2064; fax: +1 213 740 8053.
E-mail address: moe@iran.usc.edu (M. Sahimi).

0376-7388/$ – see front matter © 2009 Elsevier B.V. All rights reserved.
doi:10.1016/j.memsci.2009.02.033

pore's walls, are important. Therefore, the third approach to modeling of transport and separation of mixtures through nanoporous materials has been based on atomistic simulations [19,20]. Most of such models are based on atomistic simulation of flow and transport of a fluid mixture through a *single* nanopore. As described above, however, the pore space of a membrane layer (as well as that of its support) consists of a three-dimensional (3D), or quasi-2D, network of interconnected pores, with sizes that are distributed according to a PSD. In order to accurately model any membrane and the phenomena that take place there, one must take into account the effect of its pores' interconnectivity. Thus, there have recently been some attempts to generate more realistic atomistic models of nanoporous materials [21–23] with interconnected pores. Our group has also carried out extensive molecular simulation of transport and separation of gaseous mixtures in atomistic models of the CMS membranes [24–26], as well as of some adsorbents [27–31].

In this paper and its sequel, hereafter referred to as Part II, we propose a new molecular pore-network model for nanoporous membranes, with a pore space that contains pores of irregular shapes and sizes that follow a certain PSD. The approach, which is quite general, combines a purely geometrical concept with molecular simulations, in order to develop a 3D pore-network model with many virtues that a real nanoporous membrane may be expected to have (see below). To test the accuracy of the model, we utilize it to compute the adsorption isotherms of nitrogen in three nanoporous membranes. In Part II we will utilize the adsorption-validated model to simulate the transport and separation of binary gaseous mixtures in the same membranes, in order to demonstrate the predictive power of the model.

We describe the model by developing it for a nanoporous SiC membrane. Due to its many desirable properties, such as high thermal conductivity [32], high thermal shock resistance [33], biocompatibility [34], resistance in acidic or alkali environments, chemical inertness, and high mechanical strength [35,36], SiC has attracted wide attention for various applications. As mentioned above, our group has been fabricating SiC membranes for gas separation applications [8–11], such as hydrogen separation.

The rest of this paper is organized as follows. In the next section, we describe how the molecular model of the SiC, as the material for the membrane, is developed. Section 3 provides a description of the geometrical concepts for developing the pore-network model, and how it is combined with the atomistic model of the membrane material, in order to develop the model for the SiC membrane. Equilibrium molecular simulations of nitrogen adsorption in the SiC membranes are described in Section 4 . The results are described and compared with the experimental data in Section 5 . The paper is summarized in Section 6 , where we describe the application of the model to other types of materials and membranes.

2. Molecular model of the membrane material

As mentioned in the introduction, we describe the new model by developing it for nanoporous SiC membranes that we have been fabricating [10,11]. The model is applicable to both β-SiC, which is the crystalline state of SiC, and *a*-SiC, which represents the amorphous state. The first step in the construction of the model is the development of an atomistic model for the membrane material—in this case SiC. If the model is intended for SiC in its crystalline state, then, its atomistic structure is well-known and straightforward to generate. Fig. 1 presents the atomistic structure of β-SiC. Thus, one generates a large crystalline SiC structure by repeating the basic cell shown in Fig. 1. The distances between the various atoms are known and are, therefore, fixed. For example, the first neighbor Si–C pairs are fixed at the experimental distance of 1.88 Å.

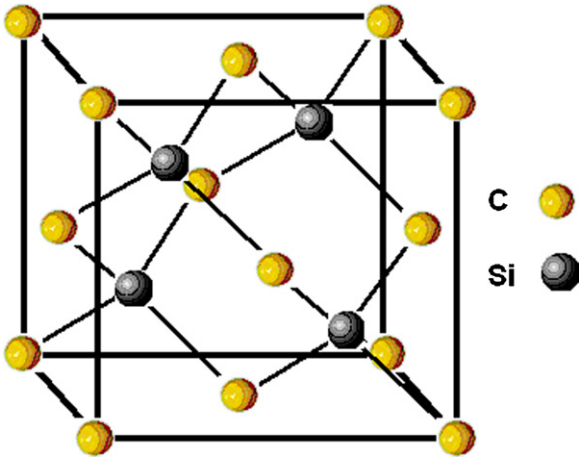

Fig. 1. The unit cell of the crystal structure of β-SiC.

To generate the model for *a*-SiC – the amorphous state of SiC – we proceed as follows. We begin with the crystalline structure of SiC, as described above. The simulation cell contains the unit cell of the SiC in the crystalline state, repeated a large number of times, in order to generate a large structure. Energy minimization and molecular dynamics (MDs) simulation are then utilized, in order to establish the most stable state of SiC at the desired temperature. To carry out the MD simulations, one must specify a force field (FF) that accurately describes SiC. Several accurate FFs have been developed in the past for describing SiC [20]. Among them are those due to Tersoff [37], Stillinger and Weber [38] and its modification [39], and Brenner [40] and its extended versions [41,42]. They all provide accurate description of SiC. In the present work we utilized the extended Brenner FF [42].

In the extended Brenner FF, the total energy E of the material is written as

$$E = \sum_i \sum_{j>i} [E_R(r_{ij}) + B_{ij}(r_{ij}) E_A(r_{ij})]. \quad (1)$$

Here, subscripts R and A denote, respectively, the repulsive and attractive parts of the the total energy of the system, given by

$$E_A(r_{ij}) = f_{ij}(r_{ij}) \frac{D_{ij}^0 S_{ij}}{S_{ij}-1} \exp\left[-\sqrt{\frac{2}{S_{ij}}}\beta_{ij}(r_{ij}-r_{ij}^0)\right], \quad (2)$$

$$E_R(r_{ij}) = f_{ij}(r_{ij}) \frac{D_{ij}^0 S_{ij}}{S_{ij}-1} \exp\left[-\sqrt{2S_{ij}}\beta_{ij}(r_{ij}-r_{ij}^0)\right], \quad (3)$$

where D_{ij}^0 is the well depth, and r_{ij}^0 is the equilibrium distance between atoms i and j. The quantities $f_{ij}(r_{ij})$ are cutoff functions, given by

$$f_{ij}(r) = \begin{cases} 1, & r \le R_{ij}^{(1)} \\ \frac{1}{2} + \frac{1}{2}\cos[\pi(r - R_{ij}^{(1)})/(R_{ij}^{(2)} - R_{ij}^{(1)})], & R_{ij}^{(1)} < r < R_{ij}^{(2)} \\ 0, & r \ge R_{ij}^{(2)} \end{cases} \quad (4)$$

The function B_{ij} is given by

$$B_{ij} = \frac{1}{2}(b_{ij} + b_{ji}) + F_{ij}[N_i^{(C)}, N_i^{(Si)}]. \quad (5)$$

B_{ij} depends on the environment around atoms i and j, since the function F_{ij} – a correction term which is used only for carbon–carbon bonds – depends on the two functions $N_i^{(C)}$ and $N_i^{(Si)}$ defined below.

Here,

$$b_{ij} = \left\{ 1 + \sum_{k \neq i,j} g(\theta_{ijk}) f_{ik}(r_{ik}) \exp(\alpha_{ijk}[(r_{ij} - R_{ij}^0) - (r_{ik} - R_{ik}^0)]) + H_{ij}[N_i^{(C)}, N_i^{(Si)}] \right\}^{-\delta_i}, \quad (6)$$

where θ_{ijk} is the angle between bonds ij and ik, δ_i a fitting parameter, and the function H_{ij} is another correction term, used only for hydrocarbons. The function $g(\theta_{ijk})$ is given by,

$$g(\theta_{ijk}) = a_0 \left[1 + \frac{c_0^2}{d_0^2} - \frac{c_0^2}{d_0^2 + (h_i + \cos\theta_{ijk})^2} \right], \quad (7)$$

where h_i is a function that, depending on the atom i, may depend on the environment around i. For the C atoms, $h_i = 1$. The cutoff functions $f_{ij}(r)$ are used for defining the various quantities. Thus,

$$N_i^{(Si)} = \sum_{j=\{Si\}} f_{ij}(r_{ij}), \quad (8)$$

$$N_i^{(C)} = \sum_{j=\{C\}} f_{ij}(r_{ij}), \quad (9)$$

where, for example, {C} denotes the set of the carbon atoms. Here, $N_i^{(j)}$ is the number of atoms of j bonded to atom i.

It is clear that the extended Brenner FF has a very large number of parameters that must be fitted to the experimental data. The fitting has already been carried out for a large number of compounds, and the fitted values of the parameters have been tabulated [42]. We used the fitted values of the parameters [42] for SiC in the simulations. Utilizing the extended Brenner FF, MD simulations were carried out to melt the SiC crystalline structure. The initial 3D simulation box contained a large number of Si and C atoms, arranged in the β-SiC crystalline structure. Since the final product is an amorphous material, periodic boundary conditions cannot be used. The time step Δt used in the simulations was, $\Delta t = 1.47 \times 10^{-4}$ ps. The melting temperature of SiC is 3103 K. Therefore, the SiC crystalline structure was heated up to 4000 K to melt completely, so as to generate the amorphous SiC. After the system reached equilibrium, the temperature was gradually lowered in steps of 5 K back to 300 K, using MD simulations. Each step of lowering the temperature took about 10^3 time steps to reach equilibrium. Thus, the final amorphous SiC structure was obtained from a single heating-cooling process.

To check whether the material is in a truly amorphous state, we computed its radial distribution function, $g(r)$. Fig. 2 presents the results at 300 K. The computed $g(r)$, and in particular the locations of the various peaks that correspond to the three types of the covalent bonds, are in very good agreement with the experimental data [43], hence confirming the amorphous state of the SiC.

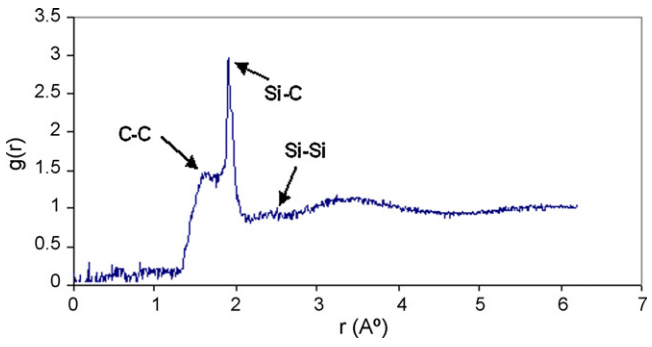

Fig. 2. The computed radial distribution function $g(r)$ of a-SiC. Arrows indicate the locations of the peaks, corresponding to the covalent bonds.

Clearly, if one wishes to model the crystalline structure at any temperature below the melting temperature of SiC, the same MD simulation procedure can be used to heat up the crystalline structure to the desired temperature.

3. The molecular pore-network model

In order to generate the pore-network model of the membrane, we created a 3D simulation box of the atomistic model of the membrane material that was developed by the MD simulations described above. The dimensions of the simulation box depend on the computation time that one can afford. In Part II we will study the effect of the system's size, which represents essentially the thickness of the membrane layer, on the separation properties of the membrane. For computing the adsorption isotherms (see below), we used boxes with a linear size of 65.4 Å.

We then tessellated the simulation box by inserting in it a number of Poisson points, i.e., points that are inserted randomly in the system. Each Poisson point is the basis for the construction of a Voronoi polyhedron. Each polyhedron (consisting of some of the atoms of the membrane material) is that part of the simulation box which is closer to its Poisson point than to any other Poisson point. Fixing the size of the simulation box and varying the number of the Poisson points allow one to vary the average of the PSD. We used between 2600 and 3000 Poisson points in the simulations.

To carry out the tessellation, we utilized parallel computations using space decomposition, message-passing interface strategy, and 300 processors. This reduced the computational time by nearly two orders of magnitude. Each processor tessellated a certain part of the simulation box. Using larger simulation boxes (with a larger number of Poisson points) increases the efficiency of the computations.

The pore space was then generated by specifying the porosity of the membrane, and selecting a number of the polyhedra in the tessellated space in such a way that, their total volume fraction equals the specified porosity. The selected polyhedra were then designated as the membrane's pores. All the atoms that are inside such pores were removed, including those that were dangling, i.e., connected to only *one* other atom. Removal of the dangling atoms was necessitated by the fact that, in a real porous material, it is physically impossible to have such atoms connected to the internal surface of the pores. The remaining atoms in the simulation box constitute the membrane's solid matrix, while the pore space consists of interconnected empty pore polyhedra of various shapes and sizes.

Two points are worth mentioning here. One is that, in principle, one should carry out a second energy minimization after the removal of the atoms inside the pore polyhedra, since the removal creates a new environment to which the remaining atoms might respond. We assumed, however, that the SiC material in the membrane is rigid, since there are no experimental indications that the SiC is very flexible. Thus, no further energy minimization was carried out. The second point worth mentioning is that, after some of the atoms are removed, the atoms that are connected to them have a free valence, i.e., contain some charge. Therefore, one must take those charges into account.

The designation of the polyhedra as the pores can be done by at least two methods. If the pore polyhedra are selected at random, then, provided that the size of the simulation box is large enough, the size distribution of the polyhedra will always be Gaussian, regardless of the pore space's porosity. From a practical point of view, however, this is not realistic because membranes that are used in practice do *not* usually have a Gaussian PSD, rather they are skewed with a tail that represents the larger pores in their support. In the second method, one designates the pore polyhedra in such a way that the resulting PSD mimics that of a real membrane. To

Table 1
The porosities of the three membranes, and the simulations' parameters. N_P, N_C, and N_{Si} represent, respectively, the number of Poisson points, and carbon and silicon atoms.

Membrane	Porosity	N_P	N_C	N_{Si}	Average pore size (Å)
I	0.4	3000	7816	7849	6.5
II	0.43	2800	7069	7076	6.6
III	0.5	2600	6384	6363	6.7

obtain such PSDs, we first sorted and listed the polyhedra in the box according to their sizes (volumes), from the largest to smallest. We then designated the polyhedra as the pores according to their sizes, starting from the largest ones in the list. In this way, three model membranes were generated for the adsorption simulations (see below). Table 1 lists their porosities and the number of Poisson points used in the tessellations, as well as the number of Si and C atoms that they contain.

Let us point out that the statistics of Voronoi tessellations have been used in the past to characterize the porosity distribution in porous materials [24,25,28,44,45]. However, the method that we propose in this paper is different from the previous works [44,45] in that, here, we first develop the atomistic model of the *n* onporous material by molecular simulations, and then generate the porosity in it by tesselating the resulting nonporous molecular structure. In the previous works [44,45] one simulates a binary fluid mixture in which one of the components serves as a template material. The final porous material is then generated by removing the template particles from the mixture.

Fig. 3 presents a 2D pore network with 50% porosity, in which the white polygons represent the membrane's matrix, while the rest are the pores. In the simulation of the sorption isotherms described below, as well as in Part II, we utilized 3D structures. Fig. 4 depicts a small portion of a 3D pore network obtained by this method.

In Fig. 5 we present the PSD computed for the three model SiC membranes. They resemble the PSD measured experimentally (see below). Since the pore polyhedra are not selected at random, the mean pore size depends on the porosity, as well as the number of the Poisson points used in the simulations, if the size of the simulation box is held fixed.

An important aspect of the model, which is also a property of real porous materials, is the interconnectivity of the pores. We characterize the pores' interconnectivity by the coordination number *Z*, defined as the number of the pores connected to a given pore, which is a spatially distributed quantity. To demonstrate this

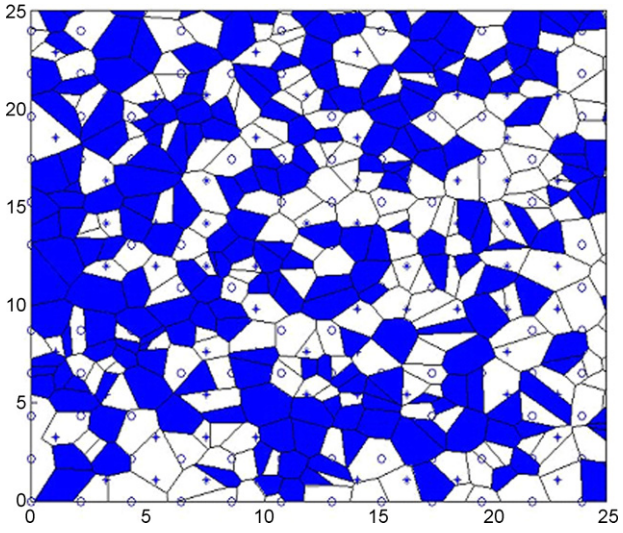

Fig. 3. An example of 2D Voronoi pore network. Black polygons are the pores.

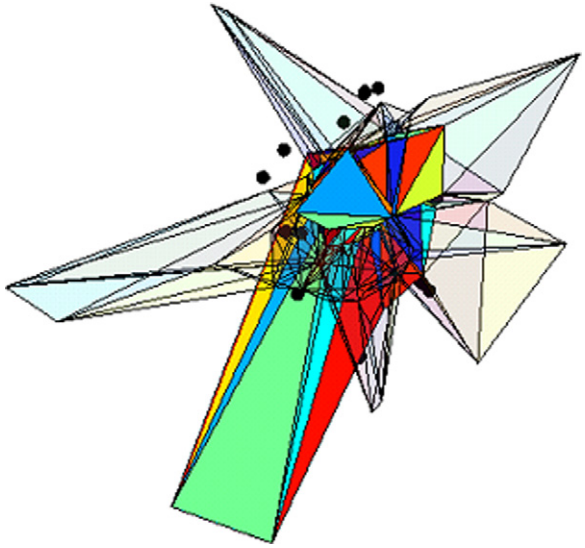

Fig. 4. The structure of the polyhedra and their connectivity in a small portion of a 3D Voronoi pore network. Light and dark colours represent, respectively, the pore and matrix polyhedra. (For interpretation of the references to color in this figure legend, the reader is referred to the web version of the article.)

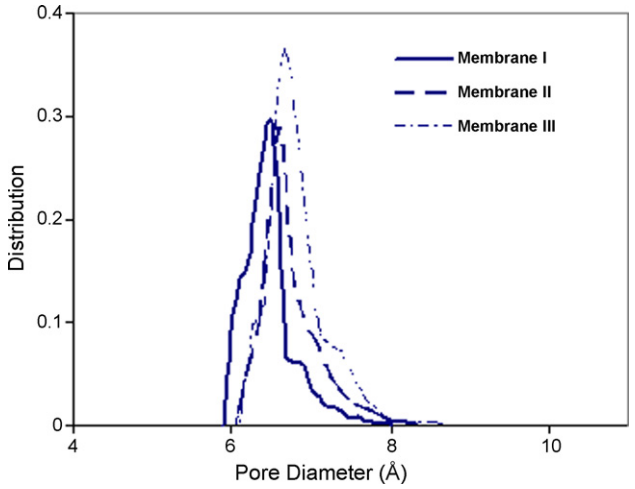

Fig. 5. The computed pore size distribution of the three SiC membranes.

aspect, we computed the distribution of the coordination number for a model SiC membrane with porosity of 0.5. The results are presented in Fig. 6. As can be seen there, the coordination number varies anywhere from 0 (isolated pore) to as high as 20. The average coordination number is about 10. Lower porosities would, of course, result in lower average coordination numbers.

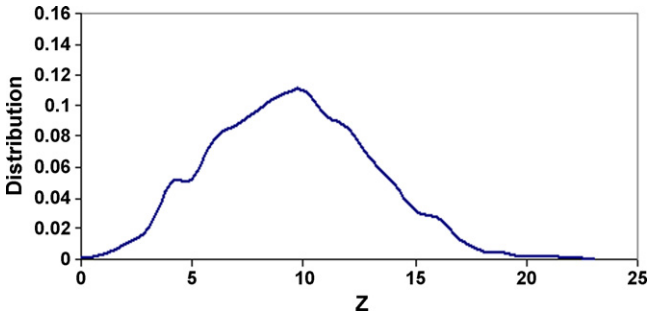

Fig. 6. The distribution of the coordination number in a 3D Voronoi pore network with porosity of 0.5.

The model has several virtues that are expected for any inorganic membrane of the type that we have been studying: (i) It generates PSDs that mimic those measured. (ii) The pores have irregular shapes. (iii) The interconnectivity of the pores is automatically taken into account. (iv) Removing the dangling atoms generates pore surface roughness, which is expected to exist in any real membrane.

Let us point out that, although tessellating the membrane material by the Voronoi algorithm and designating some of the resulting polyhedra as pores may seem as abstract, it is, in fact, quite natural. The pore space of many natural porous materials, ranging from biological materials, wood, and foam [2,46], to sandstone and other types of rock [4], can be well represented by Voronoi-type structures. In addition, the Voronoi algorithm affords one great flexibility for constructing disordered pore networks with many variations in the shapes and sizes of the polyhedra. One can, in fact, modify the algorithm, in order to generate pore polyhedra with a great variety of shapes, from completely random to very regular shapes [47].

4. Molecular simulation of nitrogen adsorption

To test whether the model can reproduce experimental data for the SiC membranes, we computed the adsorption isotherm of nitrogen in three model membranes at 77 K, and compared them with the experimental data. To do so, we employed equilibrium MD (EMD) simulations. The standard cut-and-shifted Lennard–Jones (LJ) potential,

$$U(r) = \begin{cases} U_{\mathrm{LJ}}(r) - U_{\mathrm{LJ}}(r_c) & r \le r_c, \\ 0 & r > r_c, \end{cases} \tag{10}$$

was used to describe the interactions between the nitrogen molecules, as well as between them and the C and Si atoms in the membrane, where $U_{\mathrm{LJ}}(r)$ is the 12-6 LJ potential. The cutoff distance r_c was taken to be quite large, $r_c \simeq 15.25$ Å. We used, $\sigma_{\mathrm{N}_2} = 3.7$, $\sigma_{\mathrm{C}} = 3.4$, and $\sigma_{\mathrm{Si}} = 3.74$ (all in Å) for the LJ size parameters, and $\epsilon_{\mathrm{N}_2}/k_B = 95.05$, $\epsilon_{\mathrm{C}}/k_B = 28$, and $\epsilon_{\mathrm{Si}}/k_B = 23.6$ (all in K) for the LJ energy parameters, where k_B is the Boltzmann's constant. The Lorentz–Berthelot rules, $\epsilon_{ij} = (\epsilon_i \epsilon_j)^{1/2}$, and $\sigma_{ij} = (1/2)(\sigma_i + \sigma_j)$, were utilized for calculating the size and energy of the unlike pairs of atoms.

In the simulation we used the Verlet velocity algorithm [48] in order to determine the atoms' trajectories. If the simulations are carried out with the crystalline structure, periodic boundary conditions are utilized. Such boundary conditions cannot be used with the amorphous material. In that case, the no-flow (closed walls) boundary conditions are used. After discarding the first 4×10^5 time steps for equilibration of the system, the trajectories of the atoms were collected over a typical period of 4×10^5 time steps. The chemical potentials were calculated using Widom's test particle method [49–51],

$$\mu_e = -k_B \ln \left\langle exp\left(\frac{-\Delta U}{k_B T}\right)\right\rangle, \tag{11}$$

where μ_e is the excess chemical potential of the system, ΔU the change in the potential energy of the system as a result of adding a test particle, and $\langle\cdot\rangle$ denotes an average over time and active test particles. The chemical potentials were then converted to pressure using the equation of state for the LJ fluids [52].

At the beginning of each simulation run, the simulation cell was divided into a large number of small subcells and a test particle was assigned to each subcell. The simulation cell was discretized into $n_x \times n_y \times n_z$ grid points along the three directions, with, $n_x = n_y = n_z = 143$, thus resulting in over 2,924,207 small subcells. The test particle–solid wall interaction energies and their three derivatives, associated with all the subcells, were then calculated and recorded. They also served as the grid points values for the interpolation calculations described below. The test particles with interaction energies, in units of k_BT, less than a certain positive value $\mathcal{E}$ (for example, 20) were considered as "active" test particles, and those with interaction energies larger than $\mathcal{E}$ were considered as "idle" states, since they make essentially no contribution to the chemical potential.

In each sampling step, computation of the chemical potentials and the adsorption isotherms typically required a small percentage of the active test particles which were randomly selected. The actual value depended on the loading and the porosity. Depending on the loading of the adsorbate molecules and the size of the simulation cell, the number of the active test particles varied from 2000 to 4000. Energy conservation in the system was monitored in each simulation, and the time step was adjusted according to the loading of the adsorbate molecules and the size of the pores, such that the standard deviations of the total energy relative to the mean was about 5×10^{-4} or less. Typical value of the time steps selected in this way was 7.4×10^{-3} ps. To reduce the simulation time for calculating the interaction between a gas molecule and the atoms in the molecular network, we used a 3D piecewise cubic Hermite interpolation [53,54](which interpolates a function and its first three derivatives) to compute the potential energy and forces for the gas particle at any position using the previously recorded information at the $n_x \times n_y \times n_z$ grid points. The (*NVE*) ensemble was utilized to calculate the adsorption isotherms.

5. Adsorption results and comparison with experimental data

Three sets of data for N_2 adsorption isotherms in three SiC membranes were used for comparison with the computed isotherms using the model. One isotherm was measured in our own laboratory, using the SiC membrane that we have fabricated [10,11]. We refer to it as membrane I. The separation properties of the same membrane for binary gaseous mixtures were also measured. They will be directly compared with the computed results in Part II. The other two isotherms were reported by Suda et al. [55], and are referred to as isotherms for membranes II and III.

The nitrogen adsorption isotherm with membrane I was measured using the BET method. We first measured the isotherm in the membrane's support (which was also SiC), and then generated the BET data in the supported membrane. This way we were able to obtain the isotherm in the membrane layer itself (since the model represents the membrane layer). Fig. 7 shows the adsorption isotherms in both the support and the supported membrane. The membrane's thickness was estimated to be 9 μm. Using the adsorption isotherm and the MP (micropore analysis) method [3], we estimated that the porosity of the membrane was about 0.4. Since the estimate of the average pore size by the BET instrument is based on the Horvath–Kawazoe (HK) method [3,4], which is not very accurate, we treated the average pore size of membrane I as an adjustable parameter. Thus, we ran a set of EMD simulations with various average pore sizes and porosity 0.4, using the Voronoi model. We found that the EMD simulations results match the experimental isotherm almost perfectly with an average pore size of 6.5 Å. This is shown in Fig. 8.

The PSD of membrane II [55] is shown in Fig. 9. Although it contain several peaks and a long tail, only its left-most side that corresponds to the membrane layer is of interest to us. The membrane's porosity, estimated by the MP method, is about 0.43. Its average pore size was determined by the simulation, and turned out to be 6.6 Å. Suda et al. [55] reported the average pore size of membrane II to be about 6.4 Å, which had been, however, estimated by the HK method. Fig. 10 compares the computed isotherm, using the Voronoi model at the same porosity, with the experi-

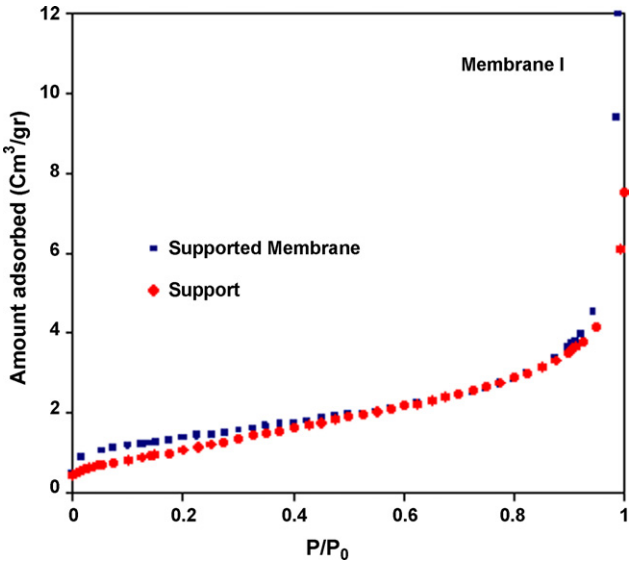

Fig. 7. The measured nitrogen sorption isotherms of membrane I and its support at 77 K.

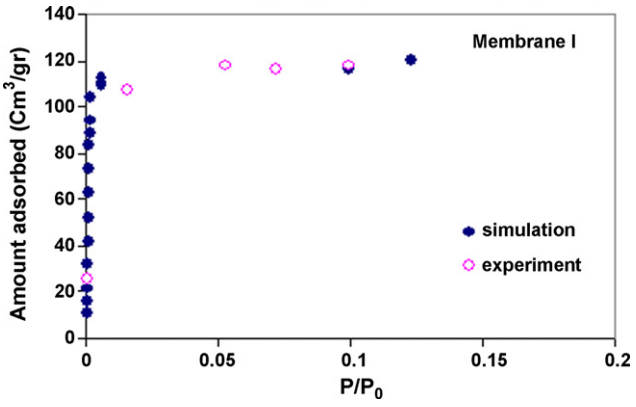

Fig. 8. Comparison of the computed and measured nitrogen sorption isotherms for membrane I.

mental data for membrane II. The agreement is, once again, very good.

The PSD of membrane III [55] is presented in Fig. 11, which is similar to that shown in Fig. 9. The HK average pore size of the membrane was reported to 7.2 Å. Its porosity was estimated by the

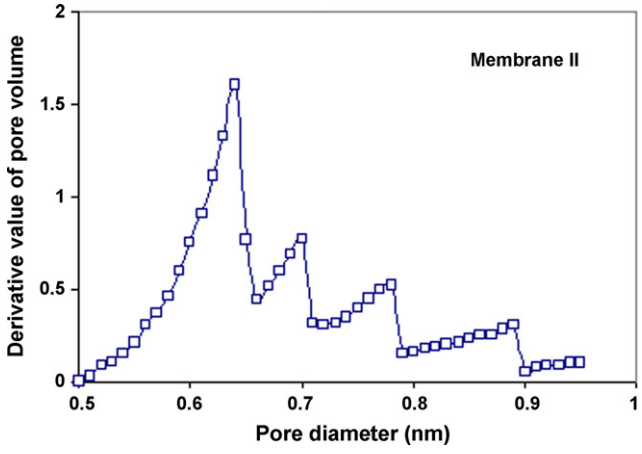

Fig. 9. Pore size distribution of membrane II, adopted from Suda et al. [55].

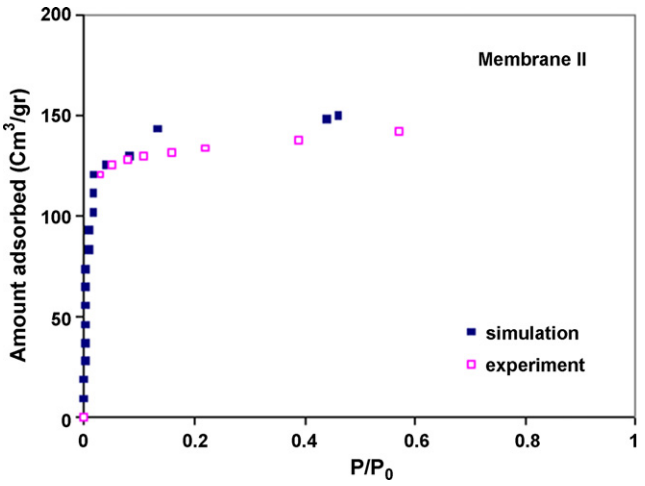

Fig. 10. Comparison of the computed and measured nitrogen sorption isotherms for membrane II.

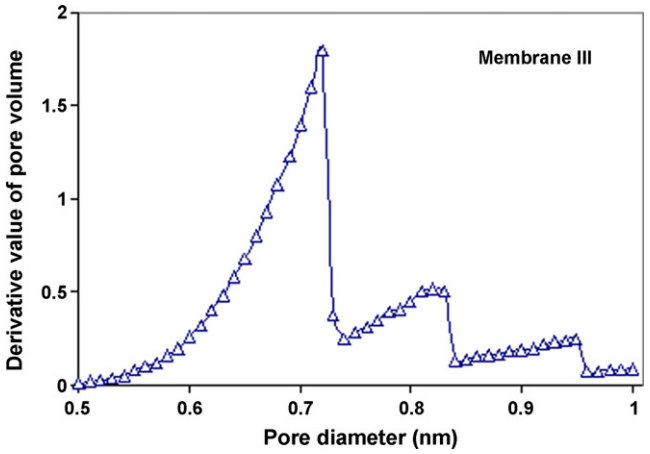

Fig. 11. Pore size distribution of membrane III, adopted from Suda et al. [55].

MP method, and turned out to be 0.5. Using these values, the simulated isotherm did not quantitatively agree with the data. However, fixing the porosity at 0.5 and lowering the average pore size to 6.8 Å (a difference of about 5%) produced the isotherm shown in Fig. 12, where it is compared with the data of Suda et al. [55]. Once again the agreement is very good. Note that, the average pore sizes of the three membranes are rather close to each other.

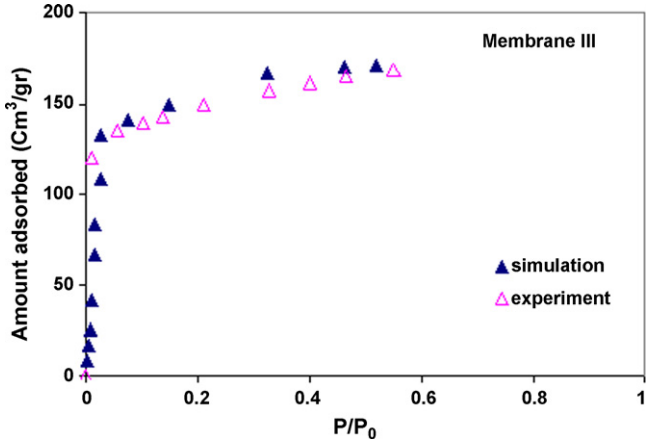

Fig. 12. Comparison of the computed and measured nitrogen sorption isotherms in membrane III.

Let us point out that, if the porosity of a membrane is relatively large – not too close to its percolation threshold [56]– then often a single realization of the model produces the correct isotherm. However, if the porosity is low, or if the system is close to a phase transition (which often happens at low temperatures), then, one must either generate several realizations of the model and average the results, or use a relatively large size model.

Thus, by adjusting *at most* one parameter, the Voronoi model for the SiC membrane can accurately predict nitrogen sorption data that are in agreement with the experimental data. A stringent test of the model can be made, if we use the model of the membranes to predict, *without using any additional adjustable parameter*, their separation properties. This will be taken up in Part II.

6. Summary

A new molecular pore-network model for inorganic nanoporous membranes was proposed. The model is based on generating an atomistic model of the membrane material, tessellating the atomistic model using the Voronoi algorithm, and designating the pores in a physically reasonable manner. The model was tested against experimental data for nitrogen adsorption in three SiC membranes. Adjusting *at most* one parameter – the average pore size – produced isotherms that are in very good agreement with the data.

In Part II we will use the model developed in this paper, in order to study the transport and separation of binary gas mixtures in the SiC membrane I. We will demonstrate that, using the model obtained by computing the sorption isotherm, and utilizing no additional adjustable parameter, we can accurately predict the separation properties of the membrane.

Acknowledgments

Parallel computations for the work described in this paper were supported by the University of Southern California Center for High-Performance Computing. This work was supported in part by the National Science Foundation and the Department of Energy.

References

[1] T.J. Pinnavaia, M.F. Thorpe (Eds.), Access in Nanoporous Materials, Plenum, New York, 1995.
[2] K.K. Unger, J. Rouquerol, K.S.W. Sing, H. Kral (Eds.), Characterization of Porous Solids, Slsevier, Amsterdam, 1988.
[3] S. Lowell, J.E. Shields, M.A. Thomas, M. Thommes, Characterization of Porous Solids and Powders: Surface Area, Pore Size and Density, Kluwer Academic, Dordrecht, 2004.
[4] M. Sahimi, Flow and Transport Through Porous Media and Fractured Rock, VCH, Weinheim, 1995.
[5] M.G. Sedigh, W.J. Onstot, L. Xu, W.L. Peng, T.T. Tsotsis, M. Sahimi, Experiments and simulation of transport and separation of gas mixtures in carbon molecular-sieve membranes, J. Phys. Chem. A 102 (1998) 8580.
[6] M.G. Sedigh, L. Xu, T.T. Tsotsis, M. Sahimi, Transport and morphological characteristics of polyetherimide-based carbon molecular sieve membranes, Ind. Eng. Chem. Res. 38 (1999) 3367.
[7] M.G. Sedigh, M. Jahangiri, P.K.T. Liu, M. Sahimi, T.T. Tsotsis, Structural characterization of polyetherimide-based carbon molecular sieve membranes, AIChE J. 46 (2000) 2245.
[8] V. Suwanmethanond, E. Goo, P.K.T. Liu, G. Johnston, M. Sahimi, T.T. Tsotsis, Porous silicon carbide sintered substrates for high-temperature membranes, Ind. Eng. Chem. Res. 39 (2000) 3264.
[9] R.J. Ciora, B. Fayyaz, P.K.T. Liu, V. Suwanmethanond, R. Mallada, M. Sahimi, T.T. Tsotsis, Preparation and reactive applications of nanoporous silicon carbide membranessilicon carbide membranes for gas separation applications, Chem. Eng. Sci. 59 (2004) 4957.
[10] B. Elyassi, M. Sahimi, T.T. Tsotsis, Silicon carbide membranes for gas separation applications, J. Membr. Sci. 288 (2007) 290.
[11] B. Elyassi, M. Sahimi, T.T. Tsotsis, A novel sacrificial interlayer-based method for the preparation of silicon carbide membranes, J. Membr. Sci. 316 (2008) 73.
[12] F. Chen, R. Mourhatch, T.T. Tsotsis, M. Sahimi, Experimental studies and computer simulation of preparation of nanoporous silicon-carbide membranes by chemical-vapor deposition and infiltration techniques, Chem. Eng. Sci. 63 (2008) 1460.
[13] M. Sahimi, G.R. Gavalas, T.T. Tsotsis, Statistical and continuum models of fluid–solid reactions in porous media, Chem. Eng. Sci. 45 (1990) 1443.
[14] M. Sahimi, Flow phenomena in rocks: from continuum models to fractals, percolation, cellular automata, and simulated annealing, Rev. Mod. Phys. 65 (1993) 1393.
[15] C. Rieckmann, F.J. Keil, Multicomponent diffusion and reaction in three-dimensional networks: general kinetics, Ind. Eng. Chem. Res. 36 (1997) 3275.
[16] C. Rieckmann, F.J. Keil, Simulation and experiment of multicomponent diffusion and reaction in three-dimensional networks, Chem. Eng. Sci. 54 (1999) 3485.
[17] F.J. Keil, Diffusion and reaction in porous networks, Catal. Today 53 (1999) 245.
[18] F. Chen, R. Mourhatch, T.T. Tsotsis, M. Sahimi, Pore network model of transport and separation of binary gas mixtures in nanoporous membranes, J. Membr. Sci. 315 (2008) 48.
[19] L.D. Gelb, K.E. Gubbins, R. Radhakrishnan, M. Sliwinska-Bartkowiak, Phase separation in confined systems, Rep. Prog. Phys. 62 (1999) 1573.
[20] M. Sahimi, T.T. Tsotsis, M. Rieth, W. Schommers, in: Handbook of Theoretical and Computational Nanotechnology, American Scientific, New York, 2006.
[21] J. Pikunic, P. Llewellyn, R. Pellenq, K.E. Gubbins, Argon and nitrogen adsorption in disordered nanoporous carbons: simulation and experiment, Langmuir 21 (2005) 4431.
[22] T.X. Nguyen, S.K. Bhatia, S.K. Jain, K.E. Gubbins, Structure of saccharose-based carbon and transport of confined fluids: hybrid reverse Monte Carlo reconstruction and simulation studies, Mol. Simul. 32 (2006) 567.
[23] A.P. Terzyk, S. Furmaniak, P.A. Gauden, P.J.F. Harris, J. Wloch, P. Kowalczyk, Hyper-parallel tempering Monte Carlo Simulations of Ar adsorption in new models of microporous non-graphitizing activated carbon: effect of microporosity, J. Phys.: Condens. Matter 19 (2007) 406208.
[24] L. Xu, T.T. Tsotsis, M. Sahimi, Nonequilibrium molecular dynamics simulations of transport and separation of gas mixtures in nanoporous materials, Phys. Rev. E 62 (2000) 6942.
[25] L. Xu, T.T. Tsotsis, M. Sahimi, Statistical mechanics and molecular simulation of adsorption of ternary gas mixtures in nanoporous membranes, J. Chem. Phys. 114 (2001) 7196.
[26] M. Sahimi, T.T. Tsotsis, Molecular pore network models of nanoporous materials, Physica B 338 (2003) 291.
[27] X. Yi, J. Ghassemzadeh, K.S. Shing, M. Sahimi, Molecular dynamics simulations of gas mixtures in porous media. I. Adsorption, J. Chem. Phys. 108 (1998) 2178.
[28] J. Ghassemzadeh, L. Xu, T.T. Tsotsis, M. Sahimi, Statistical mechanics and molecular simulation of adsorption of gas mixtures in microporous materials: pillared clays and carbon molecular-sieve membranes, J. Phys. Chem. B 104 (2000) 3892.
[29] J. Ghassemzadeh, M. Sahimi, Molecular modeling of adsorption of gas mixtures in montmorillonites intercalated with Al_{13}-complex pillars, Mol. Phys. 102 (2004) 1447.
[30] N. Kim, Y. Kim, T.T. Tsotsis, M. Sahimi, Atomistic simulations of nanoporous layered double hydroxide materials and their properties. I. Structural modeling, J. Chem. Phys. 122 (2005) 214713.
[31] N. Kim, A. Harale, T.T. Tsotsis, M. Sahimi, Atomistic simulation of nanoporous layered double hydroxide materials and their properties. II. Adsorption and diffusion, J. Chem. Phys. 127 (2007) 224701.
[32] K. Maeda, Y. Matsushita, Y. Takeda, K. Nakamura, Effects of elemental additives on electrical resistivity of silicon carbide ceramics, J. Am. Ceram. Soc. 70 (1987) 266.
[33] K. Schulz, M. Durst, Advantages of an integrated system for hot gas filtration using rigid ceramic elements, Filtr. Sep. 31 (1994) 25.
[34] A.J. Rosenbloom, D.M. Sipe, Y. Shishkin, Y. Ke, R.P. Devaty, W.J. Choyke, Nanoporous SiC: a candidate semi-permeable material for biomedical applications, Biomed. Microdev. 6 (2004) 261.
[35] C.A. Zorman, A.J. Fleischman, A.S. Dewa, M. Mehregany, C. Jacob, S. Nishino, P. Pirouz, Epitaxial growth of 3C–SiC films on 4 in. diam (1 0 0) silicon wafers by atmospheric pressure chemical vapor deposition, J. Appl. Phys. 78 (1995) 513.
[36] S.H. Kenawy, W.M.N. Nour, Microstructural evaluation of thermally fatigued SiC reinforced Al_2O_3/ZrO_2 matrix composites, J. Mater. Sci. 40 (2005) 3789.
[37] J. Tersoff, Modeling solid-state chemistry: interatomic potentials for multicomponent systems, Phys. Rev. B 39 (1989) 5566.
[38] F.H. Stillinger, T.A. Weber, Computer simulation of local order in condensed phases of silicon, Phys. Rev. B 31 (1985) 5262.
[39] P. Vashishta, R.K. Kalia, A. Nakano, J.P. Rino, Interaction potential for silicon carbide: a molecular dynamics study of elastic constants and vibrational density of states for crystalline and amorphous silicon carbide, J. Appl. Phys. 101 (2007) 103515.
[40] D.W. Brenner, Empirical potential for hydrocarbons for use in simulating chemical vapor deposition of diamond films, Phys. Rev. B 42 (1990) 9458.
[41] J. Che, T. Cagin, W.A. Goddard III, Generalized extended empirical bond-order dependent force fields including nonbond interactions, Theor. Chem. Acc. 102 (1999) 346.
[42] A.J. Dyson, P.V. Smith, Improved empirical interatomic potential for C–Si–H systems, Mol. Phys. 96 (1999) 1491.
[43] M. Ishimaru, I.-T. Bae, Y. Hirotsu, Radial distribution functions of amorphous silicon carbide, Mater. Res. Soc. Symp. Proc. 742 (2003) 73.
[44] H. Dominguez, M. Rivera, Studies of porosity and and diffusion coefficient in porous matrices by computer simulations, Mol. Phys. 100 (2002) 3829.
[45] M. Rivera, H. Dominguez, Pore matrices prepared at supercritical temperature by computer simulations: matrix characterization and studies of diffusion coefficients of adsorbed fluids, Mol. Phys. 101 (2003) 2953.

[46] L.J. Gibson, M.F. Ashby, Cellular Solids, 2nd ed., Cambridge University Press, Cambridge, 1997.
[47] P.T. Cromwell, Polyhedra, Cambridge University Press, Cambridge, 1997.
[48] J.M. Haile, Molecular Dynamics Simulations, Wiley, New York, 1990.
[49] B. Widom, Potential-distribution theory and the statistical mechanics of fluids, J. Phys. Chem. 346 (1964) 593.
[50] K.S. Shing, K.E. Gubbins, Free energy and vapour–liquid equilibria for a quadrupolar Lennard–Jones fluid, Mol. Phys. 45 (1982) 129.
[51] G.L. Deitrick, L.E. Scriven, H.T. Davis, Efficient molecular simulation of chemical potentials, J. Chem. Phys. 90 (1989) 2370.
[52] J.K. Johnson, J.A. Zollweg, K.E. Gubbins, The Lennard–Jones equation of state revisited, Mol. Phys. 78 (1993) 591.
[53] M.H. Schultz, Spline Analysis, Prentice-Hall, Englewood Cliffs, NJ, 1973.
[54] D. Kahaner, C. Moler, S. Nash, Numerical Methods and Software, Prentice-Hall, Englewood Cliffs, NJ, 1989.
[55] H. Suda, H. Yamauchi, Y. Uchimaru, I. Fujiwara, K. Haraya, Structural evolution during conversion of polycarbosilane precursor into silicon carbide-based microporous membranes, J. Ceram. Soc. Jpn. 114 (2006) 539.
[56] M. Sahimi, Applications of Percolation Theory, Taylor & francis, London, 1994.

Elsevier Editorial System(tm) for Materials Chemistry and Physics
Manuscript Draft

Manuscript Number: MATCHEMPHYS-D-09-00341R1

Title: Effect of Polystyrene on the Morphology and Physical Properties of Silicon Carbide Nanofibers

Article Type: Full Length Article

Keywords: Silicon Carbide; Amorphous Nanofibers; Adsorption; TEM

Corresponding Author: Mr. Bahman Elyassi,

Corresponding Author's Institution: USC

First Author: Bahman Elyassi

Order of Authors: Bahman Elyassi; Tae Wook Kim, PhD; Muhammad Sahimi, PhD; Theodore T Tsotsis, PhD

Abstract: Silicon carbide nanofibers were fabricated by immersion of anodized aluminum oxide templates in allyl-hydridopolycarbosilane (AHPCS) solutions, and subsequent pyrolysis at 750 oC. The technique offers better control on the final morphology of the nanofibers, hence resolving some of the fabrication difficulties encountered in the past. The effect of polystyrene - the pore former - on the formation of the nanofibers in the confined channels of the templates was studied. Low concentrations of polystyrene in the AHPCS solution resulted in ellipsoidal hollow regions inside the SiC nanofibers, whereas high concentrations resulted in the formation of some completely hollow fibers. The fibers prepared by adding polystyrene possessed higher surface areas than those without polystyrene. The morphology and surface area of the SiC nanofibers were studied using the SEM, TEM, and BET analyses.

Dear Professor Lin,

We undertook the changes reviewers commented on in the revised manuscript. Since the reviewers' main concern was mostly based on the technical English of the manuscript, we edited the manuscript accordingly to accommodate their comments and concerns.

Best Regards,
Bahman Elyassi

Mork Family Department of Chemical Engineering & Materials Science
USC Viterbi School of Engineering
University of Southern California
925 Bloom Walk, HED 216
Los Angeles, CA 90089-1211

office (213) 740 2063
fax (213) 740 8053
cell (213) 479 5492

We thank the reviewers for their thorough reports. Since the reviewers' main concern was mostly based on the technical English of the manuscript, we edited the manuscript accordingly to accommodate their comments and concerns.

Reviewer #1:

1- There are some long sentences which may confusing the reader. It is better to re-written in short sentences instead.

The technical English of the manuscript was polished and modified in response to the reviewer's comment.

2- All the article sections are written in one paragraph manner each. It will be conclusive and clearer for the reader - who is our target from the publication process - if such sections are divided into titles and subtitles.

The article has been divided into sections and subsections, as the reviewer suggested.

Reviewer #2:

1- English requires revision, some sentences not clear and difficult to understand.

The manuscript has been polished and rewritten, in order to address the reviewer's comment.

2- Introduction needs to modify.

We have rewritten the Introduction in order to present a clearer discussion of the past work, and the motivation for the present work.

3- P 3 line 1 (what's mean by C3H6? because its may be Cyclopropane, or Propylene.

The reviewer's point is well taken. In fact, in the reference article:

Li ZJ, Zhang JL, Meng A, Guo JZ, Large-area highly-oriented SiC

nanowire arrays: Synthesis, Raman, and photoluminescence properties, Journal of Physical Chemistry B 2006 (110) 22382,

the authors just mentioned C3H6. We contacted the authors to clarify this, however, we did not receive any response from them.

4- Write the formula of allyl-hydridopolycarbosilane (AHPCS).

The chemical formula of AHPCS was added to the manuscript.

5- p3 from the bottom," The main theme of this report, however, is studying the effect on the structure and property of the nanofibers that adding polystyrene (PS), as a pore former, into the AHPCS precursor solution has." Not clear

We changed the sentence to:

The main goal of the present paper is, however, studying the effect of polystyrene (PS), as a pore former, on the morphology and physical properties of the nanofibers.

3- Results and Discussion
- Some results and discussion unclear.

The Results and Discussion section was rewritten and clarified, to the best of our ability.

Effect of Polystyrene on the Morphology and Physical Properties of Silicon Carbide Nanofibers

Bahman Elyassi, Tae Wook Kim, Muhammad Sahimi, and Theodore T. Tsotsis*

Mork Family Department of Chemical Engineering & Materials Science, University of Southern California, Los Angeles, CA 90089-1211, USA

Keywords: *Silicon Carbide; Amorphous Nanofibers; Adsorption; TEM*

Abstract: Silicon carbide nanofibers were fabricated by immersion of anodized aluminum oxide templates in allyl-hydridopolycarbosilane (AHPCS) solutions, and subsequent pyrolysis at 750 ^{o}C. The technique offers better control on the final morphology of the nanofibers, hence resolving some of the fabrication difficulties encountered in the past. The effect of polystyrene - the pore former - on the formation of the nanofibers in the confined channels of the templates was studied. Low concentrations of polystyrene in the AHPCS solution resulted in ellipsoidal hollow regions inside the SiC nanofibers, whereas high concentrations resulted in the formation of some hollow fibers. The fibers prepared by adding polystyrene possessed higher surface areas than those without polystyrene. The morphology and surface area of the SiC nanofibers were studied using the SEM, TEM, and BET analyses.

* Corresponding author. Tel.: +1-213-740-2069; fax: +1-213-740-8053
Email address: tsotsis@usc.edu (Theodore T. Tsotsis)

1. Introduction

Due to its many desirable properties, such as high thermal conductivity, stability, chemical inertness, high strength, and high oxidation resistance, silicon carbide (SiC) is a promising candidate for a wide range of applications that involve harsh environments. SiC has potential for application as a high-temperature, high-power, and high-frequency semiconductor in the aerospace industry [1], as a gas sensor [2] and hydrogen storage medium for the automotive industry [3,4], as a material from which hydrogen permselective [5,6] or even biocompatible membranes for the bioMEMS industry [7] are made, as a catalyst support [8-10], as well as a reinforcing material [11].

Due to its many potential and actual applications, there has been increasing interest in producing various nanostructures with SiC. In the production of such nanostructured materials carbon nanotubes (CNT) have been commonly employed as the templates, to react with Si or SiO vapors at high temperatures and under ultra-low pressures [12-15]. Such a synthesis route results in crystalline SiC nanotubes and nanowires. However, it is difficult to use the technique and maintain uniformity and control on the final product. The approach is also costly because the process must operate at high temperatures and low pressures for long periods of time. Another method for producing SiC nanostructures involves catalyst-assisted chemical-vapor deposition (CVD), during which silicon and carbon-containing compounds are reacted on metallic catalysts [11,16-18].

A third method involves the use of templates of anodic aluminum oxide (AAO) and utilizing the CVD technique, or a solution deposition of polymeric precursors, in order to produce SiC nanotubes and nanowires inside the substrates. Li et al. [19], for example,

prepared SiC nanowires inside the AAO channels by reacting SiO vapors with C_3H_6 at 1230 ^oC. Xu et al. [20] reported the preparation of amorphous SiC nanorods inside the AAO templates by the RF sputtering. Yen et al. [21] reported the preparation of silicon oxycarbide nanotubes by infiltration of polycarbosilane (PCS) into the AAO templates, followed by pyrolysis at 1100 ^oC in a vacuum furnace. Cheng et al. [22] prepared SiC nanotubes by the CVD of SiC polymeric precursor with the trade-name SP-4000 (Starfire® Systems, Inc., with nominal structure $[SiH_2CH_2]_n$, n=2-8, including branched and cyclic isomers [23]) and the solution infiltration of polysilaethylene (PSE) into the AAO at 1000 ^oC. The CVD technique produced uniform SiC nanotubes, but the solution deposition technique produced SiC nanofibers with a bamboo-like structure, which were explained to be the result of the Rayleigh fluid instability [24].

In this paper we report on the synthesis of uniform porous SiC nanofibers by infiltration and pyrolysis of allyl-hydridopolycarbosilane (AHPCS) into the AAO templates. The AHPCS is a hyperbranched structure of the type, $[R_3SiCH_2\text{-}]_x[\text{-}SiR_2CH_2\text{-}]_y[{=}SiR(CH_2\text{-})]_z[{\equiv}Si(CH_2\text{-})]_l$, R= H or allyl ($CH_2{=}CHCH_2$-) [22], which is a polymeric precursor that can be converted to SiC with a near stoichiometric ratio at relatively low temperatures in an inert atmosphere, without the need for any catalyst or oxygen for cross-linking [5,25]. Aside from the work of Cheng et al. [22], we are not aware of any other reports on the solution infiltration method used for producing SiC nanofibers. The study of Cheng et al. produced nanofibers with a bamboo-like structure. The main goal of the present paper is, however, studying the effect of polystyrene (PS), as a pore former, on the morphology and physical property of the nanofibers. Such nanofibers are being used by our group in the preparation of nanoporous hydrogen perm-selective membranes

[26]. Due to their very high surface areas (see below), they could potentially also be used as catalyst supports.

2. Experimental

The AAO disks (Anodisc®, Whatman Inc.) were used as the templates. They are asymmetric alumina disks consisting of a top layer with a thickness of 2 μm and an average pore size of about 100 nm, sitting on top of a support layer with a thickness of 58 μm and an average pore size of about 250 ±50 nm [27].

The solution that contained the SiC precursor was prepared by dissolving AHPCS with a concentration of either 20 or 30 wt% (SMP-10, Starfire® Systems, Inc.) in hexane. In order to study the effect that adding polystyrene to the AHPCS solution has on the nanofiber morphology, polystyrene was added to the AHPCS in toluene solutions. 5, 15, and 30 wt% of the PS (on a per AHPCS basis, i.e., gram of the PS per gram of the AHPCS in the solution) were added to a 20 wt% solution of the AHPCS in toluene. Prior to immersing the AAO disk templates in the solutions, they were dried at 70 ^{o}C in air for 1 h. The templates, after being infiltrated by the solutions, were heated in flowing Ar in a tube furnace (Lindberg/Blue, Model STF55433C) at a rate of 2 °C/min, first to 200 °C at which they were kept for 1 h, then to 400 °C where they were kept for 1 h, and finally to 750 °C at which they were kept for an additional 2 h for pyrolysis. Subsequently, they were cooled down to the room temperature in flowing Ar with a cooling rate of 3 °C/min. After the pyrolysis, the disks were immersed and dissolved in a 6 M NaOH solution for 48 h. The SiC nanofibers were separated by centrifuging the solution at 2600 rpm for 20 min, and were then washed several times with deionized water. The process of washing

with water and re-centrifuging was continued until the pH of the solution was at the neutral value. The morphology of the resulting nanofibers was then studied using the SEM (Cambridge 360) and TEM (Philips EM420). The nitrogen adsorption isotherm of the nanofibers was measured at 77 K with a Micromeritics ASAP 2010 apparatus.

3. Results and Discussion

In what follows we present and discuss the results, and describe the effect of several important factors on the formation of the nanofibers**.**

3.1. Effect of AHPCS concentration on the SiC nanofiber formation

The photographs of the two sides of the AAO templates, shown in Fig. 1, indicate that their top layer has an average pore size of about 100 nm, sitting on a bottom layer with an average pore size of about 250 nm. Using low concentrations (2-5 wt%) of the AHPCS in hexane as the starting solution did not yield any SiC nanofiber. This may be due to the fact that, at such concentrations the polymer matrix is below the percolation threshold [28], i.e., the minimum volume fraction for the formation of stable and connected structures, or that weak structures form that break down during or after the removal of the template.

Using higher concentrations of the AHPCS, such as 20 wt% and 30 wt%, made it possible to form SiC nanofibers. Although 20 wt% of polymer translates to 14 vol%, which is slightly below the percolation threshold for *random* continuous materials (about 17%), i.e., the minimum volume fraction at which a continuous macroscale matrix is formed, one should recognize that the polymer does not necessarily have a random

structure. It is likely that there are some positive correlations in the polymer morphology, which result in a lower percolation threshold [28]. Figure 2 shows the SEM and TEM photographs of the SiC nanofibers, obtained using 30 wt% solutions of the AHPCS in hexane. The diameter of the nanofibers is, as expected, within the range of the template pore sizes which is about 250 nm.

3.2. Effect of polystyrene concentration on the SiC nanofiber morphology

Polystyrene has been used by several investigators as a pore former, in order to improve the separation characteristics of the PCS-derived SiC membranes [29-32]. Such membranes possess high permeances, which are the result of the contribution of the gaseous products of polystyrene pyrolysis to the formation of the 3D material structure. On the other hand, if the material is intended for use in the membrane formation, one should be cautious in indiscriminately adding polystyrene, as it may segregate and form distinct PS ellipsoidal domains within the PCS bulk after solvent removal, which would then result in defects during the PS decomposition, leading to adverse impact on the membrane selectivity [31,32]. Here, the idea behind adding the PS to the AHPCS precursor during the preparation of the various SiC nanofibers was to investigate whether the addition impacts the morphological characteristics of the materials in a way similar to that observed during the formation of SiC nanoporous membranes. One expects that, by increasing the amount of the PS added to the AHPCS precursor solution, one can produce a broad range of morphologies, ranging form the uniform porous nanofibers that are produced in the absence of the PS, to porous nanofibers containing large ellipsoidal

porous domains, and nanotubes formed when the polystyrene domains segregate and create a central sacrificial PS core.

Figure 3 shows the nanofibers that are formed by adding the PS, at a concentration of 10 wt% (g of the PS/g of the AHPCS), to the 30 wt% AHPCS in toluene solution. The selected-area electron diffraction (SAED) pattern in Fig. 3 reveals the amorphous structure of the nanofibers. During the pyrolysis, increasing the temperature causes evaporation of the solvents and, thus, leads the stable solution to cross the binodal or spinodal curves of the ternary (AHPCS-toluene-PS) phase diagram, and form polymer-rich and polymer-lean domains seen in the phase-inversion phenomenon. Phase segregation of the PS inside the nanofibers into ellipsoidal domains and their complete decomposition during the pyrolysis result in the formation of hollow ellipsoidal regions inside the nanofibers. This is indicated more clearly in the high resolution TEM images of two nanofibers that were produced from the pyrolysis of the 10 wt% PS in the AHPCS precursor solution; see Fig. 4. Visible in these photographs is the presence of hollow ellipsoidal domains. Further careful examination of the nanofibers indicates that, the region in the vicinity of the hollow domains is darker than the rest of the nanofiber in the bright field images. This indicates that, as a result of the interaction between the PS and AHPCS during the pyrolysis, the boundary regions have a denser structure. The high resolution TEM photograph of the nanofibers shown in Fig. 4 also reveals a porous structure, which was expected from our previous work on the fabrication of the AHPCS-derived SiC membranes [5,6]. Within the resolution of Fig. 4, pores as small as 5 nm can be discerned. The XRD investigations of the nanofibers confirm an amorphous structure,

which is expected for the SiC materials generated by the pyrolysis of the AHPCS at the relatively low temperature at which we prepared the nanofibers [33].

Further increase of the PS wt% fraction to 15 wt% (g of the PS/g of AHPCS) in a 30 wt% AHPCS in toluene solution resulted in an opaque solution, which indicated that the solution was in the two-phase region of the ternary phase (AHPCS-toluene-PS) diagram. Thus, further addition of the PS to the base case of 30 wt% AHPCS in toluene solution was not possible.

Lowering the concentration of the AHPCS allows one to prepare stable precursor solutions that contain larger fractions of the PS in the AHPCS solution. Therefore, a number of precursor solutions were prepared by adding the PS to a 20 wt% AHPCS in toluene. Precursor solutions that were transparent and stable were prepared by dissolving 5, 15, and 30 wt% of the PS (g of the PS/g of AHPCS) into a 20 wt% AHPCS in toluene. As can be seen in Fig. 5, increasing the concentration of the PS increases the number of the hollow domains in the fibers. With 30 wt% of the PS in the AHPCS solution one begins to see the formation of the hollow fibers. They are probably formed as the result of the coalescence of the hollow domains. Further increase of the PS fraction (to 65 wt% per AHPCS) resulted in opaque solutions, which were not studied further.

3.3. Effect of polystyrene concentration on the physical properties of the SiC nanofiber

Figure 6 presents the nitrogen adsorption isotherm of the SiC nanofibers, prepared using the 10 wt% PS in a 30 wt% AHPCS in toluene. The fibers have a high BET surface area of 457 m^2/g with a total pore volume of 0.79 cm^3/g which translates to a high porosity of about 70%. The Horvath-Kawazoe (HK) pore size distribution of the

nanofibers is characterized by a sharp peak at a pore size of about 4.5 Å, with a corresponding pore volume of 0.16 cm^3/g in the microporous region. Analysis of the BJH pore size distribution indicates an average pore size of about 7 nm in the mesoporous region of the material.

Figure 7 shows the nitrogen adsorption isotherm of the SiC nanofibers, prepared using the 30 wt% AHPCS in toluene, without adding the PS. In this case the fibers have a lower BET surface area of 366 m^2/g with a total pore volume of 0.78 cm^3/g. The HK pore size distribution of the nanofibers is again characterized by a sharp peak at a pore size of about 4.5 Å, with a corresponding pore volume of 0.12 cm^3/g in the microporous region, and a slightly larger BJH average pore size of about 8 nm. Higher surface areas for the SiC samples, prepared with the addition of the PS to the PCS solutions, were also reported by Suda et al. [31], who studied the effect of adding the PS on the formation of the SiC membranes. The higher surface areas were explained [31] to be due to the release of gases during the PS decomposition, and their contribution to the formation of the 3D structure.

4. Summary

Uniform porous SiC nanofibers with high surface area were fabricated using a template technique. Adding polystyrene, as a pore former, to the precursor AHPCS solution resulted in SiC nanofibers with ellipsoidal hollow domains inside the fibers, which is the result of phase segregation during the drying process. Increasing the concentration of the PS in the starting AHPCS precursor solution resulted in nanofibers with an increased fraction of hollow domains, and even in the formation of some hollow fibers. Formation

of the hollow domains in the material is interesting scientifically and important from a practical view point, and opens the way to encapsulation of other materials inside the nanofibers, if used instead of the PS.

Acknowledgment

This work was supported in part by the National Science Foundation and the Department of Energy**.**

References

1. Casady JB, Johnson RW: Status of silicon carbide (SiC) as a wide-bandgap semiconductor for high-temperature applications: A review, Solid-State Electronics 1996 (39)1409.

2. Spetz AL, Tobias P, Baranzahi A, Martensson P, Lundstrom I: Current status of silicon carbide based high-temperature gas sensors, IEEE Transactions on Electron Devices 1999 (46) 561.

3. Mpourmpakis G, Froudakis GE, Lithoxoos GP, Samios J, SiC nanotubes: A novel material for hydrogen storage, Nano Letters 2006 (6) 1581.

4. Pol VG, Pol SV, Gedanken A, Lim SH, Zhong Z, Lin J, Thermal decomposition of commercial silicone oil to produce high yield high surface area SiC nanorods. Journal of Physical Chemistry B 2006 (110) 11240.

5. Elyassi B, Sahimi M, Tsotsis TT, Silicon carbide membranes for gas separation applications. Journal of Membrane Science 2007 (288) 290.

6. Elyassi B, Sahimi M, Tsotsis TT, A novel sacrificial interlayer-based method for the preparation of silicon carbide membranes, Journal of Membrane Science 2008 (316) 73.

7. Rosenbloom AJ, Sipe DM, Shishkin Y, Ke Y, Devaty RP, Choyke WJ, Nanoporous SiC: A candidate semi-permeable material for biomedical applications, Biomedical Microdevices 2004 (6) 261.

8. Vannice MA, Chao YL, Friedman RM, The preparation and use of high surface-area silicon-carbide catalyst supports, Applied Catalysis 1986 (20) 91.

9. Pham-Huu C, Keller N, Ehret G, Ledoux MJ, The first preparation of silicon carbide nanotubes by shape memory synthesis and their catalytic potential, Journal of Catalysis 2001 (200) 400.

10. Nhut JM, Vieira R, Pesant L, Tessonnier JP, Keller N, Ehret G, Pham-Huu C, Ledoux MJ, Synthesis and catalytic uses of carbon and silicon carbide nanostructures, Catalysis Today 2002 (76) 11.

11. Silenko PM, Shlapak AN, Tomila TV, Bykov AI, Kuz'menko LN, Okun IY, Ragulya AV, Fe-catalyzed synthesis of SiC nanofibers from methyltrichlorosilane. Inorganic Materials 2008 (44) 388.

12. Taguchi T, Igawa N, Yamamoto H, Jitsukawa S, Synthesis of silicon carbide nanotubes, Journal of the American Ceramic Society 2005 (88) 459.

13. Sun XH, Li CP, Wong WK, Wong NB, Lee CS, Lee ST, Teo BK, Formation of silicon carbide nanotubes and nanowires via reaction of silicon (from disproportionation of silicon monoxide) with carbon nanotubes, Journal of the American Chemical Society 2002 (124) 14464.

14. Keller N, Pham-Huu C, Ehret G, Keller V, Ledoux MJ, Synthesis and characterisation of medium surface area silicon carbide nanotubes, Carbon 2003 (41) 2131.

15. Wu RBB, Yang GY, Pan Y, Chen JJ, Synthesis of silicon carbide nanorods without defects by direct heating method, Journal of Materials Science 2007 (42) 3800.

16. Leonhardt A, Liepack H, Biedermann K, Thomas J, Synthesis of SiC nanorods by chemical vapor deposition, Fullerenes Nanotubes and Carbon Nanostructures 2005 (13) 91.

17. Xie ZF, Tao DL, Wang JQ, Synthesis of silicon carbide nanotubes by chemical vapor deposition, Journal of Nanoscience and Nanotechnology 2007 (7) 647.

18. Kang BC, Lee SB, Boo JH, Growth of beta-SiC nanowires on Si(100) substrates by MOCVD using nickel as a catalyst, Thin Solid Films 2004 (464) 215.

19. Li ZJ, Zhang JL, Meng A, Guo JZ, Large-area highly-oriented SiC nanowire arrays: Synthesis, Raman, and photoluminescence properties, Journal of Physical Chemistry B 2006 (110) 22382.

20. Xu DY, He ZW, Guo YP, Wang YY, Fabrication of quasi-one dimension silicon carbide nanorods prepared by RF sputtering, Microelectronic Engineering 2006 (83) 89.

21. Yen HM, Jou S, Chu CJ, Si-O-C nanotubes from pyrolyzing polycarbosilane in a mesoporous template, Materials Science and Engineering B-Solid State Materials for Advanced Technology 2005 (122) 240.

22. Cheng QM, Interrante LV, Lienhard M, Shen QH, Wu ZZ, Methylene-bridged carbosilanes and polycarbosilanes as precursors to silicon carbide-from ceramic composites to SiC nanomaterials, Journal of the European Ceramic Society 2005 (25) 233.

23. Gallis S, Futschik U, Castracane J, Kaloyeros AE, Efstathiadis H, Sherwood W, Hayes S, Fountzoulas CG, Thermal chemical vapor deposition of silicon carbide films as protective coatings for microfluidic structures, Materials Research Society Symposium Proceedings 2003 85-93.

24. Chen JT, Zhang MF, Russell TP, Instabilities in nanoporous media, Nano Letters 2007 (7) 183.

25. Interrante LV, Whitmarsh CW, Sherwood W, Wu H-J, Lewis R, Maciel G, High yield polycarbosilane precursors to stoichiometric SiC. Synthesis, pyrolysis and application, Mater. Res. Soc. Symp. Proc. 1994 593-603.

26. Elyassi B, Sahimi M, Tsotsis TT, Application of Nanoporous Fillers in Silicon Carbide Membranes, International Congress on Membranes and Membrane Processes (ICOM 2008), Honolulu, Hawaii USA, 2008.

27. Vermisogiou EC, Pilatos G, Romanos GE, Karanikolos GN, Boukos N, Mertis K, Kakizis N, Kanellopoulos NK, Synthesis and characterization of carbon nanotube modified anodised alumina membranes, Microporous and Mesoporous Materials 2008 (110) 25.

28. Sahimi M, Heterogeneous Materials I, New York: Springer, 2003.

29. Li ZY, Kusakabe K, Morooka S, Preparation of thermostable amorphous Si-C-O membrane and its application to gas separation at elevated temperature, Journal of Membrane Science 1996 (118) 159.

30. Suda H, Yamauchi H, Uchimaru Y, Fujiwara I, Haraya K, Preparation and gas permeation properties of silicon carbide-based inorganic membranes for hydrogen separation, Desalination 2006 (193) 252.

31. Suda H, Yamauchi H, Uchimaru Y, Fujiwara I, Haraya K, Structural evolution during conversion of polycarbosilane precursor into silicon carbide-based microporous membranes, Journal of the Ceramic Society of Japan 2006 (114) 539.

32. Li ZY, Kusakabe K, Morooka S, Pore structure and permeance of amorphous Si-C-O membranes with high durability at elevated temperature, Separation Science and Technology 1997 (32) 1233.

33. Zheng J, Akinc M, Green state joining of SiC without applied pressure, Journal of the American Ceramic Society 2001 (84) 2479.

Captions:

Fig. 1. The two sides of the AAO templates, showing a pore diameter of about 100 nm on one side, and about 250 nm on the other side.

Fig. 2. The (A) TEM, and (B) SEM of the SiC nanofibers.

Fig. 3. The (A) TEM, and (B) SEM photographs of the SiC nanofibers, prepared by adding 10 wt% of the PS to the AHPCS solution. Hollow domains can be seen as the result of the PS decomposition. The embedded SAED in the TEM picture indicates the amorphous nature of the fibers

Fig. 4. The TEM picture of the SiC nanofibers, prepared by addition of 10 wt% of the PS (AHPCS basis) to the solution. The nanofibers have a porous structure, with hollow ellipsoidal domains, resulting from the PS decomposition.

Fig. 5. The TEM pictures of the SiC nanofibers and hollow fibers, prepared by adding, (A) 5, (B) 15, and (C) 30 wt% PS (AHPCS basis) to a 20 wt% AHPCS in toluene solution.

Fig. 6. Nitrogen adsorption isotherm of the SiC nanofibers, formed by addition of 10 wt% of the PS (AHPCS basis), together with the HK pore size distribution for the microporous region.

Fig. 7. Nitrogen adsorption isotherm of the SiC nanofibers, prepared by 30 wt% of the AHPCS in toluene, together with the HK pore size distribution for the microporous region.

Figure 1

Click here to download high resolution image

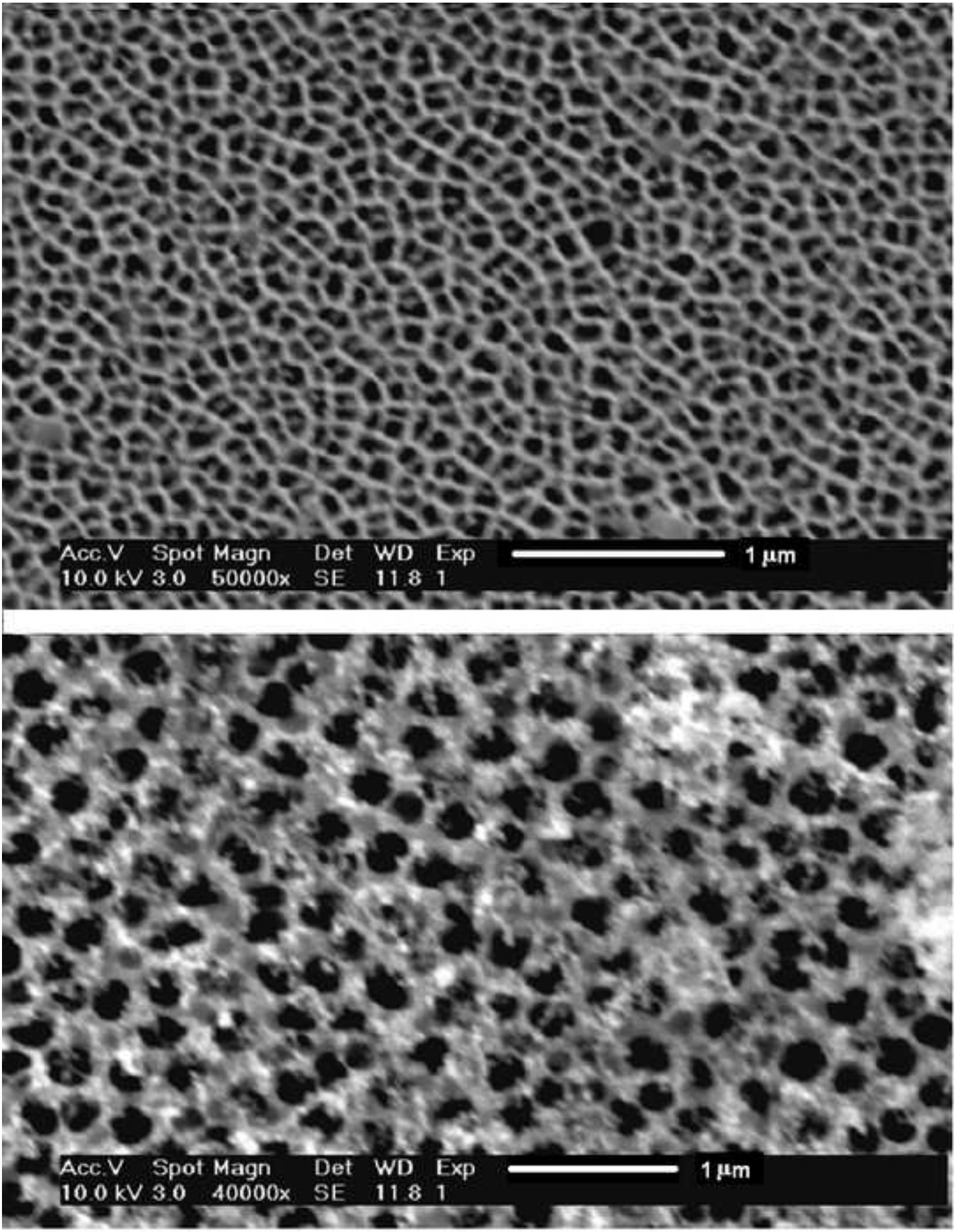

Figure 2

Click here to download high resolution image

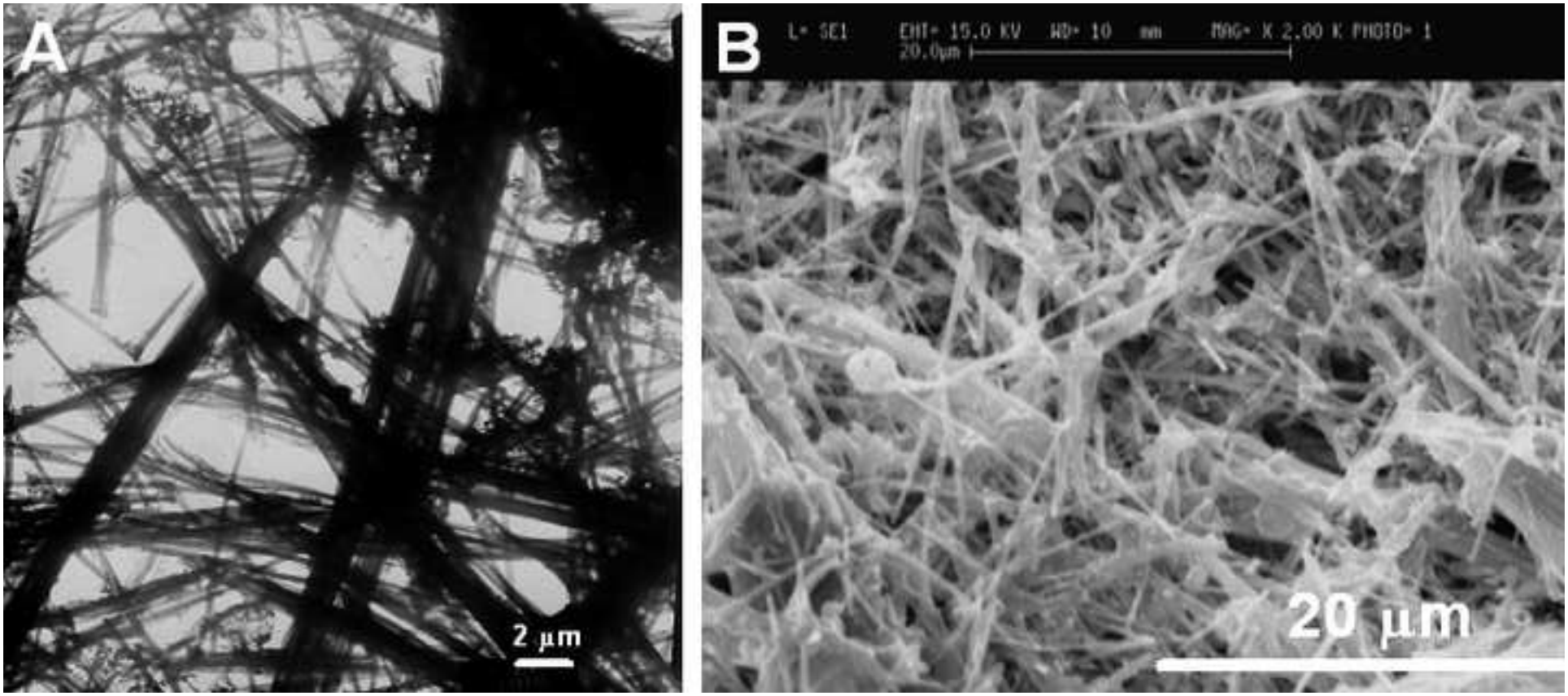

Figure 3

Click here to download high resolution image

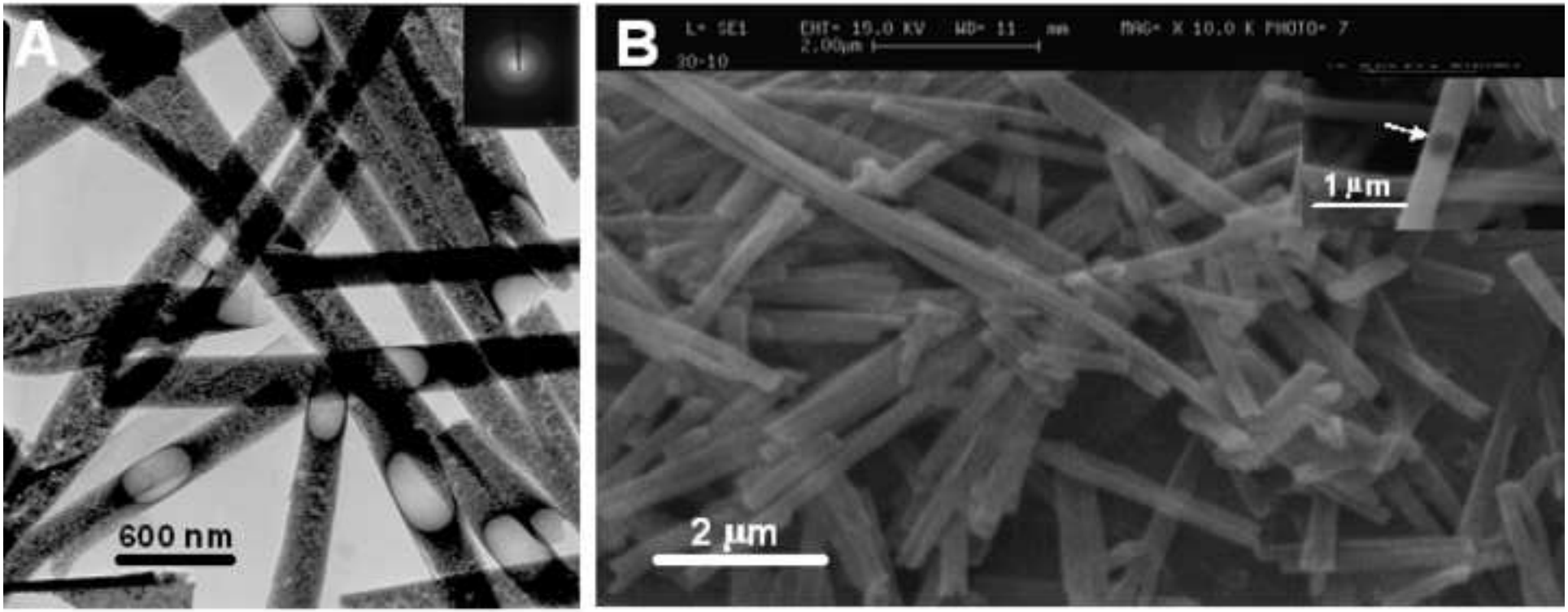

Figure 4

Click here to download high resolution image

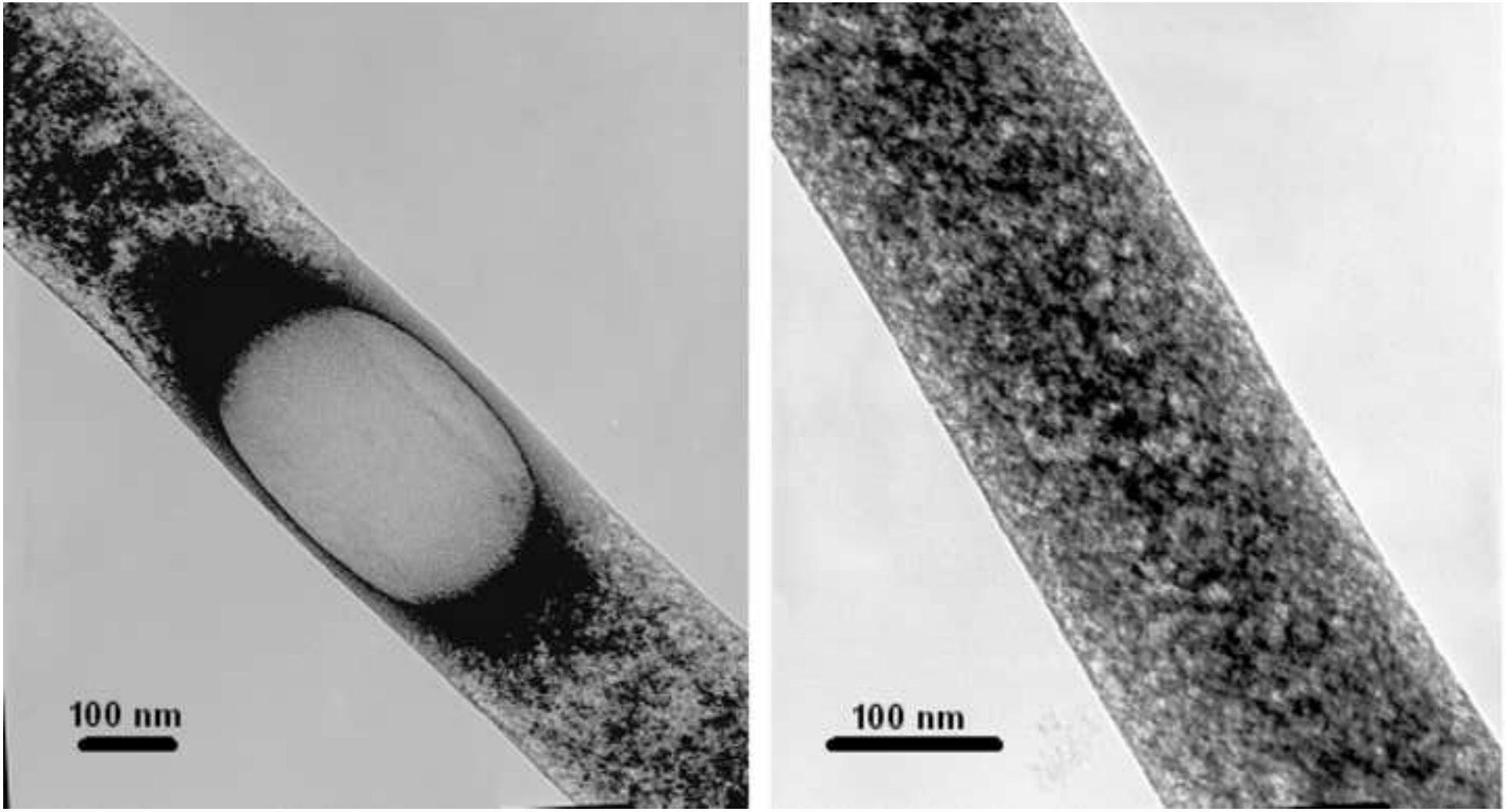

Figure 5

Click here to download high resolution image

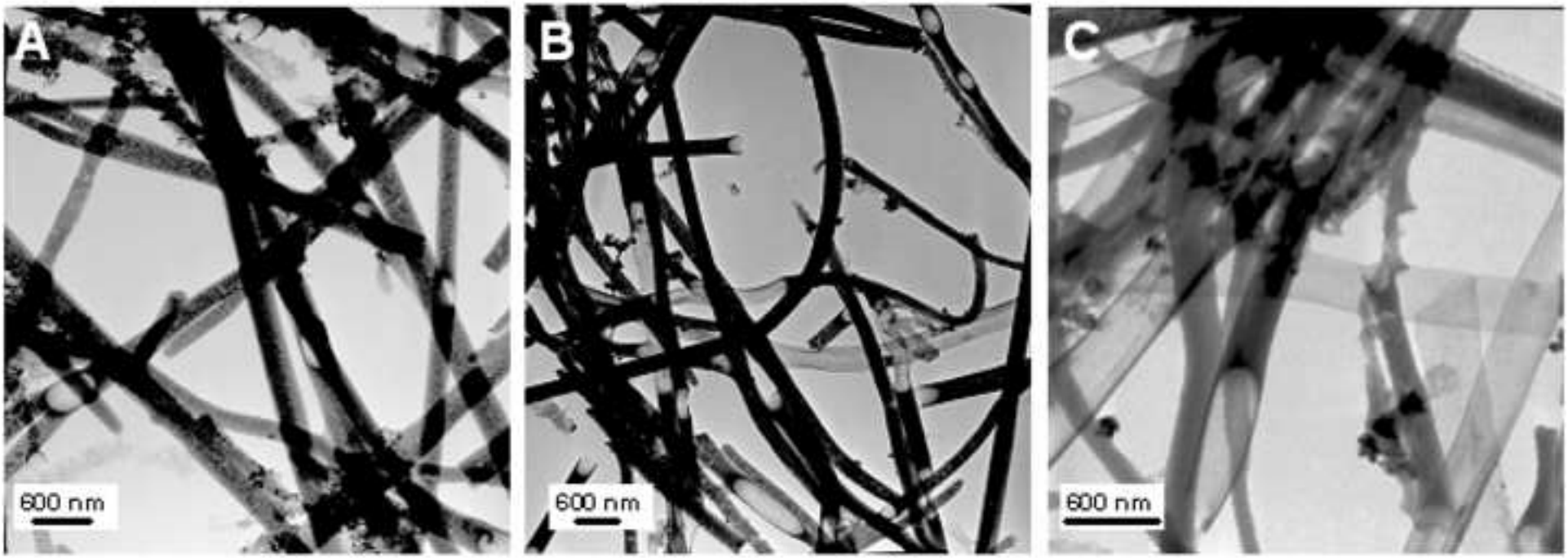

Figure 6

Click here to download high resolution image

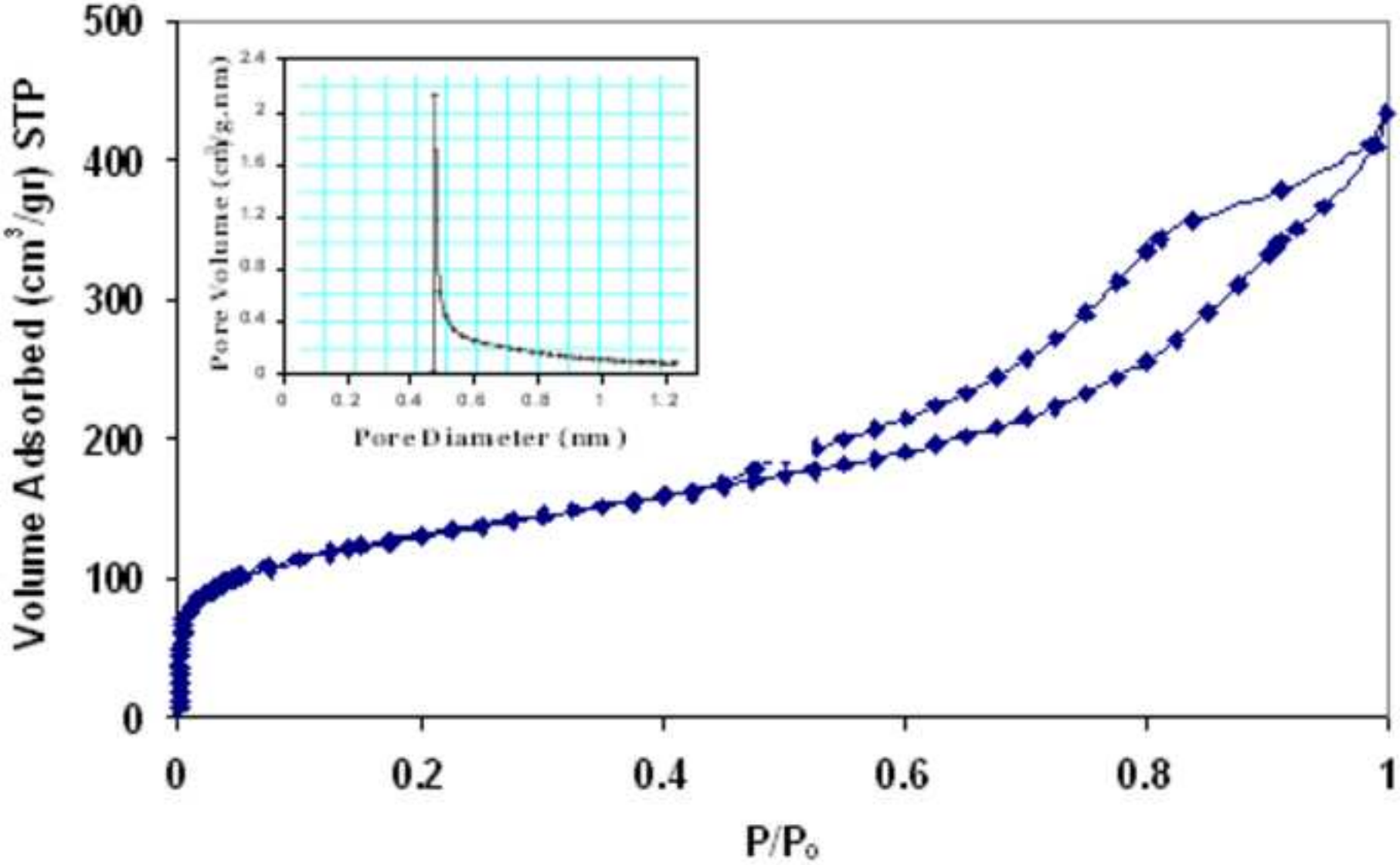

Figure 7

Click here to download high resolution image